Study of half Heusler and related structures as high-temperature thermoelectrics

A thesis

Submitted in partial fulfillment of the requirements

Of the degree of

Doctor of Philosophy

By

Kumar Saurabh

20142032

INDIAN INSTITUTE OF SCIENCE EDUCATION AND RESEARCH (IISER) PUNE

where tomorrow's science begins today

June 28, 2022

Certificate

Certified that the work incorporated in the thesis entitled *'Study of half Heusler and related structures as high-temperature thermoelectrics'*, submitted by *Kumar Saurabh* was carried out by the candidate, under my supervision. The work presented here or any part of it has not been included in any other thesis submitted previously for the award of any degree or diploma from any other University or institution.

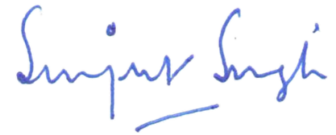

Date: June 28, 2022

Surjeet Singh
(Supervisor)

Declaration

I declare that this written submission represents my ideas in my own words and where others' ideas have been included, I have adequately cited and referenced the original sources. I also declare that I have adhered to all principles of academic honesty and integrity and have not misrepresented or fabricated or falsified any idea/data/fact/source in my submission. I understand that violation of the above will be cause for disciplinary action by the Institute and can also evoke penal action from the sources which have thus not been properly cited or from whom proper permission has not been taken when needed.

Date: June 28, 2022

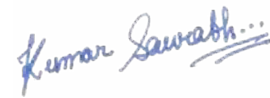

Kumar Saurabh
Roll No - 20142032

I would like to dedicate this thesis to my Mummy and Papa.

Acknowledgements

I am thankful to my supervisor Dr. Surjeet Singh for continuous guidance and support. His critical comments and focus on details have shaped this work. I learned many things such as the importance of critical thinking and asking difficult questions in science. I would like to thank and pay my regards to Late Dr. Ashutosh Abhyankar, whom we lost in COVID. He guided me during my initial research advisory committee(RAC) meetings. I would like to thank my other RAC members Dr. Aparna Deshpande and Dr. Prasenjet Ghosh for their constant guidance and support. A due thanks to Dr. Luminita Harnagea for teaching me many things like solid-state synthesis and crystal growth. I am also thankful to her for lots of cakes and pies. You have been a great source of inspiration to me. This work would not have been completed without the scientific collaboration with Dr. Prasenjit Ghosh. He was always kind enough to listen to my queries and to guide me in my work. I would like to thank Ankit and Vineet for all the calculations and discussions. I would also like to thank Gautam for our various discussions related to theoretical aspects of thermoelectrics.

I am sincerely thankful to IISER Pune for providing infrastructure and a great atmosphere. I would like to thank Nilesh, Anil, Sudheer, Prashant, Kartikeyan, and all other technical staff at IISER who helped me in my research. I would like to thank all administration staff, especially Tushar, Prabhakar, and Sayalee. I am thankful to funding agencies IISER Pune, CSIR and economic support from the endowment funds received from the Scivic Engineering Pvt Ltd. and Innoplexus Consulting Services Pvt Ltd.

A special thanks to all my present and past lab mates. I got to learn a lot in the lab from Rabindra, Prachi, and Giri. I cherish my interactions, fun, and conversations with them. Dibyata, you are fantastic, and I learned a lot from our discussions. We ganged up many a time to tease others. My time in lab 210 is wonderful also because of Sanchayeta, Prakash, Nupur, Pragna, Anupam, Ankit, Navita, Sagar, Nashra, Dinesh, and Rupesh. Navita and Ankit are taking over the thermoelectric group and I believe they will do much better than me. Ankit came to our lab to enlighten us with DFT and Raman measurements. Nashra Ji, Sagar, and Dibyata taught the whole lab about magnetism in various group meetings. I

learned a lot from all of you. From my past lab, I got friends like Amit, Anweshi, Sumit, and Mohit. You all inspire me in different ways. I would like to thank all colleagues at h-cross and the main building with whom I interacted in one or another way especially Chetan, Imran, Shatru, Avirup, Shruti, and Ashoka Ji.

I was blessed with a lot of friends at IISER. I want to thank all of them for making my life at IISER wonderful. Rohit and Vinay are the people who supported me with my decision to join IISER. I would like to thank Rohit, Vinay, and Gaurav to support me in all possible ways, they have been more than friends and family to me. I would like like to thank Nittu, Saurabh Pandey, Jojo Di, and JiJa Ji. They have been my support in Pune outside IISER. Amit Jijaji, you have been a friend and family to me. Dr. Argha Banerjee, I came to know him through a TA course, and then he has been my best buddy at IISER. I would like to thank him for all food, trips, and wonderful discussions (cultural, scientific, music, etc). I am thankful to Sayali for being my friend and for our small talks. I respect you for your intelligence and simplicity. I would like to acknowledge the support and love from three gems, Mayur, Deepak, and Yashaswi. I met them at IISER and now they are a big part of my life. We laughed, cooked, ate, and fought a lot. Mayur has been my only support during my last days at IISER when we were left alone. Though some of your actions were just to irritate me, I still love you Bhai. Yashaswi is someone with lots of courage and a great sense of humor. I am thankful to him for endless chat and lots of drama. Deepak recently got married and I could not attend his wedding still I know he will be by my side whenever I will need him. Now comes a turn to acknowledge the most important one for me whom I met at IISER. I met Shalini in 2014; we were batchmates but we became friends in 2016. Shalini accompanied me throughout my journey at IISER and outside IISER. We cooked together, ate together, went walking together and we also had several fights. She has the talent to fight with me but she is my bestie. She has seen the worst of me and tolerated my nonsense. She became my family and was standing by my side in all the good and the bad times of my life, from staying at the hospital when my sister was sick, celebrating and cooking at my home on festivals, to taking care of me when I was injured. She was even financing me when I was short of money. I learned shopping from her, she corrected my mistakes and she tortured me with her sarcasm. Her intelligence, general knowledge, and attitude toward work are something I admire the most. I cannot thank you enough for all this but I know it is just the beginning we have a long way to go.

I owe my teachers especially Manish Mishra Sir, Hari Sir, and Suman Sir for inspiring me in my life. Hari Sir, I can never be able to say enough thank you to you for all your support and motivation.

Lastly, I would like to thank my family for their endless love, support, and

comfort. My father has prepared lots of delicious dishes for me and my friends. My sisters have been my pillars, as they took care of everything at home when I was busy in my hostel life. Finally, I would like to thank God, for helping me at each step. Please, let my mom know I didn't stop because of her cancer as she was always worried about me and I will try hard to achieve all I can.

Date: June 28, 2022

Kumar Saurabh

Abbreviation

- **BSE:** *Backscattered Electron*
- **DSC:** *Diffrential Scanning Calorimetry*
- **DOS:** *Density of states*
- **DH:** *Double Heusler*
- **EDX:** *Energy Dispersive X-ray*
- **EU:** *European Union*
- **FFT:** *Fast Fourier Transform*
- **FESEM:** *Field Emission Scanning Electron Microscope*
- **FEG:** *Field Emission Gun*
- **FH:** *Full Heusler*
- **Gt:** *Gigatonne*
- **HH:** *Half Heusler*
- **HRTEM:** *High Resolution Transmission Electron Microscope*
- **IR:** *Infra Red*
- **IFFT:** *Inverse Fast Fourier Transform*
- **LFA:** *Laser Flash Analyzer*
- **LSR:** *Linseis Seebeck and Resistivity*
- **MFP:** *Mean Free Path*
- **Mtoe:** *Megatonne Oil Equivalent*
- **PGEC:** *Phonon Glass Electron Crystal*

- **PV:** *Photovoltaics*
- **PF:** *Power Factor*
- **RTEG:** *Radioisotope Thermoelectric generator*
- **SEM:** *Scanning Electron Microscope*
- **SAED:** *Selected Area Electron Diffraction*
- **TWh:** *Tera Watt hour*
- **TEG:** *Thermoelectric Generator*
- **TGA:** *Thermal Gravimetric Analysis*
- **VEC:** *Valence Electron Counting*

Abstract

Motivated by recent advancement in half-Heusler thermoelectric materials, here we studied the phase stability and thermoelectric properties of some half-Heuslers (HH) and their derivatives. From within the HH family, the HH alloys and compounds with a valence electron count (VEC) 18 per formula unit are of particular interest in the thermoelectric research as they exhibit a semiconducting behavior due to a finite energy gap between their filled bonding orbitals and empty antibonding orbitals.

Recently, it was shown that some HH compounds with VEC 19 (for example, NbCoSb) also exhibit a semiconducting behavior. This is puzzling since the extra electron is expected to give rise to a metallic behavior. Later, Xia et al. found that NbCoSb cannot be formed in a phase pure HH structure in the 111 stoichiometry but only in the stoichiometry $Nb_{0.8}CoSb$, i.e., with 20% cationic vacancy [205]. These vacancies contribute to the lowering of the lattice thermal conductivity; however their presence also affects the carrier mobility adversely.

After giving an overview of the recent thermoelectric research on HH materials in chapter 1 and the experimental techniques used in this thesis in chapter 2, in chapter 3 we study $Nb_{0.8+\delta}CoSb$ ($\delta = 0.03$) doped with Sn at the Sb site (a slight Nb excess - that is, $0.8 + \delta$ instead of 0.8 helps in electron doping and hence tuning the carrier density). Sn doping for Sb in $Nb_{0.83}CoSb$ plays two vital roles: (i) with increasing Sn doping, excess Nb concentration δ in the $Nb_{0.8+\delta}CoSb$ can be increased at least upto 0.1, which is more than 0.05 without Sn-doping, (ii) since Nb is strongly electropositive, small variations in Nb results in large fluctuations in the carrier concentration (i.e., the tuning is coarse). We show that Sn doping helps fine tune the carrier concentration to obtain an optimum concentration for maximizing the power factor. In the Sn-doped samples we obtained a zT exceeding little over 1 near 1100 K, which is 20% higher than the value previously reported for the undoped or Ni doped $Nb_{0.8+\delta}CoSb$. Detailed electronic structure calculations are done to understand the role of Sn-doping in the observed zT enhancement. We also performed Raman spectroscopy and HRTEM to investigate the short-range vacancy ordering in these compounds.

In chapters 4 and 5, we study TiNiSi structure-type compounds. These compounds have an orthorhombic structure but with Heusler-like tetrahedral coordi-

nation [100, 12, 18]. In chapter 4, we investigated five such orthorhombic ternary compounds, namely, ZrNiSi, ZrNiGe, NbCoSi, HfNiSi, and ZrNiSb [162]. Based on a theoretical study, Guo et al. [58] had predicted these compounds to stabilize with the HH structure at room temperature. However, the arc-melted samples crystallize with the TiNiSi-type orthorhombic structure. We studied the phase stability and thermoelectric properties of these samples. We show the presence of a pseudo-gap like feature in their electronic density of states except ZrNiSb where there is finite density of states at the Fermi energy. Detailed electronic structure and density of states were obtained to understand their bonding mechanism and semi-metallic behavior. In chapter 5, we have investigated the effect of doping ZrNiSi with Sb at the Si site. The solubility of Sb in ZrNiSi at the Si site is as low as 5 %, beyond which it undergoes a spinodal-like decomposition. The higher doping leads to an enhanced power factor and lower thermal conductivity. We show that zT of ZrNiSi increases by more than an order of magnitude by a small Sb doping. Effect of annealing in the Sb doped samples undergoing spinodal-like decomposition is also studied. We show that annealing leads to a small reduction in the thermoelectric performance.

Recently, double Heuslers (DH) have gained interest in thermoelectric research. Two or more elements randomly occupying the same Wyckoff position create a highly disordered structure which helps in reducing the thermal conductivity [59, 6]. In chapter 6, we study some new double Heuslers (DH) that were synthesized by mixing orthorhombic ZrNiSb (VEC 19) and cubic TiFeSb (VEC 17). Both these end-members by themselves do not exist in the pure phase. The new compounds obtained have compositions $(ZrNiSb)_{1-x}(TiFeSb)_x$ where (x = 0.4, 0.45, 0.5, 0.55, 0.6, and 0.7). The sample x = 0.5, was nearly pure with a cubic HH structure, XYZ, with X site randomly occupied by Zr and Ti, and Y site by Ni and Fe. We synthesized composition around x = 0.5 and found that compositions with x > 0.5 show a p-type behavior and those with x < 0.5 n-type. We studied these samples, for their phase purity, microstructure, and thermoelectric properties. They exhibit a very low thermal conductivity due to the presence of a high level of atomic disorder inherent to the DH alloys. For these samples, the highest thermoelectric figure of merit zT turned out to be 0.125 for the p-type and 0.2 for the n-type samples. In chapter 7, the summary of the work carried out and future directions that this work has opened up are presented.

Publications

1. **Enhancing the thermoelectric properties of TiNiSi structure-type ZrNiSi by Hf and Sb doping**; **Kumar Saurabh**, Ankit Kumar, Prasenjit Ghosh, Surjeet Singh *Phys. Rev. Materials 6(6), 065401 (2022).*

2. **Low thermal conductivity and semimetallic behavior in some TiNiSi structure-type compounds**; **Kumar Saurabh**, Ankit Kumar, Prasenjit Ghosh, Surjeet Singh *Phys. Rev. Materials 5(8), 085406 (2021)*

3. **Crystal growth of "Defective" Half-Heusler $Nb_{0.83}$CoSb**; **Kumar Saurabh**, Surjeet Singh, *under review*

4. **Crystal growth and characterization of CaTe: A potential topological material**; Luminita Harnagea, **Kumar Saurabh**, Prachi Telang, *Journal of Crystal Growth 556, 125988 (2021)*

5. **Pressure-induced phase transitions in the topological crystalline insulator SnTe and its comparison with semiconducting SnSe: Raman and first-principles studies**; Sukanya Pal, Raagya Arora, Subhajit Roychowdhury, Luminita Harnagea, **Kumar Saurabh**, Sandhya Shenoy, DVS Muthu, Kanishka Biswas, UV Waghmare, AK Sood *Phys. Rev. B 101(15), 155202 (2020)*

6. **Crystal growth of quantum materials: a review of selective materials and techniques**; Nashra Pistawala, Dibyata Rout, **Kumar Saurabh**, Rabindranath Bag, Koushik Karmakar and Luminita Harnagea, Surjeet Singh *Bulletin of Materials Science 45, 10 (2022)*

7. **Enhanced thermoelectric figure-of-merit in defective half-Heusler alloys NbCoSb**; **Kumar Saurabh**, Vineet Kumar Pandey, Ankit Kumar, Prasenjit Ghosh, Surjeet Singh, *to be submitted*

8. **Thermoelectric properties of double Heusler phase of TiFeSb(VEC 17) and ZrNiSb (VEC 19).**; **Kumar Saurabh**, Vineet Kumar Pandey, Ankit Kumar, Prasenjit Ghosh,Surjeet Singh, *to be submitted*

Contents

1 Introduction and Motivation **1**

1.1 Thermoelectricity: waste heat recovery 1

1.2 Fundamentals of Thermoelectrics 3

1.2.1 Thermoelectric effect 4

1.3 Charge transport 6

1.3.1 Electrical conductivity 7

1.3.2 Thermopower 8

1.4 Thermal transport 10

1.4.1 Thermal conductivity 10

1.4.2 Specific heat 13

1.4.3 Quality factor and weighted mobility 13

1.5 Strategies to enhance the thermoelectric figure of merit 14

1.5.1 Enhancing power factor 14

1.5.2 Strategies for decreasing the thermal conductivity 16

1.6 State of art 18

1.6.1 Chalcogenides 18

1.6.2 Oxides 20

1.6.3 Heuslers 20

1.6.4 Other materials 27

1.7 Synopsis of the work reported in this thesis 28

2 Experimental Methods **30**

2.1 Synthesis 30

2.1.1 Arc melting 30

2.1.2 Sintering the sample 33

2.1.3 Cutting and polishing 33

2.2 Structure and phase characterization 34

2.2.1 Powder x-ray diffraction 34

2.2.2 Scanning electron microscopy (SEM) 37

2.2.3 Transmission electron microscopy 39

2.2.4 Thermal Gravimetric Analysis /Differential Scanning Calorimetry . . . 42
2.3 Charge transport and thermal transport . . . 44
2.3.1 Hall measurements and Specific heat using PPMS . . . 44
2.3.2 Linseis LSR-3 . . . 47
2.3.3 Laser Flash Analyzer . . . 49

3 Sn Doping in Defective Half Heusler: $Nb_{0.83}CoSb$ 55
3.1 Introduction . . . 55
3.2 Experimental methods . . . 58
3.2.1 Experimental details . . . 58
3.3 Result and discussion . . . 61
3.3.1 Stuctural characterization . . . 61
3.3.2 Thermoelectric properties . . . 68
3.3.3 Computation results . . . 75
3.4 Summary and Conclusions . . . 91

4 Orthorhombic Ternary MTX Compounds 92
4.1 Introduction . . . 92
4.2 Experimental details . . . 94
4.3 Result and discussion . . . 96
4.3.1 Structural characterization . . . 96
4.3.2 Electronic structure calculations . . . 104
4.3.3 Thermoelectric properties . . . 113
4.4 Summary and Conclusions . . . 120

5 Doping Si Site in ZrNiSi with Sb 122
5.1 Introduction . . . 122
5.2 Experimental details . . . 123
5.3 Result and discussion . . . 124
5.3.1 Structural analysis . . . 124
5.3.2 Transport properties . . . 132
5.4 Summary and Conclusions . . . 145

6 Double Heuslers 147
6.1 Introduction . . . 147
6.2 Experimental Details . . . 148
6.3 Results and Discusssion . . . 149
6.3.1 Computation results . . . 149
6.3.2 Structructural characterization . . . 152

6.3.3 Thermoelectric properties 158
6.4 Conclusion and future perspectives 167

7 Summary and Conclusion 169

A Thermoelctric Properties of $Nb_{0.83}CoSb_{1\text{-}x}Sn_x$; x = 0.2 and 0.3 173
A.1 173

B Hall Data of $Nb_{0.83}CoSb_{1\text{-}x}Sn_x$ 175
B.1 175

C Two Phase Refinement of $(ZrNiSb)_{1\text{-}x}(TiFeSb)_x$ 181
C.1 181

D Crystal Growth of "defective" half-Heusler $Nb_{0.83}CoSb$ 186
D.1 Introduction 186
D.2 Experimental Methods 187
D.3 Results and Discussion 188
D.4 Summary and Conclusion 195

Bibliography 195

List of Figures

1.1 A schematic diagram of TEG device 3
1.2 A representative plot to show inter dependence of different quantities on each other (adapted from [101]) 4
1.3 A representative diagram showing junctions of two dissimilar materials kept at two diffrent temperatures. 5
1.4 Schematic showing (a) N-process and (b) U-process 11
1.5 Different ways for band engineering (a) explaining carrier filterng effect, (b) schematic of band picture of normal materials (c) band flattening effect (d) band convergence (e) resonant level doping (adapted from [101]). 16
1.6 (a)A schematic for all heirarchial scattering and, (b) contribution in lattice thermal conductivity depending on mean free path due to diffetrent types of defects (adapted from [208]). 17
1.7 Enhancement in zT for PbTe in past few years (adapted from [208]). 19
1.8 Elements used in transition metal-based Heuslers compounds shown in periodic table (adapted from [56]). 21
1.9 Cubic structure of (a) half-Heusler and (b) Full Heusler shown (adapted from [136]). 21
1.10 Structure of half Heusler as combination of NaCl and ZnS structure (adapted from [19]). 22
1.11 Generation of gap by formation of bonding antibonding orbitals in VEC = 18 TiCoSb(adapted from [56]). 23
1.12 Generation of gap by formation of bonding antibonding orbitals in VEC = 24 Fe_2VAl (adapted from [56]). 24
1.13 Plots showing varaition of zT with temperature for some half-Heuslers (a) n-type and (b) p-type. (c) Plot showing change in peak zT of some n type and p type half Heuslers over last few years. (adapted from [219]) 26

2.1 Arc melting machine with current source and vacuum pump 31

2.2 Arc melting chamber schematic showing different component of arc melting chamber . . . 32
2.3 Arc melted ingot of $Nb_{0.83}CoSb$ . . . 32
2.4 Sintered pellets different samples of $Nb_{1-z}CoSb$ in sealed quartz tube 33
2.5 Sintered pellets of $Nb_{0.83}CoSb$ for thermal and charge transport measurement in shape of disc and bar. . . . 34
2.6 X-ray diffraction instrument Bruker, D8 Advance diffractometer at IISER Pune. . . . 36
2.7 X-ray source, sample and detector in Bragg-Brentano geometry and schematic to show Bragg's law. . . . 36
2.8 FESEM Ultra Zeiss plus at IISER Pune. The instrument was used for observing microstructure, chemical composition and EDX analysis. 38
2.9 Schematic diagram showing important omponents and working of scanning electron microscope. . . . 39
2.10 HRTEM JEOL JEM 2200FS at IISER Pune. The instrument was used for observing microstructure, selected area diffraction patter (SAED), EDX analysis and chemical mapping. . . . 40
2.11 Comparision of working of light microscope and transmission electron microscope. The image is adapted from JEOL TEM manuals ([75]). . 41
2.12 TGA/DSC From Netzsch, Germany for thermal analysis of sample. . 42
2.13 TGA/DSC From Netzsch,simultaneous TGA/DSC schematic diagram. Image is adapted from TGA/DSC manual from Netzsch website ([78]). 43
2.14 PPMS from Quantum Design in Lab 210 at IISER Pune. . . . 45
2.15 Hall puck for Hall measurement with two samples loaded for measurement in four probe geometry. . . . 46
2.16 Schematic diagram of Hall measurements on a Hall bar. . . . 46
2.17 Schematic diagram of specific heat measurement in PPMS. . . . 47
2.18 Linseis LSR-3, Germany for resistivity and Seebeck coefficient simultaneous measurements. . . . 48
2.19 LSR sample loaded between platinum electrodes and voltage probe for simultaneous measurement of resistivity and Seebeck coefficient. . 49
2.20 Schematic showing (a) Seebeck coefficient measurements under a temperature gradient and (b) resistivity measurements. Image adapted from LSR manual from Linseis website ([76]). . . . 50
2.21 Laser Flash Analyzer (LFA) Linseis, Germany for thermal diffusivity measurements on disc shaped samples. . . . 51
2.22 LFA schematic for thermal diffusivity measurements on disc shaped samples. Image is adapted from Linseis LFA manual ([77]). . . . 53

2.23 Fitting of measured thermal diffusivity data using different models. This image is adapted from LFA Manual available on Linseis website ([77]). . . . 53

3.1 Structure of$Nb_{0.83}CoSb$ a) tetrahedral coordination of Co with Sb, b) octahedral coordination of Nb with Sb, c)octahedral coordination of Sb with Nb, and (d) tetrahedral coordination of Sb with Co. 59
3.2 Temperature deviation of specific heat for temperature range 250 K to 340 K. . . . 60
3.3 Powder X-ray diffraction pattern of $Nb_{0.83}CoSb_{1-x}Sn_x$ (x= 0, 0.01, 0.05 0.1, 0.2, 0.3) . . . 62
3.4 Sintered Pellet after polishing and cutting . . . 62
3.5 Reitveld refinement on x-ray data of $Nb_{0.83}CoSb$. . . . 63
3.6 Reitveld refinement on x-ray data of $Nb_{0.83}CoSb_{0.95}Sn_{0.05}$. . . . 63
3.7 Reitveld refinement on x-ray data of $Nb_{0.83}CoSb_{0.99}Sn_{0.01}$. . . . 64
3.8 Reitveld refinement on x-ray data of $Nb_{0.83}CoSb_{0.9}Sn_{0.1}$. . . . 64
3.9 Reitveld refinement on x-ray data of $Nb_{0.83}CoSb_{0.8}Sn_{0.2}$. . . . 65
3.10 Reitveld refinement on x-ray data of $Nb_{0.83}CoSb_{0.7}Sn_{0.3}$. . . . 65
3.11 (a) Variation in lattice parameter with Sn doping percentage (b) elemental composition of samples with variation of nominal Sn doping percentage. . . . 66
3.12 Carrier concentration variation with nominal Sn doping percentage. The dashed line through the data point is a guide to the eye. . . . 66
3.13 FESEM image of polished pellet of $Nb_{0.83}CoSb$ with false colour representation of elemental mapping. . . . 67
3.14 FESEM images taken in backscattering mode and chemical mapping shown with false colour representation for $Nb_{0.83}CoSb_{0.95}Sn_{0.05}$. . . . 68
3.15 FESEM images taken in backscattering mode for (a) $Nb_{0.83}CoSb$ (b) $Nb_{0.83}CoSb_{0.7}Sn_{0.3}$. . . . 69
3.16 DSC measurement done on 30 % Sn doped sample show peak due to Sn melting. . . . 70

3.17 High-resolution transmission electron microscopy (HRTEM) image for $Nb_{0.83}CoSb$ (a) low magnification HRTEM image of a single grain; (b) HRTEM image showing [200] family of planes and its fast Fourier transform (FFT) image in inset where we observe spots due to lattice planes and diffused bands due to short-range ordering of vacancies at Nb site; (c) selected area electron diffraction (SAED) pattern shown for (b), where we can also observe spots due to lattice planes and diffused bands; (d) masking the spots only in FFT of (b) we generated the inverse fast Fourier transform (IFFT) image and a zoom portion of the black square is shown, also planes marked are 200 planes. Some stacking faults are also visible. 71
3.18 High resolution transmission electron microscopy (HRTEM) image for $Nb_{0.83}CoSb_{0.99}Sn_{0.01}$ (a) low magnification HRTEM image of a single grain; (b) HRTEM image showing [111] family of planes and its FFT shown in inset; (c) SAED pattern taken on image (b) showing lattice points for [111] family of planes; (d) IFFT of black square marked in (b), planes marked with dashed yellow lines are 111 planes. 72
3.19 High resolution transmission electron microscopy (HRTEM) image for $Nb_{0.83}CoSb_{0.95}Sn_{0.05}$ (a) low magnification HRTEM image of a single grain; (b) HRTEM image showing [220] family of planes and its FFT shown in inset; (c) SAED pattern taken on image (b) showing lattice points for [220] family of planes; (d) IFFT of black square marked in (b), planes marked with dashed yellow lines are 220 planes. 73
3.20 High resolution transmission electron microscopy (HRTEM) image for $Nb_{0.83}CoSb_{0.7}Sn_{0.3}$ (a) low magnification HRTEM image of a single grain; (b) HRTEM image showing [220] family of planes and its FFT shown in inset; (c) SAED pattern taken on image (b) showing lattice points for [220] family of planes; (d) IFFT of black square marked in (b), planes marked with dashed yellow lines are 220 planes. 74
3.21 Band structure and DOS of (a) $Nb_{0.8}CoSb$ and (b) $Nb_{0.8}CoSb_{0.9}Sn_{0.1}$ and (c) $Nb_{0.9}CoSb$ and (d)$Nb_{0.9}CoSb_{0.9}Sn_{0.1}$ (Calculations done by Vineet Kumar Pandey under supervision Dr. Prasenjit Ghosh). . . . 76

3.22 (a) Conduction band structure of $Nb_{0.8}CoSb$ and $Nb_{0.9}CoSb_{0.9}Sn_{0.1}$ scaled to obtain minima of the band at M point at same energy for both structure, and (b) band structure schematic of samples with actual composition $Nb_{0.81}CoSb$ and $Nb_{0.85}CoSb_{0.9}Sn_{0.1}$ considering calculated band structure in part (a), fermi level shifting is in accordance with the actual carrier concentration of samples obtained using Hall measurements. The solid green bands have excess Nb contribution mainly. The dashed green band has contributions from excess Nb hybridization with all other elements and appears in excess Nb sample (right image) (Calculations done by Vineet Kumar Pandey under supervision of Dr. Prasenjit Ghosh). 76
3.23 (a) Contribution of added Nb-d states in the band structure and (b) its partial DOS for $Nb_{0.9}CoSb_{0.9}Sn_{0.1}$. Here, the term "excess" represent atoms nearest to added Nb. (Calculations done by Vineet Kumar Pandey under supervision Dr. Prasenjit Ghosh) 77
3.24 Temperature variation of electrical conductivity of samples $Nb_{0.83}CoSb_{1-x}Sn_x$ (x = 0, 0.01, 0.05, 0.1 and 0.15). Lines drawn through data points are guide to the eye 80
3.25 Temperature variation of Seebeck coefficients of samples $Nb_{0.83}CoSb_{1-x}Sn_x$ (x = 0, 0.01, 0.05, 0.1 and 0.15). Lines drawn through data points are guide to the eye. 81
3.26 Variation of electrical conductivity and Hall mobility with Sn doping percentage at 300 K. 81
3.27 Pisarenko's plot: Variation of Seebeck coefficient with carrier concentration.Different dashed lines show Pisarenko plot for different m_d^* . . 82
3.28 (a) Temperature variation of weighted mobility and power factor for samples $Nb_{0.83}CoSb_{1-x}Sn_x$ (x = 0, 0.01, 0.05, 0.1 and 0.15) 84
3.29 (a) Weighted mobility and (b) power factor plotted against nominal Sn doping percentage at 300 K (black) and 1100 K (Red)). 85
3.30 Temperature variation in thermal conductivity and lattice thermal conductivity for the samples $Nb_{0.83}CoSb_{1-x}Sn_x$ (x = 0, 0.01, 0.05, and 0.1) 86
3.31 Temperature variation of (a) Lorenz's number obtained from Seebeck coefficient using Eq. 1.20 (b) electronic part of thermal conductivity obtained using electrical conductivity and Lorenz's number for samples $Nb_{0.83}CoSb_{1-x}Sn_x$ (x = 0, 0.01, 0.05, and 0.1) 87
3.32 Temperature variation of (a) μ_w/κ_L and (b) B factor for samples $Nb_{0.83}CoSb_{1-x}Sn_x$ (x = 0, 0.01, 0.05, and 0.1) 88

3.33 (a) Raman spectrum of samples $Nb_{0.83}CoSb_{1-x}Sn_x$ (x = 0, 0.01, and 0.3), Raman spectrum of samples $Nb_{0.83}CoSb_{1-x}Sn_x$ with multiple peak fitting (b) x = 0, (c) x = 0.01 , and (d) x = 0.3 respectively. . . 89
3.34 Temperature variation of figure of merit, zT for the samples $Nb_{0.83}CoSb_{1-x}Sn_x$ (x = 0, 0.01, 0.05, and 0.1) 90
3.35 Few reports of thermoelectric figure of merit of NbCoSb and its comparison to this work. 90

4.1 Crystal structure of TiNiSi structure-type ZrNiSi. (a) Orthorhombic unit cell showing the coordination of Zr and Ni by the Si. The crystal structure as viewed along the: (b) *b*–axis, (c) *c*–axis, and (d) *a*–axis is shown (see text for details). 94
4.2 Powder X-ray diffraction pattern of arc-melted ZrNiSi, ZrNiGe, HfNiSi and NbCoSi samples . A simulated powder X-ray diffraction pattern for ZrNiSi (TiNiSi structure-type) is also shown for comparison. . . . 96
4.3 A representative FESEM image each of (a) ZrNiSi, (b) HfNiSi, (c) ZrNiGe, and (d) NbCoSi taken in the backscattering mode. The elemental chemical mapping in each case is shown using a false colour representation. 97
4.4 FESEM image in back scattering mode of HfNiSi 99
4.5 The TEM images of ZrNiSi sample: (a) a typical low-resolution TEM image showing a micrograin; (b) HRTEM image collected by focusing over a small portion of this micrograin. The dashed lines indicate some representative lattice planes: (103), (121) and (211) with interplanar spacing d_1 = 0.219nm, d_2 = 0.177nm, and d_3 = 0.237nm, respectively. The FFT is shown as an inset; (c) The SAED image showing sharp diffraction spots. The points labeled 1, 2 and 3 correspond to the lattice planes (103), (121), and (211); (d) zoomed-in IFFT of the square area marked as a1 in panel (b). 100
4.6 The powder X-ray diffraction pattern for various arc-melted $Zr_{1-x}NiSb$ (x = -0.05, 0, 0.05, 0.1, 0.15 and 0.25), and the annealed $Zr_{1.05}NiSb$ are shown. The simulated pattern for the main ZrNiSb phase (TiNiSi structure-type) is also shown. The peaks due to secondary phases $ZrNi_2Sb$, $Zr_3Ni_3Sb_4$,Zr_2Sb and Ni_3Sb are also labeled. 101
4.7 The powder X-ray diffraction pattern for various arc-melted $Zr_{1-x}NiSb$ (x = -0.05, 0.05, 0.1, 0.15, 0.25). The simulated pattern for the main $Zr_3Ni_3Sb_4$ phase (TiNiSi structure-type) is also shown. The peaks due to secondary phases $ZrNi_2Sb$, ZrNiSb, Zr_2Sb and Ni_3Sb are also labeled. 102

4.8 A representative FESEM image each of ZrNiSb (left), and $Zr_{1.05}NiSb$ (right) collected in the backscattering mode. The dark grey regions in the image on the left are due to the impurity phase $ZrNi_2Sb$. The composition of the main matrix in both cases is close to $Zr_{1.1}Ni_{0.83}Sb$ 103
4.9 Chemical mapping of $Zr_{1.05}NiSb$, false colour map to show homogeneity of the sample 104
4.10 The TEM images of a $Zr_{1.05}NiSb$ sample: (a) a low-resolution TEM image of a micrograin; (b) HRTEM image taken by focusing the electron beam on a small region of this micrograin. The lattice planes (013) and (011) are shown with interplanar spacing $d_1 = 0.22$nm(013) and $d_2 = 0.36$nm(011). The SAED image is shown as an inset where the points labeled 1 and 2 correspond to the lattice planes (011) and (013); (c) and (d) zoomed IFFT of the areas shown with white dashed lines marked as a1 and a2 respectively in panel (b), circles have been drawn to show some of the stacking faults in the region a1 which are present in high density as compared to region a2. 105
4.11 TX bonds scheme in ZrNiSi 106
4.12 Charge density isosurfaces of (a) ZrNiSi and (b) NbCoSi. The isovalues corresponding to these plots are 0.398 and 0.438 e/$\AA^3$ for ZrNiSi and NbCoSi respectively. Fermi surface plots of (c) ZrNiSi and (d) NbCoSi. The electron and hole Fermi surfaces are shown in blue and red, respectively (Calculations done in collaboration with Dr. Prasenjit Ghosh). 107
4.13 Fermi surface plots of (a) HfNiSi (b) ZrNiGe (c) ZrNiSb; Charge density isosurfaces of (d) HfNiSi (e) ZrNiGe (f) ZrNiSb, where the isovalues corresponding to these plots are 0.398, 0.344 and 0.351 $e/\AA^3$ for HfNiSi, ZrNiGe and ZrNiSb respectively (Calculations done in collaboration with Dr. Prasenjit Ghosh) 108
4.14 Band structure and DOS plots of (a) ZrNiSi, (b) ZrNiGe, (c) ZrNiSb (Calculations done in collaboration with Dr. Prasenjit Ghosh). 109
4.15 Band structure and DOS plots of (a) HfNiSi, (b) NbCoSi. (Calculations done in collaboration with Dr. Prasenjit Ghosh) 110
4.16 Comparison of the total DOS for the five compounds: ZrNiSi, ZrNiGe, ZrNiSb, HfNiSi, NbCoSi. (Calculations done in collaboration with Dr. Prasenjit Ghosh) 111

4.17 DOS projected onto the Zr/Nb and Ni/Co d–states and Si p–states in (a) ZrNiSi and (b) NbCoSi. In each panel, the projected DOS has been divided into five regions. The ILDOS isosurfaces showing the hybridization of the atomic orbitals in each region for the two compounds are shown in the inset. The isovalues corresponding to these plots vary between 0.0121 to 0.162 e/$\mathring{A}^3$. (Calculations done in collaboration with Dr. Prasenjit Ghosh) 112
4.18 Temperature variation of (a) electrical conductivity (σ), and (b) Seebeck coefficient (S) for all the studied samples. Here, 'ZrNiSb' represents the sample with nominal stoichiometry $Zr_{1.05}NiSb$. The lines through the data points are guide to the eye. 115
4.19 The temperature variation of thermal conductivity (κ) of the samples studied here. The legend 'ZrNiSb' corresponds to the sample with nominal composition $Zr_{1.05}NiSb$. Lines through the data points are used as a guide to the eye. 116
4.20 The (a) electronic (κ_l) and (b) lattice (κ_l) thermal conductivity. The lines are used as a guide to the eye. In panel (b), the black dashed line at the top shows the $1/T$ dependence. 117
4.21 Figure of merit (zT) plot Vs temperature for different arc melted samples, namely ZrNiSi, ZrNiGe, HfNiSi, NbCoSi and ZrNiSb. 120

5.1 Powder x-ray diffraction of all arc-melted samples with nominal composition $ZrNiSi_{1-x}Sb_x$, $HfNiSi_{0.8}Sb_{0.2}$ and $Zr_{0.5}Hf_{0.5}NiSi_{0.8}Sb_{0.2}$. The simulated stick patterns based on the orthorhombic TiNiSi structre type are also shown for ZrNiSi and ZrNiSb 125
5.2 (a) Representative backscattered FESEM images of $ZrNiSi_{0.95}Sb_{0.05}$ showing homogeneous chemcial distribution of elements in $ZrNiSi_{0.95}Sb_{0.05}$ (b) Si, (c) Zr, (d) Sb, and (e) Ni. 126
5.3 (a) Representative backscattered FESEM images of $ZrNiSi_{0.9}Sb_{0.1}$ showing a spinodal-type phase segregation in $ZrNiSi_{0.9}Sb_{0.1}$. The chemical elemental composition in two cases is also shown using the false color representation; (b) Sb, (c) Ni, (d) Zr, and (e) Si. 127
5.4 (a) Representative backscattered FESEM images of $ZrNiSi_{0.85}Sb_{0.15}$ showing a spinodal-type phase segregation in $ZrNiSi_{0.85}Sb_{0.15}$. The chemical elemental composition in two cases is also shown using the false color representation; (b) Sb, (c) Ni, (d) Zr, and (e) Si. 127

5.5 (a) Representative backscattered FESEM images of $ZrNiSi_{0.8}Sb_{0.2}$ showing a spinodal-type phase segregation in $ZrNiSi_{0.8}Sb_{0.2}$. The chemical elemental composition in two cases is also shown using the false color representation; (b) Zr, (c) Si, (d) Sb, and (e) Ni. 127
5.6 (a) Representative backscattered FESEM images of $HfNiSi_{0.8}Sb_{0.2}$ showing a spinodal-type phase segregation in $HfNiSi_{0.8}Sb_{0.2}$. The chemical elemental composition in two cases is also shown using the false color representation; (b) Si, (c) Ni, (d) Hf, and (e) Sb. 128
5.7 (a) Representative backscattered FESEM images of $ZrNiSi_{0.8}Sb_{0.2}$ showing a homogeneous distribution in $Zr_{0.5}Hf_{0.5}NiSi_{0.8}Sb_{0.2}$. The chemical elemental composition in two cases is also shown using the false color representation; (b) Si, (c) Zr, (d) Ni, (e) Sb and (f) Hf . . . 128
5.8 A comparison of PXRD pattern of $ZrNiSi_{0.9}Sb_{0.1}$ and $ZrNiSi_{0.8}Sb_{0.2}$ before and after the annealing process. The extra peaks are marked with an asterisk 129
5.9 Representative backscattered FESEM images of $ZrNiSi_{0.9}Sb_{0.1}$ and $ZrNiSi_{0.8}Sb_{0.2}$ post annealing 130
5.10 Top panel: (a) HRTEM micrograph of ZrNiSi, inset at right bottom shows the FFT image of the micrograph; (b) SAED pattern taken on the micrograph where *hkl* indices of points marked with 1, 2, and 3 corresponding to d[11-2] = 0.156 nm, d[211] = 0.234 nm, and d[103] = 0.227 nm, respectively are shown; (c) IFFT of the white square shown in (a) showing d spacing of planes 1, 2 and 3. Bottom panel: HRTEM micrograph of $ZrNiSi_{0.8}Sb_{0.2}$, the panels (d), (e) and (f) are analogous to (a), (b) and (c). In (e) *hkl* indices of points marked with 1 and 2 are [111] and [211], respectively. In (e) the planes [211] with d[211] = 0.227 nm are shown 131
5.11 A representative HRTM image of a grain of $Zr_{0.5}Hf_{0.5}NiSi_{0.8}Sb_{0.2}$. The lower inset shows the SAED pattern. The upper inset shows the intensity profile along the direction marked within the red square. . 132
5.12 Temperature dependence of: (a) Seebeck coefficient (S) and (b) electrical conductivity of $ZrNiSi_{1-x}Sb_x$ and $Zr_{0.5}Hf_{0.5}NiSi_{0.8}Sb_{0.2}$ 133
5.13 Temperature dependence of weighted mobility (μ_w) in $ZrNiSi_{1-x}Sb_x$ and $Zr_{0.5}Hf_{0.5}NiSi_{0.8}Sb_{0.2}$ 135
5.14 Temperature dependence of Power factor (PF) in $ZrNiSi_{1-x}Sb_x$($x = 0, 0.05, 0.1, 0.15, \& \ 0.2$) and $Zr_{0.5}Hf_{0.5}NiSi_{0.8}Sb_{0.2}$ 136

5.15 (a) Band structure of ZrNiSi (black) and 12.5 % doped (unfolded); the dashed horizontal lines above Fermi energy indicate chemical potential corresponding to 5 %, 10 %, 12.5 % and 15 % electron doping. (b-f) Constant energy surfaces at different electron chemical potentials that corresponds to 0 %, 5 %, 10 %, 12.5 %, 15 % electron doping showing the evolution of the electron (blue) and hole (red) pockects with increased doping. The scale bar in (a) is the magnitude (increasing, white-blue-green) of spectral weight, which characterizes the probability of the primitive cell eigenstates contributing to a particular supercell eigenstate of the same energy (calculated in collaboration with Dr. Prasenjith Ghosh). 137
5.16 The temperature variation of thermal conductivity κ in samples $ZrNiSi_{1-x}Sb_x(x = 0, 0.05, 0.1, 0.15, \& \ 0.2)$ and $Zr_{0.5}Hf_{0.5}NiSi_{0.8}Sb_{0.2}$ 138
5.17 The temperature variation of lattice (κ_{Latt}) and electronic (κ_{ele}) components of κ_{Tot} are shown in (a) and (b), respectively for samples $ZrNiSi_{1-x}Sb_x(x = 0, 0.05, 0.1, 0.15, \& \ 0.2)$ and $Zr_{0.5}Hf_{0.5}NiSi_{0.8}Sb_{0.2}$ . . 140
5.18 Temperature variation of the thermoelectric figure of merit zT of $ZrNiSi_{1-x}Sb_x$ ($x = 0$ and 0.05 141
5.19 Temperature variation of the thermoelectric figure of merit zT of $ZrNiSi_{1-x}Sb_x(x = 0, 0.05, 0.1, 0.15, \& \ 0.2)$ and $Zr_{0.5}Hf_{0.5}NiSi_{0.8}Sb_{0.2}$ . . 142
5.20 Temperature variation of the thermoelectric B factor zT of $ZrNiSi_{1-x}Sb_x(x = 0, 0.05, 0.1, 0.15, \& \ 0.2)$ and $Zr_{0.5}Hf_{0.5}NiSi_{0.8}Sb_{0.2}$ from 300 K to 500 K. 142
5.21 of arc melted (solid lines) and annealed (open data) sample of $ZrNiSi_{0.9}Sb_{0.1}$ and $ZrNiSi_{0.8}Sb_{0.2}$ post annealing 143
5.22 κ_e and κ_L of arc melted (solid lines) and annealed (open data) sample of $ZrNiSi_{0.9}Sb_{0.1}$ and $ZrNiSi_{0.8}Sb_{0.2}$ post annealing 144
5.23 Figure of merit of arc melted (solid lines) and annealed (open data) sample of $ZrNiSi_{0.9}Sb_{0.1}$ and $ZrNiSi_{0.8}Sb_{0.2}$ post annealing 145

6.1 Structure of $(ZrNiSb)_{0.5}(TiFeSb)_{0.5}$ composition1. 150
6.2 Structure of $(ZrNiSb)_{0.5}(TiFeSb)_{0.5}$ composition2. 150
6.3 Density of states and band structure of $(ZrNiSb)_{0.5}(TiFeSb)_{0.5}$ composition1. 151
6.4 Phonon density of states of $(ZrNiSb)_{0.5}(TiFeSb)_{0.5}$ composition1. . . . 151
6.5 Powder Xray diffraction of composites of TiFeSb and ZrNiSb 152
6.6 The double Heusler alloy $(Zr_{0.5}Ti_{0.5})(Ni_{0.5}Fe_{0.5})Sb$. The unit cell is cubic (space group *F-43m* as that of HH XYZ but with X site shared by Zr and Ti and Y site shared equally by Ni and Fe.) 153

6.7 Lattice parameter and cell volume of $(ZrNiSb)_{1-x}(TiFeSb)_x$ in half Heusler structure with spacegroup *F-43m* obtained from refinement . 154
6.8 (a) ,Unit cell volume of $(ZrNiSb)_{1-x}(TiFeSb)_x$ in half Heusler structure with spacegroup *F-43m* and (b) unit cell volume of secondary phase (orthorhombic TiNiSi structure type, space group Pmna). . . . 154
6.9 Refinement of powder Xray diffraction of $(ZrNiSb)_{0.5}(TiFeSb)_{0.5}$ . . . 155
6.10 FESEM of ZrNiSb and TiFeSb showing existence of two phases . . . 155
6.11 Chemical mapping of the double Heusler phase of $(ZrNiSb)_{0.5}(TiFeSb)_{0.5}$ sample using FESEM . . . 156
6.12 Chemical mapping of large area of $(ZrNiSb)_{0.5}(TiFeSb)_{0.5}$ sample using FESEM . . . 157
6.13 Representative backscattered image of the Double Heusler phase using FESEM of $(ZrNiSb)_{0.5}(TiFeSb)_{0.5}$ . . . 157
6.14 Chemical mapping of the Double Heusler phase using FESEM of $(ZrNiSb)_{0.6}(TiFeSb)_{0.4}$ . . . 158
6.15 Chemical mapping of the Double Heusler phase using FESEM of $(ZrNiSb)_{0.55}(TiFeSb)_{0.45}$ . . . 159
6.16 Chemical mapping of the Double Heusler phase using FESEM of $(ZrNiSb)_{0.45}(TiFeSb)_{0.55}$ . . . 159
6.17 Chemical mapping of the Double Heusler phase using FESEM of $(ZrNiSb)_{0.4}(TiFeSb)_{0.6}$ . . . 160
6.18 Chemical mapping of the Double Heusler phase using FESEM of $(ZrNiSb)_{0.3}(TiFeSb)_{0.7}$ . . . 160
6.19 (a)HRTEM microstructure of $(ZrNiSb)_{0.5}(TiFeSb)_{0.5}$ SAED image is shown in inset (b) FFT of the microstructure shown in (c) zoomed image of microstructure shown in (a) where we observe disorder in structure. . . . 161
6.20 Chemical mapping of $(ZrNiSb)_{0.5}(TiFeSb)_{0.5}$ grains using HRTEM imaging . . . 162
6.21 Thermopower of different samples of $(ZrNiSb)_{1-x}(TiFeSb)_x$ with x = 0, 0.3, 0.4, 0.45, 0.5, 0.6 and 1 . . . 163
6.22 Electrical conductivity of different samples of $(ZrNiSb)_{1-x}(TiFeSb)_x$ with x = 0, 0.3, 0.4, 0.45, 0.5, 0.6 and 1 . . . 163
6.23 Total thermal conductivity of different samples of $(ZrNiSb)_{1-x}(TiFeSb)_x$ with x = 0, 0.3, 0.4, 0.45, 0.5, 0.6 and 1 . . . 164
6.24 Lattice thermal conductivity of different samples of $(ZrNiSb)_{1-x}(TiFeSb)_x$ with x = 0.3, 0.4, 0.45, 0.5 and 0.6. . . . 165
6.25 Electrical thermal conductivity of different samples of $(ZrNiSb)_{1-x}(TiFeSb)_x$ with x = 0.3, 0.4, 0.45, 0.5 and 0.6. . . . 165

6.26 Weighted mobility of different samples of $(ZrNiSb)_{1-x}(TiFeSb)_x$ with x = 0.3, 0.4, 0.45, 0.5 and 0.6. 165
6.27 Bfactor of different samples of $(ZrNiSb)_{1-x}(TiFeSb)_x$ with x = 0.3, 0.4, 0.45, 0.5 and 0.6. 166
6.28 Power factor of different samples of $(ZrNiSb)_{1-x}(TiFeSb)_x$ with x = 0, 0.3, 0.4, 0.45, 0.5, 0.6 and 1. 166
6.29 Figure of merit, zT of different samples of $(ZrNiSb)_{1-x}(TiFeSb)_x$ with x = 0, 0.3, 0.4, 0.45, 0.5, 0.6 and 1. 167

A.1 (a) Electrical Conductivity, (b) Seebeck coeff., (c) thermal conductivity, and (d) power factor of $Nb_{0.83}CoSb_{1-x}Sn_x$ where $x = 0.2$ & 0.3 are shown. 173
A.2 174

B.1 Schematic of connection used for Hall measurements on Hall puck in PPMS(a) four-probe geometry (b) five-probe geometry 175
B.2 Hall voltage plotted against magnetic field for $Nb_{0.83}CoSb$ taken in five probe geometry at 70 K. 176
B.3 Hall voltage plotted against magnetic field for $Nb_{0.83}CoSb_{0.99}Sn_{0.01}$ taken in four-probe geometry at 70 K. 177
B.4 Hall voltage plotted against magnetic field for $Nb_{0.83}CoSb_{0.95}Sn_{0.05}$ taken in four-probe geometry at 70 K. 177
B.5 Hall voltage plotted against magnetic field for $Nb_{0.83}CoSb_{0.9}Sn_{0.1}$ taken in five probe geometry at 70 K. 178
B.6 Hall voltage plotted against magnetic field for $Nb_{0.83}CoSb_{0.8}Sn_{0.2}$ taken in five probe geometry at 70 K. 179
B.7 Hall voltage plotted against magnetic field for $Nb_{0.83}CoSb_{0.7}Sn_{0.3}$ taken in five probe geometry at 70 K. 179

C.1 Refinement of powder Xray diffraction of $(ZrNiSb)_{0.6}(TiFeSb)_{0.4}$ . . . 182
C.2 Refinement of powder Xray diffraction of $(ZrNiSb)_{0.55}(TiFeSb)_{0.45}$ . . 182
C.3 Refinement of powder Xray diffraction of $(ZrNiSb)_{0.5}(TiFeSb)_{0.5}$ . . . 183
C.4 Refinement of powder Xray diffraction of $(ZrNiSb)_{0.45}(TiFeSb)_{0.55}$ . . 183
C.5 Refinement of powder Xray diffraction of $(ZrNiSb)_{0.4}(TiFeSb)_{0.6}$ . . . 184
C.6 Refinement of powder Xray diffraction of $(ZrNiSb)_{0.3}(TiFeSb)_{0.7}$ . . . 184

D.1 (a-h) Some single crystals of $Nb_{0.83}CoSb$ are shown, these were obtained from CVT growth. (h) A single crystal of length > 2 mm of $Nb_{0.83}CoSb$ has been shown. 189

D.2 (a) X-ray diffraction pattern obtained on a single crystalline piece of $Nb_{0.83}CoSb$. The single-crystal X-ray diffraction shows peaks of [111] family of planes. (b)Powder X-ray diffraction pattern on a finely ground single crystal of $Nb_{0.83}CoSb$. The X-ray diffraction pattern can be recognized by the cubic $F-43m$ phase. The diffraction pattern was refined using FullProf Suite and the composition obtained is $Nb_{0.82}CoSb$. 190
D.3 Crystal structure of the sample obtained through Reitveld refinement. Inset show zoomed image of area marked with white dashed line around spot marked as 213 hkl plane. 191
D.4 A representative Laue back reflection diffraction pattern obtained on Fig. D.1(h). 192
D.5 Few representative FESEM images of $Nb_{0.83}CoSb$ single crystals taken in backscattering mode. 192
D.6 A representative FESEM image showing chemical mapping done on a single crystal of $Nb_{0.83}CoSb$ backscattering mode. 192
D.7 The high-resolution TEM images taken on pulverized $Nb_{0.83}CoSb$ single crystal showing micrograph in (a), and the SAED pattern in (b). The presence of diffused bands forming wave-like patterns, coexisting with the sharp diffraction spots can be seen in the SAED pattern. The weak spots and the hexagonal patterns at the bottom left and top right corners indicate the presence of superstructure. The 220 planes are labeled in the SAED pattern. The inset in panel (a) shows the FFT of the micrograph 193
D.8 The TGA/DSC signals for a $Nb_{0.83}CoSb$ crystal specimen measured under an inert atmosphere. The sharp peaks, discussed in the main text, are not due to melting or decomposition of the sample. 194
D.9 Temperature variation of resistance of the single crystal of $Nb_{0.83}CoSb$ measured using a lab-based low temperature (Liq. Nitrogen) four-probe setup using Keithley instruments and Lab-View program. In the inset, we have shown a single crystal with gold wire contact using silver paint for resistance measurements. 194

List of Tables

3.1 Power factor and themal conductivity of various high zT half Heusler 57

3.2 Density of different samples obtained by measuring dimension and sample mass 59

3.3 Occupancy of different elements from Fullprof refinement 61

3.4 Calculated carrier concentration of all the samples based on composition obtained from refinement using Zintl phase chemistry. 75

3.5 Raman modes for $Nb_{0.83}CoSb_{1-x}Sn_x$ (x = 0, 0.01, and 0.3) samples . 89

4.1 Lattice parameters of various orthorhombic MTX compounds as obtained experimentally and using the DFT calculations. 98

4.2 T-X bond lengths in T-X distorted tetrahedra for different samples (Calculations done in collaboration with Dr. Prasenjit Ghosh). . . . 106

6.1 Average sound velocities (v) and cut off frequencies θ_i for $(ZrNiSb)_{0.5}(TiFeSb)_{0.5}$. These are used to compute $\kappa_{l,min}$ using Eqn. 6.1. 150

6.2 Phase composition of HH-phase and orthorhombic phase obtained from FESEM chemical mapping of $(ZrNiSb)_{1-x}(TiFeSb)_x$ where $x = 0.4,\ 0.45,\ 0.5,\ 0.55,\ 0.6, and\ 0.7$ 161

C.1 Parameters obtained from Reitveld refinement of the $(ZrNiSb)_{1-x}(TiFeSb)_x$ where $x = 0.4,\ 0.45,\ 0.5,\ 0.55,\ 0.6, and\ 0.7$ showing χ^2, R_p, R_{wp}, R_{exp} and composition in HH phase 185

D.1 Crystallographic data obtained for $Nb_{0.83}CoSb$ single crystal using Reitveld refinement. 191

Chapter 1

Introduction and Motivation

1.1 Thermoelectricity: waste heat recovery

Global energy demand is continuously rising with the increase in population and industrialization. For a developing economy like India, the energy demand has by 3 times from 300 Mtoe in 1990 to 908 Mtoe in 2020. Here, Mtoe stands for mega tonne oil equivalent which is defined as the amount of energy released by burning one megatonne of crude oil. As for the world, this has gone up from 8500 Mtoe to 13500 Mtoe over the same period of time [38]. We can say that an average increase of around 2 % has been observed in global energy demand annually (considering a small decline in 2020 due to pandemic). While the energy requirement worldwide is rising, our dependence on coal, oil, and natural gases has remained almost unaltered. Currently, the fossil fuels provide for more than 80 % of primary global energy consumption [16]. The use of fossils to meet our energy demands leads to the emission of harmful gases that results in pollution and global warming. Among these gases, CO_2 emission is one of the biggest factors contributing to the global warming. CO_2 emission has increased to around 33 Gt in 2021 from 20.5 Gt in 1990 [87]. Electricity generated by renewables is set to increase by 8 % in 2021, with solar Photovoltaics (PV) and wind comprising more than two-thirds of this increase [87]. Our total electricity production has reached around 27000 TWh in the year 2020. Including hydropower, the renewable contributes around 28 % (in 2020 with hydropower comprising 16 %) in electricity production with an increase in solar PV and wind energy contribution [38]. As we can see the major portion of electricity generation comes from fossil fuels. Another disadvantage of using fossil fuels is that they have a very low power conversion efficiency with coal around 30-35 %, gas around 45 %, and oil around 35 % and a major proportion of this energy escapes in the form of heat energy. So around 60 % of heat expelled by these fuels is lost as waste heat. If we use alternative ways of energy harvesting, there is a

good possibility of recovering some proportion of this waste heat. Papapetrou et al. in their paper [138] estimated the potential in waste heat recovery for European Union (EU) for the year 2015 to be around 304 TWh/year, which was about 10 % of the total energy consumption in the industry in 2015 in EU. The waste heat recovery potential can be considered in different temperature ranges such as less than 200 ^{o}C, in the range 200-500 ^{o}C, and above 500 ^{o}C. Among these ranges, one-third possibility lies in less than 200 ^{o}C range. Thermoelectricity can be used to recover some portion of the waste heat. Thermoelectricity is not a new concept, it was first demonstrated as early as 1948 when an oil-burning lamp was used to power a radio using the first commercial thermoelectric generator based on the material ZnSb [123]. Later, H Julian Goldsmid demonstrated the cooling effect using Bi_2Te_3 in 1954 [53]. Thermoelectricity has been used in deep space missions for powering satellites using radioisotope thermoelectric generators (RTEG). Some of the missions powered by RTEGs are Appolo, Galileo, Casini, Voyagers, etc. Until now thermoelectrics was used mostly in some niche applications but recently the focus has shifted to their use as a waste heat recovery system and finding other possible general-purpose applications of thermoelectricity, which we will discuss in the coming paragraphs.

In the report Global Thermoelectric Generator Market 2017-2021 [155], it is estimated that the overall thermoelectric generator (TEG) market is going to grow from USD 406 million in 2021 to USD 635 million by 2026. Thermoelectricity has a market at different scales ranging from low power ($<$ 10 W), medium power (10 W to 1 KW) to high power ($>$ 1 KW). The market is based on requirements of heat sources, thermoelectric modules, electric load, etc. Thermoelectric materials are being used in various sectors to generate energy from different sources of waste heat including industrial, transport, and household. Various applications among these sectors are automotive exhaust thermoelectric generators (AETEGs), wearable thermoelectric generators, solar thermoelectric generators, miniature thermoelectric generators, radioisotope thermoelectric generators, thermoelectric generators in aerospace sectors, thermoelectric coolers, etc. Thus, thermoelectrics is offering a new hope to meet our energy demands. The increase in fuel efficiency, control on the emission of harmful gases, energy demand in remote areas, and maintenance-free production of electricity without any complexity of moving parts are a few driving forces for further research in thermoelectric materials. The high initial cost and low efficiency of TEGs are however two big challenges in this field. Thus, for TEGs to be a viable solution to the energy crisis, we should discover cheaper thermoelectric materials with better efficiencies.

In this work, we have studied some new and some already known half-Heusler based and chemical similar thermoelectric materials. The goal of our work is to

simultaneously enhance the power factor and reduce the thermal conductivity to obtain state of art thermoelectric materials. In the next section, we will first present the fundamentals of thermoelectricity that are useful to understand our work. We will then present the most common strategies used in the past to enhance the thermoelectric performance of a material. We will discuss some state of art materials and half-Heuslers as potential thermoelectrics. In the later chapters, we will present discuss the experimental techniques used and the new results obtained along with their critical interpretation and future scope.

1.2 Fundamentals of Thermoelectrics

Thermolectric generators work on the principle of Seebeck effect. A typical schematic of a thermoelctric generator is shown in Fig. 1.1. The schematic depicts a two-legged device in which p-type and n-type legs are connected in series electrically. The device is sandwiched between a zone with a temperature gradient with the top surface of the device in thermal contact with a high-temperature heat source and the lower surface is in contact with a heat sink. For better performance, it is required that the n-type and p-type legs should have similar mechanical and chemical properties. The arrows in the figure show the direction of the current flow. The maximum efficiency of a typical thermoelectric device is given by the following formula [52],

$$\eta = \frac{T_h - T_c}{T_h} \frac{\sqrt{1 + zT_m} - 1}{\sqrt{1 + zT_m} + \frac{T_c}{T_h}}, \tag{1.1}$$

where zT_m is a dimentionless quantity (defined further), T_h and T_c are temperatures at the hot end and the cold end, respectively, and $T_m = \frac{T_h+T_c}{2}$. zT is known as the figure of merit of the material. The figure of merit of a material at any temperature T (in Kelvin) is defined as:

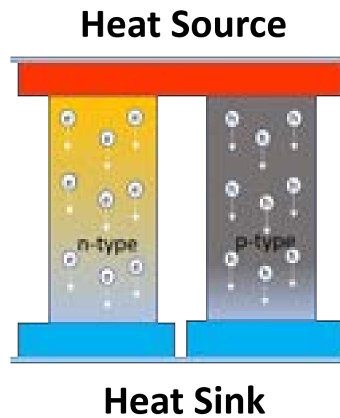

Figure 1.1: A schematic diagram of TEG device

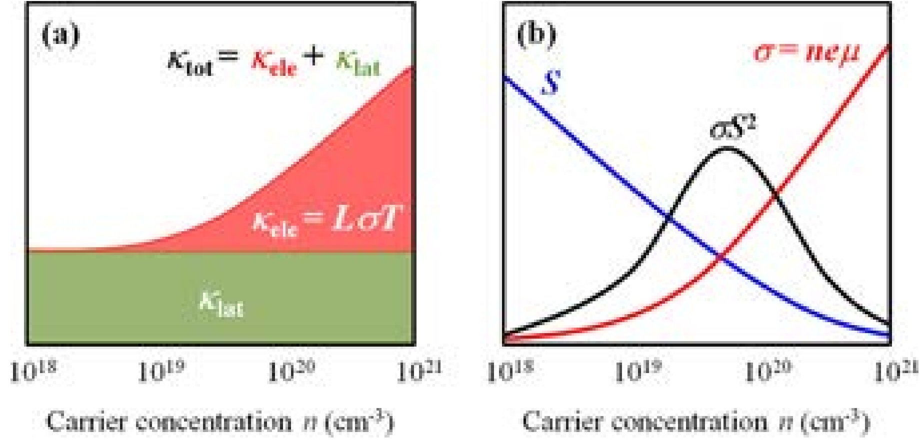

Figure 1.2: A representative plot to show inter dependence of different quantities on each other (adapted from [101])

$$zT = \sigma S^2 T/\kappa, \tag{1.2}$$

where σ, S and κ denote, respectively, the electrical conductivity, Seebeck coefficient and thermal conductivity at temperature T [52, 64, 176, 222]. zT is a dimensionless quantity. The quantity σS^2 in the numerator is called the power factor (PF). From the functional form of zT it is rather obvious that for a good TE, the PF should be high and simultaneously the thermal conductivity as low as possible. However, since σ, S and κ are contra-indicating properties, optimization of zT for a given TE material or to discover new TE materials with high zT is a challenging problem. This can be understood from the plot in Fig.1.2, where the Seebeck coefficient, electrical conductivity, thermal conductivity, and power factor are plotted against the carrier concentration.

We will discuss these quantities in detail in the coming sections. However, here we note that with increasing carrier concentration while the electrical conductivity increases the thermopower decreases monotonically leading to a maximum in the PF. Similarly, the thermal conductivity goes on increasing with the carrier concentration (This increase is due to an increase in κ_{ele} which is directly related to σ through the Wiedemann-Franz law).

1.2.1 Thermoelectric effect

Seebeck effect, Peltier effect, and Thomson effect are collectively referred to as thermoelectric effects. Here we will introduce them one by one and show how they relate to each other. We will also introduce a few more concepts related to the thermoelectric effect, which helped in the advancement of this field.

Seebeck effect

In 1821 Thomas Johann Seebeck observed deflection in magnetic compass due to a current-carrying loop made of the junction of two different electrical conductors kept at two different temperatures. The schematic for the same can be seen in Fig. 1.3.

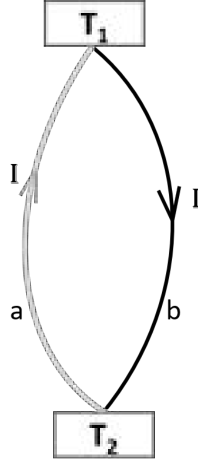

Figure 1.3: A representative diagram showing junctions of two dissimilar materials kept at two diffrent temperatures.

This effect was called the thermomagnetic effect by Seebeck. Later it was understood the magnetic field is due to the current flowing in the closed-loop. When the junctions of two different electrical conductors are kept at two different temperatures we observe the generation of potential difference in it in the open circuit condition. This potential was found to be proportional to the temperature difference. Julius C. von Yelin also discovered thermomagnetic around the same time as Seebeck but Seebeck was the first one to report it to the scientific community, hence it is called the Seebeck effect. Oersted gave the correct explanation that the current is produced due to temperature difference and coined the term thermoelectricity. Mathematically this can be written as follows:

$$V = S(T_h - T_c) \tag{1.3}$$

where V is the voltage difference created due to the Seebeck effect T_h is the temperature at the hot junction and T_c is the temperature at the cold junction, S is the Seebeck coefficient of the material. T. J. Seebeck is also credited for the discovery of piezooptic and photoplasticity [55].

Peltier effect

In 1834 a French watchmaker Jean Charles Athanase Peltier observed a reverse Seebeck effect which is called the Peltier effect. Peltier found that an electrical current gives rise to a heating or cooling effect at the junction of two dissimilar metals in a circuit. Later, Lenz proved that the direction of current determines whether heat is absorbed or emitted at the junction. Peltier effect for a single homogeneous conductor can be written mathematically as follows

$$\dot{Q} = \pi I \tag{1.4}$$

where, $\dot{Q}$ is rate of heat flow, π is Peltier coefficient and I is current. Also,

$$\pi = ST \tag{1.5}$$

hence,

$$\dot{Q} = STI. \tag{1.6}$$

Thomson effect

William Thomson discovered an additional thermoelectric effect that is named after him as the Thomson effect. The Thomson effect involves the generation and absorption of heat in a homogeneous conductor subject to a temperature gradient, and that carries a current through it. Mathematically, the Thomson effect can be given by the following relation

$$\dot{Q} = -\tau \vec{J}.\vec{\nabla} T, \tag{1.7}$$

where $\dot{Q}$ is rate of heat flow, τ is Thomson coefficient, J is current density and ∇T is Temperature gradient. Also,

$$\tau = \frac{d\pi}{dt} - S, \tag{1.8}$$

is called first Thomson relation. Since $\pi = ST$, we can rewrite τ as

$$\tau = T\frac{dS}{dt}. \tag{1.9}$$

1.3 Charge transport

As discussed, the power factor is dependent on the electronic properties of a material. Electrical conductivity and thermopower defines power factor and hence

understanding these quantities and their dependency on carrier concentration, band structure, band degeneracy, grain boundaries, and microstructure have great importance. Both of these quantities have a dependence on charge carrier concentration of material such that an increase in one quantity would decrease the other, hence decoupling the two quantities is important as well as a difficult task. If the quantities are not decoupled we need a trade-off to maximize the net figure of merit. We will try to understand electrical conductivity and thermopower in the next section.

1.3.1 Electrical conductivity

Electrical conductivity of a material is given by:

$$\sigma = \mu n q \tag{1.10}$$

where μ is mobility n is charge carrier concentration and q is charge. For a system with both type of carriers it can be written as:

$$\sigma = \mu_h n_h p + \mu_e n_e e, \tag{1.11}$$

with e and p being charges of electron and hole respectively; μ_h and μ_e mobilities of hole and electron respectively, and n_h and n_e are the concentration of holes and electrons respectively. In an intrinsic semiconductor n_h and n_e are equal. In a degenerate semiconductor, one type of carrier is much more than the other. Direct dependence on carrier concentration means electrical conductivity increases with an increase in carrier concentration, provided mobility is constant. Hence carrier concentration is a key factor to control electrical conductivity. The next important factor to control electrical conductivity is mobility. Mobility is given by $\mu = v_d/E$ where v_d is drift velocity and E is applied electric field. Drift velocity is defined as $v_d = eE\tau/m_e$ where τ is the relaxation time of the carriers and m_e is the band effective mass which depends on the shape of the band near the Fermi energy. For example, for a sharp band, m_e is less than for a flat band. Carriers with low m_e and large τ thus have higher mobility as $\mu = e\tau/m_e$. Thus, the mobility also plays an important role in controlling electrical conductivity. Also, the temperature dependence of mobility gives an understanding of the scattering mechanism dominating any particular system. Experimentally mobility can be obtained from measuring the temperature dependence of electrical conductivity and temperature-dependent carrier concentration using the Hall measurement. In those cases where carrier concentration does not change much with temperature, we can assume the T dependence of electrical conductivity to be the same as the T dependence for mobility. Generally, in a material more than one scattering mechanism controls the transport

of carriers thus Matthiessen's rule is applied to find effective mobility. Matthiessen's rule can be written as:

$$1/\mu = (1/\mu_1 + 1/\mu_2 + 1/\mu_3 + ...), \tag{1.12}$$

where μ_i defines the mobility due to the ith scattering mechanism.

Phonons are a source of scattering in charge transport and charges get scattered upon interacting with a phonon, either creating or destroying phonons. The interaction of charge carriers with acoustic phonons is elastic in nature. The mobility in non-polar semiconductors is dominated by acoustic phonon interactions. The mobility in such semiconductors has $T^{-3/2}$ dependence. When the carriers get scattered due to polarization field generated by the polar optical phonons, mobility is proportional to $T^{-1/2}$; in the case of non-polar optical phonon, there is no long-range distortion generated, and hence a $T^{-3/2}$ dependence is observed. In optical phonon interactions, phonon absorption and emission events are at different scattering rates. Optical phonon scattering events are inelastic in nature and thus lead to significant energy transfer. Ionized impurity scattering is elastic in nature and scatters low energy carriers strongly hence dominant at low temperature and has $T^{3/2}$ dependence, whereas for neutral impurity mobility is proportional to T^0. Alloy scattering is due to interaction with the field generated by atomic potential fluctuation, and in this case, the mobility is proportional to $T^{-1/2}$.

To understand a material's property, it is important to have a practical estimate of the electrical conductivity of different materials. Metals have very high electrical conductivity. Copper has electrical conductivity around 5.9 $\times 10^5 S/cm$ at room temperature with carrier concentration of order $10^{22} cm^{-3}$. Intrinsic semiconductors have very low electrical conductivity and their conductivity depends on defect states in the material. Silicon has a conductivity around 4 $\times 10^{-6} S/cm$ at room temperature whereas for germanium this is around 0.02 S/cm but the values changes with doping and impurity in the material. PbTe has electrical conductivity of the order 1000 S/cm and carrier concentration is of order of $10^{19} cm^{-3}$ with mobility of order of 1000 $cm^2 V^{-1} s^{-1}$ [8]. SiGe alloy is one of the materials used for high temperature thermoelectric application; the electrical conductivity of SiGe at room temperature is 600 S/cm with carrier concentration $5 \times 10^{19} cm^{-3}$ and mobility 5 $cm^2 V^{-1} s^{-1}$ [109].

1.3.2 Thermopower

Thermopower or Seebeck coefficient of a material is given by the formula

$$S = V/\Delta T, \tag{1.13}$$

where V is the potential developed when a temperature gradient of ΔT is maintained across the measuring electrode. The Seebeck coefficient for most materials changes with temperature. Within a single parabolic band (SPB) model Seebeck coefficient is given by,

$$S = \frac{8\pi^2 k_B^2 T m_d^* (\pi/n)^{2/3}}{3qh^2}, \tag{1.14}$$

where n is carrier concentration, m_d^* is density of state effective mass, k_B is the Boltzmann constant, h is the Planck's constant, q is charge and T is temperature. Also, the density of state effective mass m_d^* depends on band effective mass m_b^* and band degeneracy N_v by the relation:

$$m_d^* = N_v^{2/3} m_b^*. \tag{1.15}$$

This relation itself is sufficient to understand that thermopower is inversely proportional to carrier concentration and is directly proportional to the density of states effective mass. Also, the higher the band degeneracy, the higher is the thermopower. A flat band system will have higher m_d^* hence higher thermopower.

The other interesting relation to understand thermopower is the Mott's relation which connects thermopower to electrical conductivity. Mott's relation can be written as

$$S \propto k_B T \left[\frac{d \ln \{\sigma(E)\}}{dE} \right]_{E=E_F} \tag{1.16}$$

where k_B is the Boltzmann constant and E_F is Fermi energy. As we know that

$$\sigma = q\mu(E)n(E), \tag{1.17}$$

this gives us

$$S \propto k_B T \left(\frac{1}{\mu} \frac{d(\mu)}{dE} + \frac{1}{n} \frac{d(n(E))}{dE} \right)_{E=E_F}. \tag{1.18}$$

From the relation obtained for thermopower, we can easily say that thermopower can be enhanced by changing the density of states near the Fermi level or by changing the mobility of carriers at the Fermi level. These methods have been employed to enhance thermopower in different thermoelectric materials. We will discuss these strategies in the coming sections.

A high valley degeneracy is observed in a cubic system due to its high symmetry. PbTe has a primary light valence band maxima with valley degeneracy $Nv = 4$ at L-point in the first Brillouin zone and a secondary heavy valence band maxima at Σ-point with valley degeneracy $Nv = 12$. Thermopower of p-type PbTe is $\sim 50\mu V/K$ at 300 K and $\sim 300\mu V/K$ at 750 K [15].

1.4 Thermal transport

Specific heat and thermal conductivity of material are of great importance for determining its thermoelectric properties. We will study these in great detail in this section.

1.4.1 Thermal conductivity

The thermal conductivity of material with only one type of charge carrier can be considered to have two parts: electronic thermal conductivity (κ_e) and lattice thermal conductivity (κ_L). Heat carried by these carriers from the hot end to the cold end gives rise to the electronic thermal conductivity κ_e. The electronic thermal conductivity is directly proportional to electrical conductivity in metals. From the Drude model for metals, we can write

$$\kappa_e = L\sigma T \tag{1.19}$$

where L is the Lorenz number and the relation is called the Weidemann-Franz law. In the degenerate limit the Lorenz number is $2.44 \times 10^{-8}\ W\Omega K^{-2}$. However, significant deviation from this can occur for nondegenerate semiconductors. Lorenz number varies with temperature for many degenerate semiconductors and thus different complex methods are used to estimate the Lorenz number. Kim et al. proposed a simple formula to estimate Lorenz number that can be written as:

$$L = 1.5 + exp[\frac{-|S|}{116}] \tag{1.20}$$

where S is the Seebeck coefficient (in $\mu V/K$) and the value of L is in $10^{-8} W\Omega K^{-2}$. The equation is accurate within 5 % for the single parabolic bands considering acoustic phonon scattering and within 20 % for complex band structure [94].

Heat carried by lattice vibrations, also called phonons, give rise to the lattice part of thermal conductivity represented as κ_L. It can be estimated by subtracting the electronic part of thermal conductivity from the total measured thermal conductivity:

$$\kappa_L = \kappa_{Tot} - \kappa_e. \tag{1.21}$$

The lattice thermal conductivity can be obtained from the following relation

$$\kappa_L = \frac{C_V v l}{3} \tag{1.22}$$

here v is the group velocity, C_V is the heat capacity per unit volume and l is the mean free path. The mean free path of phonons $l = v\tau$ where τ is the relaxation time. A

phonon is defined as a particle with momentum $\hbar k$ and energy $\hbar\omega$. Two phonons defined by k_1, ω_1 and k_2, ω_2 can get destroyed to give a single phonon k_3, ω_3. In such a process, the collision can be considered elastic or inelastic depending on whether the total momentum is conserved or not. This is depicted in Fig 1.4. Panel (a) shows an elastic scattering mechanism (normal process), and (b) shows an inelastic scattering process (Umklapp process).

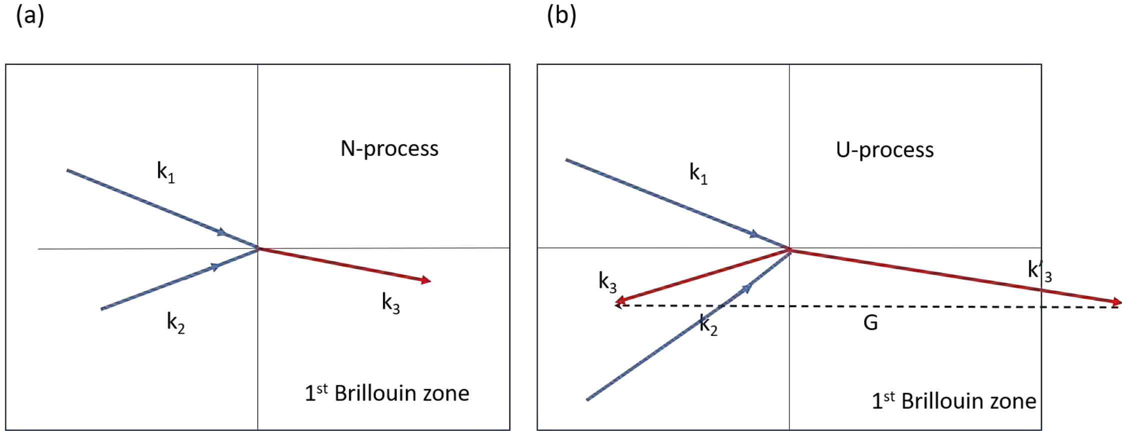

Figure 1.4: Schematic showing (a) N-process and (b) U-process

In general we can write:

$$k_1 + k_2 = k_3 + G \tag{1.23}$$

where G is $\pm\frac{2n\pi}{a}$. For normal process $n = 0$ hence

$$k_1 + k_2 = k_3 \tag{1.24}$$

thus conserving the net momentum here $\frac{-\pi}{a} \leq k_i \leq \frac{\pi}{a}$ where i = 1, 2 and 3. For a U-process (Umklapp means flip-over) $|k_3| > \frac{\pi}{a}$ and $G \neq 0$ i.e. $n \neq 0$, thus the third phonon has its momentum extending to the second Brillouin zone and hence flipped over to first Brillouin zone using reciprocal lattice vector. In U- process thus net momentum is not conserved: however, the net crystal momentum is conserved. As U process reverse the momentum direction, it is most important in resisting the heat flow.

At low-temperature, thermal phonons are sound waves and thus they have a long mean free path, hence l is independent of T, so the thermal conductivity $\kappa_L \propto C_V \propto T^3$. At high temperatures, phonon gets scattered by other phonons (Umklapp Processes). Since the phonon density is proportional to temperature hence we expect $l \propto T^{-1}$; as C_V and v are constant, $\kappa_L \propto T^{-1}$. Scattering of phonons have great implication on the lattice part of thermal conductivity, therefore, in addition to the phonon-phonon scattering, we will discuss a few other scattering mechanisms in the next paragraph.

There can be different scattering processes including phonon-phonon scattering (normal scattering and Umklapp scattering), grain boundary scattering , point defect scattering, electron-phonon scattering etc. The effective rate of scattering can be obtained using Matheissen's rule give by:

$$\tau_C^{-1} = \tau_N^{-1} + \tau_U^{-1} + \tau_G^{-1} + \tau_i^{-1} + \tau_{p-e}^{-1} \tag{1.25}$$

where τ is relaxation time of phonon, τ_C^{-1} is combined scattering rate, τ_N^{-1} is for normal process, τ_U^{-1} for U-process, τ_G^{-1} for grain boundary, τ_i^{-1} for impurity scattering, and τ_{p-e}^{-1} for electron-phonon scattering process.

The scattering rate τ^{-1} varies linearly with ω for N-processes and has ω^2 dependence for the Umklapp process, hence Umklapp processes dominate at a higher frequency. Another way of understanding the same is as follows: at a low temperature very few phonons have large k hence U-processes are rare but at high T most of the phonons have large k hence U process dominates. For grain boundary scattering τ_G^{-1} is T independent whereas for impurity scattering due to mass difference, τ_i^{-1} has ω^4 dependence. At low temperatures, these impurities and defects dominate the thermal conductivity and τ has $T^{-3/2}$ dependence.

Experimentally thermal conductivity can be obtained by measuring thermal diffusivity (D), heat capacity (C_p), and density (ρ) of the sample given by

$$\kappa_{Tot} = D\rho C_p. \tag{1.26}$$

PbTe intrinsically have a less thermal conductivity $\sim 2.2Wm^{-1}K^{-1}$ at room temperature [8]. Half Heuslers like ZrNiSn have very high thermal conductivity of order 14 $Wm^{-1}K^{-1}$ at room temperature [242].

Till now we have talked about thermal conductivity in materials where only one type of carrier is considered, but as we know in narrow bandgap semiconductors and semimetals, we have a contribution from minority carriers at high temperatures. Suppression of bipolar thermal conductivity (κ_{bip}) can help in reducing the thermal conductivity hence enhancing the figure of merit. Mostly, two strategies can be used : (i) increasing the bandgap, and (ii) increasing the majority carrier concentration. Theoretically, κ_{bip} can be estimated using the following formula :

$$\kappa_{bip} = [\Sigma_i \sigma_i S_i^2 - \frac{(\Sigma_i \sigma_i S_i)^2}{\Sigma_i \sigma_i}]T \tag{1.27}$$

S_i is Seebeck coefficient due to i carrier where i = majority (maj) and minority carriers (min) and σ_i is cinductivity due to i carrier where $i = \{\text{maj, min}\}$. Estimating S_i and σ_i individually is nearly impossible [95]. The measured S in such cases is a conductivity-weighted averages of σ_i and S_i given by:

$$S = \frac{\Sigma_i \sigma_i S_i}{\Sigma_i \sigma_i}. \tag{1.28}$$

1.4.2 Specific heat

The specific heat (C_p) at low temperatures model can be written as

$$C_p = \alpha T + \beta T^3 \tag{1.29}$$

where αT is the electronic part and βT^3 is the phononic part. For metallic systems at low T, αT is dominant as phonons freeze out. For insulating systems, at low T, $C_p \propto \beta T^3$. At high temperatures i.e. well above the Debye temperature $T \gg \theta_D$, $C_p \to 3nR$ where R is the universal gas constant and n is the number of atoms in the molecule. This is known as the Dulong-Petit law. In the intermediate temperature range, C_p can be described using the Debye or Debye-Einstein model.

1.4.3 Quality factor and weighted mobility

Other important quantities that are important from a material point of view are a quality factor and weighted mobility. Quality factor(β) depends on weighted mobility (μ_W) and lattice thermal conductivity (κ_L) [177].

$$\beta \propto \mu_W / \kappa_L, \tag{1.30}$$

and

$$\mu_W \propto \mu (m_d^*)^{3/2}, \tag{1.31}$$

where m_d^* is the density of states effective mass and μ is mobility. Goldsmid showed the importance of high mobility high density of state effective mass and low lattice thermal conductivity for thermoelectric performance. Later Slack summarised the concept called phonon glass electron crystal (PGEC).

Weighted mobility analysis can give information about the electronic structure and scattering mechanisms in materials and is helpful in understanding and optimizing thermoelectric systems. Obtaining a high value of weighted mobility μ_w, where a small change in carrier concentration does not affect drift mobility suggests an increase in density of stated effective mass. Higher weighted mobility for a given sample means a higher power factor. Weighted mobility can be obtained using electrical conductivity and Seebeck coefficient of a material [177] using equation:

$$\mu_W = \frac{3h^3\sigma}{8\pi e(2m_e k_B T)^{3/2}} \left[\frac{exp\left[\frac{|S|}{k_B/e} - 2\right]}{1 + exp\left[-5\left(\frac{|S|}{k_B/e} - 1\right)\right]} + \frac{\frac{3}{\pi^2}\frac{|S|}{k_B/e}}{1 + exp\left[5\left(\frac{|S|}{k_B/e} - 1\right)\right]} \right], \tag{1.32}$$

where S is Seebeck coefficient of the material, σ is electrical conductivity at temperature T. k_B and e is Boltzman constant and electronic charge. Similarly, quality factor β is related to the material performance and hence to the figure of merit zT. Quality factor β can be written as follows:

$$\beta = \left(\frac{k_B}{e}\right)^2 \frac{8\pi e(2m_e k_B T)^{3/2}}{3h^3} \frac{\mu_W}{\kappa_L} T. \tag{1.33}$$

In Bi_2Te_3, at a quality factor β of 0.4 $zT = 1$ is obtained [54].

1.5 Strategies to enhance the thermoelectric figure of merit

In the last few decades, several novel strategies have been developed to enhance the thermoelectric figure of merit of potential thermoelectric materials. The enhancement in the figure of merit can be obtained by enhancing the power factor or by decreasing the thermal conductivity.

1.5.1 Enhancing power factor

The power factor of a material is defined as the product of the square of thermopower and electrical conductivity. Enhancing the power factor of a material is a difficult task because the quantities thermopower and electrical conductivity are inversely correlated as was shown in Fig. 1.2(b). The Seebeck coefficient of a material with a low carrier concentration is high but its electrical conductivity is low. This is because σ depends on carrier concentration directly and the Seebeck coefficient has an inverse relation. The optimum carrier concentration that maximizes the power factor generally lies in the range of 10^{19} cm^{-3} to 10^{20} cm^{-3}, a carrier concentration typical of degenerate semiconductors or semimetals. So to have a better performance as thermoelectric material we need a trade-off between thermopower and electrical conductivity. Different strategies to enhance the power factor are carrier optimization, band engineering, nanostructuring, etc.

Carrier optimization

As discussed in the previous section, the power factor peaks near optimum carrier concentration. The easiest way to tune the carrier concentration is through doping to maximize this power factor. The dopant and doping percentage for maximizing the power factor can be determined experimentally or with some theoretical studies or both. Carrier optimization has been used as a key strategy for enhancing the PF for various materials [2, 89, 83, 84].

Band engineering

Various strategies like band flattening, band convergence, nanostructuring, carrier energy filtering, resonant doping depend on changing the electronic band or altering the density of states near the Fermi energy. These strategies have been successfully employed in different materials to enhance the power factor. Thermopower for a degenerate semiconductor can be given by the Mott equation as shown here:

$$S = (\frac{\pi^2 k_B^2 T}{3q})(\frac{\delta \ln(n(E))}{\delta E} + \frac{(\delta \ln \tau(E))}{\delta E} + \frac{\delta \ln(v(E)^2)}{\delta E})_{E=E_F}, \tag{1.34}$$

here $\mathrm{k_B}$ is the Boltzamnn constant, $\tau(E)$ is relaxation time, $n(E)$ carrier concentration. When thermopower is optimized by using variation in the relaxation time with the energy of the carriers, this effect is called the **carrier energy filtering effect** [25]. In this approach, charge carriers with low energy are filtered out by introducing energy barriers, this can be done, for example, by creating sufficient nano-inclusion of secondary phase in the thermoelectric matrix. This is shown in Fig.1.5 along with other band engineering approaches.

Nano-structuring can be done to enhance the density of states due to the quantum confinement effects. Similarly, low dimensional thermoelectric materials such as 1D quantum wires, 2D quantum wells [113, 110, 111] also show enhanced performance due to quantum confinement leading to large variations in the density of states with respect to energy near the Fermi energy. The enhancement in DOS at the Fermi level increases the thermopower using the second term in the Mott's relation (eq.1.34).

A similar enhancement in thermopower can be observed due to **band convergence** [63, 40, 172], which leads to an increase in the band degeneracy. The **resonant doping** on the other hand results in [68, 21, 25, 72, 204] a sharp peak like feature in the DOS as an effect of doping. These approaches have been helpful in a few materials to enhance the PF and resulting zT. Band convergence for two bands with similar individual Seebeck coefficients leads to an increase in electrical conductivity from individual conductivities.

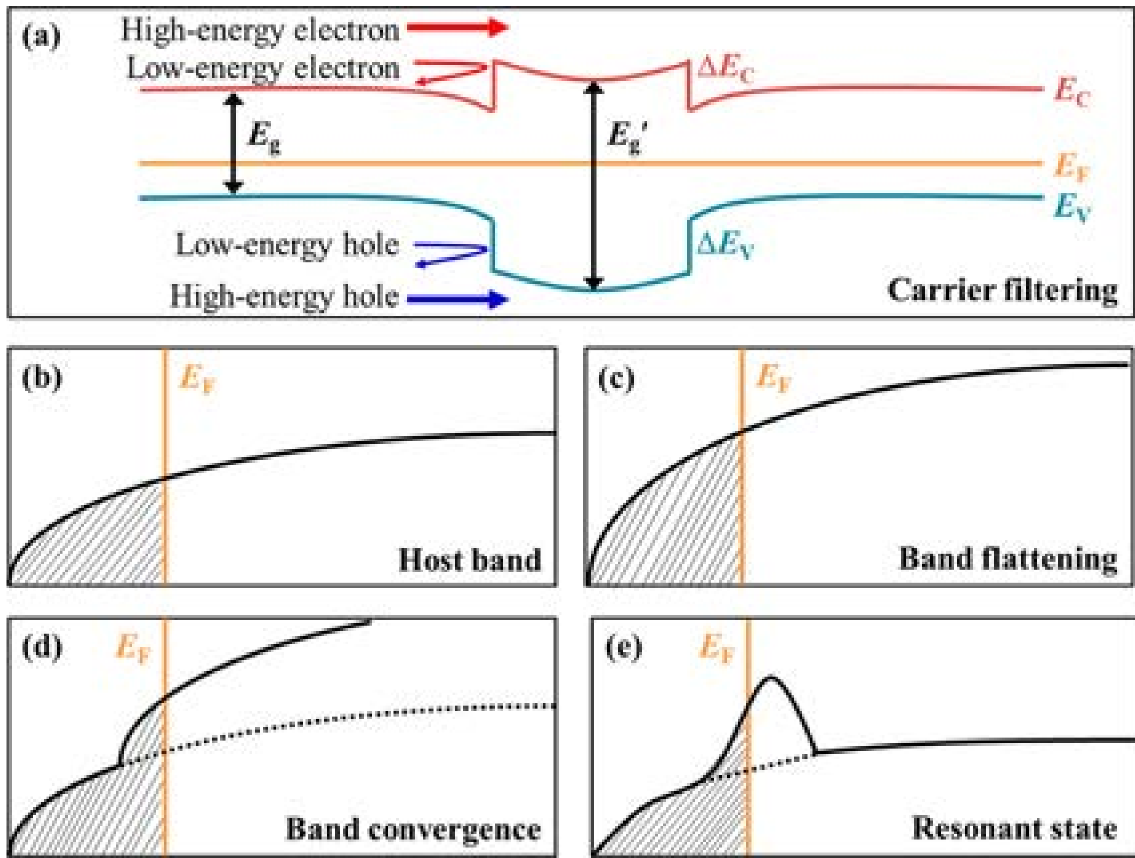

Figure 1.5: Different ways for band engineering (a) explaining carrier filterng effect, (b) schematic of band picture of normal materials (c) band flattening effect (d) band convergence (e) resonant level doping (adapted from [101]).

1.5.2 Strategies for decreasing the thermal conductivity

As mentioned earlier, the thermal conductivity of materials has mainly two components: electronic thermal conductivity (κ_e) and lattice thermal conductivity (κ_L). The electronic part κ_e depends on the electrical conductivity hence nothing much can be done about it as we do not want electrical conductivity to decrease. Reducing lattice thermal conductivity thus plays an important role in enhancing the overall efficiency of the device. Thermal conductivity can be reduced by a few approaches such as nano-structuring or nano inclusions [91, 98, 113, 110, 111, 152, 175], alloying [218, 108] and doping with different elements to create point defects, etc.

Nano-structuring

The mean free path (MFP) of phonons is an important parameter to consider while designing strategies for lowering the thermal conductivity. The average MFP of phonons is of the order of a nanometer. They are therefore scattered by the lattice defects of nanometer size. Mean free paths for different scatterers to obstruct the heat flow are different; for example grain boundary MFP is around 100 - 1000 nm,

for nano precipitates MFP is 8-100 nm, and for point defects, it is around 0 -10 nm. Thus employing an all-hierarchical approach to scatter most of the phonons by incorporating atomic-scale point defects, nano-structuring and mesoscale grain boundaries can lead to ultra-low values of thermal conductivity for a given material. A schematic showing for all hierarchical scattering and contribution in lattice thermal conductivity depending on mean free path due to different types of scatterers is shown in Fig.1.6 [91, 98, 113, 110, 111, 152, 175].

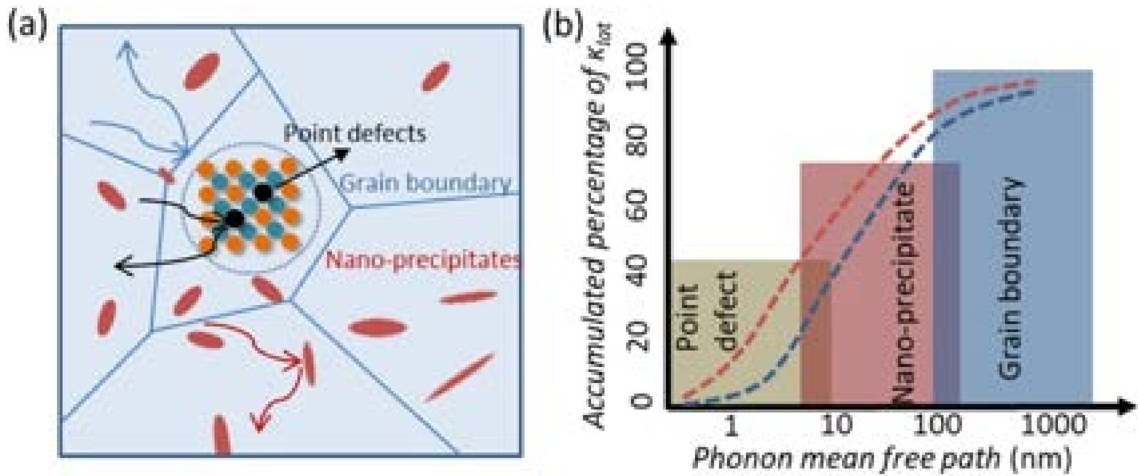

Figure 1.6: (a)A schematic for all heirarchial scattering and, (b) contribution in lattice thermal conductivity depending on mean free path due to diffetrent types of defects (adapted from [208]).

Alloying

Adding a small amount of foreign element in a given material to enhance the electronic properties is called doping, whereas adding a higher weight percentage of secondary material ($> 1\ wt\ \%$) to enhance strength, hardness, electronic and thermal properties is called as alloying. Alloying [218, 108] in various materials has helped in reducing the thermal conductivity to a great extent. The effect of alloying has been extensively studied in various systems. In PbTe-GeTe alloys, with an increase of mole percentage of GeTe in PbTe matrix κ_L reduces to half by just 5 moles % [99]. In PbSe-PbS alloys, Wang et al. reported a decrease in thermal conductivity with an increase in sulfur ($< 16\ mol\%$) [194]. This decrease was attributed to the formation of nano precipitates of PbS in the PbSe matrix. This helped in reducing the thermal conductivity by scattering phonons of the wavelength of the order of the size of the nano precipitates [9].

Doping with different elements

Doping different elements creates point defects due to differences in size and mass, which changes the lattice potential and thus scatter phonons and reduce thermal lattice conductivity. Doping with a heavier element at the site of some lighter element leads to an increase in mass fluctuation due to the difference in mass between the dopant and the original atom. Johari et al. [88] showed considerable decrease in thermal conductivity of ZrNiSn by doping Ge at Sn site from 6.5 $Wm^{-1}K^{-1}$ to 4.5 $Wm^{-1}K^{-1}$ at room temperature [22] . Similar results were obtained upon doping ZrNiSn with doping Ta [229], La [1], Nb [125], V [21], Hf [61, 160, 1, 2, 3], Ti [160, 61] at the Zr Site or Sb at the Sn site [2, 160, 3]. A similar effect has been seen in several other materials as well [8, 15, 50].

1.6 State of art

1.6.1 Chalcogenides

Chalcogenides are family of compounds consisting of atleast one anion from the chalcogens group (S, Se, Te) along with one or more electropositive elements. A long list of compounds with various structure types belong to this family. Chalcogenides as thermoelectric materials have shown great performance due to their low thermal conductivity. The major challenge is that they can be used only in low temperature regime or intermediate temperature regime, as at high temperatures they tend to decompose or melt. Among this family there are very many good thermoelectrics. For example, Bi_2Te_3 [200, 10, 201], PbTe [91, 208, 7], PbSe [194], PbS [194], Sb_2Te_3 [192, 239], Ag_2Te [241, 79], Cu_2Se [147, 214], SnTe [237, 137, 226], $AgSbTe_2$ [158, 49], GeTe [227, 72, 47, 73, 108, 106] etc. Many of these compounds have been studied thoroughly and have shown huge improvement in their thermeoelectric performance by using different strategies discussed in the previous section. We will discuss some of these compounds briefly in this section.

PbX (X = S, Se *and* Te): PbX has been studied thoroughly over the past few decades and has shown significant improvement in its TE properties [91, 208].

This is shown for PbTe in Fig. 1.7 [208]. In the work by Heremans et al [68] resonant doping in PbTe was achieved by just 2 % doping of Tl at the Pb site. The zT value increased from 0.7 to 1.5. Girad et al. [50] showed shape-controlled growth of PbS nanoparticles coherently embedded in PbTe matrix by controlling Na concentration. They also observed some alloying of PbS in PbTe which helped in band alignment and Na doping helped by promoting carriers between heavy and light bands. Androulakis et al. [7] showed the role of band alignment and tuning between light and heavy holes valence bands in Na and K co-doped PbTe.

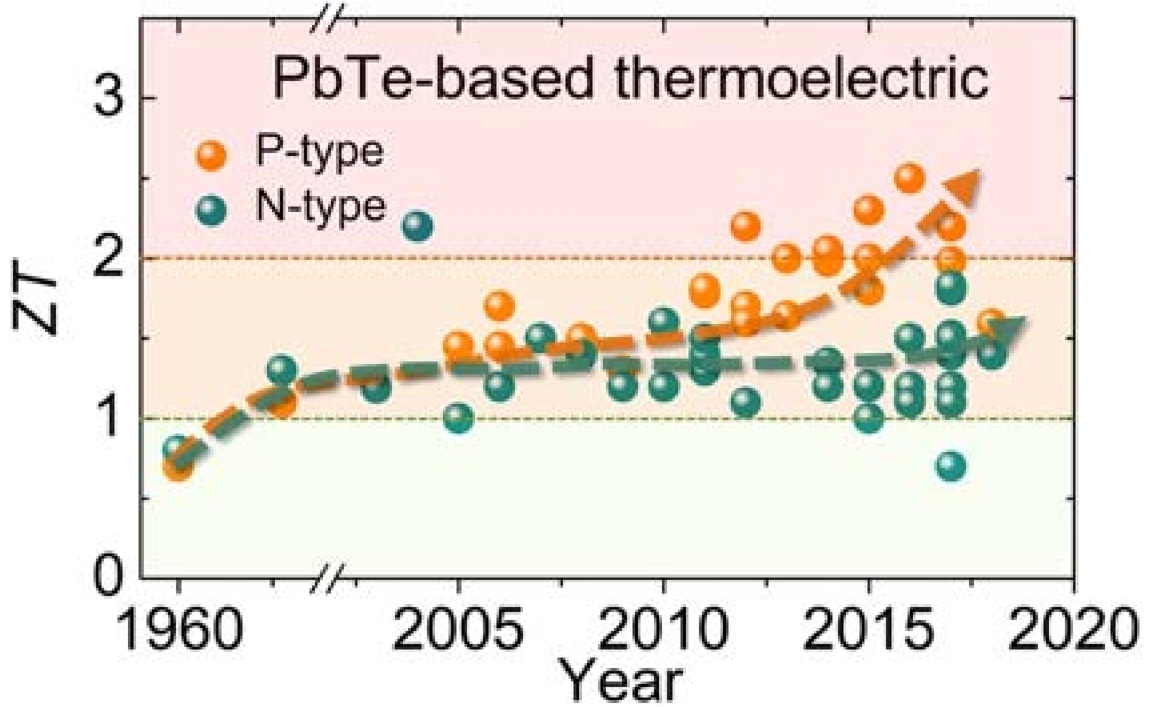

Figure 1.7: Enhancement in zT for PbTe in past few years (adapted from [208]).

Bi_2Te_3: A small bandgap of 0.14 eV has been reported for bulk Bi_2Te_3 [200, 10, 201]. The conduction band has higher mobility than the valence band, effective DOS masses being nearly the same. The combination of inversion symmetry and spin-orbit coupling in Bi_2Te_3 creates topologically protected surface states with time-reversal symmetry [200]. Bi_2Te_3 doped with Se [201] showed inherently low thermal conductivity but high electronic weighted mobility, but was limited by bipolarity due to low bandgap. Bi_2Te_3 has been also used to make flexible thermoelectric devices based on Bi_2Te_3 - carbon nanotube hybrid by Yang Li et al [110, 111]. They could achieve a figure of merit of 0.23 at 330 K in this device with a maximum power density of 0.93 $mWcm^{-2}$ under $\Delta T = 25K$.

GeTe: Recently, GeTe has attracted huge attention as a thermoelectric material. Though it has been known to be a good thermoelectric material for a long time, the recent advancement in thermoelectrics has brought it to a different level. GeTe undergoes a phase transition from low-temperature rhombohedral phase to high-temperature cubic phase around 720 K [227]. It retains its high thermoelectric performance even in the high-temperature phase. A figure of merit zT $\geq$ 2 has been achieved in this system around room temperature and mid-temperature range [227, 72, 47]. Doping Indium (around 2 %) results in resonant doping and leads to zT $\sim$ 1.3 at 355 ^oC [204]. By Sb doping at Ge site and alloying with Se, Li et al. obtained a zT $\sim$ 2 [108, 107]. Taking advantage of the Rashba effect in GeTe and using Sb and Sn co-doping, Hong et al. obtained the highest zT of 2.2 at 700 K [74].

$AgSbTe_2$: $AgSbTe_2$ has shown huge potential as a thermoelectric material [158,

49, 26, 36, 217]. Roychowdhury et al. [158] in their work obtained a figure of merit $zT \sim 1.5$ at room temperature and, a maximum $zT \sim 2.6$ at 573 K. They found that cadmium doping of $AgSbTe_2$ enhances cationic ordering which improves electronic properties and at the same time decreases the thermal conductivity.

1.6.2 Oxides

Oxide thermoelectric materials are of great interest as most of them can be used in air atmosphere. Oxide thermoelectric are also cheap and generaly non-toxic. Some examples of n type oxide thermoelectric materials are $SrTiO_3$ [216, 98, 132, 152, 126], ZnO [102, 184, 224, 134, 191, 193, 141, 140, 27], In_2O_3 [133, 13], $CaMnO_3$[197, 198, 139]. P-type oxide thermoelectric examples are $Ca_3Co_4O_9$ [187, 188, 131, 118], BiCuSeO [233, 105, 104, 112, 144], NiO [170, 115, 116].

1.6.3 Heuslers

Heusler compounds were first studied by a German mining engineer and chemist Friedrich Heusler in 1903 after whom they have been named. Friedrich Heusler studied Cu_2MnAl, which is is ferromagnetic. Heusler family has a large number of compounds. Full Heuslers (FH) and half Heuslers (HH) are two subclasses in the Heusler family. Full Heuslers have general formula X_2YZ (*Fm-3m*) and half Heuslers have general formula XYZ (*F-43m*). The general composition and constituent elements are shown in Fig. 1.8. Their structure consists of three interpenetrating face-centered cubic sub-lattices. Heuslers are known to have a special characteristic that their valence electron count can to some extent predict the property of the compound. Transition metal-based half Heuslers with valence electron count (VEC) 18 are generally semiconducting with a narrow bandgap. While alloys of the Heusler family are well known to show very interesting magnetic properties, recently they have also attracted significant attention as thermoelectric materials for energy application at high temperatures. Several half Heusler alloys, in particular, are shown to be good thermoelectric materials. Examples include ZrNiSn, NbFeSb, ZrCoSb, ZrCoBi etc.

Structure

Comparison between structure of full Heuslers and half Heuslers is shown in the Fig. 1.9. We describe here the structure of HH in detail.

Half Heuslers have the general formula XYZ, where X and Y are transition metal and Z is a main group element. The normal arrangement of most of the half Hesulers can be understood using the structure of cubic MgCuSb. In the structure, the

X_2YZ Full Heusler compounds
XYZ Half Heusler compounds

1	2	3	4	5	6	7	8	9	10	11	12	13	14	15	16	17	18
H 2.20																	He
Li 0.98	Be 1.57											B 2.04	C 2.55	N 3.04	O 3.44	F 3.98	Ne
Na 0.93	Mg 1.31											Al 1.61	Si 1.90	P 2.19	S 2.58	Cl 3.16	Ar
K 0.82	Ca 1.00	Sc 1.36	Ti 1.54	V 1.63	Cr 1.66	Mn 1.55	Fe 1.83	Co 1.88	Ni 1.91	Cu 1.90	Zn 1.65	Ga 1.81	Ge 2.01	As 2.18	Se 2.55	Br 2.96	Kr 3.00
Rb 0.82	Sr 0.95	Y 1.22	Zr 1.33	Nb 1.60	Mo 2.16	Tc 1.90	Ru 2.20	Rh 2.28	Pd 2.20	Ag 1.93	Cd 1.69	In 1.78	Sn 1.96	Sb 2.05	Te 2.10	I 2.66	Xe 2.60
Cs 0.79	Ba 0.89		Hf 1.30	Ta 1.50	W 1.70	Re 1.90	Os 2.20	Ir 2.20	Pt 2.20	Au 2.40	Hg 1.90	Tl 1.80	Pb 1.80	Bi 1.90	Po 2.00	At 2.20	Rn
Fr 0.70	Ra 0.90																

La 1.10	Ce 1.12	Pr 1.13	Nd 1.14	Pm 1.13	Sm 1.17	Eu 1.20	Gd 1.20	Tb 1.10	Dy 1.22	Ho 1.23	Er 1.24	Tm 1.25	Yb 1.10	Lu 1.27
Ac 1.10	Th 1.30	Pa 1.50	U 1.70	Np 1.30	Pu 1.28	Am 1.13	Cm 1.28	Bk 1.30	Cf 1.30	Es 1.30	Fm 1.30	Md 1.30	No 1.30	Lr 1.30

Figure 1.8: Elements used in transition metal-based Heuslers compounds shown in periodic table (adapted from [56]).

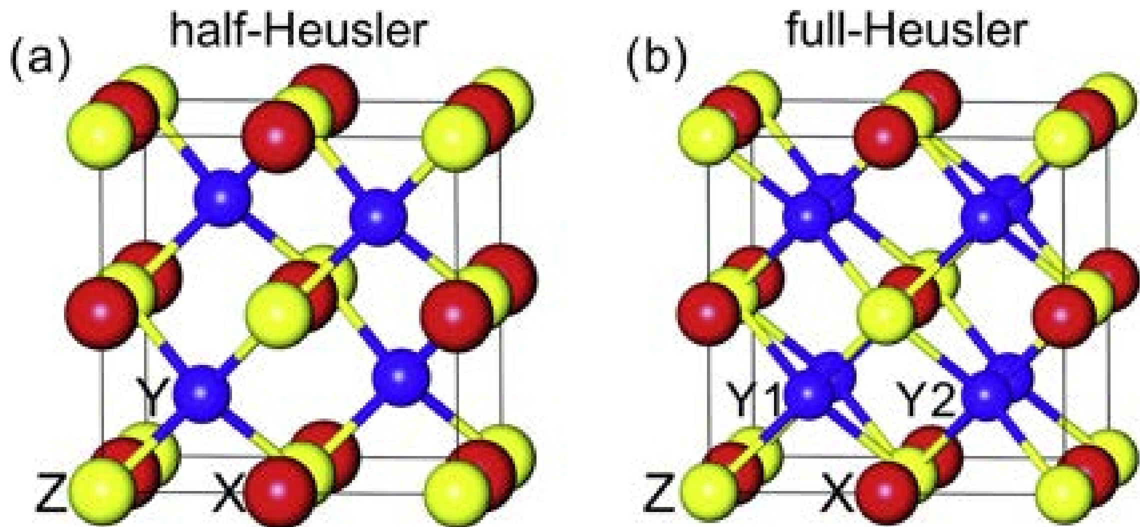

Figure 1.9: Cubic structure of (a) half-Heusler and (b) Full Heusler shown (adapted from [136]).

most electronegative element Sb and most electropositive element Mg forms NaCl type substructure. ZnS type sublattice is built by the element with intermediate electronegativity (Cu atom) and most electronegative element (Sb).

The MgCuSb structure is shown in Fig. 1.10. The Cu atom has a coordination of eight, coordinated tetrahedrally by Mg and tetrahedrally by Sb. Mg and Sb both are coordinated by each other octahedrally. MgAgAs is another prototype of half Heusler structure, but it is less common compared to MgCuSb. MgAgAs

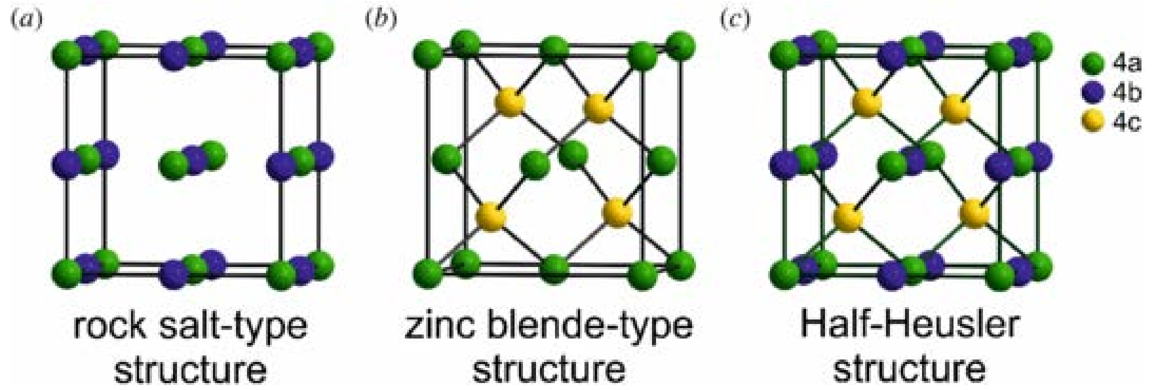

Figure 1.10: Structure of half Heusler as combination of NaCl and ZnS structure (adapted from [19]).

have a different arrangement as here, the most electropositive element Mg and the atom with intermediate electronegativity (Ag) forms NaCl type structure. While intermediate electronegative element Ag and the most electronegative element As forms covalent ZnS type substructure. Which one of the two structures is preferred depends both on the size difference and interatomic interaction between the elements involved.

Electron counting

The electron counting scheme is borrowed from Zintl chemistry. A VEC = 18 favors a semiconducting gap due to a completely filled bonding and empty antibonding orbitals. In TiCoSb, Ti corresponds to $5s^2 4d^2$, Co corresponds to $4s^0 3d^9$, and Sb corresponds to $5s^2 5p^3$ hence TiCoSb is a VEC = 18 compound [56]. The existence of the semiconducting ground state in TiCoSb is explained in Fig. 1.11. There are also some rare-earth-based half Heuslers with VEC = 18; these are, as suggested by the VEC rule, semiconducting in nature and some have interesting magnetic behaviors. For example, RPdBi (R = Ho, Dy, Gd, and Nd) show antiferromagnetic ordering at 2 K, 3.5 K, 13 K, and 4 K respectively, while ErPdBi shows paramagnetism down to 1.7 K and YPdBi shows diamagnetism [51]. This VEC rule is valid only for ternary compounds existing in the MgAgAs-type structure and is found not to be valid for other half Heusler like ternary compounds. Full Heuslers with VEC = 24 are also expected to show semiconducting behavior. In Fe_2VAl, V corresponds to $4s^2 3d^3$, Fe corresponds to $4s^0 3d^8$, and Al corresponds to $3s^2 3p^1$; hence Fe_2VAl is a VEC = 24. The existence of semiconducting ground state in Fe_2VAl is explained in Fig. 1.12 [56].

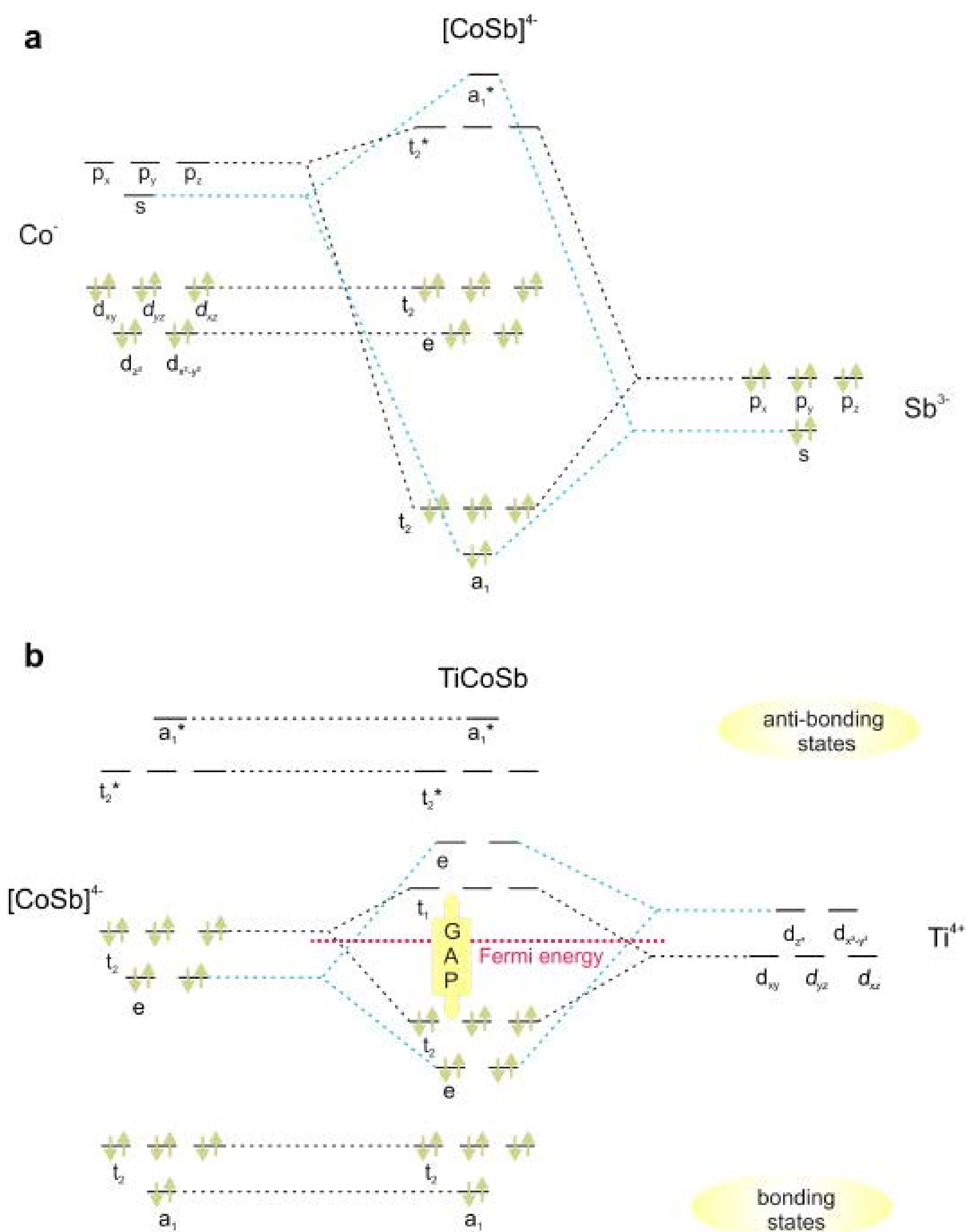

Figure 1.11: Generation of gap by formation of bonding antibonding orbitals in VEC = 18 TiCoSb(adapted from [56]).

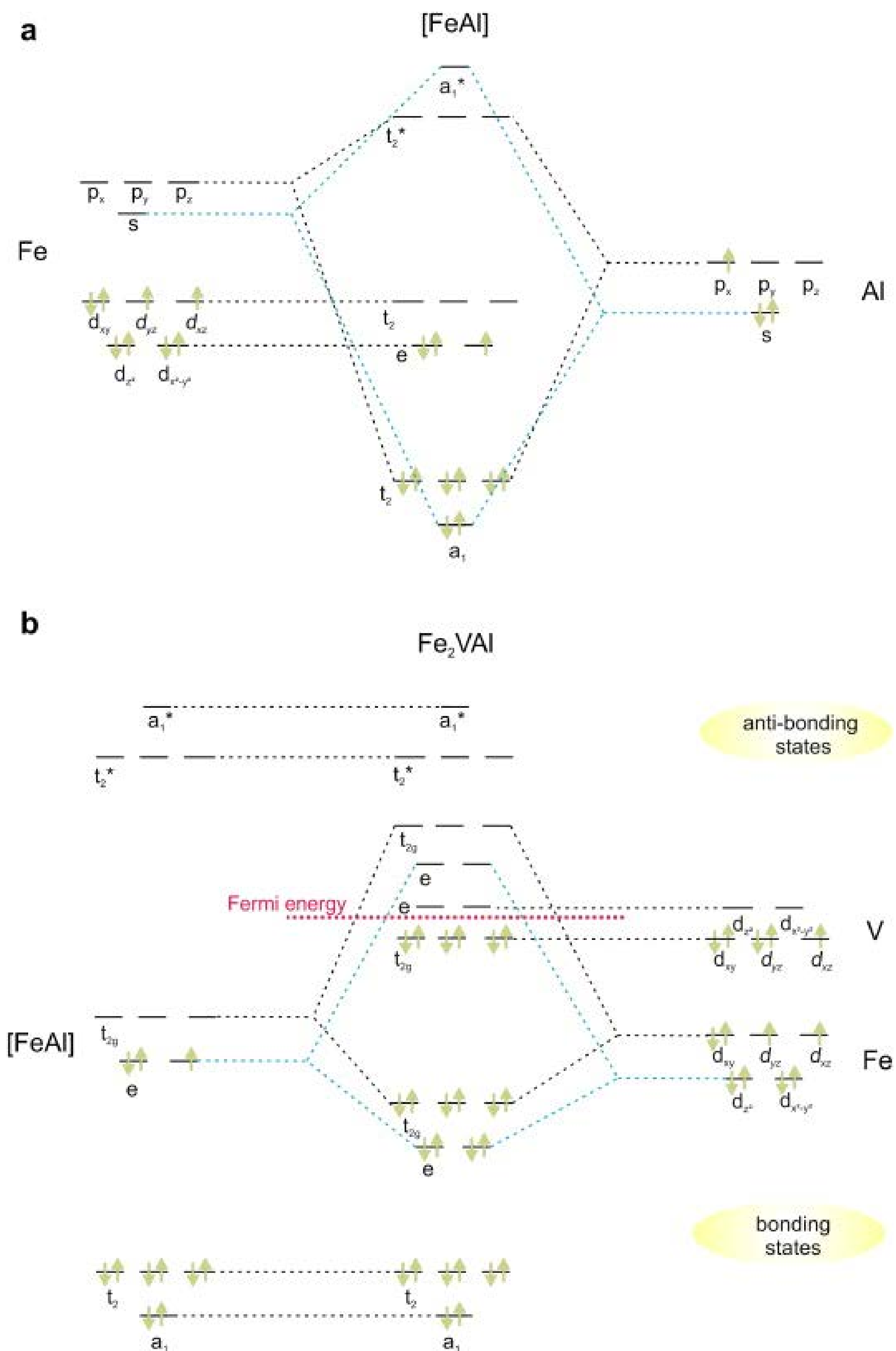

Figure 1.12: Generation of gap by formation of bonding antibonding orbitals in VEC = 24 Fe_2VAl (adapted from [56]).

Advantages and disadvantages

As discussed there are several classes of thermoelectric materials but there are some advantages of each class over the others. **Advantages of using half Heuslers**:

- Stability: Half Heuslers are stable at high temperatures where most of the other competing materials tend to decompose. For example, Bi_2Te_3 is good thermoelectric but it shows considerable deterioration after annealing at 523 K [235] but ZrNiSn has been reported stable at least till 900 K [80].

- Existence of both n-type and p-type behaviors within the half Heusler family.

- Good mechanical strength: Due to the presence of transition metals and strong covalently bonded substructures they have good mechanical strength.

- High power factors: This high power factor of half Heuslers is a direct consequence of their highly symmetric cubic structure. High symmetry leads to high valley degeneracy which further leads to a high Seebeck coefficient. These materials generally have a low bandgap and upon doping attain high values of electrical conductivity. The article by Zhou et al. [236] reveals that the high power factor of half Heusler compounds originate from a strong suppression of electron-acoustic phonon coupling. Through orbital analysis they showed that the weak acoustic phonon interaction is enabled by the non-bonding (anti-bonding) orbitals at the band edge, also this anti-bonding character in HH can be protected by crystal symmetry.

- Non-toxic: Heuslersalloys mostly contain elements that are non-toxic compared to PbTe, or PbSe. So these materials can be efficiently produced at a bulk scale and can be used everywhere without any fear of their harmful effect.

Disadvantages of using half Heuslers: Half Heuslers generally have a high thermal conductivity which limits their figure of merit, despite high power factors reported. The high thermal conductivity is mostly a result of the high crystal symmetry and low anharmonicity of the acoustic modes. Also, there is much less interaction between acoustic and optical phonons, which helps in high group velocity and hence higher lattice thermal conductivity [171]. Also, as we know half Heuslers have better performance as thermoelectric materials with high optimum carrier concentration and they have high electrical conductivity, hence it's often observed that they have a high electronic part of thermal conductivity due to the Weidemann-Franz law.

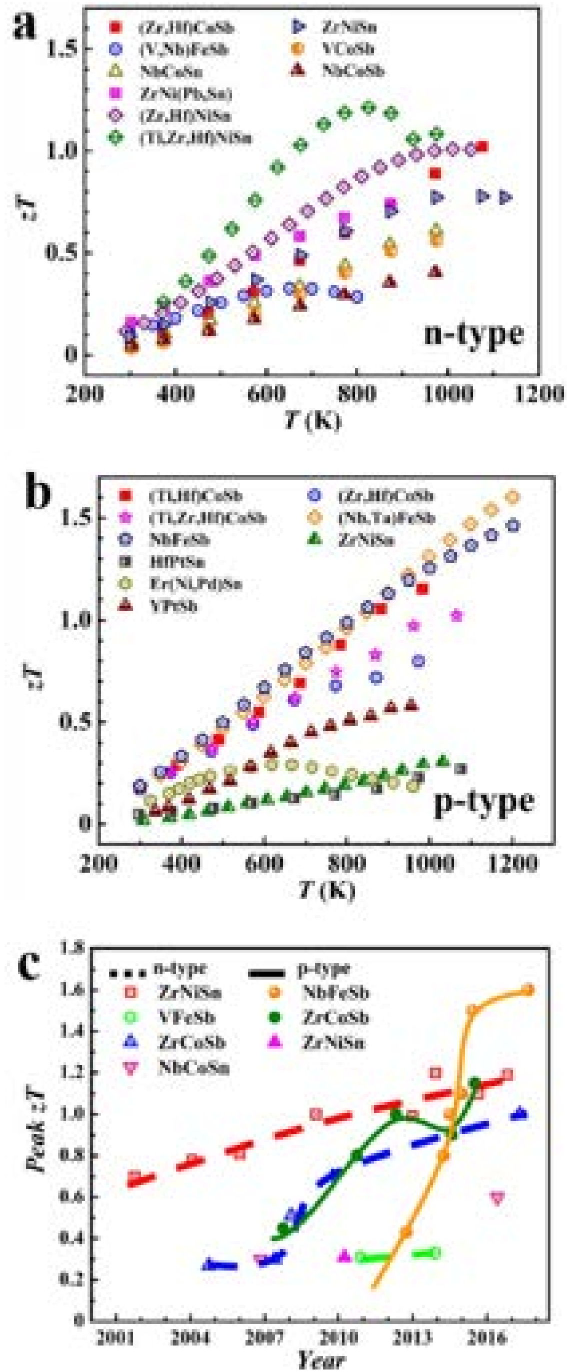

Figure 1.13: Plots showing varaition of zT with temperature for some half-Heuslers (a) n-type and (b) p-type. (c) Plot showing change in peak zT of some n type and p type half Heuslers over last few years. (adapted from [219])

Literature review

ZrNiSn [71, 165, 46, 210] ;[85], NbFeSb [212, 90, 129, 181, 154, 168], ZrCoSb [207, 166, 23, 24, 220, 231], ZrCoBi [238, 145, 230], NbCoSb [205, 222, 206] are a few half-Heuslers studied thoroughly for their thermoelectric performance. Figure of merit of some n-type and p-type half-Heuslers are shown in Fig. 1.13. Also, how the peak zT of some n-type and p-type half-Heuslers evolved over the past few years is shown. We will outline some recent works on ZrNiSn (n-type) and NbFeSb (p-type) in detail in this section.

ZrNiSn: ZrNiSn is one of the most studied HH for thermoelectric application. ZrNiSn as a thermoelectric material has a small bandgap of 0.5 eV calculated theoretically. The experimental band gap is obtained to be smaller for both p-type and n-type variants [165]. The smaller bandgap in ZrNiSn is due to Ni occupying gap states which creates an extra state near the conduction band and thus gives a smaller bandgap [165, 46, 210]. Huang et al studied the effect of the addition of ZrO_2 nanoparticles in ZrNiSn as an extra mode of phonon scattering [85]. Qiu et al. studied the effect of Zr/Sn antisite disorder in ZrNiSn through ab-initio calculation and experiments [148]. No precipitates were observed in annealed samples and a zT of 0.64 at 800 K was obtained for an annealed ZrNiSn sample. The figure of merit, zT = 0.8 at 875 K has been obtained by carrier optimization using Sb doping in ZrNiSn by Xie et al. [210]. A high figure of merit of 1.5 at 700 K was obtained by Ti substitution in (ZrHf)NiSn that was further improved by doping it by Sb at Sn site [160].

NbFeSb: NbFeSb is a promising p-type candidate in half-Heusler based thermoelectric materials. It has shown a zT $>$ 1 hence it is a desirable material for high-temperature thermoelectric applications. NbFeSb has been improved by doping Ti and Hf at the Nb site to obtain a zT of 1.1 [43] and 1.47 [44], respectively via band engineering. Further, Junjie Yu et al. reported a zT of 1.6 at 1200 K by Ta alloying in Ti-doped NbFeSb [218].

1.6.4 Other materials

Apart from the thermoelectric materials discussed in previous sections, there are other different classes of compounds that are studied for their thermoelectric properties and have shown great potential for future energy devices and sensors. Each different classes of material have its own advantages and challenges. Some of these are Clathrates [34], Zintl compounds [93, 172, 173, 186, 185], Skutterudites [159, 121], organic thermoelectric materials [30, 228], hybrid thermoelectric materials [113, 96, 189, 224] etc. Organic thermoelectric materials are important for low-temperature thermoelectric applications for making wearable thermoelectric devices.

Skutterudites have high-temperature stability and high carrier mobility. Clathrates have good thermal stability, and the existence of a rattler in their structure lowers the thermal conductivity making them promising materials for thermoelectric applications[176].

1.7 Synopsis of the work reported in this thesis

In this thesis, half-Heuslers and their related structures were synthesized and studied for high-temperature thermoelectric applications. In chapter 1, we have given an introduction and motivation for doing the thermoelectric research. In chapter 2, we have discussed the experimental technique used in this thesis. In chapter 3, we have studied $Nb_{0.83}CoSb_{1-x}Sn_x$ samples for thermoelectric application. Previous works have shown that NbCoSb does not exist in the pure phase in 111 stoichiometry. Kaiyang Xia et al. [205] showed that it can however be synthesized in the pure HH phase only with about 20% cationic vacancy at the Nb site. These vacancies at Nb the site result in lowering the thermal conductivity. Here, we synthesized $Nb_{0.83}CoSb$ sample and doped it with Sn at the Sb site. These samples are studied for their high-temperature transport properties, thermal properties, and structure. In the Sn-doped $Nb_{0.83}CoSb$ sample we obtained a zT value of 1 near 1100 K, which is 20 % higher than the value previously reported for the undoped $Nb_{0.83}CoSb$. Detailed electronic structure calculations were done in order to understand the role of Sn-doping in zT enhancement. In chapters 4 and 5, we have studied TiNiSi structure-type compounds. These compounds have an orthorhombic structure but with a Heusler-like tetrahedral coordination. In chapter 4, we have studied five such orthorhombic ternary compounds, namely, ZrNiSi, ZrNiGe, NbCoSi, HfNiSi, and ZrNiSb [162]. In chapter 5, we have investigated the effect of doping ZrNiSi with Sb at the Si site. The solubility of Sb in ZrNiSi at the Si site is as low as 5 %, beyond which it undergoes spinodal-like decomposition. The higher doping leads to enhanced power factor and lowers thermal conductivity. We show that zT of ZrNiSi increases by more than an order of magnitude by a small Sb doping. In chapter 6, We studied a new set of compounds called double Heuslers (DH) that are stabilized by mixing orthorhombic ZrNiSb (VEC 19) and cubic TiFeSb (VEC 17). Both of these compounds by themselves do not exist in the pure phase. The new compounds obtained have compositions $(ZrNiSb)_{1-x}(TiFeSb)_x$ where (x = 0.4, 0.45, 0.5, 0.55, 0.6, 0.7). The sample x = 0.5, was nearly pure with a cubic HH structure, XYZ, with X site randomly occupied by Zr and Ti and Y site by Ni and Fe. We formed sample composition around x = 0.5, $x > 0.5$ form p-type and $x < 0.5$ as n-type. All the important results obtained in this thesis and the inferences drawn from their interpretation are summarized in chapter 7. The future scope of the work done

during this thesis is given at the end.

Chapter 2

Experimental Methods

Research in the thermoelectrics field is an amalgamation of materials science, physics, and chemistry. Thermoelectric research has various aspects, such as, the structure and phase stability of a material, its mechanical strength, electronic properties, thermal properties, and challenges involved in making devices out of the studied materials. In this chapter, we will present the experimental methods used for the structural characterization of the TE materials and evaluation of their thermoelectric properties.

2.1 Synthesis

The sample studied in this thesis are intermetallics, most of the samples come under a class of compounds called half Heuslers. The sample studied in chapters 5 and 6 are Heusler-like intermetallics also called distorted Heuslers [12] with orthorhombic crystal structure unlike the cubic structure of Heuslers. These samples are synthesized using metal pieces by mostly the arc-melting technique. To stabilize the phase and to improve homogeneity, the samples were grounded, pelletized (cold-pressing), and sintered at high temperature $\geq 900\ ^{o}$C in a quartz tube sealed under dynamic vacuum ($\simeq 10^{-5}$ bar), in a box furnace. In some cases, the as-melted ingots obtained after the arc melting were sintered directly. The samples containing Zirconium and Titanium elements, react with quartz tube at high temperatures ($\geq 900\ ^{o}$C), to avoid reaction with quartz the inner surface of the quartz tube was coated with a layer of carbon black.

2.1.1 Arc melting

Arc-melting is generally used to melt metals to form an alloy. In this process, an arc is used to melt metal pieces in a water-cooled copper hearth. The arc-melting system (Excel Instruments), used in this work is shown in Fig. 2.1. In Fig. 2.2

Figure 2.1: Arc melting machine with current source and vacuum pump

we have shown a schematic for arc melting. It has a valve and a vacuum pump attached to the chamber to create a vacuum inside the chamber, an argon gas line is connected to the main chamber to purge the chamber after every evacuation. A rotary pump is used to create a vacuum with the lowest pressure reaching down to $1 \times 10^{-2} mbar$. The sample is melted in an inert atmosphere created by multiple cycles of vacuum and purging with argon gas. To remove any small trace of oxygen in the chamber we used zirconium pieces as a getter, Zr is melted before melting the sample so that traces of oxygen are absorbed. A tungsten electrode is used to generate the arc which is also water-cooled. The tungsten electrode has a sharp tip

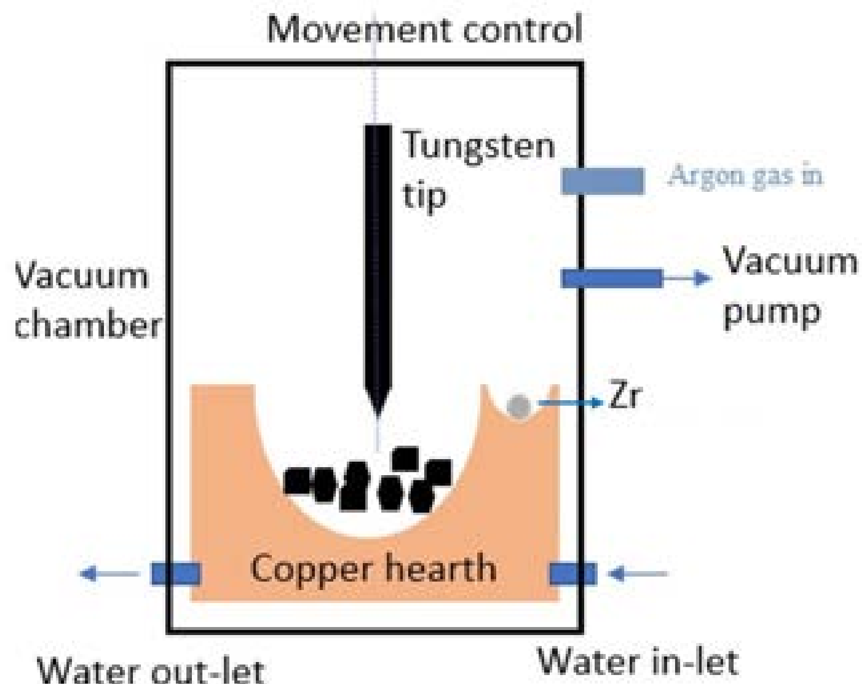

Figure 2.2: Arc melting chamber schematic showing different component of arc melting chamber

and its motion is controlled by a handle outside the vacuum chamber. The whole process is monitored from outside using a transparent quartz window. The copper hearth is grounded and the tungsten electrode is connected to high voltage. The intensity of the arc can be increased or decreased by adjusting the current supplied to the tip. The current can be adjusted between 15 - 150 Amps using an 18.4 kVA transformer. The sample is arc melted five to six times and between each melting ingot is flipped to homogenize it. In our system, three samples can be arc-melted at a time. Fig. 2.3 shows arc melted ingot of $Nb_{0.83}CoSb$ sample.

Figure 2.3: Arc melted ingot of $\mathrm{Nb_{0.83}CoSb}$

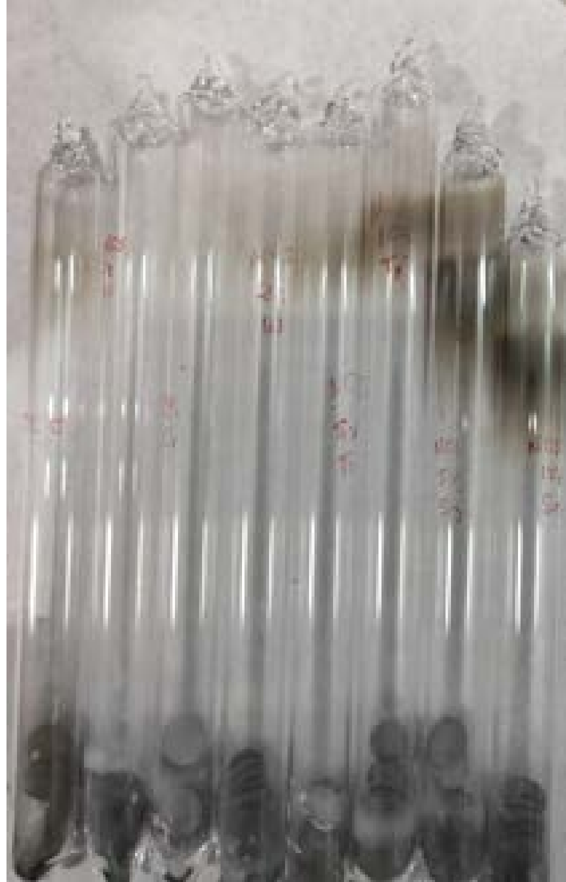

Figure 2.4: Sintered pellets different samples of $Nb_{1-z}CoSb$ in sealed quartz tube

2.1.2 Sintering the sample

As mentioned in the synthesis section, samples were sintered in a sealed quartz tube. Quartz tubes of 10mm diameter and 1 mm thickness were used for this purpose. Sealing is done under a dynamic vacuum created by a turbo molecular pump under a vacuum of order $10^{-4} mbar$. The quartz tubes were preheated for 24 hrs at 900 ^oC to remove any trace of water adsorbed on the inner wall of the tube. If the sample contained Zr and Ti metal as a component of the sample the inner wall of the quartz tube is coated with carbon soot by burning alcohol using a fire torch. This is done to avoid the reaction of silica with Zr and Ti. A box furnace from Nabertherm is used to sinter the samples at temperatures $\geq$900 ^oC. For $Nb_{1-z}CoSb$ we have used sintering temperature of 1100 ^oC. A typical time of sintering used is 7 days at the highest temperature followed by quenched in an ice water bath. Fig. 2.4 shows sintered pellets in the sealed quartz tubes.

2.1.3 Cutting and polishing

Ingots and densified pellets were cut in appropriate shape and dimensions for measurement using a low-speed diamond saw (South Bay, USA). Samples are cut in the

shape of the bar for Hall measurements, resistivity, and Seebeck coefficient measurements. For thermal conductivity square or circular discs were used. For FESEM imaging and chemical mapping, samples were polished to obtain a mirror-like finishing of the surface using Grinder/Polisher (Model 800 South Bay, USA). Fig. 2.5 shows a sintered pellet polished and cut in bar shape for transport property measurements. The disc shape is obtained by cold-pressing the powders in a stainless steel di. These pellets were subsequently annealed for densification as explained in the previous section.

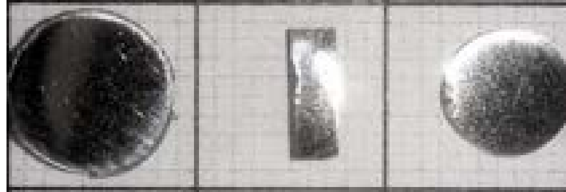

Figure 2.5: Sintered pellets of $Nb_{0.83}CoSb$ for thermal and charge transport measurement in shape of disc and bar.

2.2 Structure and phase characterization

Sample phase purity is important to understand its physical properties. The presence of secondary phases in the sample increases the disorder and affects the electronic and thermal properties. The secondary phases also influence the microstructure of the sample. To check the sample's phase purity, we use powder x-ray diffraction, FESEM imaging, HRTEM imaging, and TGA/DSC setup.

2.2.1 Powder x-ray diffraction

X-ray diffraction is one of the most important tools for crystallography. Any crystalline material gives a spectrum of peaks corresponding to angle 2Θ (where Θ is the angle the incident x-ray beam makes with the lattice planes) depending upon the wavelength (λ) of x-ray used and d-spacing of the planes in the crystal structure given by Bragg's law:

$$n\lambda = 2d \ sin\Theta. \tag{2.1}$$

The x-rays from the source fall on crystal planes and the x-ray gets scattered and a maximum intensity is obtained at the detector due to constructive interference of scattered beam. Fig. 2.7(a) shows an x-ray source, x-ray detector, and a sample stage in Bragg-Brentano geometry. The x-ray source and detector can rotate around the sample position simultaneously to collect data over a wide range of 2Θ. Different

incidence angle Θ corresponds to a particular plane identified by a set of miller indices (hkl value). This has been depicted in Fig. 2.7(b).

We have used lab-based (IISER Pune) Bruker, D8 Advance diffractometer Fig. 2.6, equipped with Lynxeye detector in Bragg-Brentano geometry to obtain powder x-ray diffraction of our samples at various stages (Fig. 2.7(a)). The source of x-ray was a Cu target ($\lambda_1 = 1.54060\mathring{A}$ and $\lambda_2 = 1.54442\mathring{A}$). The x-ray diffraction experiments were done on finely ground powder to confirm phases in the samples and to obtain lattice constants. The measured x-ray data is compared with standard data available in the ICDD PDF-2 diffraction database.

The peak position gives the idea about phases in the sample whereas the shape of the peak and their intensities gives other important information such as atoms present, atomic occupancies, grain size, strain in the structure, etc. Refining high-quality data obtained from x-ray experiments can give an understanding of these important parameters. The form factor is the measure of the scattering amplitude of a wave by an atom, which is also dependent on the nature of incident radiation. In general terms, the form factor is Fourier transform of the spatial distribution of the scattering compounds from real to reciprocal space, is given by: $f(Q) = \int \rho(r)e^{iQ.r}d^3r$, where Q is the momentum transfer and $\rho(r)$ is electron charge density about the nucleus, and the form factor is obtained by taking Fourier transform of this quantity. The intensity of the diffraction peaks is related to a quantity called structure factor, F_{hkl} which is given by the following relation

$$F_{hkl} = \sum_{j=1}^{m} N_j f_j exp[2\pi i(hx_j + ky_j + lz_j)] \tag{2.2}$$

F_{hkl} is the summation of the scattering from all of the atoms in the unit cell corresponding to peaks for hkl planes. The location of an atom on a given lattice plane defines the amplitude of scattered radiation corresponding to its peak. The scattering factor f_j estimate the efficiency of x-ray scattering at any angle by the electronic cloud of the atom.

Rietveld refinement

FullProf refinement Suit is used to refine the data. Rietveld refinement was done to get the lattice constants and occupancies. The peak profile and peak shape give information about particle size and the presence of stress/strain in the crystal structure. Therefore, identifying the right peak profile and shape to determine the FWHM of the peak is important. Peak Intensity mostly depends on the composition and atomic position of various elements in the structure. With each step of refinement, the fitting or calculated profile approach to experimental data.

The goodness of fit is determined by some parameters of the model used in the

Figure 2.6: X-ray diffraction instrument Bruker, D8 Advance diffractometer at IISER Pune.

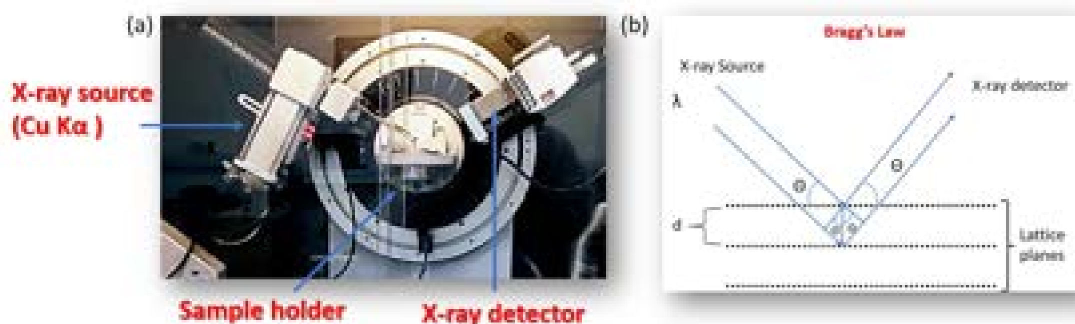

Figure 2.7: X-ray source, sample and detector in Bragg-Brentano geometry and schematic to show Bragg's law.

refinement process. We will define some goodness of fit parameters in this paragraph. The observed intensity at an angle $2\Theta_i$ is defined as $y_{O,i}$ and uncertainty in the

quantity is defined as $\sigma[y_{O,i}]$. Hence defined as $\sigma^2[y_{O,i}] = \langle(y_{O,i} - \langle y_{O,i}\rangle)^2\rangle$. Here $\langle\rangle$ indicated taking expectation value. Similarly, we define $y_{C,i}$ for calculated intensity at $2\Theta_i$. As discussed in the previous paragraph that the Rietveld refinement works on modeling the experimental data to minimize the difference between calculated and experimental data, hence the weighted sum of squared difference is obtained and minimized. The weighted sum of squared difference given by $\Sigma_i w_i(y_{C,i} - y_{O,i})^2$ where w_i is given by $\frac{1}{\sigma^2[y_{O,i}]}$. The most commonly used parameter is χ^2, which is also called goodness of fit. χ^2 is generally very large and it decreases as the difference in calculated and experimental pattern reduces.

$$\chi^2 = \frac{1}{N}\frac{\Sigma_i w_i(y_{C,i} - y_{O,i})^2}{\sigma^2[y_{O,i}]} \tag{2.3}$$

χ^2 is also expressed as square of the ratio of R_{wp} and R_{exp}. R_{wp} is weighted profile R-factor and R_{exp} is best possible weighted R-factor. R_{wp} and R_{exp} are parameters obtained from weighted sum of squared difference between the experimental and calculated intensity.

$$R_{wp} = \frac{\Sigma_i w_i(y_{C,i} - y_{O,i})^2}{\Sigma_i w_i(y_{O,i})^2} \tag{2.4}$$

$$R_{exp} = \frac{N}{\Sigma_i w_i(y_{O,i})^2} \tag{2.5}$$

2.2.2 Scanning electron microscopy (SEM)

Sample surface microstructure and its homogeneity is further characterized using scanning electron microscopy. The field emission secondary electron microscopy (FESEM) at IISER Pune is equipped with an Energy Dispersive X-ray (EDX) analysis attachment with a 20 mm^2 Oxford Inca EDX detector with an energy resolution of 129 eV. The FESEM produces clearly, less electrostatically distorted images with spatial resolution down to nanometres. It also gives three to six times better resolution than normal SEM.

A schematic of SEM is shown in Fig. 2.9. A scanning electron microscope uses a high-energy electron beam (energy $\sim$ 0-25 keV), which is focused on a small area of the sample using magnetic lenses. Field emission guns are electron guns, the emitter is sharply pointed and kept at a high negative potential (kiloVolts) with respect to a nearby electrode. A Schottky type or single-crystal tungsten tip of a radius of about 100 nm is used as an emitter. A FEG gives a more coherent electron beam, the beam diameter is smaller, with three order high current density than a regular thermionic emission-based electron gun. In FESEM, a FEG is used to generate electrons and these electrons are accelerated using an anode, accelerated beam goes

Figure 2.8: FESEM Ultra Zeiss plus at IISER Pune. The instrument was used for observing microstructure, chemical composition and EDX analysis.

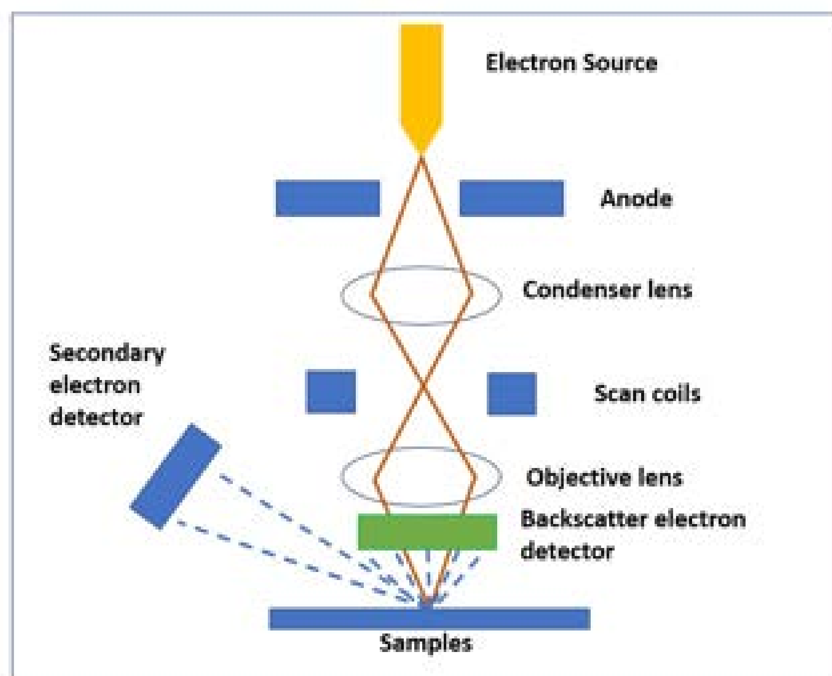

Figure 2.9: Schematic diagram showing important omponents and working of scanning electron microscope.

through a condenser lens which further defines the beam size. Scanning coils are used to raster the beam over the sample.

Incident electron beam interacts with the sample resulting in different types of emission of electrons and photons. The high-energy electron beam knocks off electrons from the samples called secondary electrons. These secondary electrons from the surface when detected by the detector give information about the surface. High energy electrons also interact with the electron cloud of individual atoms resulting in the backscattering of electrons which contain the information about the atom. Thus, images taken in backscattering mode (BSE mode) helps to identify different composition in samples. We can also obtain the distribution of different elements in a selected area. This is known as chemical mapping which shows the compositional homogeneity of the sample. In our work, 20 - 25 KeV energy beams were mostly used to obtain a BSE micrograph, chemical mapping, and EDX analysis of the samples. The average EDX composition is obtained by averaging more than 15 points.

2.2.3 Transmission electron microscopy

A high-resolution transmission electron microscope (HRTEM) has become an important tool in materials science as it gives a detailed understanding of microstructure at nm scale and provides electron diffraction pattern (DP) to visualize reciprocal

Figure 2.10: HRTEM JEOL JEM 2200FS at IISER Pune. The instrument was used for observing microstructure, selected area diffraction patter (SAED), EDX analysis and chemical mapping.

space. Transmission electron microscopes can also be used for chemical composition analysis using EDX analysis and chemical mapping. In this thesis, high-resolution transmission electron microscope JEOL JEM 2200FS, Japan (Fig. 2.10) with a 200 KeV field emission gun (FEG) and the in-column energy filter (Omega filter) that allows a zero-loss image, has been used. HRTEM was used to collect high-resolution images and for obtaining selected area electron diffraction (SAED) patterns with the GMS-3 software package to assess the crystallinity of our samples. Finely ground sample powder was dispersed in alcohol and sonicated. The solution was drop cast on an HRTEM copper grid with a layer of amorphous carbon. To remove the organic impurities, the grid was cleaned using a plasma cleaner. A magnification from

2000 to 1,200,000 times can be obtained. The system also has an attachment for EDX analysis and chemical mapping. Energy-filtered images forming with electrons at low loss or core loss energy provide chemical state or elemental information of a sample. The image processing can be done in the software where one can obtain the d-spacing of the lattice planes, the reciprocal image of a local area using fast Fourier transformation (FFT) and inverse Fourier transformed (IFFT) image to visualize the effect of one particular set of planes by masking the others.

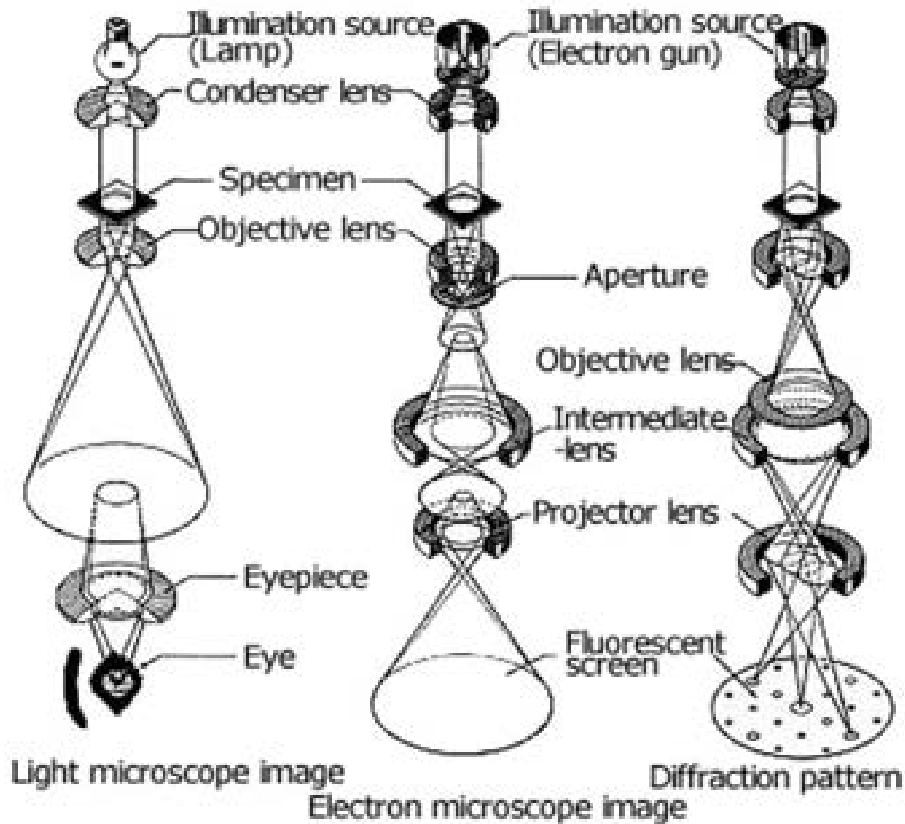

Figure 2.11: Comparision of working of light microscope and transmission electron microscope. The image is adapted from JEOL TEM manuals ([75]).

Working and construction of transmission electron microscope in comparison to the normal light microscope is shown in Fig. 2.11. In comparison to a light microscope where visible light wavelengths are used in TEM highly focused high energy electron beam is used. This beam is focused using a condenser lens to define the beam size. The beam falls on the sample specimen and transmitted beams are collected, as compared to scattered beams in SEM. The sample grain thickness of less than 100 nm is used in TEM and electron beam energy is nearly 10 times more than that of what is used in SEM. With little change in the projection, a reciprocal image is obtained in the form of a diffraction pattern.

2.2.4 Thermal Gravimetric Analysis /Differential Scanning Calorimetry

Figure 2.12: TGA/DSC From Netzsch, Germany for thermal analysis of sample.

Thermal gravimetric analysis (TGA) is thermal analysis in which change in mass of sample with change in time is studied as the temperature is also changed. Differential scanning calorimetry (DSC) measures the change in heat absorbed/released as compared to the reference with time as temperature changes. TGA/DSC is a simultaneous measurement system in which both TGA and DSC can be measured. We used TGA/DSC STA 449 F1 Jupiter Netzsch, Germany (Fig. 2.12) for finding phase stability of sample till high temperatures. This set-up can be used to a maximum temperature of 1600 ^{o}C. The weight resolution of air TGA balance is 0.025 µg and for DSC $\leq$ 1 µW. The construction and working of the device have been shown in Fig.2.13. The balance system is enclosed in a balance chamber where protective gas flow. The sample chamber is evacuated using a vacuum pump connected to the sample chamber and purged using Purge 1 and purge 2 lines. The sample is loaded on a sample carrier that has temperature sensors. In TGA/DSC mode we use TGA/DSC carrier, TGA/DSC carrier has a platinum tray. The platinum tray has slots for sample crucible and reference crucibles. The platinum tray has sensors to measure the differential heat flow to the sample crucible as compared to

the reference crucible, which gives DSC measurements. The sample carrier is fitted over balance using a radiation shield. The sample chamber is heated using a furnace (SiC/Platinum) while protective gas and purge gas flows into the chamber from the bottom and comes out from the top gas outlet.

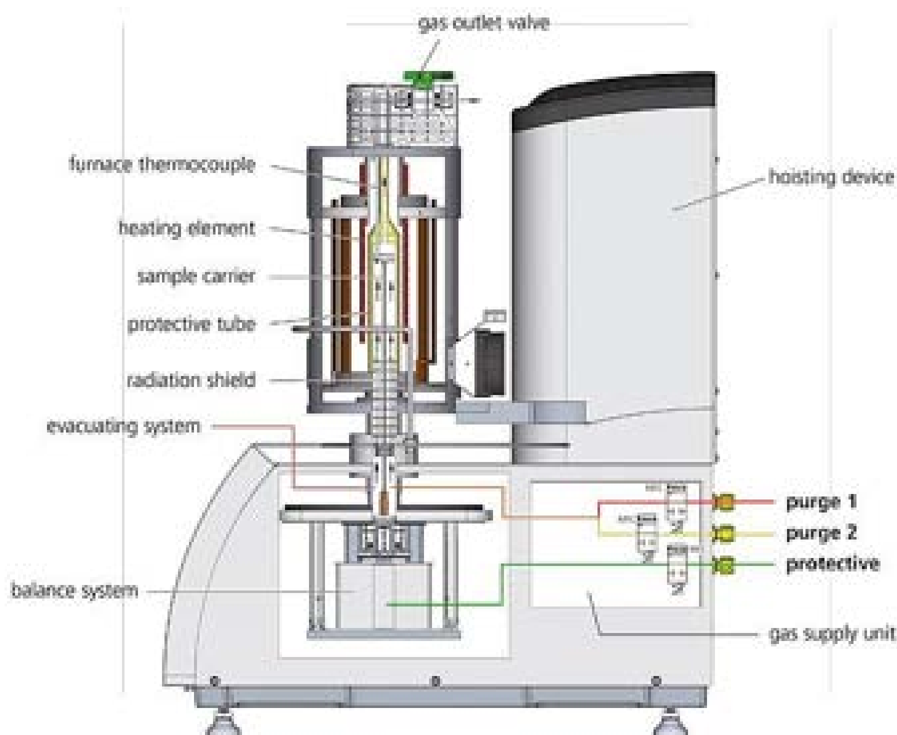

Figure 2.13: TGA/DSC From Netzsch,simultaneous TGA/DSC schematic diagram. Image is adapted from TGA/DSC manual from Netzsch website ([78]).

A small amount of sample typically 10 mg is used to study the thermal stability in the argon atmosphere. The sample chamber was evacuated and purged three to five times to remove all traces of oxygen. Temperature sensors or sample carriers should be used according to the atmosphere in the sample chamber. Regular calibration of the instrument is done at intervals of three months and standard samples are run to check the calibration. Temperature calibration and mass calibration can be done using standard materials with different melting temperatures. Temperature calibration is done using a DSC curve of three and more metals like zinc, tin, gold, etc. TGA/DSC measurements blank runs without samples are taken and used for obtaining corrected data for samples. In this thesis, all measurements were done in alumina crucibles, these crucibles are cleaned using aqua regia and water, and glowed at 1100 ^oC to remove all possible impurities before they are used in the experiment.

2.3 Charge transport and thermal transport

The final important aspect of the measurement is the charge transport and thermal transport of materials, which gives the idea of whether a material is good for application as thermoelectrics. We have measured carrier concentration, specific heat, resistivity, thermopower, and thermal conductivity of samples.

2.3.1 Hall measurements and Specific heat using PPMS

Carrier concentrations were measured using the Physical Property Measurement System (PPMS) from Quantum Design (USA). In Fig. 2.14, an image of the PPMS in our lab is shown. Samples were cut in a rectangular bar shape with minimum thickness for the Hall measurements. The Hall measurements were done using the Hall puck and the ACT measurement option of the PPMS. Samples were electrically connected in five probe or four probe geometry using gold wire. The contacts were made on the sample using silver paint as shown in Fig. 2.15. Hall voltage is measured by passing current and measuring the voltage drop in the transverse direction in the presence of a magnetic field perpendicular to the sample plane. The magnetic field was varied from -5 T to 5 T (superconducting loop). Measurements were done at T= 75 K. V_{xy} was obtained by using the formula

$$V_{xy} = V_H - V_{-H}/2, \tag{2.6}$$

where V_H and V_{-H} are the transverse voltages measured by applying positive and negative field H. V_{xy} is obtained by using the correct transverse voltage as there can be a potential difference in the direction of current due to resistance of the sample if voltage contacts are not exactly opposite to each other and perpendicular to the current. Carrier concentration is obtained using the formula

$$1/ne = V_{xy} * H/I * t, \tag{2.7}$$

where n is the carrier concentration, e is the elementary electronic charge, H is the magnetic field, and t is the sample thickness. Typically, currents of 30 mA to 100 mA were used for the Hall measurements.

A typical Hall measurement schematic is shown in Fig. 2.16. In presence of a perpendicular magnetic field Lorentz's force acts on charges (electron and holes) accumulates on the opposite side of the Hall bar in the transverse direction of the flowing current. Thus, generating a transverse voltage, V_H. Measuring this voltage V_H gives the carrier concentration by using the above-mentioned formula.

Specific heat is obtained using the Dulong-Petit law $Cp = 3nR/M$, n is the number of atoms in the formula unit and M is molar mass. For some samples, we

Figure 2.14: PPMS from Quantum Design in Lab 210 at IISER Pune.

have also measured specific heat around room temperature by using the calorimeter probe attachment of the PPMS. A schematic diagram of the calorimeter is shown in Fig. 2.17. The sample stage has an inbuilt heater and a sensor. As shown in the schematic the sample stage is suspended by 8 connecting wires (Au-Pd alloy) to provide the electrical connection to the heater and sensor and also, they serve the purpose of providing a controlled thermal coupling between the sample stage and the puck. The puck remains in thermal equilibrium with the sample chamber and any radiation losses are avoided by the vacuum in the chamber ($10^{-5} mbar$). The

Figure 2.15: Hall puck for Hall measurement with two samples loaded for measurement in four probe geometry.

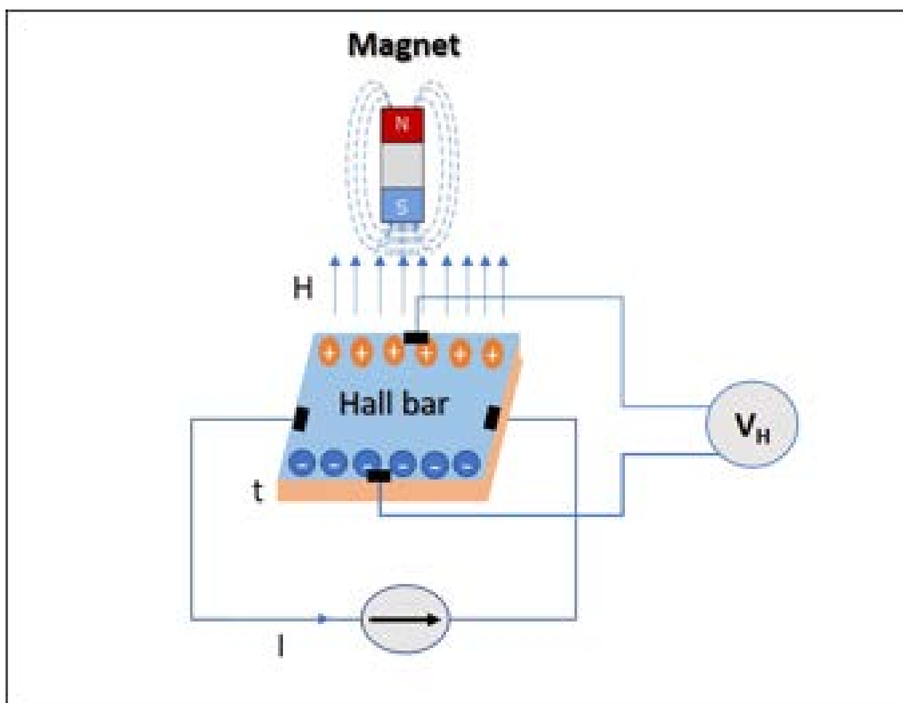

Figure 2.16: Schematic diagram of Hall measurements on a Hall bar.

thermal coupling of the sample with stage is obtained by using Apiezon-H grease for high-temperature measurements. A sample size of $3 \times 3\ mm^2$ or less can be used and the mass of the sample can vary in the range of 2 mg to 200 mg.

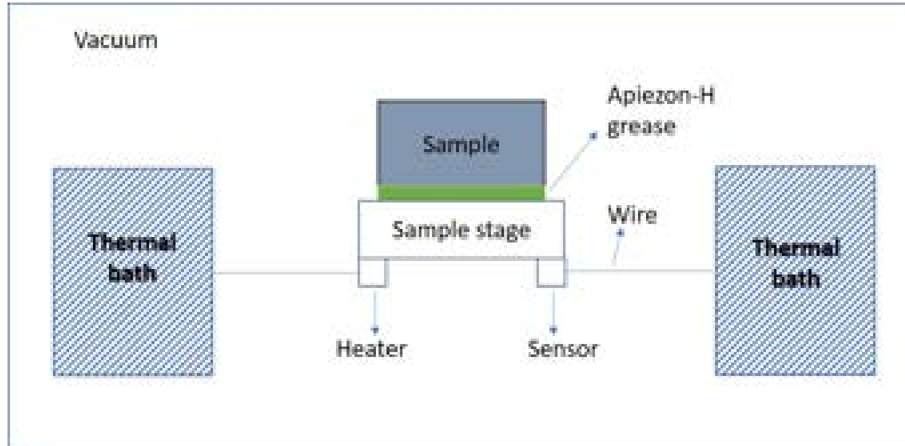

Figure 2.17: Schematic diagram of specific heat measurement in PPMS.

Measurements are done in two steps (a) sample stage with the grease only is measured (Addenda), and then (b) with sample on the stage held with grease is measured. This ensures that the contribution of grease is subtracted while measuring the sample. Typically, a sample is subjected to a thermal pulse and its temperature response is recorded. Fitting algorithms based on a model of the thermal circuit extract sample heat capacity from this curve. The Temperature response of sample stage is recorded as a function of temperature, fitting this data with a simple model considering good thermal contact between the sample and the sample stage. In a simple model, the temperature T of the sample stage as a function of time t is given by

$$C_{total}\frac{dT}{dt} = -K_w(T - T_b) + P(t), \tag{2.8}$$

where C_{total} is the total heat capacity of the sample with the sample stage, K_w is the thermal conductance of the connecting wires, T_b is the temperature of the thermal bath, and $P(t)$ is the power applied by the heater. The solution to this equation is given by exponential functions with a characteristic time constant τ. The time constant τ is expressed as C_{total}/K_w. A little complex model is used when the thermal coupling between the sample and sample stage is not good to determine the heat capacity of the sample.

2.3.2 Linseis LSR-3

Charge transport measurements such as electrical resistivity and Seebeck coefficient were done using Linseis LSR-3, Germany (Fig. 2.18). Linseis LSR-3 can do the simultaneous measurement of Seebeck coefficient and resistivity at high temperature

from room temperature to 1000 ^oC for solid-state samples. Measurements are done in an inert atmosphere (Helium) and the sample chamber is evacuated and purged several times before starting the measurement. Samples in bar-shaped geometry were used for the measurement. These bars were of height 6 mm to 15 mm and cross-section of 4 mm $\times$4 mm or less. Current in range 10 mA to 100 mA can be used and a gradient of 50 K or less can be developed between the upper and lower electrodes. Measurement can be done in two probe and four probe geometry with contacts being pressure contacts. The current electrodes, sample, and voltage probes in an LSR set-up are shown in Fig. 2.19. The measurement gives a relative Seebeck coefficient, but the absolute Seebeck coefficient can be obtained by using standard data available in the system for taking care of the contribution of the platinum wires and the platinum electrodes. Heating is done by a set of halogen lamps. The outer jacket of the furnace is water-cooled. The current in the halogen lamps is controlled with a set of PID controllers which reads the temperature in the chamber and a feedback circuit helps in stabilizing the temperature.

Figure 2.18: Linseis LSR-3, Germany for resistivity and Seebeck coefficient simultaneous measurements.

Two measurements Seebeck coefficient and resistivity are done simultaneously and the working principle of measurements is shown in Fig. 2.20. In Fig 2.20(a), we show Seebeck coefficients measurement where the thermal gradient is generated across the two electrodes and voltage and temperature difference both are measured by the central probe. The potential difference created and temperature difference between two central probes is used to calculate the Seebeck coefficient. In Fig. 2.20(b), we show the schematic of resistivity measurement where the electrodes are used to supply current from a current source and voltage is measured at the central

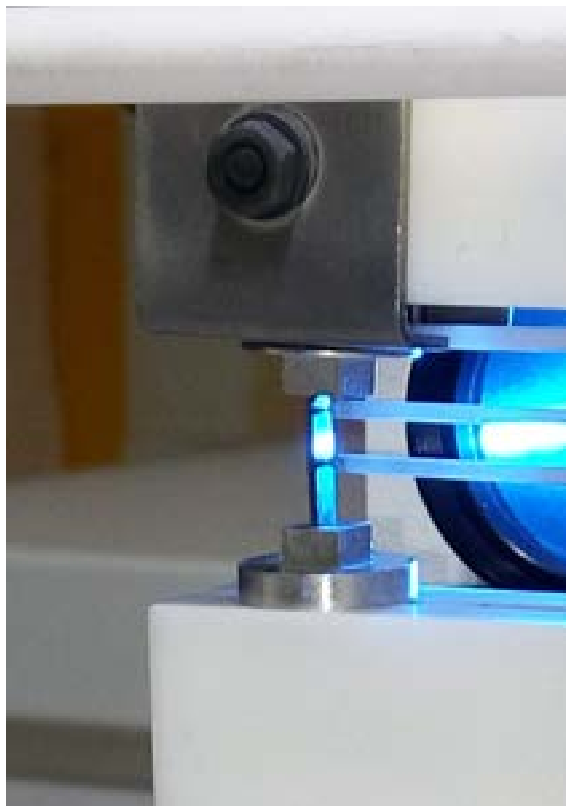

Figure 2.19: LSR sample loaded between platinum electrodes and voltage probe for simultaneous measurement of resistivity and Seebeck coefficient.

probe, this gives the resistance. Knowledge of sample cross-sectional area, and distance between the central voltage probe is used to obtain the resistivity. LSR-3 can measure thermopower in range 1 up to 2500 $\mu V/K$ and electrical conductivity in range 0.01 is $2 * 10^5$ S/cm.

Errors in electrical conductivity and thermopower measurements can occur due to errors in current, voltage, temperature gradients, and furnace temperatures. Electrical conductivity can have an extra source of error due to sample dimensions. Estimated accuracy in electrical conductivity is ± 5-8 % and thermopower is ± 5-7 %.

2.3.3 Laser Flash Analyzer

Laser Flash Analyzer (LFA-1000 Linseis, Germany) is a thermal analysis tool that helps in the measurements of thermal diffusivity (D) [142, 17]. Thermal diffusivity is used to obtain the thermal conductivity (κ) using the formula

$$\kappa = DC_p\rho, \tag{2.9}$$

where ρ is sample density and C_p is the specific heat of the sample. The laser pulse falls on the bottom surface of the pellet of a thickness (L), the heat pulse

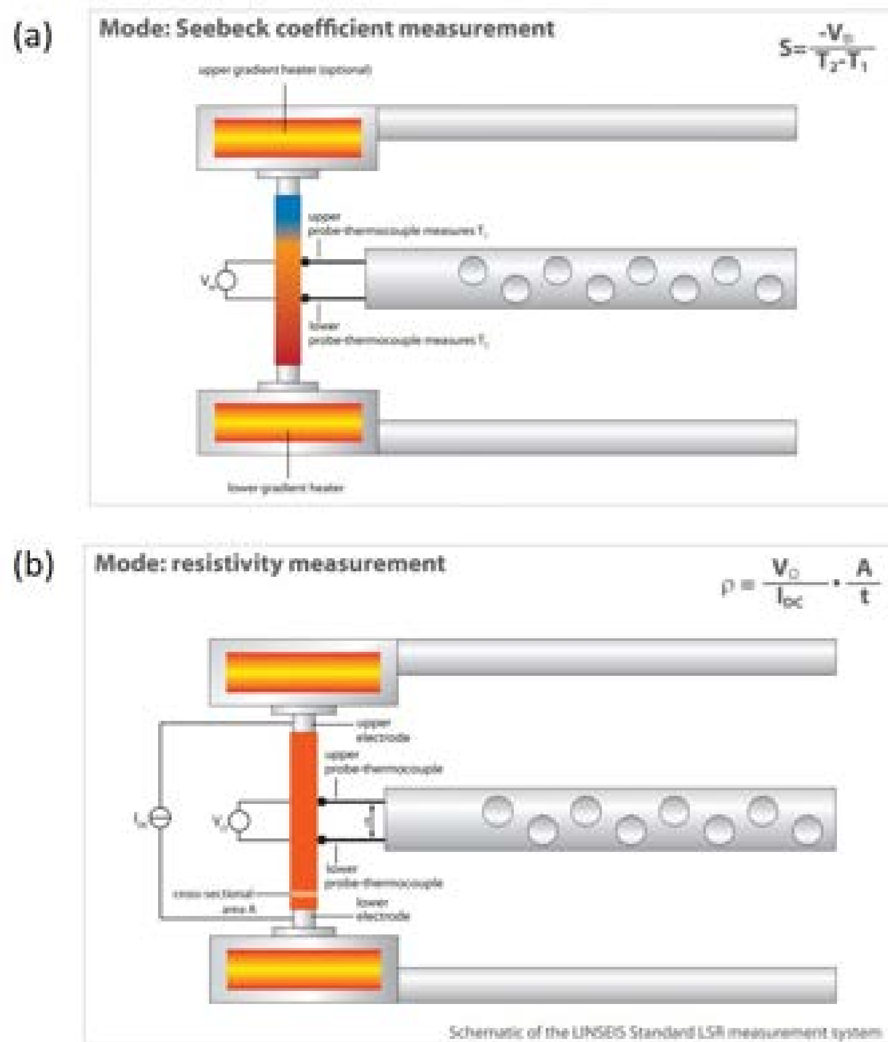

Figure 2.20: Schematic showing (a) Seebeck coefficient measurements under a temperature gradient and (b) resistivity measurements. Image adapted from LSR manual from Linseis website ([76]).

Figure 2.21: Laser Flash Analyzer (LFA) Linseis, Germany for thermal diffusivity measurements on disc shaped samples.

diffuses across the thickness, and the temperature of the top surface rises. Time taken in diffusion is used to find the thermal diffusivity as it depends on the half of time ($t_{1/2}$) to rise to obtain maximum temperature on the top surface. The schematic of measurement is shown in Fig. 2.22. The relation is given by

$$D = 0.13879(L^2/t_{1/2}), \tag{2.10}$$

Where L is the sample thickness. The sample in the form of a disc and $t_{1/2}$ is the half of the time form of a disc and $t_{1/2}$ is the half of the time required for the temperature to rise to its highest value before decreasing again This method assumes ideal conditions such as (a) instantaneous irradiation with infinite pulse width, (b) no heat loss from the sample, and (c) uniform energy density for the laser. However, for real measurements, corrections are needed to accommodate real conditions. Laser pulse duration can be varied from 0.05 to 25 Joules/pulse. Pulse duration and pulse shape can be also varied according to sample requirement. Three measurements were taken at each temperature and data point is only accepted if it has good fitting ($\geq$ 96%), different fitting models can be used some of these are dicussed in the later part of the section. The sample chamber is heated (resistance heating alloys- like Kanthal) and can go to high temperatures such as 1250 ^oC and measurements are done in a vacuum. The sample chamber is evacuated and purged with helium gas 3-4 times before starting measurement. The sample chamber is evacuated continuously during the measurement to avoid any possibilities of oxidation. LFA has different sample holders where different diameter samples can be measured, such as 15 mm, 13mm, 10 mm, 8mm, and 6 mm samples can be measured. Sample holders for 6 mm $\times$ 6 mm square pellets are also available for measurements. Sample holders can rotate and facilitate measuring multiple samples at once. Sample holders are made of graphite or silicon carbide. The sample is coated with a graphite layer using graphite spray to smoothen the surface to homogenize the diffusion of heat and also it helps in efficient absorption of heat as it behaves as a perfect black body. The heat at the top surface is measured using an IR detector (InSb). The IR detector needs to cool using Liq N_2, which was filled in the Dewar placed at the top of the device. The sample chamber and Laser unit are cooled using continuous water flow using a chiller. Fig. 2.21 show the LFA 1000 from Linseis. The system comes with software that obtains thermal diffusivity by fitting the data with available models in the software. Such a fitting is shown in the inset of image 2.22.

The analysis software has different options to find the best-fitted data. It gives you the option to compare the fitting with different models and to choose the correct model. Data modeling also requires choosing the way to identify the baseline, slope, or baseline + slope to fit the data. Some of the models used to fit the data are Cowan

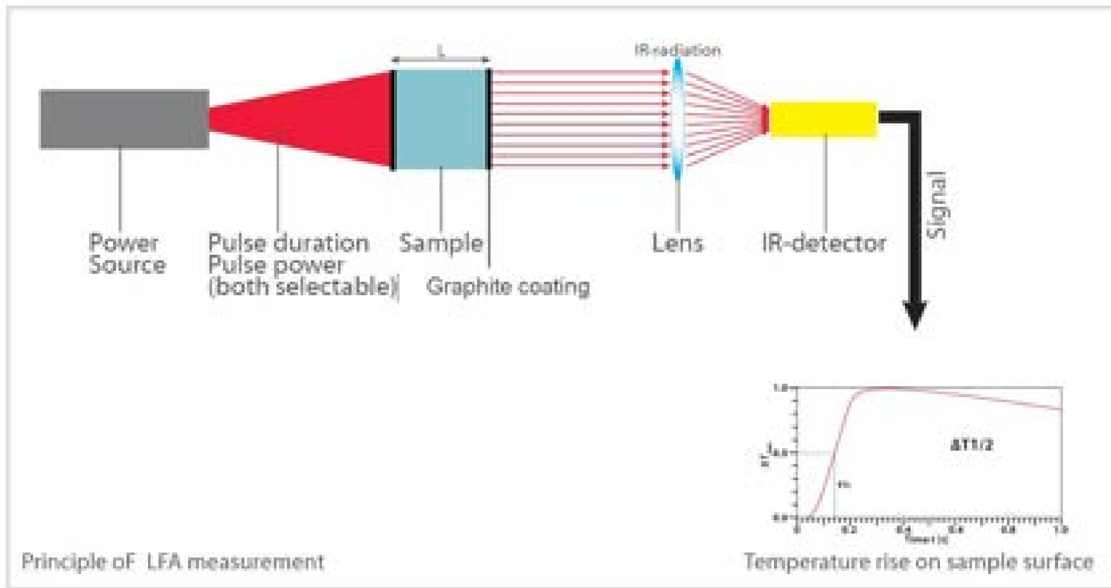

Figure 2.22: LFA schematic for thermal diffusivity measurements on disc shaped samples. Image is adapted from Linseis LFA manual ([77]).

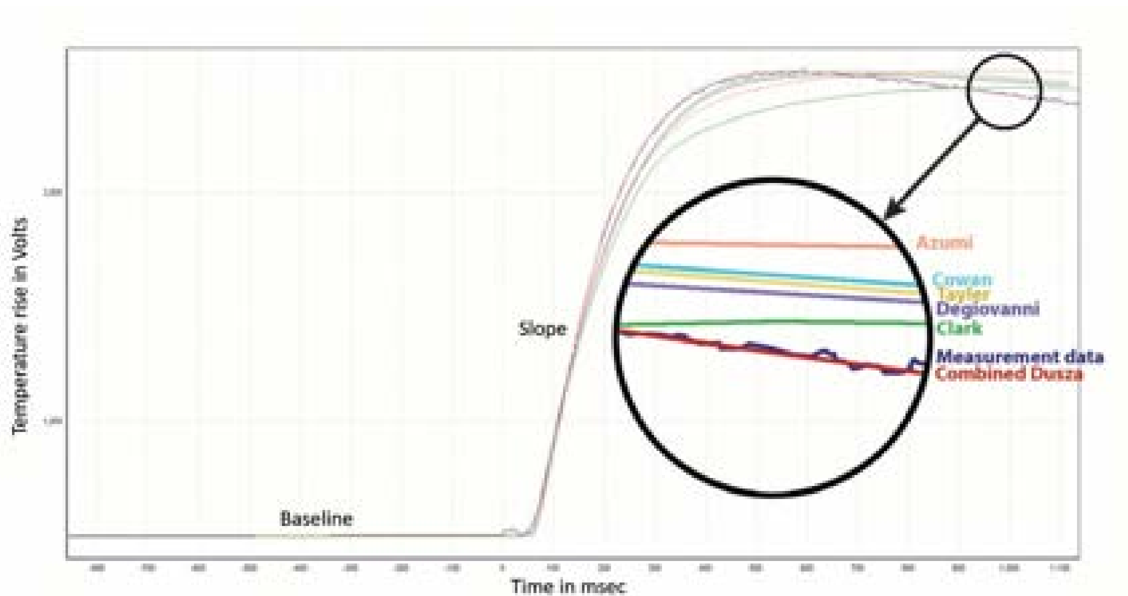

Figure 2.23: Fitting of measured thermal diffusivity data using different models. This image is adapted from LFA Manual available on Linseis website ([77]).

[29], Azumi [11], Clark [28], Degiovanni [32], heat loss, radiation, and combined [37]. Details of some of these models are given below:

- Cowan [29]: It considers only finite square wave energy pulse. No conduction loss is considered from the circumference of the sample holder is considered. Unidirectional conduction across the sample thickness is only considered. Radiation losses from the top and bottom surfaces are considered.

- Azumi [11]: This method uses Laplace transformation and term-by-term inversion, the temperature-response curve shows good convergence at the early stage of the temperature rise on the top surface. Being a logarithmic method, it is effective even in nonideal conditions and does not require correction procedures.

- Radiation loss [28]: In an ideal condition, no heat loss is considered during measurements but when radiation losses are unavoidable we need to use required corrections.

- Combined [37]: We used mostly combined model which takes care of finite pulse width, heat losses simultaneously during measurements by combining two-three models. Fitting for various models and combined models is shown in Fig. 2.23. The figure also shows the baseline and the slope of temperature rise on the top surface measured using an IR detector.

Many factors can affect the accuracy of measurements. As thermal conductivity is obtained from diffusivity, specific heat and density of the sample, each of these quantities has sources of errors. Density is estimated using sample mass and sample geometry, which can add errors. Specific heat is obtained using Dulong-Petit law ($C_p = 3nR$). Diffusivity is obtained using the LFA measurements which have an error of $\pm$ 2.2 %. In total thermal conductivity, in general, the maximum error considered here is up to $\pm$ 5 %. In the LFA measurements, there are various sources of errors related to sample thickness, sample surface, heat loss, and data fitting.

Chapter 3

Sn Doping in Defective Half Heusler: $Nb_{0.83}CoSb$

3.1 Introduction

Heusler alloys exhibit wide-ranging magnetic and thermoelectric properties [127, 128, 161, 25]. Recently, several members of the Heusler family have also come to be recognized as candidate materials for hosting non-trivial topological phases [114, 69, 127]. Generally, based on their chemical formula and structural details, one can classify Heusler alloys into four subgroups: full-Heusler (X_2YZ), half-Heusler (XYZ), inverse Heusler (XY_2Z), and quaternary Heusler ($XX'YZ$ or $XYY'Z$). While most Heusler alloys are metallic, the half-Heuslers (HHs) with a valence electron count (VEC) 18 or full-Heuslers (FHs) with VEC 24 often show semiconducting behavior with a bandgap which depends collectively on the strength of hybridization between the p-orbitals of elements X and Z, and the crystal field splitting of the element Y. In particular, the VEC 18 HHs (XYZ) with non-centrosymmetric space group *F-43m* exhibit a closed-shell electronic structure closely related to the well known semiconductors such as Si and GaAs.

Some of the conventional TEs based on elements such as Pb, Se, Te, and Bi, etc (e.g., PbTe or Bi_2Se_3), have a reasonably good zT and are used commercially in fabricating TE modules, their use however is not only deterrent to the environment, they are also not stable at high temperatures (i.e., T > 500 K to 600 K) that is typically encountered in the industrial plants and combustion engines [67, 234, 215]. The quest for good TE materials (i.e., with zT = 1 or above), with excellent thermal stability at high temperatures is therefore one of the important research areas where the role of HH alloys with VEC 18 comes into play. Due to their small bandgap, many of them exhibit a reasonably high thermoelectric power factor; however their relatively high thermal conductivity (on an average 10 $Wm^{-1}K^{-1}$ as opposed to 1

$Wm^{-1}K^{-1}$ for the mid-ranged TEs mentioned above), adversely affects their overall zT. To substantiate this point, in Table 3.1 we show the PF and κ at two different temperatures (300 K and 700 K) for some of the well-known VEC 18 HH alloys. For example, at 300 K (700 K), the PF of $Nb_{0.86}Hf_{0.14}FeSb$ is close to 46 (60) $\mu Wcm^{-1}K^{-2}$, which is a factor of 10 (8) higher than that of SnSe [232] (a TE with a record high zT of 2 around 900 K). On the other hand, the κ is around 7 (5) $Wm^{-1}K^{-1}$, which is almost 10 times that of SnSe. It is therefore quite evident that even with very high power factors HHs are limited due to their high thermal conductivity as compared to other classes of TEs where κ can easily be as low as $1Wm^{-1}K^{-1}$.

To mitigate this problem, recently, the focus has been shifted to a new class of so-called "defective" HHs. These are compounds that only stabilize in a pure HH (cubic *F-43m*) phase in the presence of a large concentration of cationic vacancies created to have a valence balanced condition leading to a valence electron count of 18. Thus, in a defective HH while on one hand the semiconducting behavior is expected due to a closed-shell electronic structure ensured by VEC 18; on the other hand, a much reduced thermal conductivity can be contemplated due to the presence of cationic vacancies. The vacancies act as a point defect resulting in pronounced phonon scattering, lowering the lattice thermal conductivity. Here, we consider NbCoSb which has a VEC of 19 in the 1: 1: 1 stoichiometry. However, attempts to synthesize this compound in a pure form proved unsuccessful until it was discovered that a pure HH phase can only be obtained for the stoichiometry Nb : Co : Sb $\equiv$ 0.8 : 1 : 1, which ensures valence balance condition (net valence $NV = +4(Nb_{0.8}^{+5}) - 1(Co^{-1}) - 3(Sb^{-3}) = 0$ along with a VEC of 18 ($VEC = 0.4 \times 5 + 1 \times 9 + 1 \times 5 = 18$) [222]. This provides the necessary thermodynamic stability for the formation of this alloy. The thermoelectric properties of $Nb_{0.8}CoSb$ are rather sensitive to exact chemical composition [205], [206]. Even a slight excess of highly electropositive Nb increases the electronic concentration leading to a degenerate n-type behavior. Recently, control of carrier concentration using Co-excess in $Nb_{0.8}Co_{1+z}Sb$ has also been reported where excess Co leads to a decrease in the carrier concentration following the Zintl-Klemm concept [83].

In recent studies, zT up to 0.9 and with κ as low as $\sim 3.5\ Wm^{-1}K^{-1}$ has been reported for the phase pure $Nb_{0.8+\delta}CoSb$ at 1123 K, without any extrinsic doping [205], and is comparable to (Zr, Hf, Ti)(Ni)(Sn, Sb) alloys where zT up to 1.5 has been reported [160]. Even though Ni-doping at the Co-site does seem to affect the transport properties considerably, zT could not be increased beyond 0.9 [206]. Interestingly,$Nb_{0.83}CoSb$ also exhibits the phenomenon of short-range vacancy ordering that manifests itself in the form of diffused bands across the reciprocal lattice points in HRTEM SAED images [206].

Table 3.1: Power factor and themal conductivity of various high zT half Heusler

Half Heusler	PF	κ	zT	PF	κ	zT	References
		300 K			700 K		
	$\mu W/cmK^2$	W/mK		$\mu W/cmK^2$	W/mK		
$NbCoSn_{0.9}Sb_{0.1}$	19.5	9.2	0.063	32.6	6.3	0.36	[66]
$ZrCo_{0.92}Ni_{0.08}Sb$	3.5	13.1	0.008	16.8	7.7	0.15	[230]
$ZrCo_{0.97}Pd_{0.03}Bi$	7.0	13.1	0.160	21.2	7.6	0.19	[231]
$Nb_{0.86}Hf_{0.14}FeSb$	46.6	7.3	0.19	59.5	5.0	0.8	[45]
$(Zr_{0.5}Hf_{0.5})_{0.5}Ti_{0.5}NiSn$	19.6	3.0	0.196	57.2	3.2	1.2	[160]
(ZrNiSn	4.4	11.3	0.037	13.8	6.7	0.18	[25]

Motivated by these results, in this chapter, we investigate the effect of Sn-doping at the Sb site on the thermoelectric properties and vacancy ordering in nominal "$Nb_{0.83}CoSb$". In Fig. 3.1, we have shown the structure of $Nb_{0.8}CoSb$, and also shown the coordination polyhedra for the three elements. The homogeneity range δ in $Nb_{0.8+\delta}CoSb$ was established as $0 \geq \delta < 0.03$ [205]; therefore, we selected the composition$Nb_{0.83}CoSb$ for our study. Since NbCoSn is a thermodynamically stable HH compound with VEC 18, with Sn doping for Sb in $Nb_{0.83}CoSb$, the Nb concentration of the HH phase should increase, and should eventually converge to 1 : 1: 1 for complete replacement of Sb by Sn. Therefore, in our $Nb_{0.83}CoSb_{1-z}Sn_z$, with a progressive increase in z, while on one hand, the carrier concentration will increase due to an increase in the electropositive Nb in the HH matrix, on the other, Sn-doping will allow for a finer control on the carrier concentration; Sn being more electronegative compared to Sb. Thus, a tradeoff can be reached for optimal Sn doping where zT attains its maximum value. We show that with a small amount of Sn-doping (ranging from 1 % to 5 %) while the electrical conductivity increases, the thermal conductivity decreases simultaneously leading to zT exceeding slightly over 1.0 at 1100 K. The experimental results are complemented by ab initio DFT calculations of the electronic structure and phonon spectrum.

3.2 Experimental methods

3.2.1 Experimental details

$Nb_{0.83}CoSb_{1-x}Sn_x$ (x = 0, 0.01, 0.05, 0.1, 0.15, 0.2, and 0.3) were prepared by arc-melting the constituents. High-purity Nb (Sigma Aldrich 99.9%), Co (Sigma Aldrich 99.5%), Sb (Alfa Aesar 99.999%), and Sn (Sigma Aldrich 99.8%) were taken in stoichiometric amounts. During melting about 10 % excess Sb was added to compensate for the weight loss during melting. The ingots obtained after first melting were flipped over and re-melted. This procedure was repeated 4-5 times to ensure homogeneity. The final product thus obtained was hand-grinded using agate mortar and pestle. The fine powder obtained is used to make pellets of 8 mm diameter by cold-pressing. These pellets were placed in a preheated quartz ampoules inside an Argon-filled glove-box where the O_2 and moisture levels were maintained at less than 1 ppm. The ampoules were sealed under a dynamic vacuum better than 10^{-4} mbar and placed in a muffle furnace for sintering at 1100^oC for 7 days. This resulted in very high-density pellets. The sample's mass density was estimated at room temperature using the expression: $\rho_m = M/\pi R^2 H$ where R, H and M are, respectively, the radius, height, and mass of the sintered pellet. The relative mass density (i.e., density with respect to the theoretical density) of all our samples are shown in Table

Table 3.2: Density of different samples obtained by measuring dimension and sample mass

Compound	density	density percentage
$Nb_{0.83}CoSb$	7.8	94%
$Nb_{0.83}CoSb_{0.99}Sn_{0.01}$	7.2	87%
$Nb_{0.83}CoSb_{0.95}Sn_{0.05}$	7.5	90%
$Nb_{0.83}CoSb_{0.9}Sn_{0.1}$	7.7	92%
$Nb_{0.83}CoSb_{0.8}Sn_{0.2}$	8.0	95%
$Nb_{0.83}CoSb_{0.7}Sn_{0.30}$	7.9	94%

3.2.

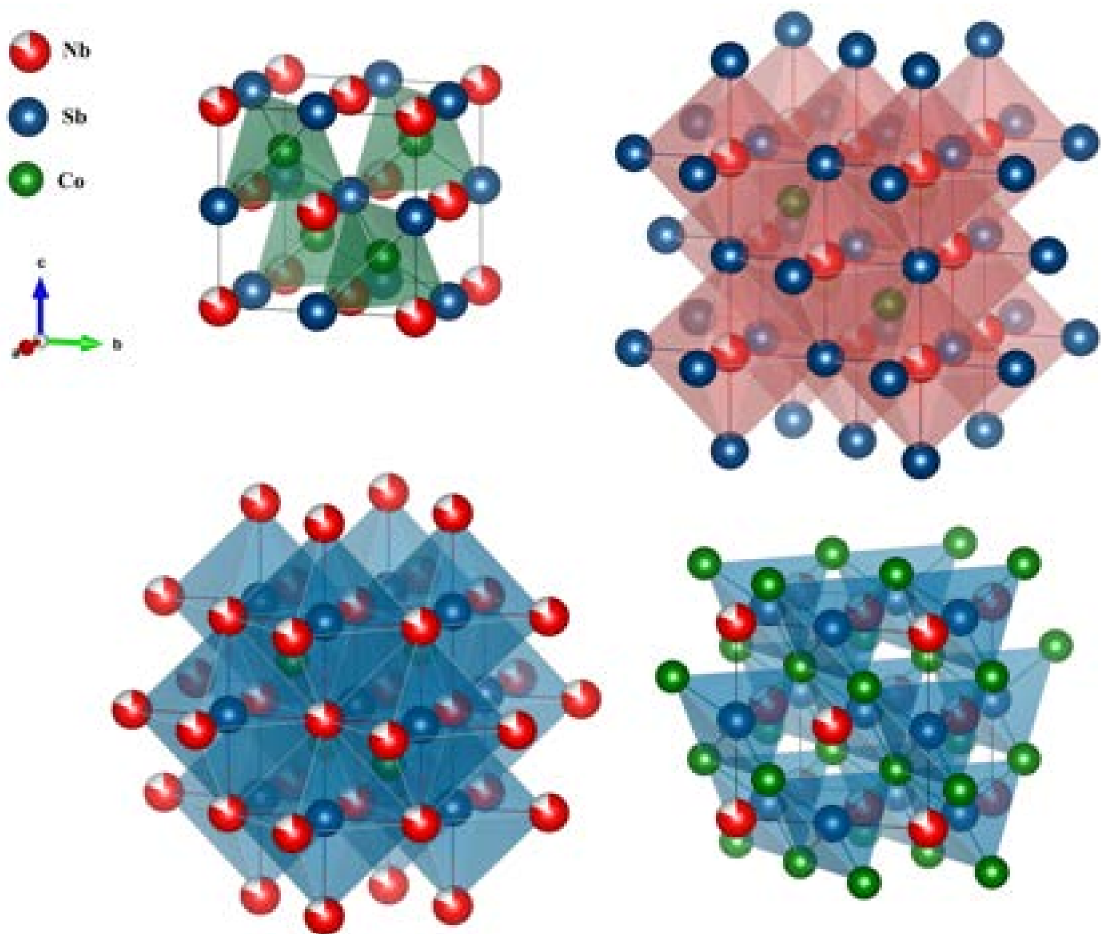

Figure 3.1: Structure of$Nb_{0.83}$CoSb a) tetrahedral coordination of Co with Sb, b) octahedral coordination of Nb with Sb, c)octahedral coordination of Sb with Nb, and (d) tetrahedral coordination of Sb with Co.

The phase purity of the samples was confirmed using the powder X-ray diffrac-

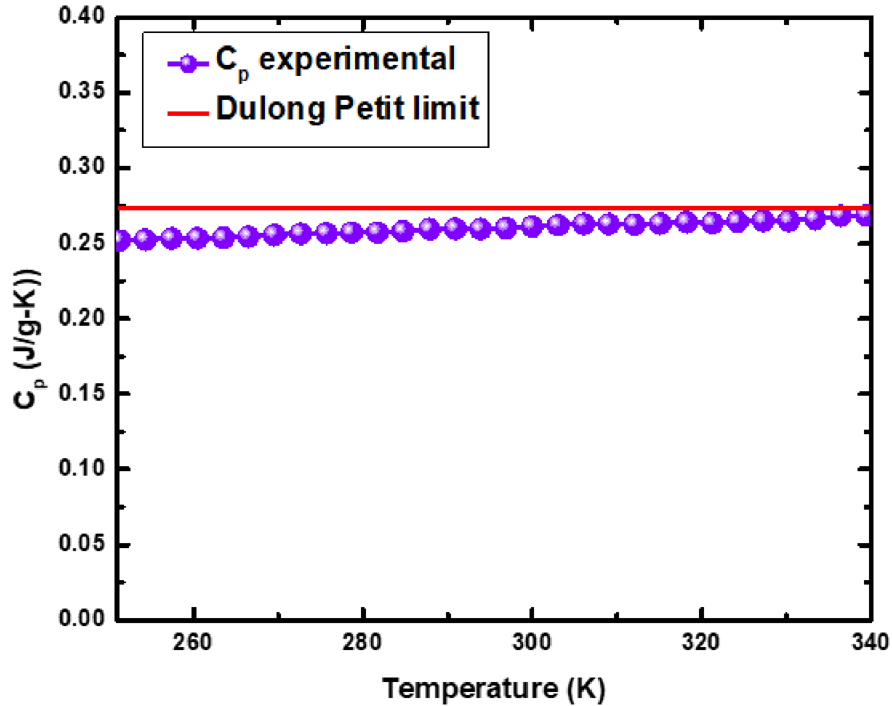

Figure 3.2: Temperature deviation of specific heat for temperature range 250 K to 340 K.

tion technique in a Bruker, D8 Advance diffractometer. Rietveld refinement was done to obtain the structural parameters. High-resolution transmission electron microscopy (HRTEM) was used for high-resolution imaging and for obtaining SAED patterns (JEOL JEM 2200FS 200 Kev). For HRTEM imaging, the samples were thoroughly ground in ethanol. A dilute suspension of the same was centrifuged, and the nanoparticles suspended solution was drop casted on a copper grid with amorphous carbon coating using a micropipette and oven-dried at 80 $°C$. Further, samples were plasma cleaned to remove all organic depositions and traces of solvent. Polished pellets were examined using a scanning electron microscope equipped with an energy dispersive absorption X-ray spectroscopy (EDAXS) attachment (Zeiss Ultra plus). Thermal diffusivity (D) was measured using the Linseis LFA-1000 set-up on 8 mm diameter polished pellets by applying a homogeneous graphite coating. Thermal conductivity was obtained from the thermal diffusivity using the formula $\kappa = DC_p\rho_m$, here ρ_m is the mass density, and c_p is the specific heat. The specific heat of a few representative samples was measured between 250 K and 325 K using the Physical Property Measurement System (PPMS) from Quantum Design, USA. For all samples, C_p near 300 K approached the classical Dulong-Petit limit of 3nR. We, therefore, used this value of C_p for obtaining the thermal conductivity.

The Seebeck coefficient and electrical conductivity were measured simultaneously on rectangular-shaped samples using the Linseis LSR-3 set-up. The charge carrier

Table 3.3: Occupancy of different elements from Fullprof refinement

Compound	Nb	Co	Sb	Sn
$Nb_{0.83}CoSb$	0.812	1	1.0	0.00
$Nb_{0.83}CoSb_{0.99}Sn_{0.01}$	0.82	1	0.99	0.01
$Nb_{0.83}CoSb_{0.95}Sn_{0.05}$	0.844	1	0.95	0.05
$Nb_{0.83}CoSb_{0.9}Sn_{0.1}$	0.847	1	0.9	0.1
$Nb_{0.83}CoSb_{0.8}Sn_{0.2}$	0.874	1	0.80	0.20
$Nb_{0.83}CoSb_{0.7}Sn_{0.30}$	0.9	1	0.7	0.3

concentration was estimated from the measurement of the Hall coefficient using the ac transport option in a PPMS. To improve the signal-to-noise ratio, the sample was cooled down to 70 K, and at each field value at least 10 data points were collected for averaging. The transverse voltage was collected in the field ranging from H = -3 T to + H = +3 T, and from there the Hall voltage is determined using the expression V_{Hall} = [V(+H) - V(-H)]/2, which eliminates any magnetoresistance contribution to the measured voltage. The melting behavior and temperature were determined using the Netzsch, Jupiter F1, STA 449 simultaneous TGA-DSC set-up.

3.3 Result and discussion

3.3.1 Stuctural characterization

The powder X-ray diffraction pattern of our samples is shown in Fig. 3.3. For all samples, the only diffraction peaks that appear in the diffractogram correspond to the desired HH phase with a cubic MgCuSb-type structure shown in Fig. 4.1. In some of the patterns, minor extra peaks indicating small quantities of unidentified parasitic phase(s) are also present. These are labeled separately. As shown in the adjacent panel where an expanded view of the region around 220 is shown, with increasing Sn doping there is a clear shift of the peak towards the lower 2-theta values indicating lattice expansion, which is expected as the atomic radius of Sn is slightly greater than that of Sb. The nearly linear variation of lattice constant (a) of the cubic unit cell with Sn doping is shown in Fig.3.11(a). The lattice constant for the undoped sample (5.900 Å) is in good agreement with the previous reports [205].

Refinement: FullProf Suite was used for refining powder X-ray diffraction data taken on all the samples. First, the peak profile parameters and lattice parameter

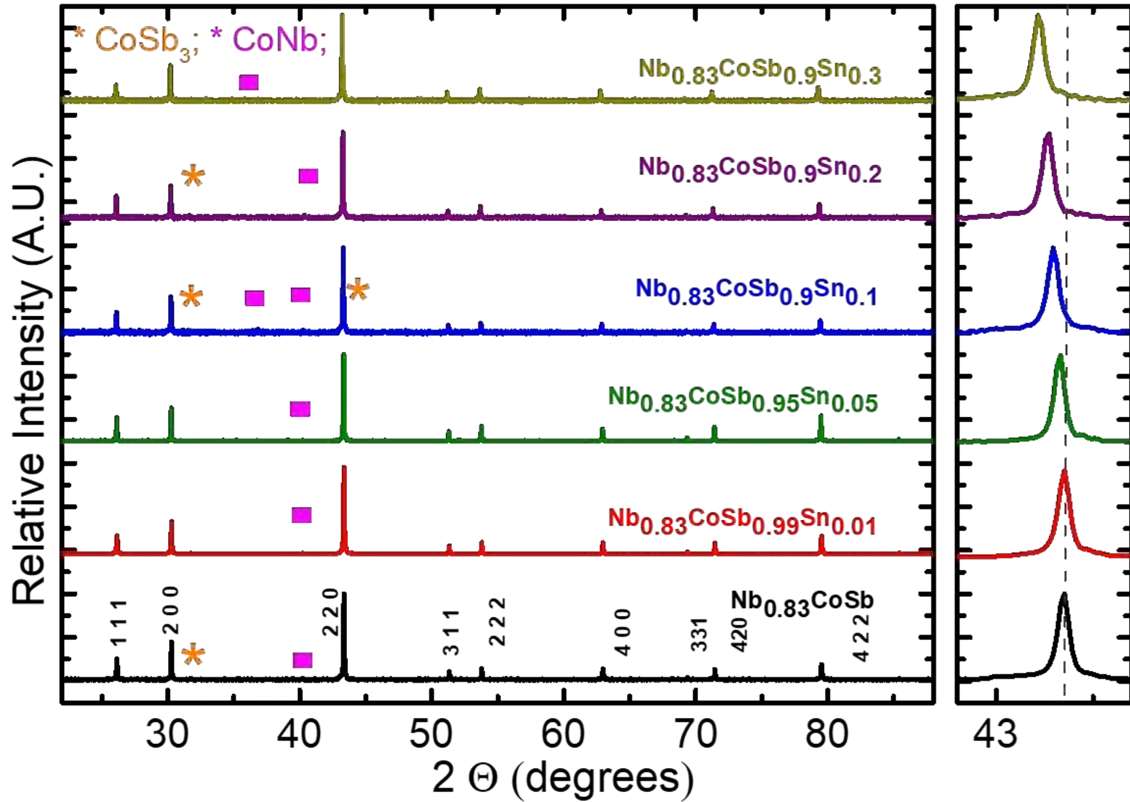

Figure 3.3: Powder X-ray diffraction pattern of $Nb_{0.83}CoSb_{1-x}Sn_x$ (x= 0, 0.01, 0.05 0.1, 0.2, 0.3)

were refined, then the occupancy of the elements at different Wyckoff positions was determined. We fixed Sn and Sb occupancy according to the doping percentage and refind the Nb occupancy. Thus, occupancies of Sb+Sn were fixed at 100 % at the 4 b site and that of Co as 100 % at the 4 c site. Whie nominal composition of all our samples is $Nb_{0.83}CoSb_{1-x}Sn_x$ with increasing x, Nb concentration is expected to increase in order to maintain the valanced balanced condution. Hence, we varied the Nb occupancies to get the best fits and hence the actual Nb concentration of our samples. We took care of the Sb losses while arc melting by taking an appropriate quantity of excess Sb. Some of Nb and Co loss can happen due to formation of minor secondary phases in very small quantities. The value of χ^2 of our refinement is on

Figure 3.4: Sintered Pellet after polishing and cutting

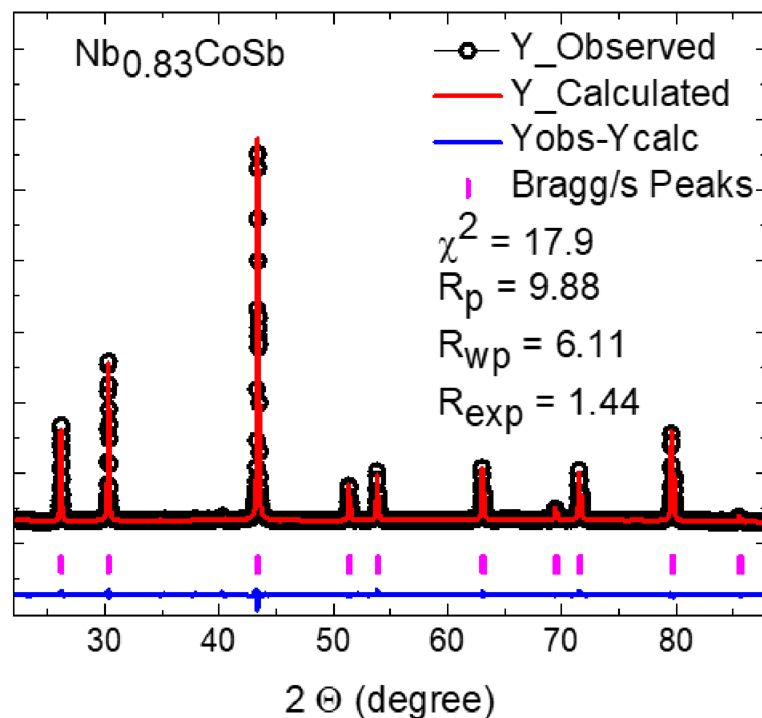

Figure 3.5: Reitveld refinement on x-ray data of $Nb_{0.83}CoSb$.

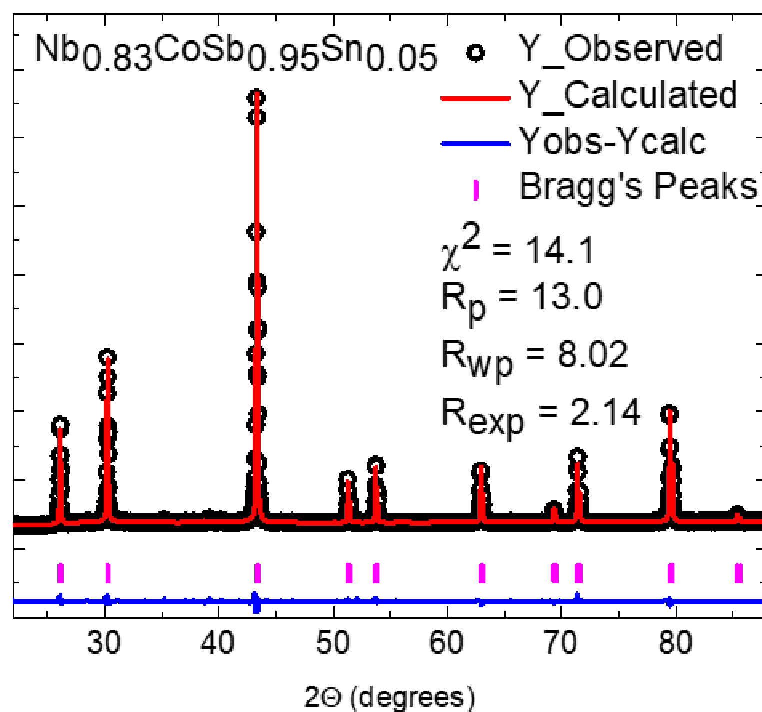

Figure 3.6: Reitveld refinement on x-ray data of $Nb_{0.83}CoSb_{0.95}Sn_{0.05}$.

the higher side since we did not consider the secondary phases and carried out the refinement for the HH phase only. The refinement results are shown in Figs. 3.5 to 3.10. The variation in occupancy of Nb atom at the 4a site in our samples is shown

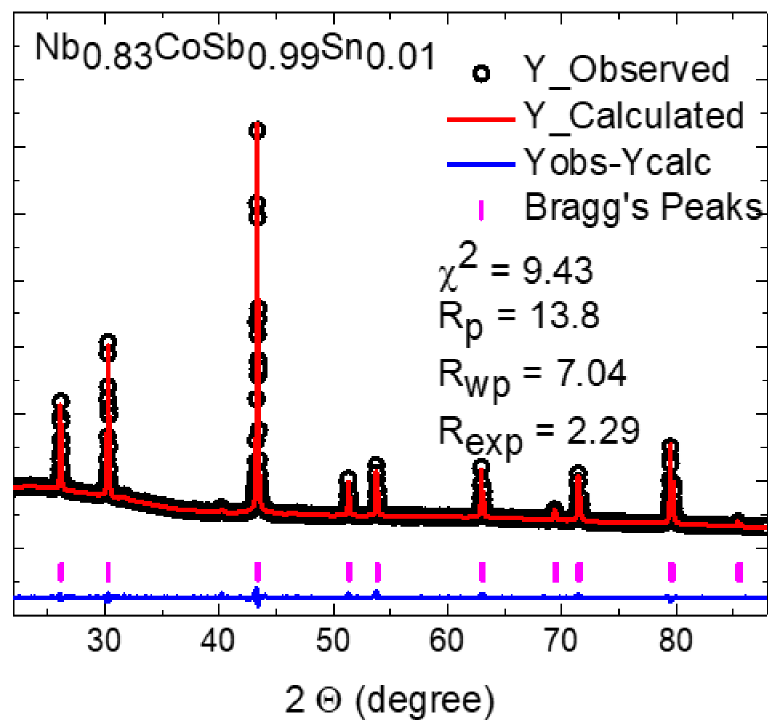

Figure 3.7: Reitveld refinement on x-ray data of $Nb_{0.83}CoSb_{0.99}Sn_{0.01}$.

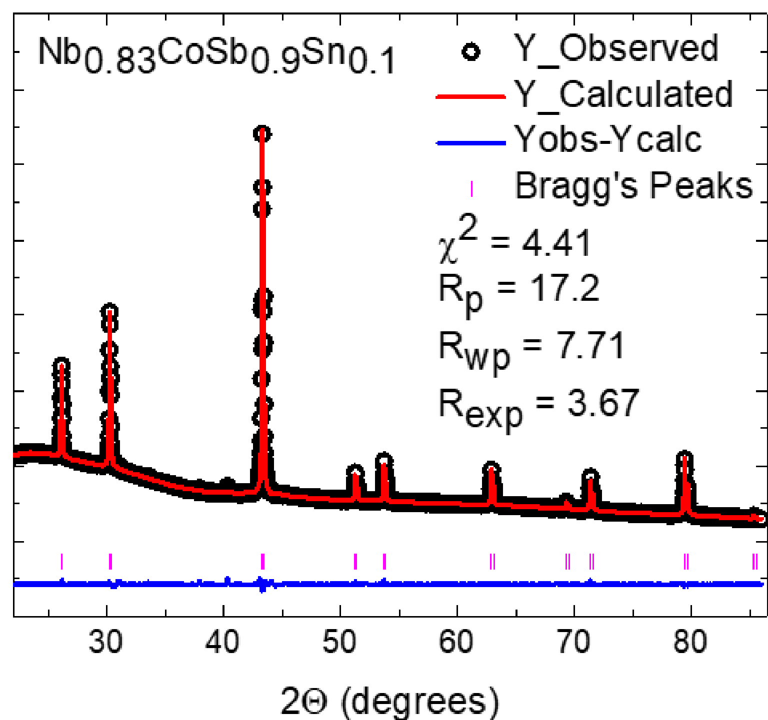

Figure 3.8: Reitveld refinement on x-ray data of $Nb_{0.83}CoSb_{0.9}Sn_{0.1}$.

in Fig. 3.11(b) along with the occupancies of other elements at their respective sites. We can see there is an increase in Nb occupancy as we go to higher Sn doped samples. The Nb concentartion has increased from $Nb_{0.81}$ for undoped to $Nb_{0.9}$ for

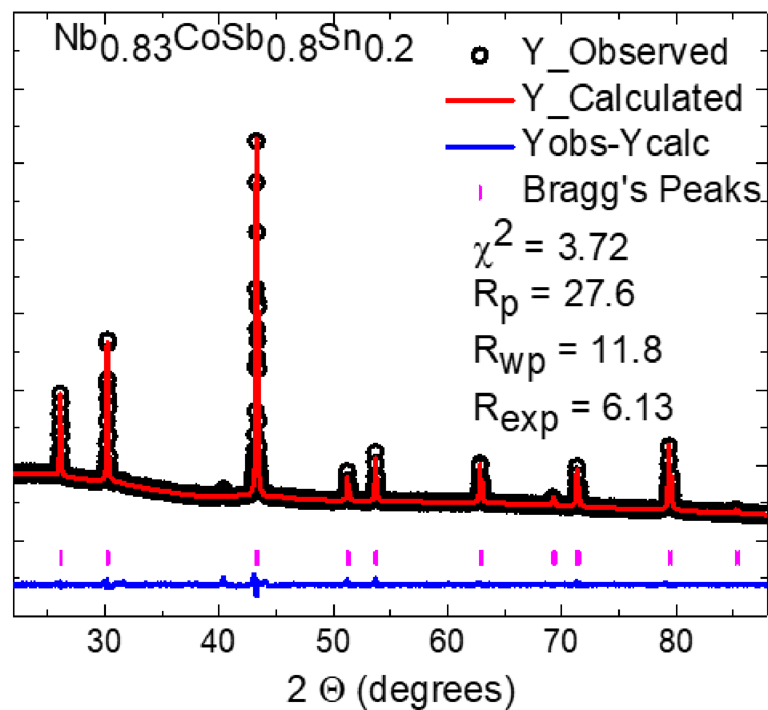

Figure 3.9: Reitveld refinement on x-ray data of $Nb_{0.83}CoSb_{0.8}Sn_{0.2}$.

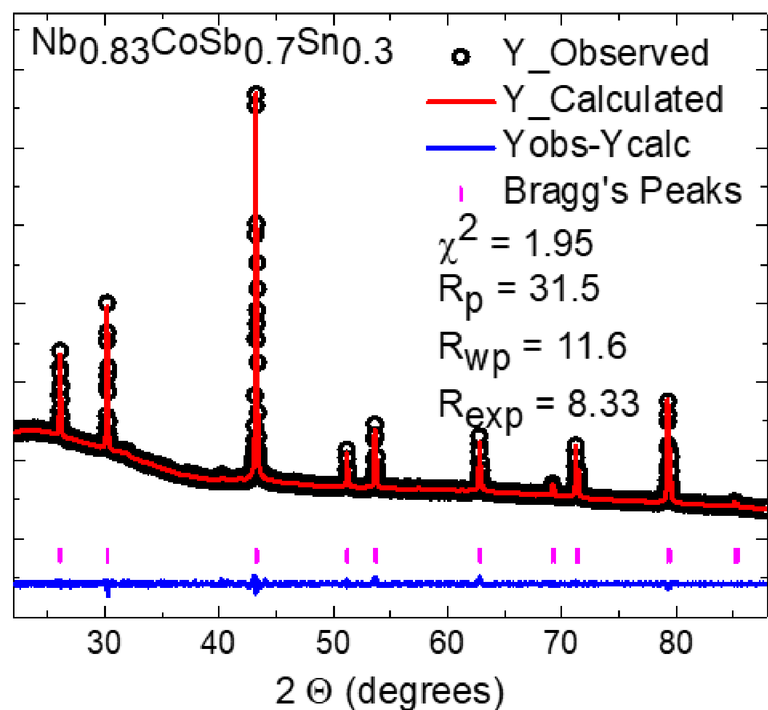

Figure 3.10: Reitveld refinement on x-ray data of $Nb_{0.83}CoSb_{0.7}Sn_{0.3}$.

30 % Sn doped sample. This data has been also depicted in Table. 3.3.

The scanning electron microscopy (SEM) was done on polished surfaces. Fig. 3.13 shows a representative SEM image for a $Nb_{0.83}CoSb$ sample in the backscat-

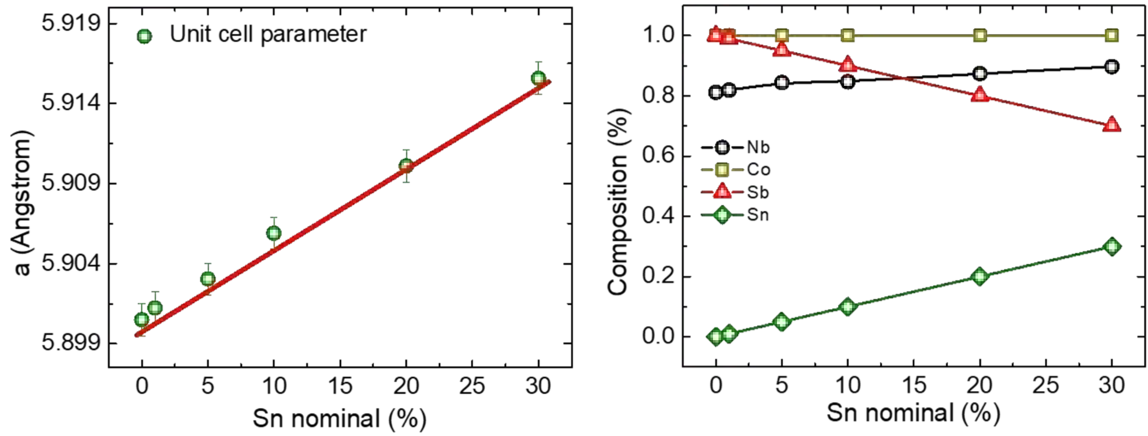

Figure 3.11: (a) Variation in lattice parameter with Sn doping percentage (b) elemental composition of samples with variation of nominal Sn doping percentage.

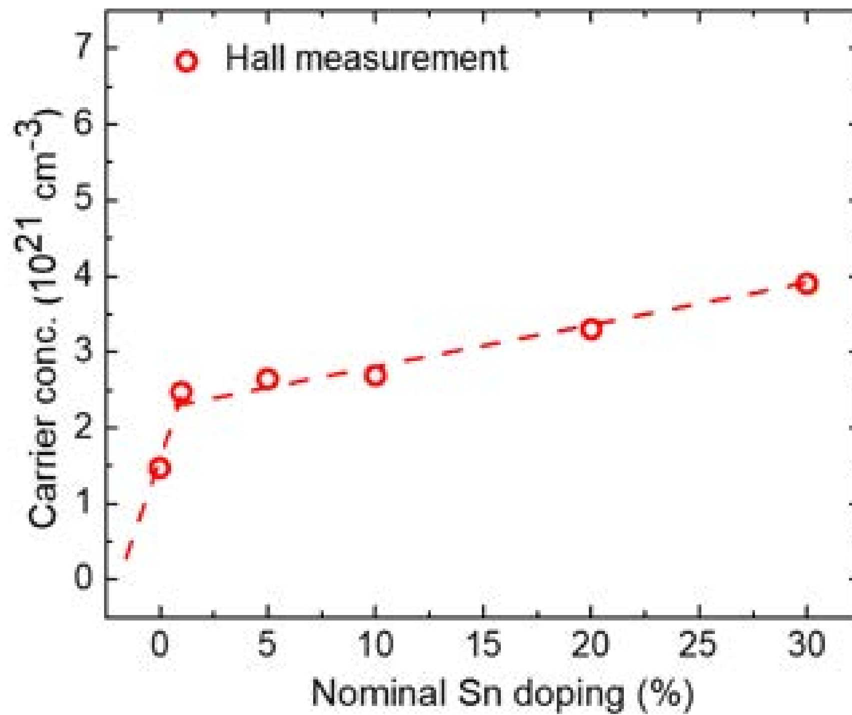

Figure 3.12: Carrier concentration variation with nominal Sn doping percentage. The dashed line through the data point is a guide to the eye.

tering mode. The chemical mapping for individual elements is also shown using the false-color representation. The chemical mapping indicates a homogeneous distribution of elements throughout the sample. Small precipitates of Nb-rich phases (likely CoNb) are also seen. Similar observations were made in the Sn-doped sample up to about 5 % of Sn doping as shown in Fig. 3.14. However, for higher doping of Sn $>$ 10%, small Sn precipitates ($\leq$ 1-2 %) were also found; this is shown in Fig. 3.15(b). The effect of Sn precipitation is also observed in transport properties shown in Appendix A . This precipitation-related effect was confirmed using DSC measurement

on 30 % Sn doped sample shown in Fig. 3.16. In the Fig. 3.16, we observe two endothermic peaks, one at $\sim 515\ K$ and other at $\sim 790\ K$. The endothermic peak at 515 K is due to melting of Sn precepitates in the 30 % Sn-doped sample. The reason for the peak at 790 K is unknown and needs more understanding.

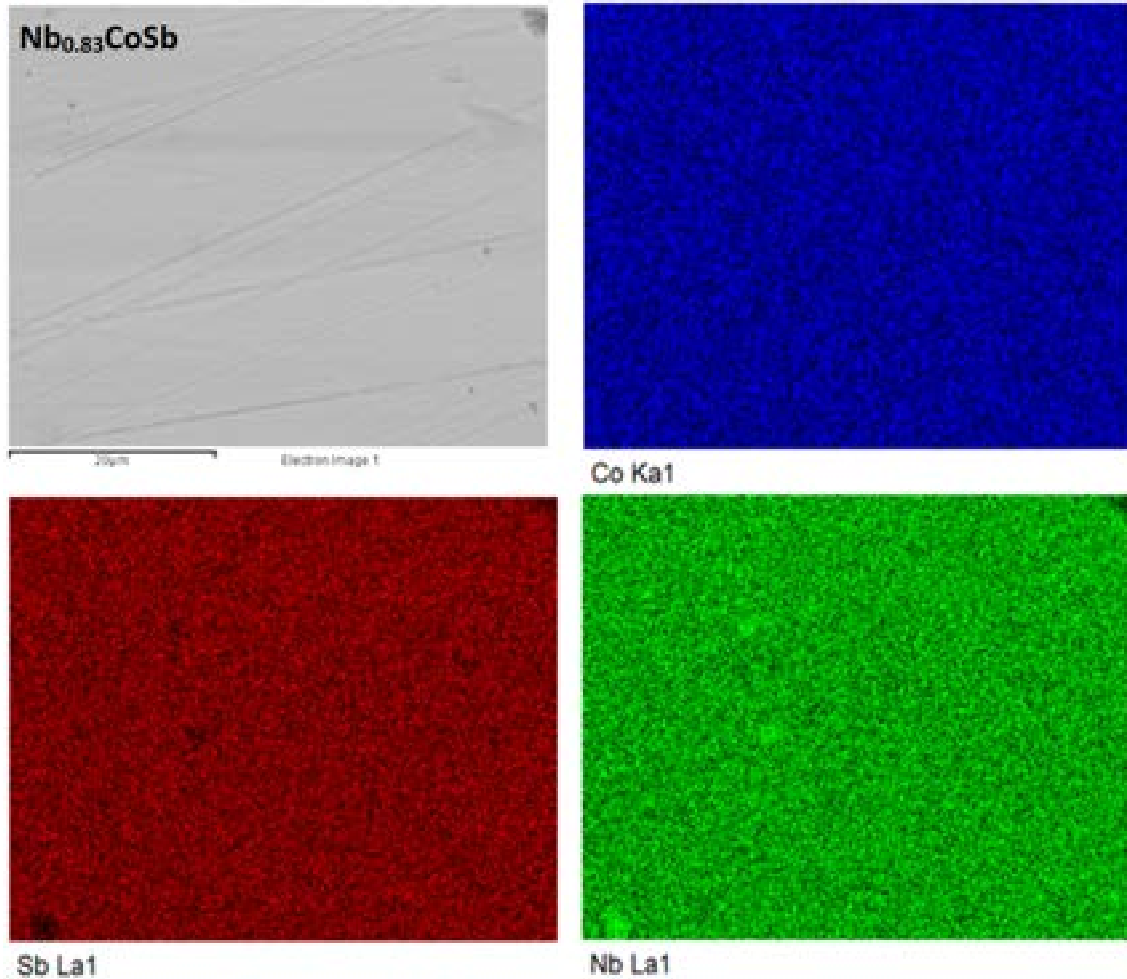

Figure 3.13: FESEM image of polished pellet of $Nb_{0.83}CoSb$ with false colour representation of elemental mapping.

A few representative HRTEM images along with the SAED patterns for undoped, 1 % 5 %, and 30 % Sn doped samples are shown in Fig. 3.17, Fig. 3.18, Fig. 3.19 and Fig. 3.20 respectively. An HRTEM image of an undoped sample grain, measuring approximately 300 nm (panel Fig. 3.17a), showing [200] family of planes is presented in Fig. 3.17b. The corresponding SAED image is shown in the adjacent panel (Fig. 3.17c). The presence of sharp diffraction spots in the SAED pattern are indicative of the high crystallinity of our samples. Interestingly, the SAED pattern also exhibits the presence of rather pronounced diffused bands, running around the diffraction spots forming a wave-like pattern. The occurrence of these diffused bands in the SAED image indicates the presence of short-range vacancy ordering in our sample, in agreement with Xia et al. [206]. Similar diffused bands due to short-range ordering

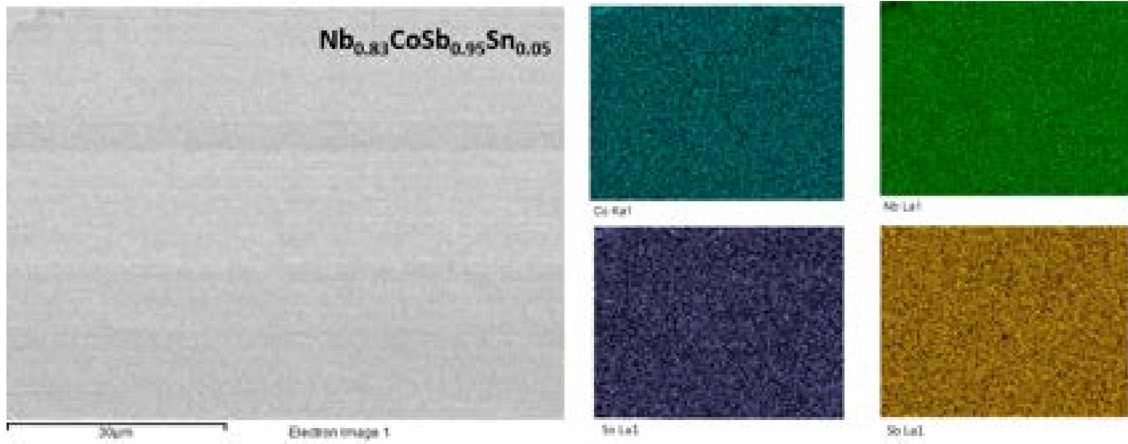

Figure 3.14: FESEM images taken in backscattering mode and chemical mapping shown with false colour representation for $Nb_{0.83}CoSb_{0.95}Sn_{0.05}$.

of the cations have been previously reported in several niobium or vanadium carbides [33, 14, 163, 151, 97]. The corresponding HTEM images for 1 % and 5 % Sn doped samples are shown in Fig. 3.18 and 3.19 respectively. In 5% Sn sample, shown in Fig. 3.19, the HRTEM image depicts [220] diffraction planes (panel b), taken on a grain measuring around 200 nm (panel a). The diffraction spots, in this case, are as sharp as for the undoped sample (panel c). Similarly, the diffused bands are also seen. This indicates that the crystalline quality or vacancy ordering is not affected by Sn doping. Similarly, for 30 % Sn doped samples sharp diffused pattern, as shown in Fig. 3.20, is seen. This is an interesting observation since the Nb concentration for this sample is $Nb_{0.9}$ instead of $Nb_{0.83}$. This suggests that short-range vacancy ordering continues to persist even if the actual vacancy concentration has almost halved. This result id in variace with Ref. [206] where the short-range Nb ordering is argued to be sensitive to the Nb vacancy concentration.

3.3.2 Thermoelectric properties

Carrier concentration

We first investigate the effect of Sn doping on the charge carrier concentration (n). Since Sn substitution for Sb causes Nb doping to increase, and as Nb is highly electropositive, we expect this to result in electron doping. To obtain the carrier concentration of our samples Hall measurements were done at 70 K. The Hall data of all samples and calculations for the carrier concentration is shown in Appendix B. The sign of the Hall coefficient in all cases turned out to be negative indicating that the majority charge carriers are electrons. The carrier concentration in our samples is of the order of 10^{21} cm^{-3}, which indicates that these are n-type heavily-doped degenerate semiconductors. A plot of carrier concentration with Sn-doping

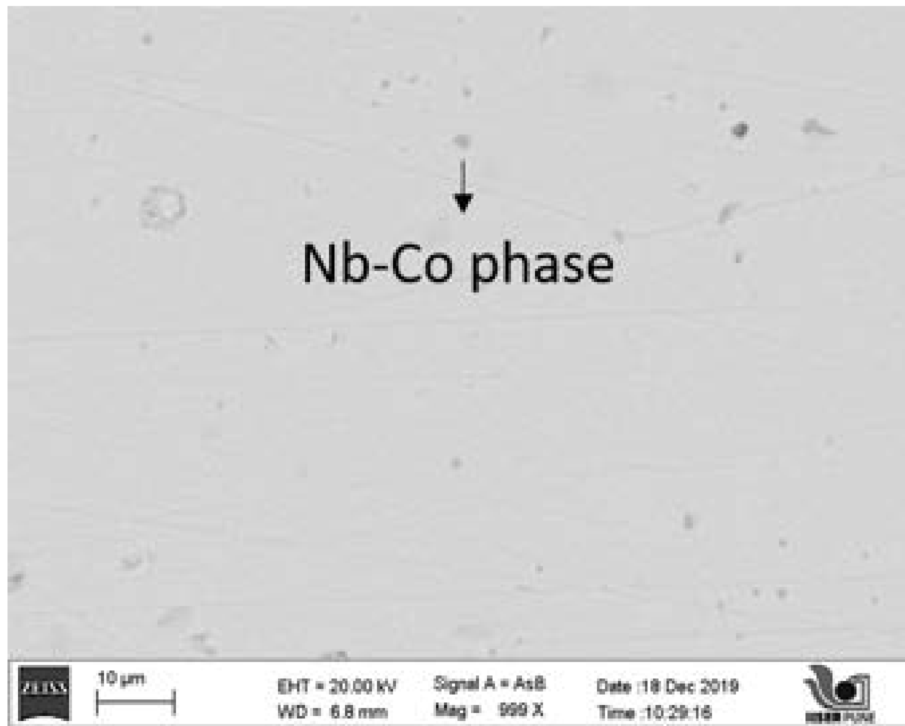

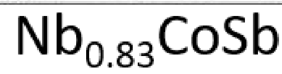

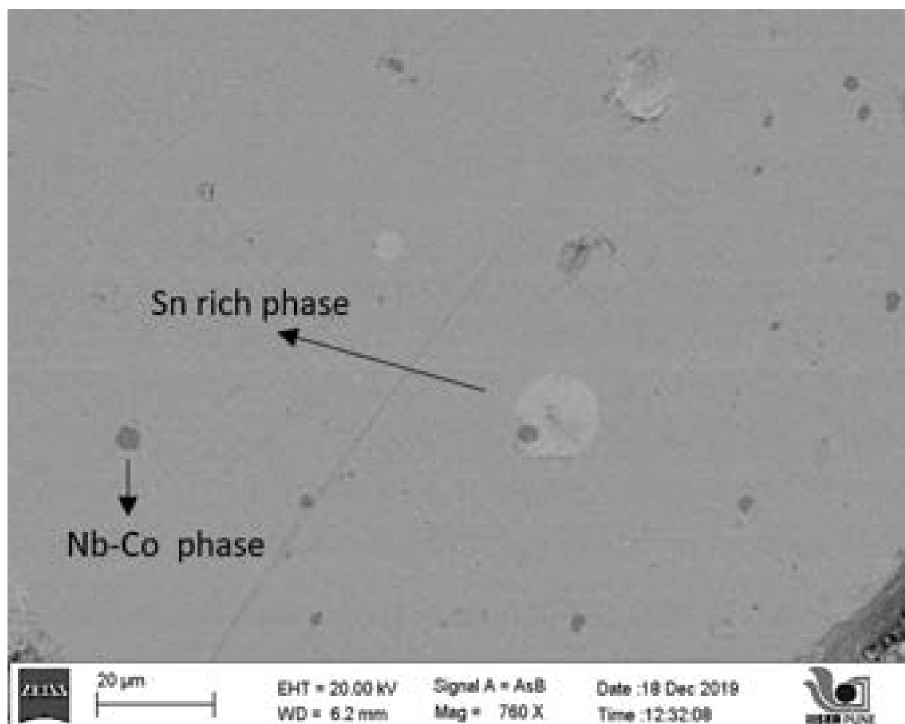

Figure 3.15: FESEM images taken in backscattering mode for (a) $Nb_{0.83}CoSb$ (b) $Nb_{0.83}CoSb_{0.7}Sn_{0.3}$.

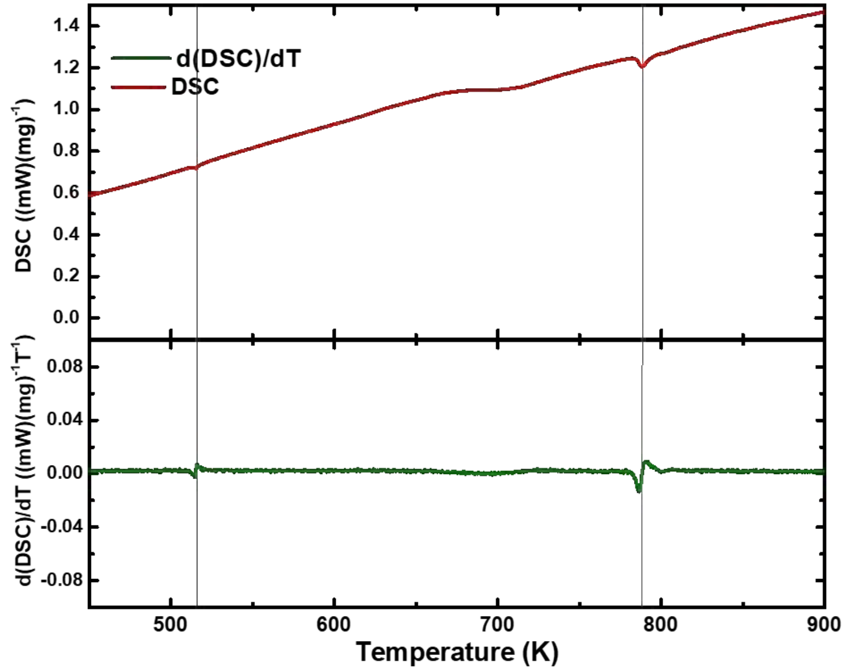

Figure 3.16: DSC measurement done on 30 % Sn doped sample show peak due to Sn melting.

is shown in Fig. 3.12. For the undoped $Nb_{0.83}CoSb$ sample, $n \approx 1.47 \times 10^{21}$ cm^{-3} is obtained. This is in good agreement with Xia et al. [205] who reported the carrier concentration in $Nb_{1-z}CoSb$ to lie in the range 3.5×10^{21} cm^{-3} (z = 0.15) to 0.7×10^{21} cm^{-3} (z = 0.2). They also showed that the optimized n to obtain maximum zT is around 2.5×10^{21} cm^{-3}. In our case, the carrier concentration in the absence of any Sn-doping is already near its alleged optimum value. The control of carrier concentration with Nb-doping alone is difficult as, the downside of this approach is that Nb being highly electropositive increases the carrier concentration dramatically(see Fig. 1b in Ref. Xia et al.[205]). Therefore, fine-tuning n through Nb doping alone is difficult. On the other hand, as we have shown above, Sn doping for Sb mandates an increase in the Nb concentration to maintain the VEC 18 condition of the HH phase. This concept can be exploited to fine-tune the carrier density while limiting the formation of secondary Nb-rich phases. As shown in Fig. 3.12 , upto 5% Sn doping, the carrier concentration jumps to almost twice its value but with further increase in Sn, n increases rather slowly with x and stays around the desired range from $2.5 \times 10^{21} cm^{-3}$ to $4 \times 10^{21} cm^{-3}$. To understand this difference between tuning n with and without Sn doping we carried out DFT calculations which we shall come to in the next section.

Zeier et al. [222] reported a carrier concentration of $5.5 \times 10^{21} cm^{-3}$ for NbCoSb sample where through synchrotron refinement they obtained the HH phase component as $Nb_{0.84}CoSb$. The calculated carrier concentration was 3.9×10^{21} cm^{-3}. The

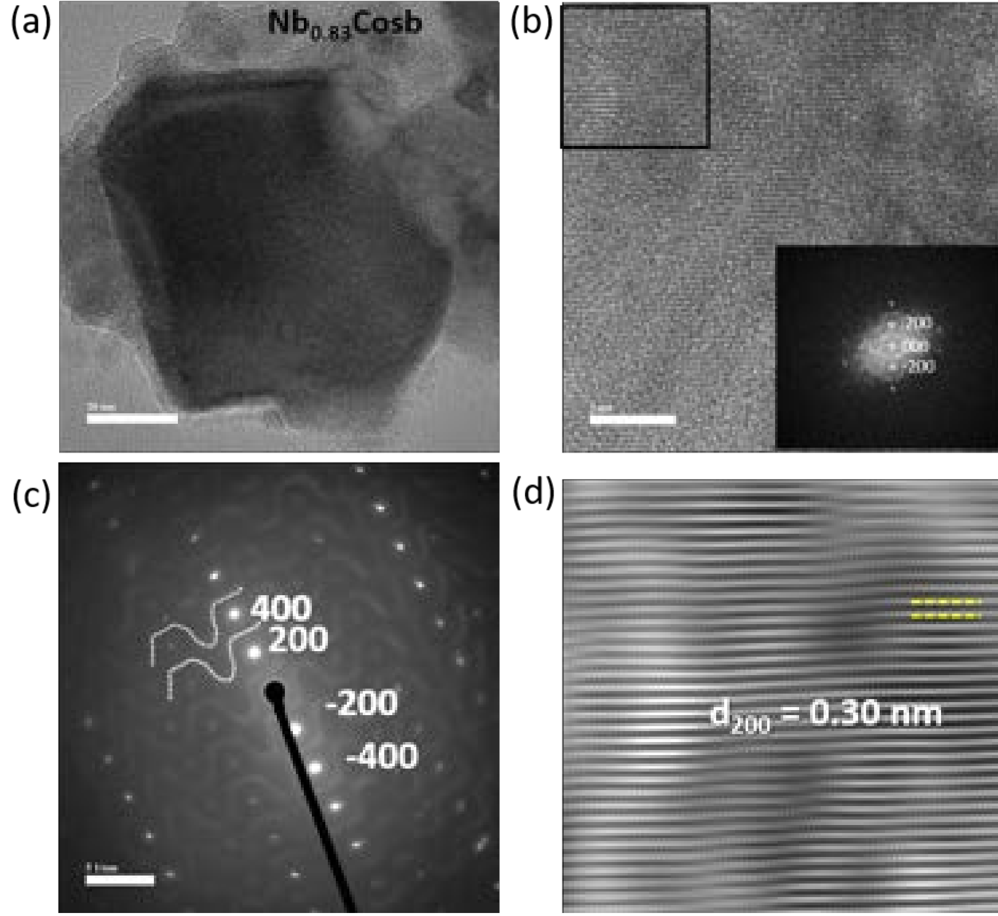

Figure 3.17: High-resolution transmission electron microscopy (HRTEM) image for $Nb_{0.83}CoSb$ (a) low magnification HRTEM image of a single grain; (b) HRTEM image showing [200] family of planes and its fast Fourier transform (FFT) image in inset where we observe spots due to lattice planes and diffused bands due to short-range ordering of vacancies at Nb site; (c) selected area electron diffraction (SAED) pattern shown for (b), where we can also observe spots due to lattice planes and diffused bands; (d) masking the spots only in FFT of (b) we generated the inverse fast Fourier transform (IFFT) image and a zoom portion of the black square is shown, also planes marked are 200 planes. Some stacking faults are also visible.

difference is 1.6 $\times 10^{21}$ cm^{-3} which is 40 % of the calculated value, was attributed to statistical error in composition and secondary phases contributing carriers in Hall measurement. Xia et al. reported carrier concentration in the range (0.7 to 6.7)$\times$ 10^{21} cm^{-3} for $Nb_{0.8+\delta}CoSb$ where the HH phase has composition, where δ ranging from -0.01 to 0.03. Xia et al. has attributed variation in carrier concentration to this δ and secondary phase present in not so pure sample. For the $Nb_{0.8}CoSb$ sample they report composition $Nb_{0.79}CoSb_{0.98}$ which corresponds to VEC equals to 17.85 (p type n_H = 3 $\times$ 10^{21} cm^{-3}), but the carrier concentration reported is 7$\times$ 10^{20} cm^{-3} which approximately corresponds to a phase $Nb_{0.807}CoSb$. Hence a small statistical error of 0.01 in Nb composition corresponds to an eroor of 1 $\times$ 10^{21} cm^{-3} in carrier concentration. In addition, secondary phases can also contribute in Hall

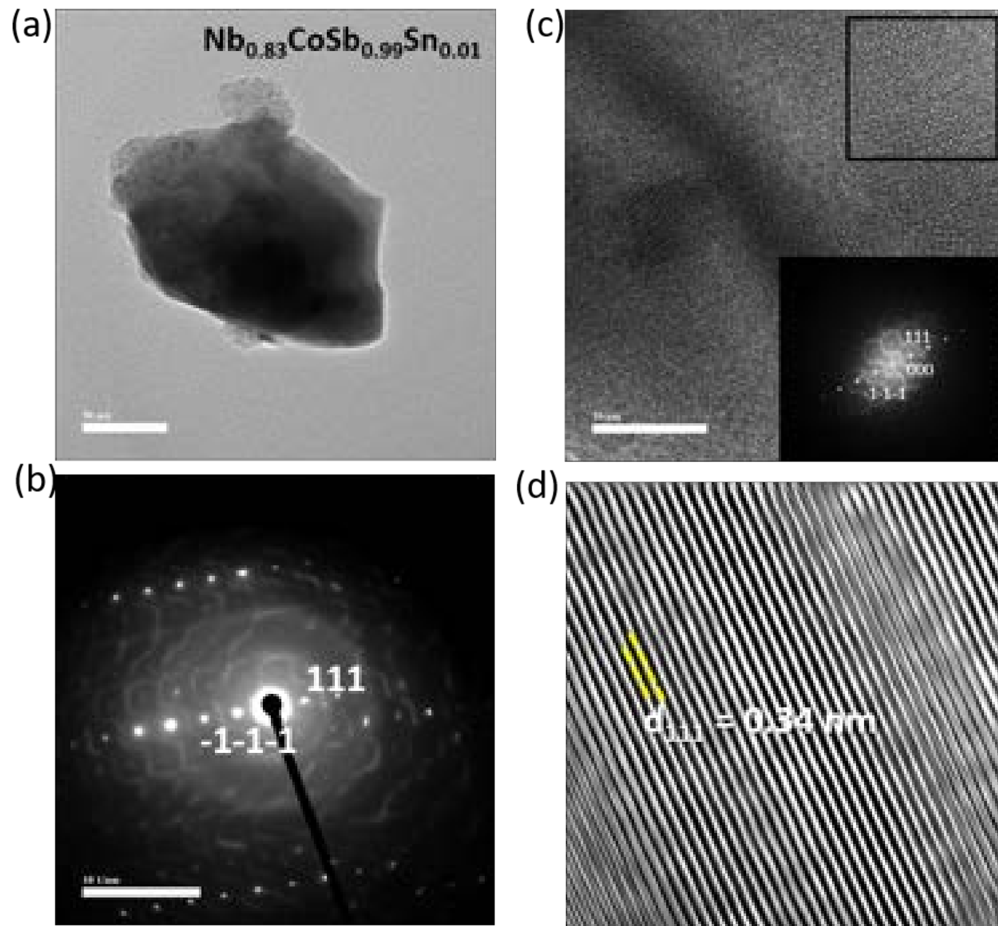

Figure 3.18: High resolution transmission electron microscopy (HRTEM) image for $Nb_{0.83}CoSb_{0.99}Sn_{0.01}$ (a) low magnification HRTEM image of a single grain; (b) HRTEM image showing [111] family of planes and its FFT shown in inset; (c) SAED pattern taken on image (b) showing lattice points for [111] family of planes; (d) IFFT of black square marked in (b), planes marked with dashed yellow lines are 111 planes.

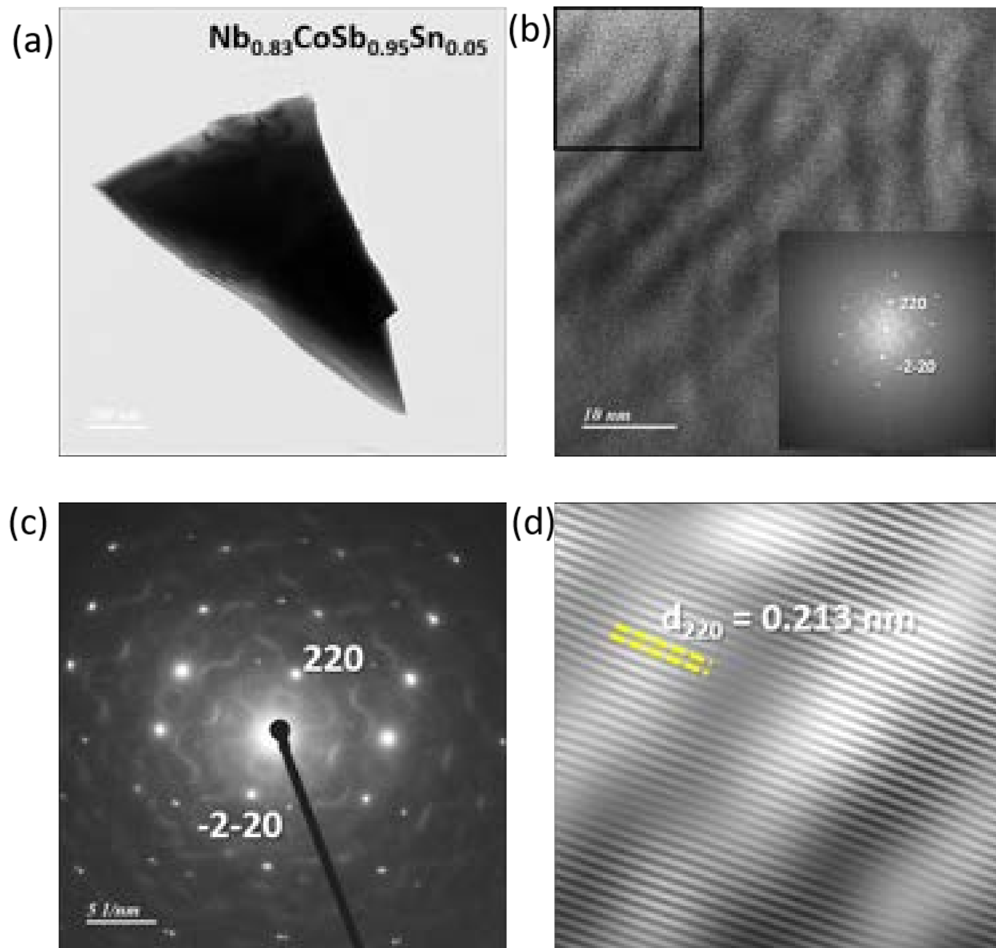

Figure 3.19: High resolution transmission electron microscopy (HRTEM) image for $Nb_{0.83}CoSb_{0.95}Sn_{0.05}$ (a) low magnification HRTEM image of a single grain; (b) HRTEM image showing [220] family of planes and its FFT shown in inset; (c) SAED pattern taken on image (b) showing lattice points for [220] family of planes; (d) IFFT of black square marked in (b), planes marked with dashed yellow lines are 220 planes.

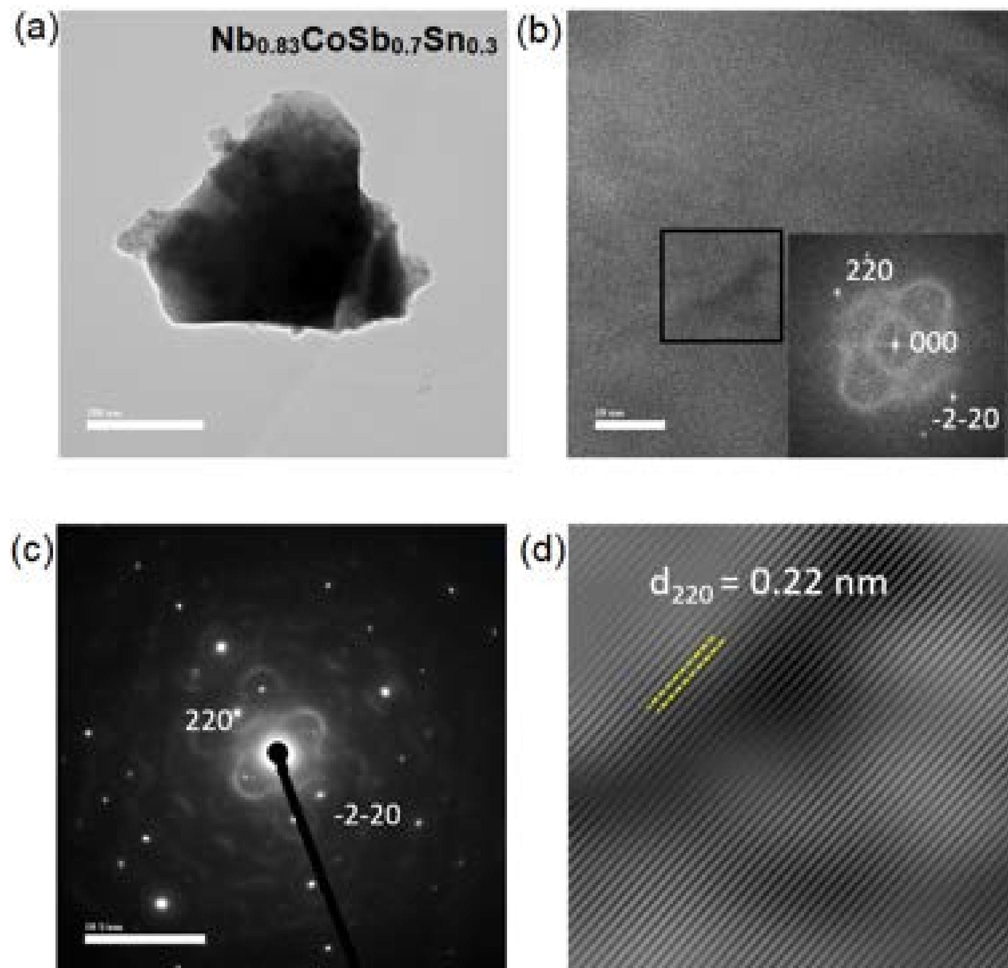

Figure 3.20: High resolution transmission electron microscopy (HRTEM) image for $Nb_{0.83}CoSb_{0.7}Sn_{0.3}$ (a) low magnification HRTEM image of a single grain; (b) HRTEM image showing [220] family of planes and its FFT shown in inset; (c) SAED pattern taken on image (b) showing lattice points for [220] family of planes; (d) IFFT of black square marked in (b), planes marked with dashed yellow lines are 220 planes.

Table 3.4: Calculated carrier concentration of all the samples based on composition obtained from refinement using Zintl phase chemistry.

Compound	refined composition	VEC	carrier conc. (10^{21} cm^{-3})
$Nb_{0.83}CoSb$	$Nb_{0.812}CoSb$	18.06	1.17
$Nb_{0.83}CoSb_{0.99}Sn_{0.01}$	$Nb_{0.82}CoSb_{0.99}Sn_{0.01}$	18.09	2.20
$Nb_{0.83}CoSb_{0.95}Sn_{0.05}$	$Nb_{0.844}CoSb_{0.95}Sn_{0.05}$	18.17	3.31
$Nb_{0.83}CoSb_{0.9}Sn_{0.1}$	$Nb_{0.847}CoSb_{0.9}Sn_{0.1}$	18.135	2.63
$Nb_{0.83}CoSb_{0.8}Sn_{0.2}$	$Nb_{0.874}CoSb_{0.8}Sn_{0.2}$	18.17	3.30
$Nb_{0.83}CoSb_{0.7}Sn_{0.30}$	$Nb_{0.9}CoSb_{0.7}Sn_{0.30}$	18.20	3.88

measurement though it is expected that they will not change transport properties of semiconducting HH matrix very much [222].

Table 3.3 shows composition obtained for various samples by refining the powder X-ray diffraction data. Considering Zintl phase chemistry we have obtained VEC for each composition. For 5 % Sn doped sample, for example we have obtained the composition as $Nb_{0.844}CoSb_{0.095}Sn_{0.05}$ which will give a VEC = 0.844*5(Nb) + 1*9(Co) + 0.95*5(Sb) + 0.05*4(Sn) = 18.17. Thus carrier concentration was calculated using formula n = z*(VEC-18)/(cell volume), where z is the number of formula units in a unit cell. The calculated carrier concentration shows a good agreement with the measured Hall data. The calculated carrier concentration is shown in Table 3.4.

3.3.3 Computation results

We studied the doping effect of Sn in $Nb_{0.8}CoSb$ using DFT calculations. We also studied the effect of extra Nb addition with Sn doping, as observed experimentally to understand the electronic and transport properties. All the calculations are done in collaboration with Vineet Kumar Pandey under the supervision of Dr. Prasenjit Ghosh.

NbCoSb possesses a fcc crystal structure with space group *F-43m*. Nb, Co and Sb atoms are located at (0,0,0), (0.25,0.25,0.25) and (0.50, 0.50, 0.50) positions respectively. Nb is octahedrally coordinated to Sb and vice versa. Co is tetrahedrally coordinated to Nb and Sb and vice versa. The optimized lattice parameter of NbCoSb is found to be 5.97 Å. However, its experimental lattice parameter is 5.90 Å[[205]]. The bond distances of Nb-Co, Nb-Sb, and Co-Sb are 2.59 Å, 2.99 Å, and 2.59 Å.

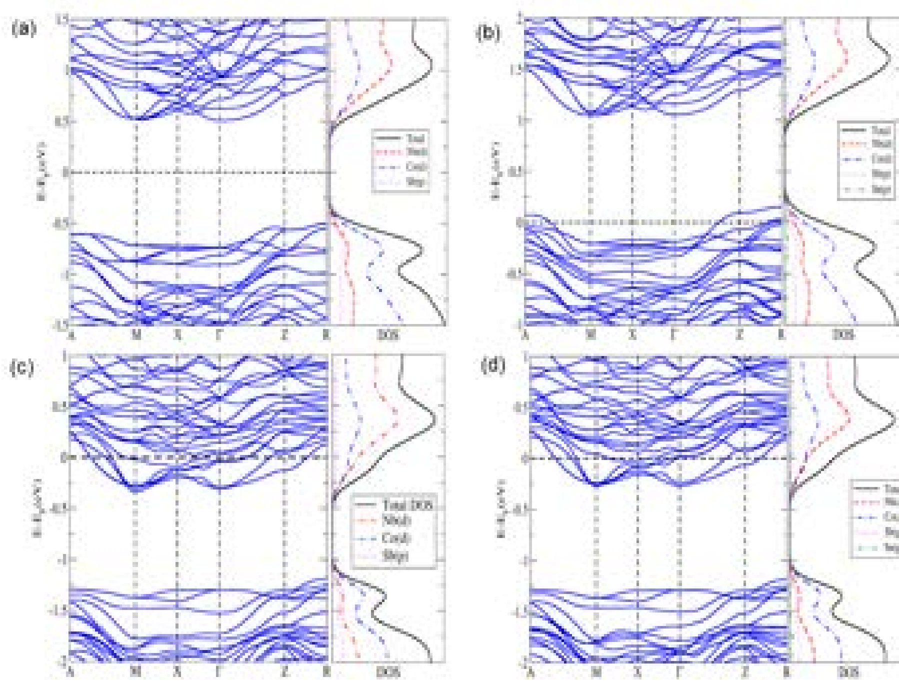

Figure 3.21: Band structure and DOS of (a) $Nb_{0.8}CoSb$ and (b) $Nb_{0.8}CoSb_{0.9}Sn_{0.1}$ and (c) $Nb_{0.9}CoSb$ and (d)$Nb_{0.9}CoSb_{0.9}Sn_{0.1}$ (Calculations done by Vineet Kumar Pandey under supervision Dr. Prasenjit Ghosh).

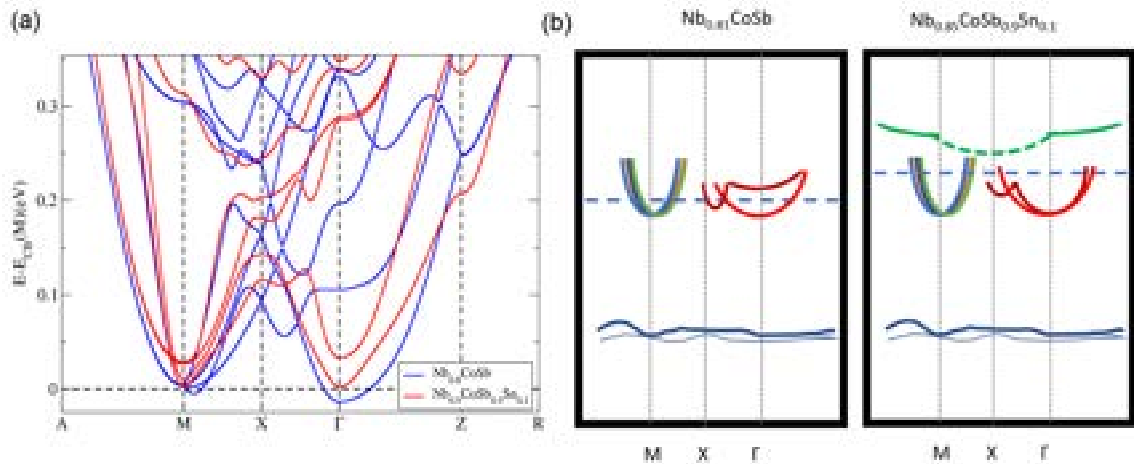

Figure 3.22: (a) Conduction band structure of $Nb_{0.8}CoSb$ and $Nb_{0.9}CoSb_{0.9}Sn_{0.1}$ scaled to obtain minima of the band at M point at same energy for both structure, and (b) band structure schematic of samples with actual composition $Nb_{0.81}CoSb$ and $Nb_{0.85}CoSb_{0.9}Sn_{0.1}$ considering calculated band structure in part (a), fermi level shifting is in accordance with the actual carrier concentration of samples obtained using Hall measurements. The solid green bands have excess Nb contribution mainly. The dashed green band has contributions from excess Nb hybridization with all other elements and appears in excess Nb sample (right image) (Calculations done by Vineet Kumar Pandey under supervision of Dr. Prasenjit Ghosh).

Zeier et al. [222] showed that NbCoSb with 20 % Nb vacancy ($Nb_{0.8}CoSb$) adopts a tetragonal crystal structure with space group (I-4). The initial structure

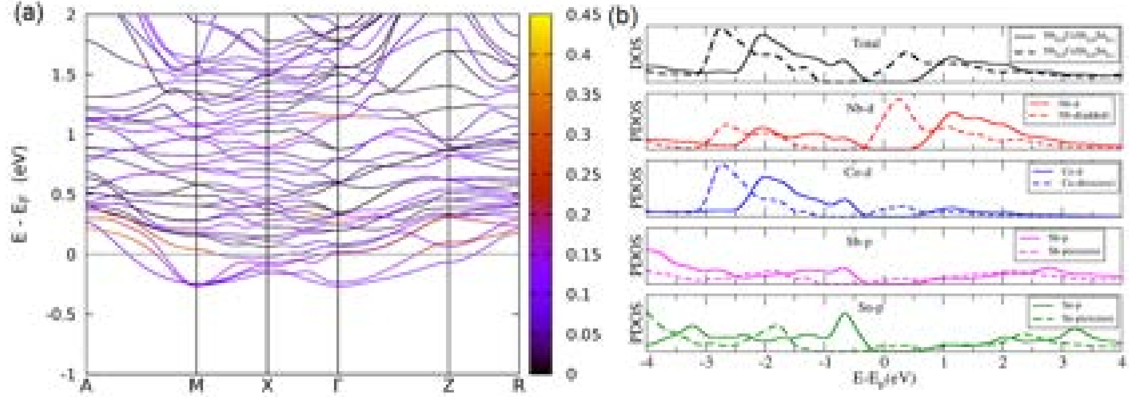

Figure 3.23: (a) Contribution of added Nb-d states in the band structure and (b) its partial DOS for $Nb_{0.9}CoSb_{0.9}Sn_{0.1}$. Here, the term "excess" represent atoms nearest to added Nb. (Calculations done by Vineet Kumar Pandey under supervision Dr. Prasenjit Ghosh)

of $Nb_{0.8}CoSb$ was taken from their paper [222]. We optimized the structure at the PBE level and found the lattice parameter to be 9.34 Å along the a direction and 5.96 Å along the c direction, which is in good agreement with Zeier et al. [222]. The electronic band structure of $Nb_{0.8}CoSb$ along with its partial DOS is given Fig.3.21(a)). $Nb_{0.8}CoSb$ is semiconducting with a bandgap 1.01 eV, which matches well with Zeier et al. The Valence band maxima (VBM) and conduction band minima (CBM) lie at R and Γ points, respectively. The conduction band of $Nb_{0.8}CoSb$ has four electron pockets at M point, which is 0.02 eV above the CBM at the Γ point. Its partial DOS analysis reveals that the valence band has a major contribution of Co-d orbitals along with Nb-d and Sb-p orbitals. However, the conduction bands are derived primarily from the Nb-d orbitals with some admixture of Co-d and Sb-p orbitals.

To understand the effect of Sn doping and excess Nb onto the transport properties of $Nb_{0.8}CoSb$, we first substituted 10 % Sb with Sn. For this, we further relaxed the structure to minimize the forces knowing the fact that Sn doping does not change the lattice parameter significantly, as shown in fig3.11(a). The relaxation of the structure leads to a small displacement of atoms from the parent structure $Nb_{0.8}CoSb$. The Electronic band structure of $Nb_{0.8}CoSb_{0.9}Sn_{0.1}$ along with its partial DOS is given in Fig.3.21(b). Doping of Sn pushes the Fermi level into the valence band. There is very little change of band curvature in both the valence and the conduction band owing to the minimal contribution of Sn orbitals. The DOS analysis of 10 % Sn doped $Nb_{0.8}CoSb$ shows no significant difference than DOS of $Nb_{0.8}CoSb$ owing to a minimum contribution of Sn p orbital near the Fermi energy.

We now consider the effect of extra Nb in $Nb_{0.8}CoSb_{0.9}Sn_{0.1}$ which corresponds to our experimental samples. After Sn substitution, there are two different types

of vacancies, one where Nb is surrounded by six Sb and the other where Nb is attached to five Sb and one Sn. We notice that added Nb goes to the vacancy site where Sn is present. The calculated electronic band structure and partial DOS of the system $Nb_{0.9}CoSb_{0.9}Sn_{0.1}$ which is shown in Fig. 3.21(d). Adding an extra Nb in $Nb_{0.8}CoSb_{0.9}Sn_{0.1}$ pushes the Fermi level up into the conduction band. The presence of states due to extra Nb at the Fermi level makes more carriers available for conduction which is evident from the partial DOS given in Fig. 3.23(b).

To summarize, the Sn doping shifts the Fermi energy into the valence bands. From the DOS of the $Nb_{0.8}CoSb_{0.9}Sn_{0.1}$ it is evident that the Sn doping has any significant contribution to the valence bands only. Further, addition of an excess Nb pushes the Fermi level into the conduction band.

To have a better understanding of the effect of excess Nb and Sn doping, we have shown a zoomed in view of the conduction band near its minima in Fig. 3.22(a). In $Nb_{0.8}CoSb$ system, near the conduction band edge, there are six degenerate bands (four at M-point, one band near X-point, and one at Γ-point). The band at Γ-point has a nearby flat band at an energy of 0.12 eV above the CBM. This band moves down and converges to the band at CBM upon incorporating excess Nb. Another interesting change that happens is the appearance of an extra flat band that appears centered at X-point nearly 0.24 eV above conduction band minima. This band will not contribute significantly, if Fermi level is far below this band, but if Fermi level is just below the band (in order of $k_B T$) then at high temperatures, this band will also contribute to transport property. Being a flat band with respect to other bands, this might further enhance the Seebeck coefficient and increase the number of channels for conduction. These changes are depicted schematically in Fig. 3.22(b) where the relevant low energy bands near the conduction band minimum are shown.

Electrical transport: conductivity and thermopower

We next show the electrical conductivity and thermopower of all the samples with varying Sn doping up to $x = 0.1$ in Fig. 3.24 and Fig. 3.25 respectively. The transport properties of samples with higher Sn doping ($x = 0.20$ and 0.30), which contain precipitates of an Sn-rich phase, have been discussed separately in Appendix A. For the undoped sample, the electrical conductivity decreases with increasing temperature ranging from 500 S cm-1 at 300 K to 400 S cm-1 at the highest temperature (1100 K). However, merely 1% of Sn doping leads to a significant enhancement of σ near room temperature, but with further increase in Sn doping up to 10 %, the electrical conductivity decreases slightly but remains higher than the undoped sample. This is consistent with the fact that with 1% Sn doping the carrier concentration jumps from $n = 1.5 \times 10^{21}$ cm^{-3} to $n = 2.5 \times 10^{21}$ cm^{-3}, but with further Sn-doping the increase in the carrier concentration is much slower. In fact, for our 5%

($x = 0.05$) and 10% ($x = 0.1$) samples, there is only a marginal increase in n; on the other hand, due to an increase in lattice potential fluctuation due to higher doping, the alloy scattering for these samples is expected to be more pronounced, which in turn would result in a slight decrease in the carrier mobility and hence lower electrical conductivity. As we shall see further, the observed behavior of σ for samples with intermediate Sn doping is related to changes in the electronic band structure upon Sn doping. For the undoped sample, a slight increase in σ at a temperature above 800 K is also observed, leading to a shallow minimum near 900 K, signifying the thermal activation of minority charge carriers around this temperature. The absence of a similar minimum in the temperature variation of σ for the 1 % Sn-doped samples ($x = 0.01$) suggests that Sn and Nb co-doping suppresses the bipolarity as Fermi energy goes deeper into the conduction band. With further doping ($x = 0.05$ and $x = 0.1$), we observe reappearance of the conductivity minimum. We will explain this corroborating with band picture and thermopower data at the end of the section. Generally, the acoustic phonon scattering [209, 92, 135, 82, 45] should be the dominant mode of scattering mechanism for which σ goes as $T^{-1.5}$. However, it is clear from Fig. 3.24(a) that this is not the case here as in our samples σ varies as $T^{-0.5}$ to $T^{-0.6}$, which suggests that the Nb vacancy induced alloy disorder scattering for which σ goes as $T^{-0.5}$ is more prevalent, which is expected due to large concentration of Nb vacancies in these samples.

All samples exhibit a negative Seebeck coefficient in agreement with the sign of the Hall coefficient discussed above. For the undoped sample, S increases from -120 $\mu V K^{-1}$ at 300 K to -200 $\mu V K^{-1}$ at 800 K before decreasing again slightly upon further heating revealing a broad maximum centered around 900 K, mirroring the minimum at the same temperature in σ. Upon 1 % Sn doping, S decreases over the whole range with a value of about -100 (-180) $\mu V K^{-1}$ at 300 (1100) K which appears to be a direct consequence of the increased carrier concentration. Also, unlike the undoped sample, no maxima can be seen till the highest temperature. Upon increasing the Sn-doping further, $|S|$ increases slightly but remain less than that for the undoped sample. However, what is remarkable is that above 800 K, the thermopower of the doped samples continues to grow and does not show a decrease that is seen for the undoped sample. This is a significant change. To put it in perspective, we note that in $Nb_{1-z}CoSb$ [205] series also with increasing z the thermopower shows an increasing behavior without a maximum; howevr, the overall magnitude of the thermopower also plummets quite strongly with z. This reveals the advantage of Sn and Nb co-doping for tuning the carrier concentration and band structure.

The carrier mobility ($\mu = \sigma/ne$) for the undoped sample is around 2 $cm^2V^{-1}s^{-1}$, which is in good agreement with that reported by Xia et al. [205] for $Nb_{1-z}CoSb$

samples; but this is smaller in comparison with n-type $ZrNiSn_{1-y}Sb_y$ samples whose mobility is on the order of 30 $cm^2V^{-1}s^{-1}$. The Hall mobility (μ_H) and conductivity at 300 K are plotted in Fig. 3.26 but taking the carrier concentration measured at 70 K which is justified by temperature dependence Hall measurements in Ref. [205]. At room temperature [Fig. 3.26(a)], the Hall mobility for samples up to 10 % Sn doping ($x < 0.1$) decreases which suggests an increase in the band effective mass (m^*).

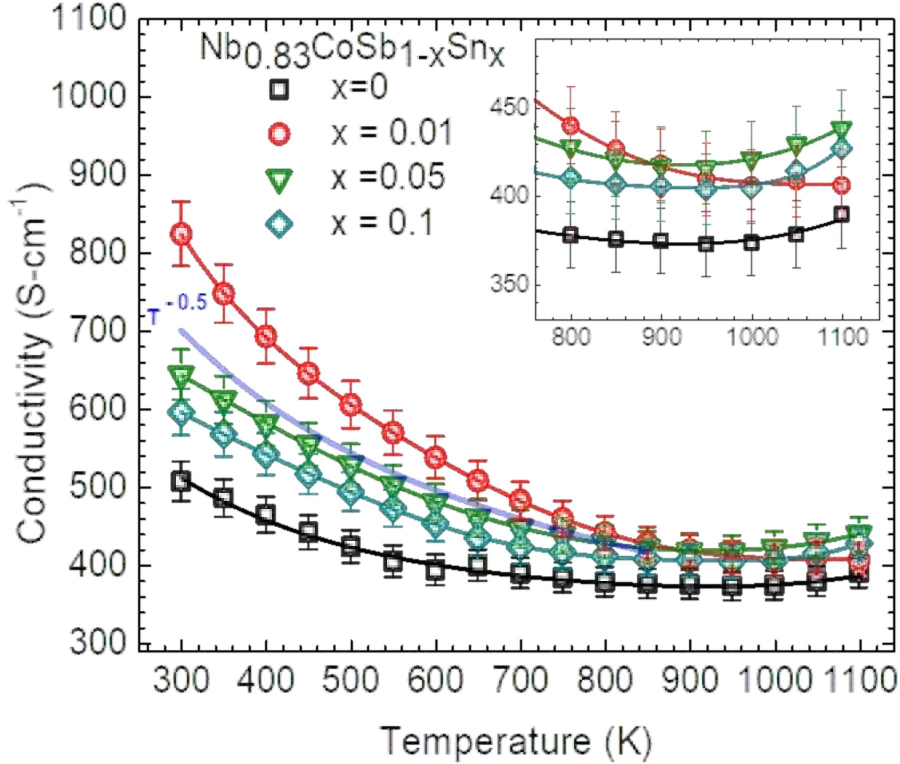

Figure 3.24: Temperature variation of electrical conductivity of samples $Nb_{0.83}CoSb_{1-x}Sn_x$ (x = 0, 0.01, 0.05, 0.1 and 0.15). Lines drawn through data points are guide to the eye

We also show variation of thermopower with doping percentage of Sn at 300 K in Fig. 3.26. At room temperature, thermopower shows an inverse behavior as compared to mobility, which is what is normally observed. Hall mobility can be used to estimate the band-effective mass. The lower the Hall mobility the higher the band effective mass, which means the flatter the band leading to a higher value of the thermopower.

To get further insight, we plot the variation of S with the carrier concentration at 300 K. This is shown in Fig.3.27. As shown in Ref.[205], in the $Nb_{1-z}CoSb$ samples the carrier concentration does not vary much between room-temperature and 2 K, therefore, we can safely assume that the carrier concentration at 300 K is near about the same as at 70 K. Within the Single Parabolic Band (SPB) approach, one can

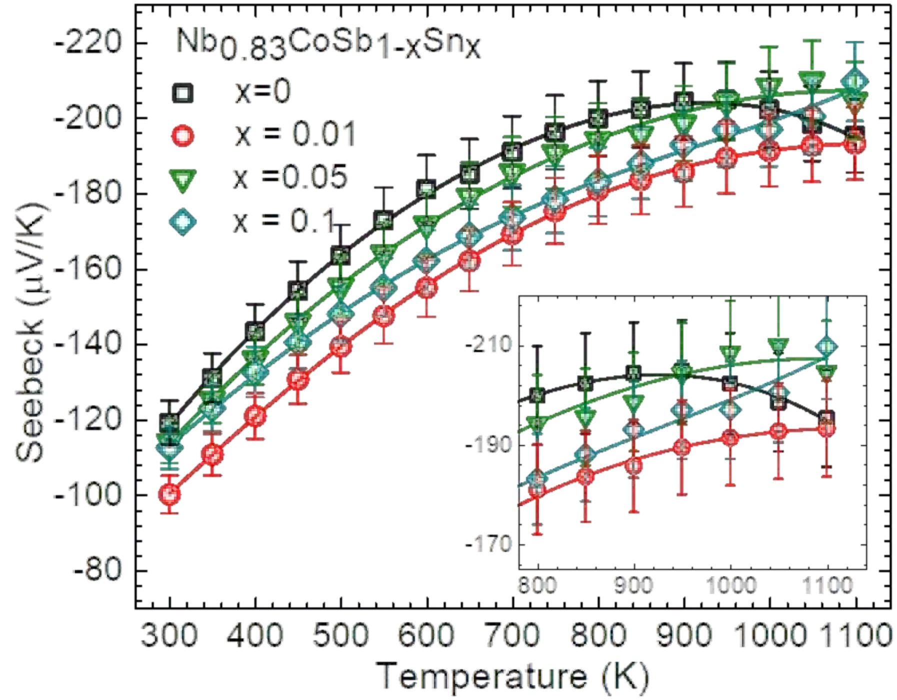

Figure 3.25: Temperature variation of Seebeck coefficients of samples $Nb_{0.83}CoSb_{1-x}Sn_x$ (x = 0, 0.01, 0.05, 0.1 and 0.15). Lines drawn through data points are guide to the eye.

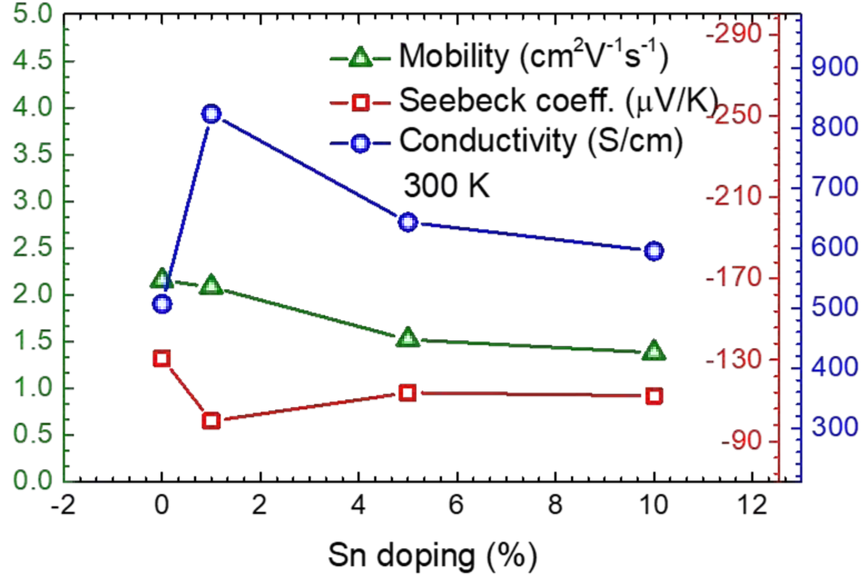

Figure 3.26: Variation of electrical conductivity and Hall mobility with Sn doping percentage at 300 K.

also draw the Pisarenko plots for various values of the density of states effective mass (m_d^*). In Fig. 3.27, one such plot for $m_d^* \simeq 8.1m_e$, where m_e is the free electron mass, is shown. From this plot it is evident that m_d^* for $Nb_{0.83}CoSb$ is close to $8.1m_e$,

which is in good agreement with the value reported previously ($7.7m_e$) for various samples in the $Nb_{1-z}CoSb$ series. We also notice that lightly Sn-doped samples are located above the calculated curve suggesting higher m_d^* for these samples. However, $x = 0.2$ and 0.3 samples lie slightly below this plot. Thus, m_d^* first increases with Sn doping and then decreases for higher dopings tending towards the value reported for Sb doped NbCoSn (7.1 m_e for 10 % doping [66]). The thermopower and electrical conductivity of $x = 0.2$ and $x = 0.3$ samples is shown in Appendix A.

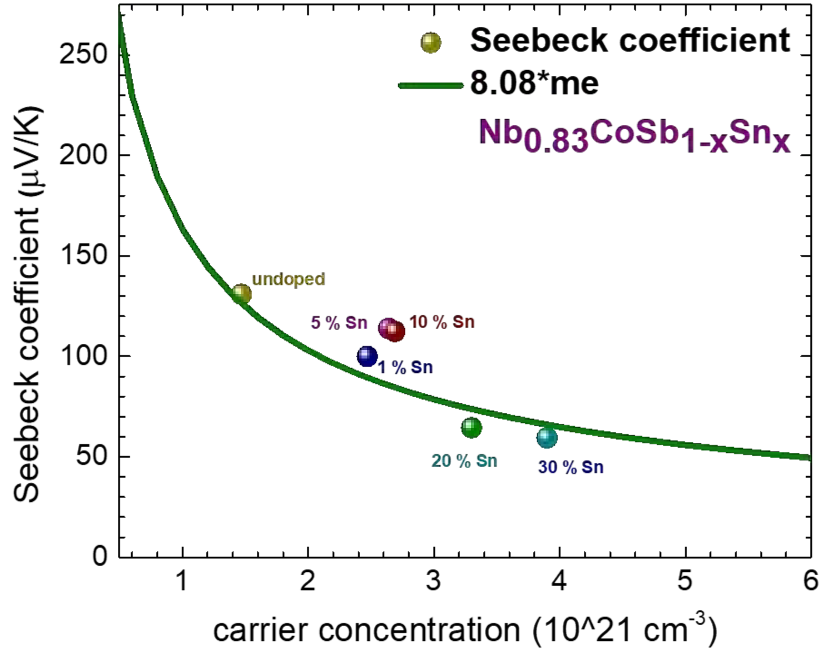

Figure 3.27: Pisarenko's plot: Variation of Seebeck coefficient with carrier concentration.Different dashed lines show Pisarenko plot for different m_d^*

In order to understand the transport properties we have shown a schematic diagram of the band structure of $Nb_{0.8}CoSb$ and $Nb_{0.9}CoSb_{0.9}Sn_{0.1}$ near the top and bottom of their valence and conduction bands respectively in Fig. 3.22(b). The bands are drawn by considering the calculated electronic band structure of the $Nb_{0.8}CoSb$ and $Nb_{0.9}CoSb_{0.9}Sn_{0.1}$. The Fermi energy scales according to the carrier concentration of the sample obtained from hall measurements. The electrical conductivity shown in Fig. 3.24 has an upturn in the undoped sample and around the same temperature the thermopower shows a down turn, due to activation of minority carriers at $\sim 900K$. For 1 % Sn doped sample, we see a clear suppression of bipolarity as the Fermi level goes deeper into the conduction band due to increase in the majority carrier concentration with doping. The decrease in mobility as shown in Fig. 3.26 is likely due to a close proximity of the Fermi level to the flat band at Γ point. This increases the band effective mass, leading to a decrease in the mobility and high S despite an increasing carrier concentration. The decrease in electrical

conductivity beyond 1 % of Sn doping can be attributed to extra scattering due to alloying of Sn at the Sb site and the upturn in electrical conductivity at high temperatures ($\sim 900K$) for these samples can be attributed to convergence of the flat green bands at the Γ point as shown in Fig. 3.21(b). Additionally, for high Sn doping a new flat bannd, centered around the X point comes into picture. This is shown with a broken line in the panel b of the Fig. 3.22. This is expected to increase the electrical conductivity due to additional carriers at high temperature. At the same time, this prevents the thermopower from decreasing as both band convergence and band flattening favors high thermopower. This band is not expected to contribute to the electrical conductivity at low temperatures as it is about 0.076 eV above the Fermi level for $x = 0.1$ sample ($k_BT \approx 0.07$ eV at 800 K). Similar effect was observed in the $Pb_{0.98}Na_{0.02}Se$- x % HgSe samples due to convergence of a secondary flat valence band at high temperature [70]. It is also important to see the origin of this band. From the band structure and partial DOS shown in Fig. 3.23, it is evident that this band has mostly contribution from excess Nb and its hybridization with other elements. Thus, to prevent S from collapsing it is crucial to increase the Nb content (δ) in $Nb_{0.8}CoSb$, which can be achieved by simply doping Sn at the Sb site. Without Sn doping the maximum value that δ can take is less than 0.03.

Power factor, thermal conductivity, figure of merit

Power factor has been plotted in Fig.3.28(a) which clearly shows an increase for the Sn doped samples, particularly at high temperatures. This is a direct consequence of the fact that the thermopower in our Sn-doped samples doesn't collapse despite an increase in the carrier concentration. The weighted mobility of our samples is shown in Fig. 3.28(b). In the temperature range 500 K to 1100 K, μ_W obeys a $T^{-\alpha}$ dependence with $\alpha \approx 1$. The variation in temperature dependence for weighted mobility at high temperatures is also interesting. We show the weighted mobility, and power factor at 300 K and 1100 K in Fig. At 1100 K, the weighted mobility show monotonically increasing behavior. Since $\mu_W/\mu = (m^*_{DOS}/m_o)^{3/2}$, this suggests an increase in the DOS effective mass with an increase in Sn doping percentage which is in aggrement with σ and S variation with x discussed in the previous section. Also, the variation in power factor directly follows the trend of weighted mobility both at 300 K and 1100 K, which signifies the role of DOS effective mass.

Thermal conductivity of our samples is shown in the Fig.3.30(a). Thermal conductivity of all samples show a decreasing behavior with temperature. A reduction of thermal conductivity is observed for 1 % and 5 % Sn doped samples due to addition of extra scattering factor due to doping and due to smaller sample density (see table 3.2). Lorenz number (L) for the samples [183], [205] were obtained from the thermopower data using expression 1.20 given in chapter 1 rather than using

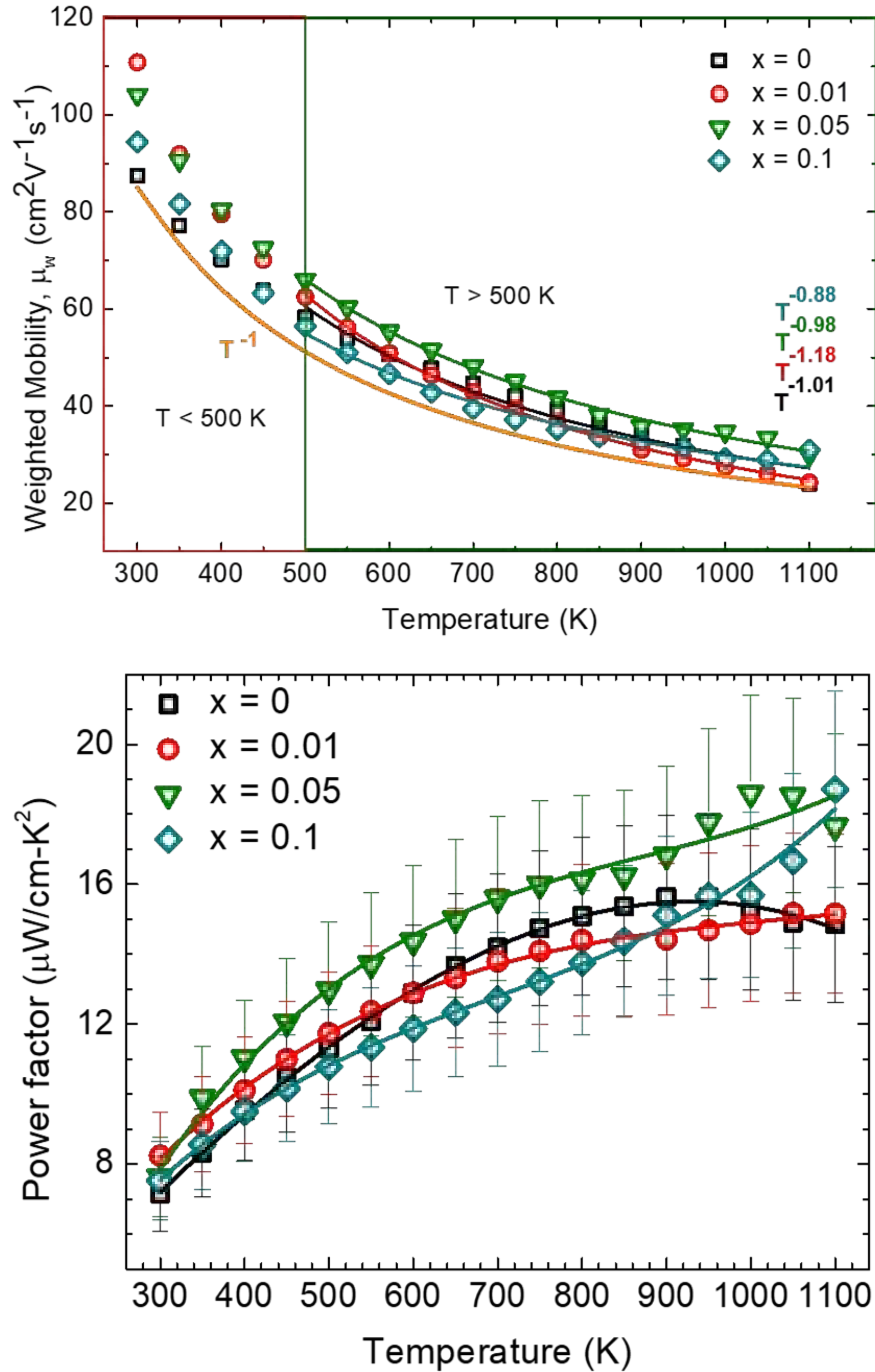

Figure 3.28: (a) Temperature variation of weighted mobility and power factor for samples $Nb_{0.83}CoSb_{1-x}Sn_x$ (x = 0, 0.01, 0.05, 0.1 and 0.15)

$2.45 \times 10^{-8}\ W\Omega K^{-2}$ (degenerate semiconductor) which is constant throughout the temperature range. The variation of L with T is shown in Fig.3.31(a)). This Lorenz number gives κ_e (See Fig. 3.31(b)) by using the Wiedemann-Franz law

$$\kappa_e = \sigma LT \tag{3.1}$$

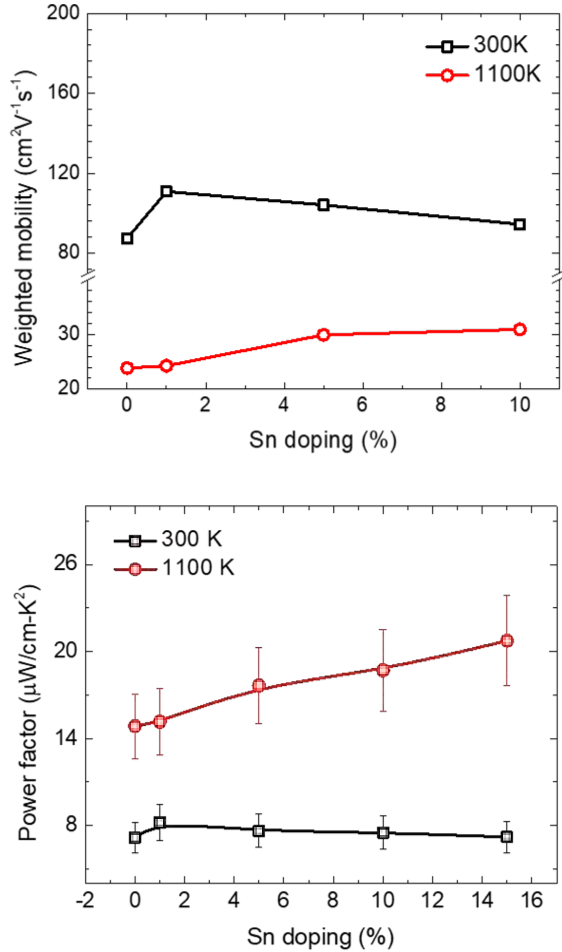

Figure 3.29: (a) Weighted mobility and (b) power factor plotted against nominal Sn doping percentage at 300 K (black) and 1100 K (Red)).

[146, 190, 176].

Lattice thermal conductivity κ_L is obtained by subtracting the electronic contribution from total thermal conductivity. In Fig.3.30(b) lattice thermal conductivity has been shown. Due to a large amount of vacancies in the system, the dominance of point defect scattering ($T^{-0.5}$) of phonons can be observed [205]. The existence of vacancies and short-range ordering have been observed in undoped and low doping. For higher doping, the Nb vacancy concentration decreases (for example in 10 % Sn doped sample the vacancy concentration is almost 3/4 of $Nb_{0.8}CoSb$), which leads to an overall increase in lattice thermal conductivity.

To investigate the vacancy ordering in $Nb_{0.83}CoSb$ samples, we did Raman spectroscopy of our samples. In NbCoSb we expect a total of 9 phonon modes; 1 (triply degenerate) acoustic and 2 optical (triply degenerate). Fig 3.33 shows Raman spectra obtained for $Nb_{0.83}CoSb_{1-x}Sn_x$ (x = 0, 0.01, and 0.3) samples. We do not see distinct Raman modes, rather three broad humps are observed. Theoretically, we should observe only two peaks in the stoichimetric $NbCoSb$ Raman spectra due to two triply degenerate optical modes. We tried to fit the observed Raman data with

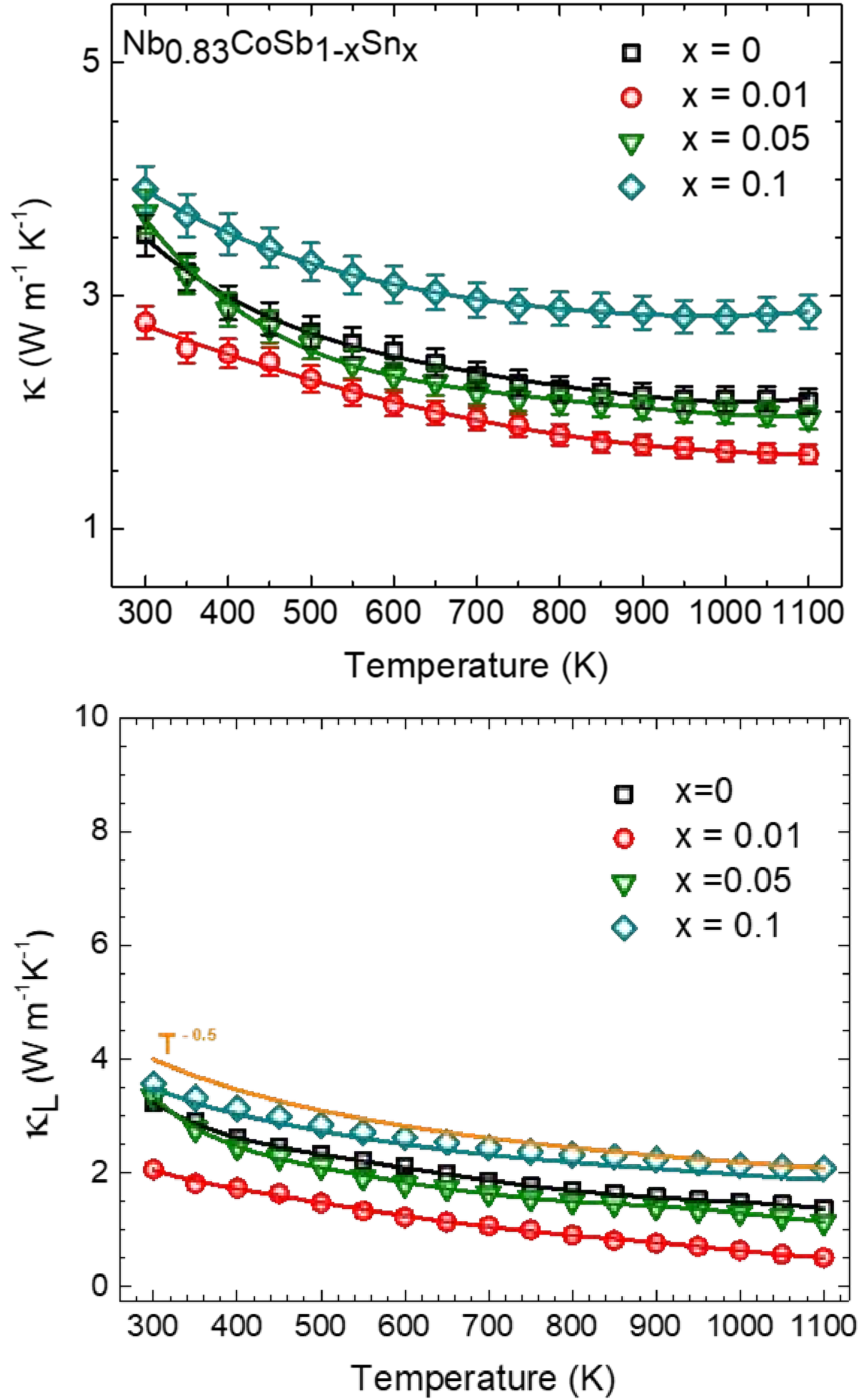

Figure 3.30: Temperature variation in thermal conductivity and lattice thermal conductivity for the samples $Nb_{0.83}CoSb_{1-x}Sn_x$ (x = 0, 0.01, 0.05, and 0.1)

eight peaks which gives a good fitting, as shown in Fig. 3.33. The observed peak positions for three samples are listed in Table 3.5. The modes P_3, P_4, and P_8 show a strong doping dependence. Theoretical work to understand the complex Raman spectra in these alloys is in progress nd will be reported elsewhere.

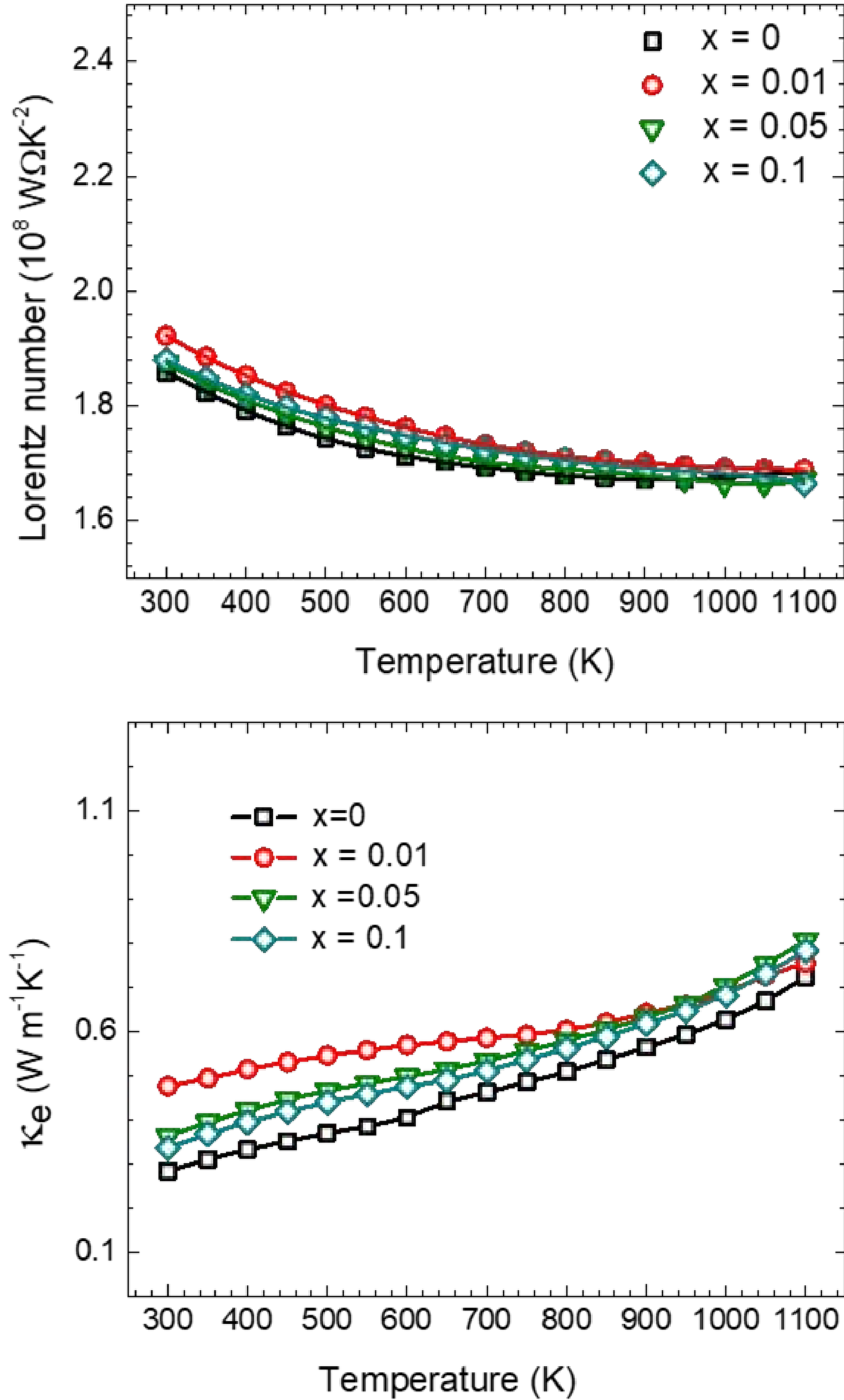

Figure 3.31: Temperature variation of (a) Lorenz's number obtained from Seebeck coefficient using Eq. 1.20 (b) electronic part of thermal conductivity obtained using electrical conductivity and Lorenz's number for samples $Nb_{0.83}CoSb_{1-x}Sn_x$ (x = 0, 0.01, 0.05, and 0.1)

Further, we obtained μ_w/κ_L and β factor which show enhancement for 1 % and 5 % Sn doped samples as compared to undoped sample, plots are shown in Fig.3.32.

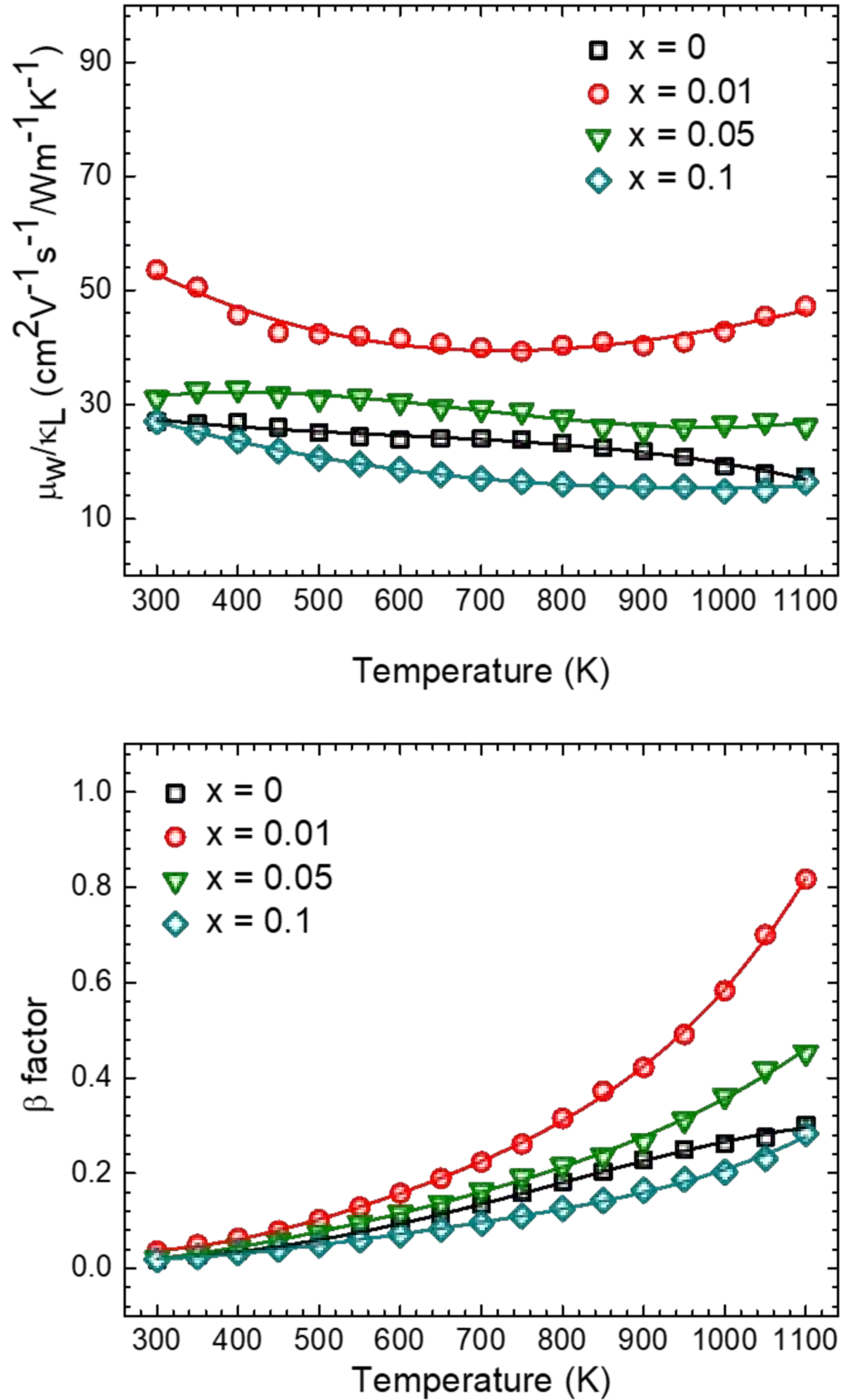

Figure 3.32: Temperature variation of (a) μ_w/κ_L and (b) B factor for samples $Nb_{0.83}CoSb_{1-x}Sn_x$ (x = 0, 0.01, 0.05, and 0.1)

From this we conclude that small Sn doping (≤ 5 %) helps in enhancing the material property to give better performance. Finally, we plot the figure of merit, zT of our samples, and its temperature dependence in Fig. 3.35. As seen from the temperature dependence plot β factor 1 % and 5 % Sn doped samples have higher performance

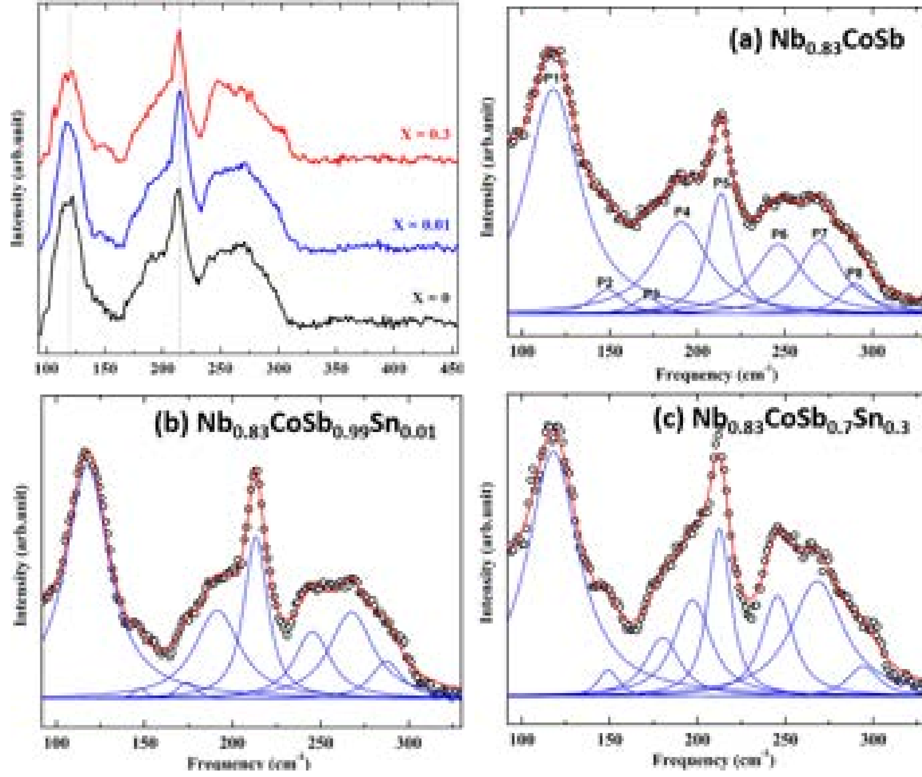

Figure 3.33: (a) Raman spectrum of samples $Nb_{0.83}CoSb_{1-x}Sn_x$ (x = 0, 0.01, and 0.3), Raman spectrum of samples $Nb_{0.83}CoSb_{1-x}Sn_x$ with multiple peak fitting (b) x = 0, (c) x = 0.01 , and (d) x = 0.3 respectively.

Table 3.5: Raman modes for $Nb_{0.83}CoSb_{1-x}Sn_x$ (x = 0, 0.01, and 0.3) samples

Raman modes (cm^{-1})	$Nb_{0.83}CoSb$	$Nb_{0.83}CoSb_{0.99}Sn_{0.01}$	$Nb_{0.83}CoSb_{0.7}Sn_{0.3}$
P1	117.7	117.7	117.90
P2	148.8	147.6	149.4
P3	171.3	174.1	180.3
P4	190.9	191.5	197.2
P5	213.6	213.3	212.5
P6	246.5	245.4	245.6
P7	270.0	267.5	268.2
P8	289.9	287.4	294.4

(β factor) than the undoped sample. Similarly we see that the zT is also higher for these two samples as compared to the undoped sample. Highest zT $\sim$ 1 is observed for 1 % and 5 % Sn doped samples near $T = 1100\ K$ The zT of the undoped sample (0.76) is in good aggrement with Ref.[205] where zT of 0.8 was reported for the same composition.

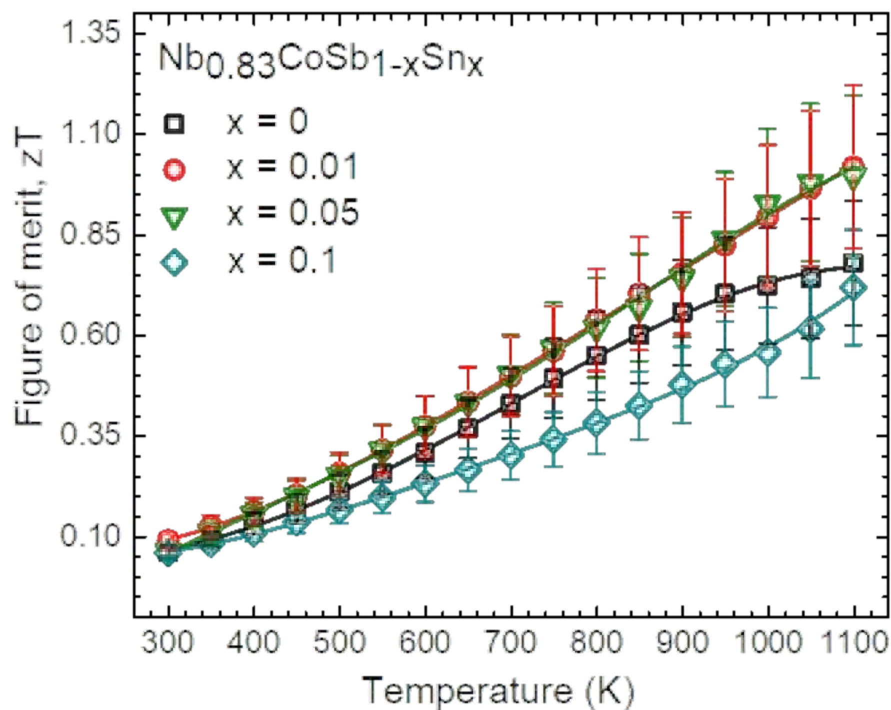

Figure 3.34: Temperature variation of figure of merit, zT for the samples $Nb_{0.83}CoSb_{1-x}Sn_x$ (x = 0, 0.01, 0.05, and 0.1)

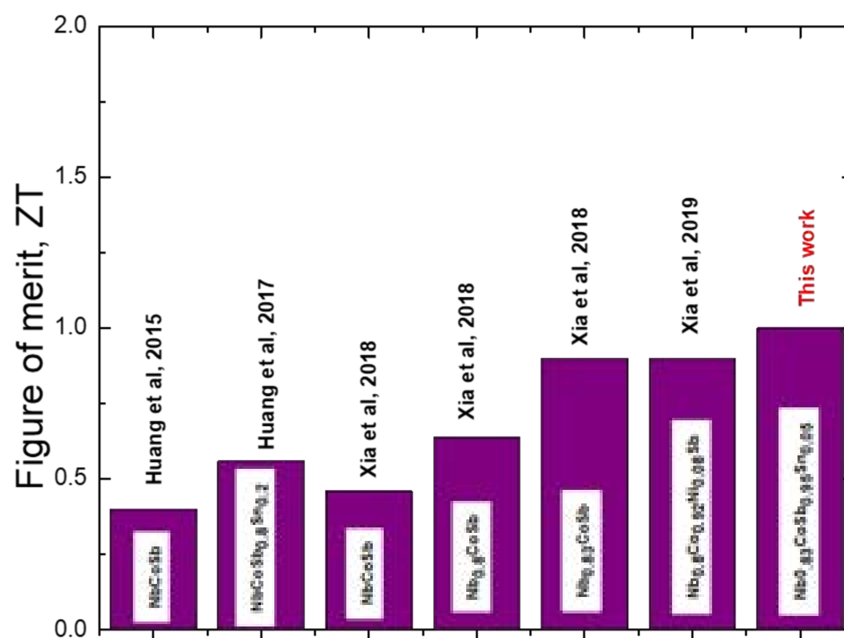

Figure 3.35: Few reports of thermoelectric figure of merit of NbCoSb and its comparison to this work.

3.4 Summary and Conclusions

$Nb_{0.83}CoSb_{1-x}Sn_x$ samples were studied for their structure, phase purity, and thermoelectric properties. Samples are found to crystallize in the *F-43m* cubic phase. A large concentration of cationic vacancies were present in the system which tends to show short-range ordering. The nominal composition of the samples studied here can be written as $Nb_{0.83}CoSb_{1-x}Sn_x$ ($x = 0, 0.01, 0.05, 0.1, 0.2, 0.3$). The samples $x = 0.2, 0.3$ were found to contain unreacted Sn or a Sn rich phase, hence their thermoelectric properties were not studied in detail. The chemical homogeneity δ of Nb in $Nb_{0.80+\delta}CoSb$ was previously reported to be $0 \leq \delta \leq 0.02$. The excess Nb acts as an electron donor. We show that doping Sn allows Nb composition to be increased progressively far beyond the previously reported homogeneity limit with δ reaching up to 0.05 for $x = 0.1$ sample. The excess Nb in the structure prevents the thermopower from collapsing despite an increase in the carrier concentration. To understand this we carried out electronic structure calculations that revealed the presence of a low-lying flat band in the conduction band close to the band edge arising due to the excess Nb (δ) in the structure. Further, due to Sn doping the carrier concentration also changes in a controlled manner since while Nb acts as an electron donor, Sn acts oppositely thus slowing down the rate of increases in the carrier concentration with increasing Nb doping. The highest power factor obtained is around 20 $\mu W cm^{-1} K^{-2}$ which is much less that what obtained Serrano st al. in NbCoSn with mere 5 % Pt doping at the Co site [167]. In some other HH, such as ZrNiSn a very high value ofpower factor $PF = 50\ \mu W cm^{-1} K^{-2}$ has been reported [179]. For our 1 % and 5 % Sn doped samples, we found zT to exceed slightly above 1 at 1100 K. The previously highest reported zT for these alloys was 0.9 at 1100 K. The zT enhancement has been attributed to the band engineering which allows both σ and S to be high simultaneously. The short-range vacancy ordering is manifested in the form of diffused bands in HRTEM. The Raman spectra show extra Raman modes due to presence of Nb vacancies showing short-range ordering at room-temperature.

Chapter 4

Orthorhombic Ternary MTX Compounds

4.1 Introduction

The orthorhombic MTX family, where M is a transition metal, T is a late transition metal, and X is a main group element, constitute a very large class of intermetallic compounds crystallizing with the TiNiSi structure-type. Recently, compounds of this structure class have attracted significant attention due to their interesting magnetostructural, transport and thermodynamic properties, including, giant magnetocaloric effect [48], [153], cycloidal magnetic ordering [39], coexisting hexagonal and orthorhombic phases showing an interplay of planar and spiral magnetic ground states [122], and promising thermoelectric properties [119]. In a recent work, a novel nodal-line topological phase was proposed for several members of this family based on the first-principles electronic structure calculations [174].

The compound TiNiSi has a orthorhombic symmetry (Space group Pnma, Pearson symbol oP12) as shown in Fig. 4.1a. The structure consists of corrugated 2D sheets of edge-sharing Ni_3Si_3 hexagonal rings stacked along the a–axis (Fig. 4.1b and 4.1d) of the orthorhombic unit cell. When viewed along the b–axis, a distinctive chair-shaped ... Si–Ni–Si–Ni ... framework running parallel to the a–axis with Si–Ni–Si bond angle close to 110° can be seen (see Fig. 4.1(c)). A similar structural architect in SnSe has been argued as one of the factors responsible for its ultralow thermal conductivity [232]. In the TiNiSi structure, while the Ti atoms are five-fold coordinated by Si, the coordination of Ni atoms is four-fold, forming a distorted NiS_4 tetrahedron (Fig. 4.1a).

The quest for high-performance thermoelectric materials in this family has recently led to several high-throughput computational studies to evaluate their potential as efficient thermoelectrics [57, 18, 42, 150, 12]. In several of these studies,

the MTX compounds have been identified with the cubic half-Heusler (hH) structure, and promising thermoelectric properties have been predicted, including a high power factor of 400 μW cm^{-1} K^{-2} (p-type) and 650 μW cm^{-1} K^{-2} (n-type) for hH NbCoSi [57]. The hH phase is often considered in such calculations as it is argued to be more stable at low temperatures. However, if the vibrational entropy is also considered explicitly, as done recently by Guo et al. [58] who considered the vibrational contribution to the Gibbs free energy in their first-principles calculations, then the hexagonal or orthorhombic phases become energetically favorable.

The experimental effort towards synthesizing and evaluating the phase stability and thermoelectric properties of these compounds has been limited so far. Recently, Huang et al. reported the thermoelectric properties of TiNiSi with V doping at the Ti site [86]. They reported a maximum thermopower of -43 μV K^{-1} at 560 K for a sample doped with 20 % vanadium. In CaAgSb, which crystallize in the same TiNiSi structure-type, a thermoelectric figure-of-merit (zT) of 0.1 was previously reported that was shown to increase dramatically to $zT = 0.7$ upon Ce doping for Ca with simultaneous Ag vacancies to retain the valence balanced condition [195]. It is therefore believed that orthorhombic MTX compounds may provide an alternative avenue for realizing efficient high-temperature thermoelectrics. Their proximity to the related higher symmetry hexagonal and cubic (hH) phases further enhances this possibility [57, 60, 58].

In this chapter, we report the electronic structure, synthesis, structural characterizations and thermoelectric properties of the compounds ZrNiSi, HfNiSi, ZrNiGe, NbCoSi and ZrNiSb. We show that all the studied compounds crystallize with the orthorohmic TiNiSi structure-type. While ZrNiSi, HfNiSi, ZrNiGe and NbCoSi (nominal valence electron count 18) form readily upon arc-melting, ZrNiSb (nominal valence electron count 19) forms but with precipitous amounts of secondary phases which can be suppressed by taking 5 % excess Zr (hereafter, for this sample we shall us 'ZrNiSb' or $Zr_{1.05}NiSb$ interchangeably).

The first principles electronic band structure calculations reveal that these compounds are semimetals with a pseudogap in their density of states except ZrNiSb, which appears more metal-like with a substantially large hole Fermi surface compared to that due to electrons. While the Fermi level (E_F) is located slightly above the pseudogap in ZrNiX (X = Si, Ge) and HfNiSi with electrons as the majority carriers, it is located below the pseudogap in NbCoSi, where the majority carriers are holes. The sign of experimentally measured Seebeck coefficient is found to be in agreement with this assessment. The measured electrical conductivity (σ) of our samples near 300K ranged from $\approx$ 1000Scm^{-1} (ZrNiSi) to $\approx$ 4000Scm^{-1} (ZrNiSb). These values are intermediate between those of degenerate semiconductors and metallic alloys, in line with their semimetallic behavior inferred from the first-

principles calculations. The thermal conductivity (κ) of these samples is found to be generally low, varying from $\approx 15\text{Wm}^{-1}\text{ K}^{-1}$ (ZrNiSi) to as low as $\approx 4\text{Wm}^{-1}\text{ K}^{-1}$ (ZrNiSb) near 300K. The lattice thermal conductivity (κ_l) of ZrNiSb, in particular, is found to be very low ($\sim 1\text{Wm}^{-1}\text{ K}^{-1}$) near 300K despite its highest electrical conductivity.

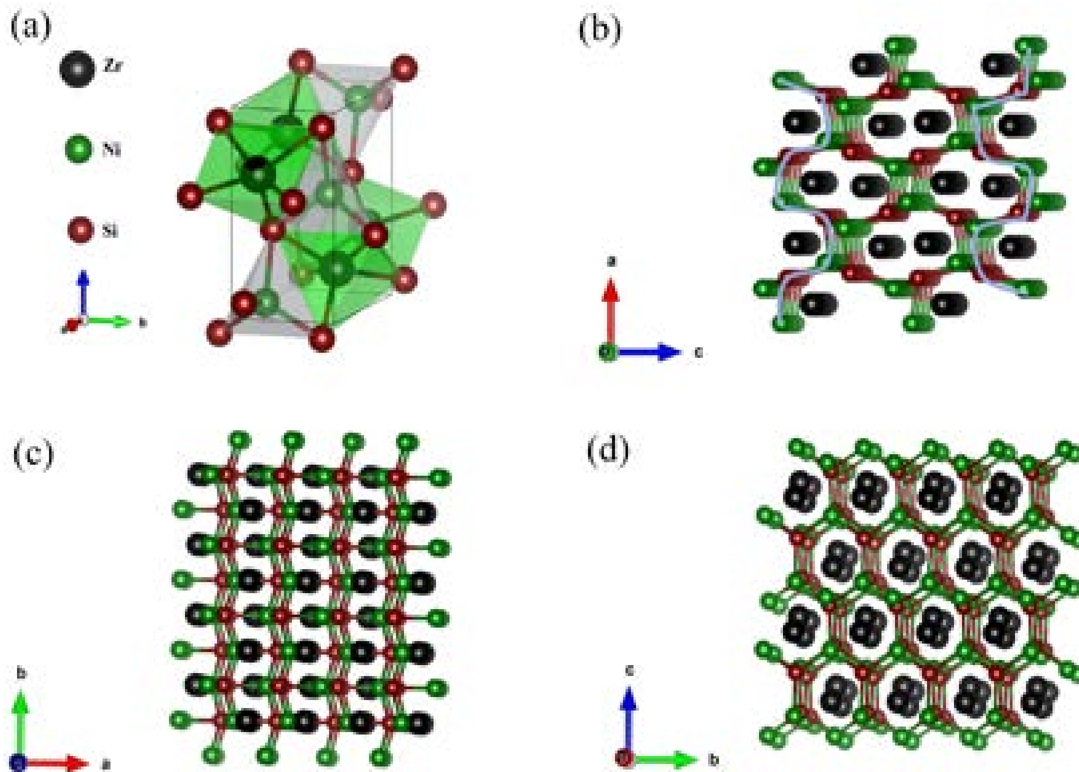

Figure 4.1: Crystal structure of TiNiSi structure-type ZrNiSi. (a) Orthorhombic unit cell showing the coordination of Zr and Ni by the Si. The crystal structure as viewed along the: (b) *b*–axis, (c) *c*–axis, and (d) *a*–axis is shown (see text for details).

4.2 Experimental details

Samples were synthesized using the arc-melting technique under a high-purity argon gas. Stoichiometric amounts of Zr (Sigma Aldrich, $\geq$ 99%), Nb (Sigma Aldrich, $\geq$ 99.9%), Co (Sigma Aldrich, 99.5%), Ni (Sigma Aldrich, $\geq$ 99.9%), Si (Sigma Aldrich, 99.5%), Sn shots (Sigma Aldrich, 99.8%), Hf pieces (Sigma Aldrich,99.7% trace metal basis) and Sb shots(Alfa Aesar, $\geq$ 99.999%) were used. The starting precursors were weighed according to the required stoichiometry and loaded on the water cooled copper hearth of the arc-furnace. The chamber was evacuated and purged with a high-purity argon gas repeatedly for several times before striking the arc. A zirconium getter was used to absorb any remnant oxygen in the chamber. The

ingot was flipped over and re-melted five to six times to ensure a good homogeneity. For the synthesis of ZrNiSi, ZrNiGe, HfNiSi and NbCoSi, the starting precursors were taken in the molar ratio 1 : 1 : 1. In the case of ZrNiSb, a total of *six* samples with nominal composition $Zr_{1-x}NiSb$ ($x = -0.05, 0, 0.05, 0.1, 0.15$ and 0.25) were synthesized. In each case, approximately 10% extra Sb was added to compensate for the Sb loss during melting. The amount of excess Sb to be added was estimated by weighing the ingot before and after arc-melting at a fixed power and for a fixed duration. The arc-melted ingot of $Zr_{1.05}NiSb$ (or 'ZrNiSb'), which is the only sample that forms as nearly single-phase, was cut into two parts. The smaller part was crushed into fine powder by hand-grinding in air using an agate mortar and pestle, and subsequently pelletized using a KBr press. The pressed pellet was annealed at 900°C for 6 days in a vacuum-sealed quartz tube coated inside with a thin layer of carbon to avoid the pellet from reacting with silica. The physical properties were measured only on the as-melted sample. For this purpose, the arc-melted ingots were cut using a low-speed diamond saw (South Bay, USA) into a disc shaped specimen for the measurement of thermal conductivity, and rectangular bar shaped specimen for resistivity and thermopower.

To check the phase formation and presence of secondary phase(s), if any, powder X-ray diffraction was done at various stages of the sample synthesis (Bruker, D8 Advance). The lattice parameters were obtained by least-square refinement using the UNITCELL program. Polished specimens cut from the as-melted ingots were also examined using a Field Effect Scanning Electron microscope (FESEM) (Ultra Zeiss plus), equipped with an Energy Dispersive X-ray (EDX) analysis attachment (Oxford Instruments). The resistivity and thermopower were measured simultaneously using the Linseis LSR-3 set-up. The average uncertainties in these measurements is less than 5%. The thermal diffusivity (D) was measured using the Linseis LFA-1000 instrument on polished discs that were homogeneously coated with a very thin layer of graphite. The average uncertainty in thermal diffusivity using this set-up is near 5 %. Thermal conductivity (κ) was obtained from the thermal diffusivity by the formula $\kappa = D\ \rho C_{\mathrm{p}}$ where ρ is the mass density, and C_{p} is the specific heat for which we used the value corresponding to the Dulong-Petit limit ($3nR = 74.8 Jmol^{-1}\ K^{-1}$). While this may be a little overestimation, especially near room-temperature, we used this to get an upper bound on κ. For mass density, we used the sample dimensions and sample mass both of which were reasonably accurately accessible. The arc-melted ingots were free of micorpores as revealed in the electron and optical microscope images of the polished specimens. The mass density is estimated to be close to 95% for all the samples. The $Zr_{1.05}NiSb$ specimen turned porous after the annealing treatment, however, the physical properties were measured only for the as melted sample. HRTEM (JEOL JEM 2200FS 200 kev)

was used to collect high-resolution images and for obtaining SAED patterns with GMS-3 software package to assess the crystallinity of our samples. For examining the sample under the HRTEM, a piece of ingot was hand grinded into a fine powder, which was transferred onto a TEM Cu grid in an ethanol based solution that was oven dried at 50°C for close to an hour. The Cu grid was subsequently loaded on the TEM sample stage and plasma cleaned at 250 eV for about 15 minutes.

4.3 Result and discussion

4.3.1 Structural characterization

ZrNiSi, HfNiSi, ZrNiGe and NbCoSi

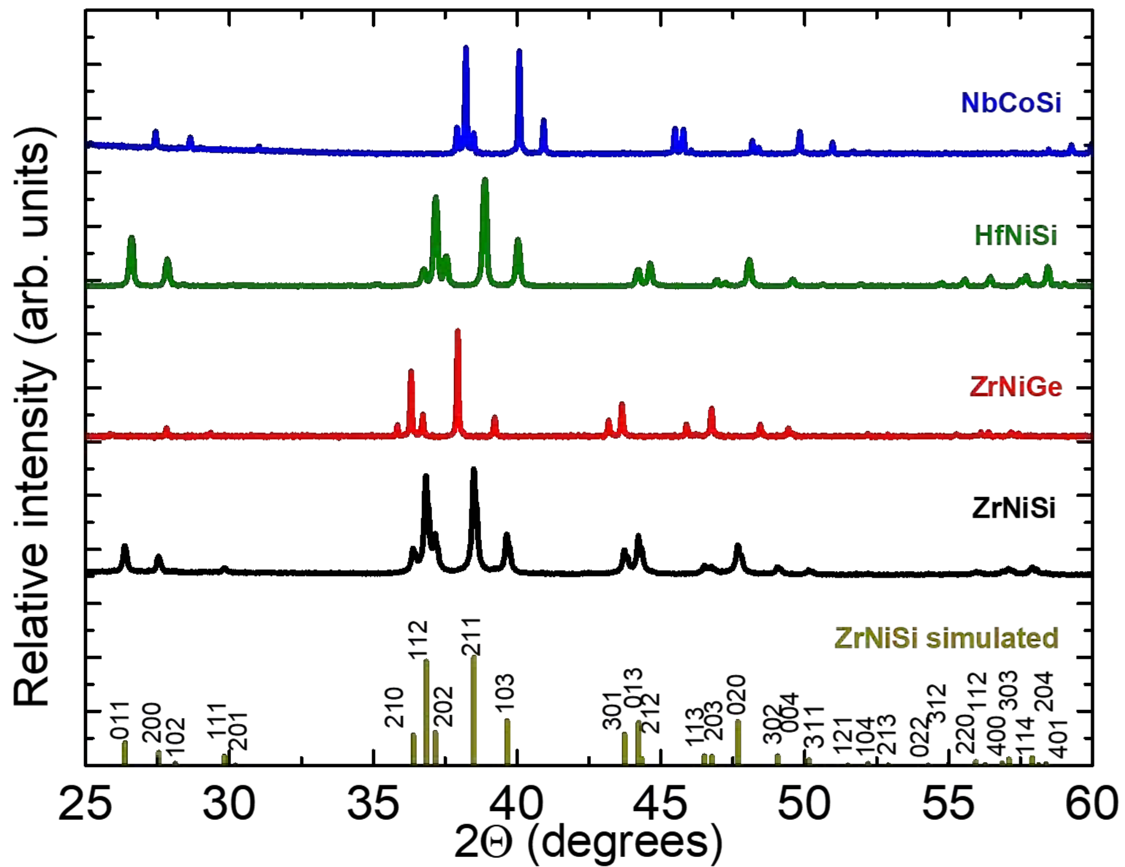

Figure 4.2: Powder X-ray diffraction pattern of arc-melted ZrNiSi, ZrNiGe, HfNiSi and NbCoSi samples . A simulated powder X-ray diffraction pattern for ZrNiSi (TiNiSi structure-type) is also shown for comparison.

The powder X-ray diffraction patterns of our arc-melted ZrNiSe, ZrNiGe, HfNiSi and NbCoSi samples are shown in Fig. 4.2. The observed pattern can be satisfactorily indexed based on the orthorhombic TiNiSi structure-type. In particular, no trace of secondary phases could be detected in any of the patterns shown. Thus, the

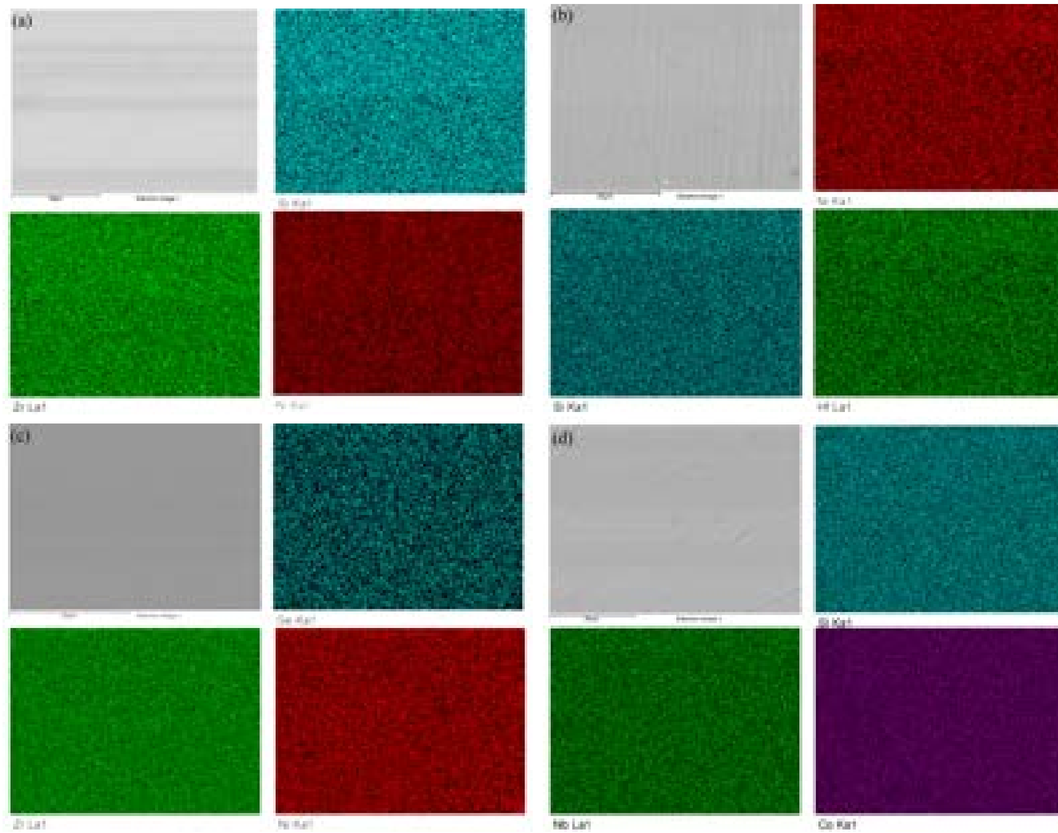

Figure 4.3: A representative FESEM image each of (a) ZrNiSi, (b) HfNiSi, (c) ZrNiGe, and (d) NbCoSi taken in the backscattering mode. The elemental chemical mapping in each case is shown using a false colour representation.

samples are single-phase within the detection limit of this technique. The lattice parameters are shown in Table. 4.1. As expected, the unit cell volume of ZrNiGe is larger than that of ZrNiSi owing to the larger ionic radius of Ge compared to Si. Between ZrNiSi and HfNiSi, the Hf analogue has smaller lattice parameters, which can be attributed to the lanthanide contraction. A similar relationship between the cell parameters of Zr and Hf analogues was previously reported for the ternary siliciates $M_2Cr_4Si_5$ (M =Ti, Zr, and Hf) [31]. NbCoSi has the smallest lattice parameter owing to a much smaller size of Nb compared to either Zr or Hf.

Few representative backscattered FESEM micrographs for each of the four samples ZrNiSi, ZrNiGe, HfNiSi and NbCoSi is shown in the Fig. 4.3. The chemical mapping for individual elements is also shown, which reflects a homogenous distribution of the constituents, corroborating their single-phase nature. The elemental molar ratio as determined using the EDX probe is $Zr_{36.0}Ni_{31.7}Si_{32.2}$, $Zr_{37.3}Ni_{31.4}Ge_{31.3}$, $Hf_{30.4}Ni_{30.4}Si_{39.1}$, and $Nb_{35.9}Co_{31.1}Si_{33.0}$.

These indicate some deviations from actual composition, which is particularly noticeable in HfNiSi whose EDX composition suggests $Hf_{1-x}Ni_{1-x}Si_{1+2x}$ to be the chemical formula with possible compositional disorder at all three crystallographic

Table 4.1: Lattice parameters of various orthorhombic MTX compounds as obtained experimentally and using the DFT calculations.

Samples	Experimental				Calculated				Reference
	a (Å)	b (Å)	c (Å)	Vol(Å^3)	a (Å)	b (Å)	c (Å)	Vol(Å^3)	
ScNiSi	6.407	4.007	6.970	178.9	-	-	-	-	[62]
TiNiSi	6.152	3.671	7.021	158.5	-	-	-	-	[100]
ZrNiSi	6.472	3.812	7.276	179.5	6.485	3.810	7.299	180.3	This work
HfNiSi	6.400	3.782	7.214	174.6	6.415	3.787	7.214	175.2	This work
ZrNiGe	6.496	3.944	7.356	188.5	6.584	3.899	7.398	189.9	This work
NbCoSi	6.141	3.761	7.073	163.4	6.239	3.657	7.051	160.8	This work
'ZrNiSb'	6.732	4.153	7.490	209.4	6.765	4.172	7.667	216.4	This work

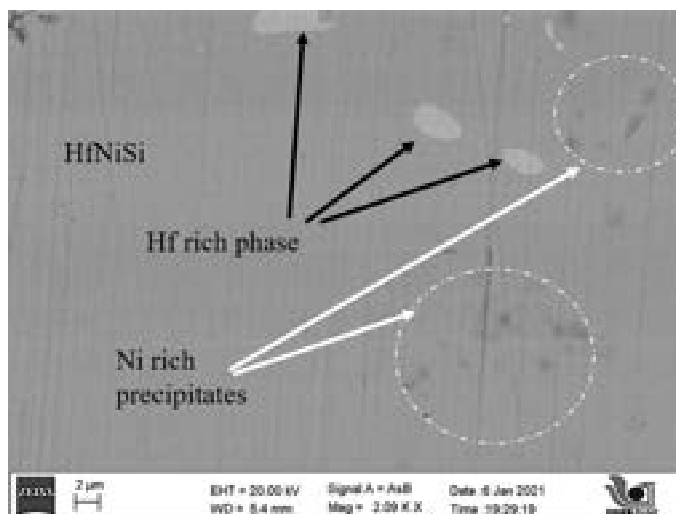

Figure 4.4: FESEM image in back scattering mode of HfNiSi

sites. It should be emphasized that even though the EDX composition of HfNiSi is close to 3 : 3 : 4, the powder X-ray diffraction confirms that the crystal structure is still orthorhombic TiNiSi type as shown in Fig. 4.2. The presence of secondary Hf and Ni rich phases occasionally seen in the SEM micrographs might be related to the less Hf and Ni in the main phase (see Fig. 4.4). Since the errors associated with the EDX probe can often be large (up to 5 at. %), to get a more accurate estimate of the compositional disorder in these materials, it will be useful to perform inductively coupled plasma mass spectrometry (ICP-MS).

A low-resolution TEM image of a ZrNiSi micrograin, on which further analysis is done, is shown in Fig. 4.5a. A high-resolution TEM image is shown in panel b. One can clearly see neatly lined-up lattice planes which indicate a high-crystallinity of our sample. A fast fourier transform (FFT) image is shown as an inset, where the *hkl* indices of some of the diffraction spots is also labeled. In Fig. 4.5c, the selected area electron diffraction (SAED) pattern is shown, which is similar to the FFT image. The diffraction spots observed in SAED are rather sharp, which corroborates the high crystallinity of the sample.

ZrNiSb

In analogy with the hH compounds, the compounds ZrNiSi, HfNiSi, ZrNiGe and NbCoSi can be thought of as having a formal valence electron count (VEC) of 18 where the closed-shell electronic structure typically results in a semiconducting behavior within the Zintl concept. On the other hand, ZrNiSb has a formal VEC of 19 (VEC = 4 (Zr) + 10 (Ni) + 5 (Sb) = 19). We found that when arc-melted by taking Zr, Ni and Sb in the stoichiomteric ratio (with some extra Sb to compensate for the losses during melting, see section 4.2), the orthorhombic ZrNiSb phase forms

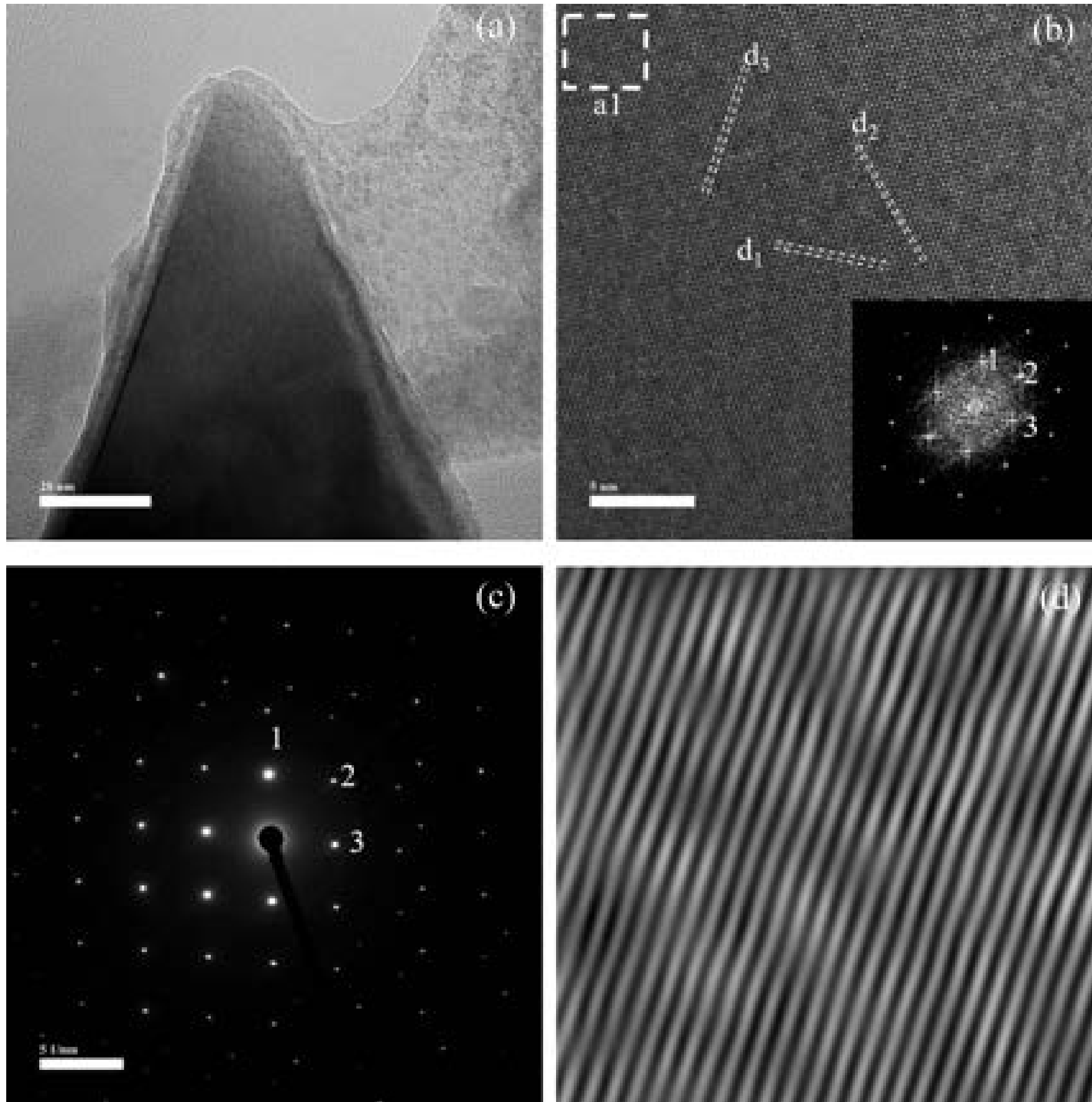

Figure 4.5: The TEM images of ZrNiSi sample: (a) a typical low-resolution TEM image showing a micrograin; (b) HRTEM image collected by focusing over a small portion of this micrograin. The dashed lines indicate some representative lattice planes: (103), (121) and (211) with interplanar spacing d_1 = 0.219nm, d_2 = 0.177nm, and d_3 = 0.237nm, respectively. The FFT is shown as an inset; (c) The SAED image showing sharp diffraction spots. The points labeled 1, 2 and 3 correspond to the lattice planes (103), (121), and (211); (d) zoomed-in IFFT of the square area marked as a1 in panel (b).

but with several parasitic phases present unlike the other four compounds where the phase formation happens readily during the arc-melting. In order to obtain a phase pure ZrNiSb, attempts were made by changing the starting Zr composition (to change the VEC). Thus, six different alloys with varying starting Zr stoichiometry were arc-melted.

The powder X-ray diffraction pattern of our $Zr_{1-x}NiSb$ samples is shown in Fig. 4.6, where the simulated patterns for ZrNiSb based on TiNiSi structure-type is also

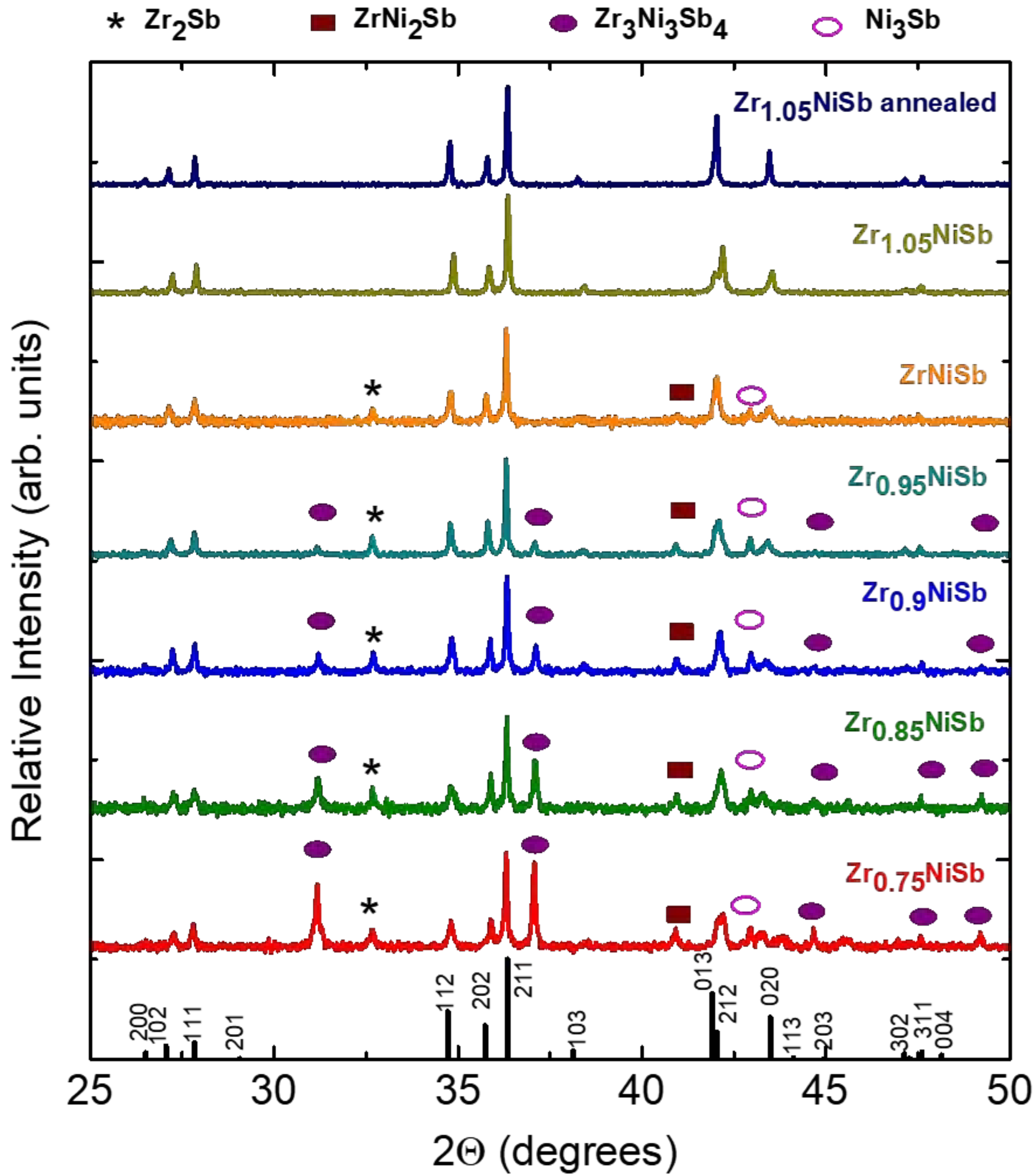

Figure 4.6: The powder X-ray diffraction pattern for various arc-melted $Zr_{1-x}NiSb$ (x = -0.05, 0, 0.05, 0.1, 0.15 and 0.25), and the annealed $Zr_{1.05}NiSb$ are shown. The simulated pattern for the main ZrNiSb phase (TiNiSi structure-type) is also shown. The peaks due to secondary phases $ZrNi_2Sb$, $Zr_3Ni_3Sb_4$,Zr_2Sb and Ni_3Sb are also labeled.

shown. The X-ray pattern of stoichiometric ZrNiSb ($x = 0$) shows, besides peaks due to the main phase, extra peaks which can be attributed to the secondary phases Zr_2Sb and $ZrNi_2Sb$. Upon decreasing the quantity of Zr in the starting precursors ($x = 0.05$ and 0.1), the diffraction pattern remains nearly unchanged but the intensity of peaks due to secondary phases grew stronger; and a new secondary phase, namely, $Zr_3Ni_3Sb_4$ also emerged. Attempts to purify these samples by annealing at 900 $°C$ for 6 days rather increased the $Zr_3Ni_3Sb_4$ phase further at the expense of

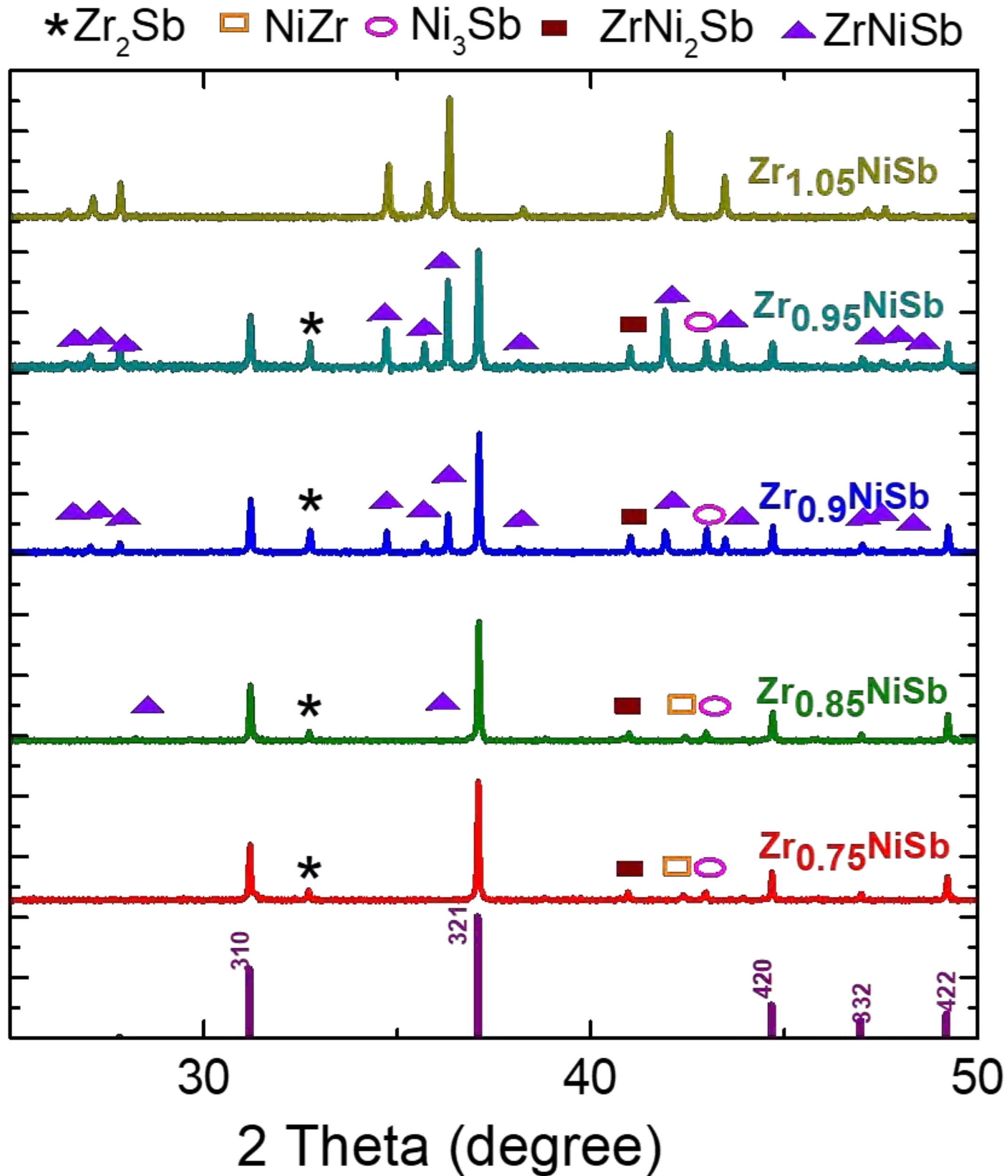

Figure 4.7: The powder X-ray diffraction pattern for various arc-melted $Zr_{1-x}NiSb$ (x = -0.05, 0.05, 0.1, 0.15, 0.25). The simulated pattern for the main $Zr_3Ni_3Sb_4$ phase (TiNiSi structure-type) is also shown. The peaks due to secondary phases $ZrNi_2Sb$, ZrNiSb, Zr_2Sb and Ni_3Sb are also labeled.

the ZrNiSb phase. We also arc-melted a sample corresponding to the stoichiometry $Zr_{0.75}NiSb$ which should have a formal VEC of 18; this was done to check if it mimics the behaviour of VEC 19 compound NbCoSb, which forms as a single phase when Nb concentration is close to 0.8 [222]. We found that $Zr_{0.75}NiSb$ also does not form as a single phase sample, which, in a way, corroborates Landrum et al. [100] who suggested that the Zintl concept does not hold for these orthorhombics. On the other hand, we find $Zr_{1.05}NiSb$ to be nearly phase pure. The X-ray diffraction pattern of

our arc-melted sample shows only one small extra peak due to some unidentified phase near 42°, adjacent to the twin (013)/(212) peak of the main phase. However, upon annealing at 900°C for 6 days even this extra peak disappeared, resulting in a phase pure sample.

We have done annealing experiments on other samples with different Zr stoichiometry, these sample are shown in Fig. 4.7. The sample with stoichiometry $Zr_{0.75}NiSb$, $Zr_{0.85}NiSb$, $Zr_{0.9}NiSb$ and $Zr_{0.95}NiSb$ forms in primarily cubic $Zr_3Ni_3Sb_4$ phase with increasing orthoerhombic ZrNiSb phase as secondary phase. Finally, we observe $Zr_{1.05}NiSb$ as pure orthorhombic TiNiSi-phase.

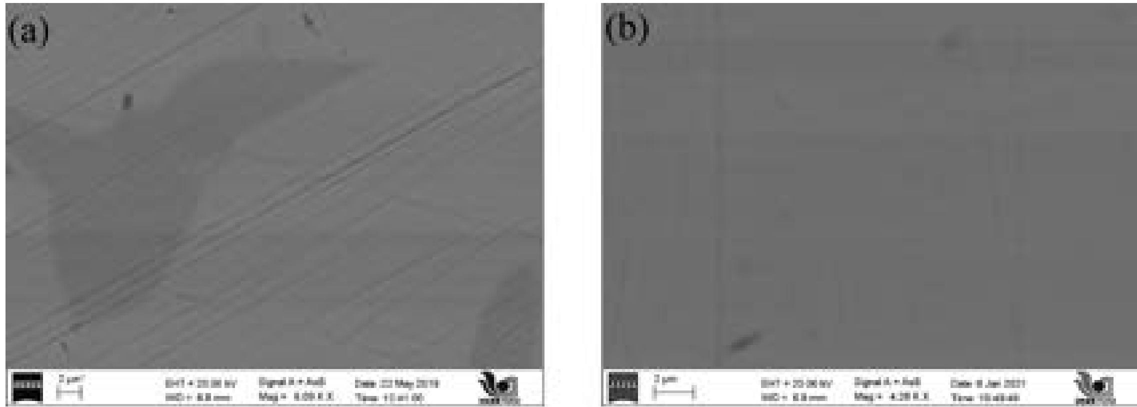

Figure 4.8: A representative FESEM image each of ZrNiSb (left), and $Zr_{1.05}NiSb$ (right) collected in the backscattering mode. The dark grey regions in the image on the left are due to the impurity phase $ZrNi_2Sb$. The composition of the main matrix in both cases is close to $Zr_{1.1}Ni_{0.83}Sb$

In Fig. 4.8 representative FESEM images of arc-melted ZrNiSb and $Zr_{1.05}NiSb$ specimens are shown. The presence of secondary phase(s) in ZrNiSb are reflected in the phase contrast image where the dark grey regions are seen embedded in the matrix of the main phase whose average EDX composition was found to be $Zr_{1.1}Ni_{0.8}Sb$. The composition of the dark-grey region is $Zr_{1.1}Ni_{1.9}Sb$ which is close to that of the Heusler phase $ZrNi_2Sb$. In $Zr_{1.05}NiSb$, on the other hand, a much smaller precipitation is observed. The average composition of the main phase in this case is $Zr_{38.3}Ni_{27.8}Sb_{33.9}$. From these observation we can infer that the desired orthorhombic phase forms with nearly 5 % excess Zr. It may be that some or all of this excess Zr resides at the Ni site. A chemical map for the the elements Zr, Ni and Sb in $Zr_{1.05}NiSb$ is shown in the Fig. 4.9 which suggests a homogeneous distribution of these elements.

Some representative HRTEM images of a $Zr_{1.05}NiSb$ sample are shown in Fig. 4.10. As shown in panel (b), regions with well-defined arrays of lattice planes (one such region labeled a2 is shown) are interspersed by regions with defects (one such region labeled a1 is shown). The high crystallinity of region such as a2 is corroborated by the presence of sharp diffraction spots in the SAED image shown as an

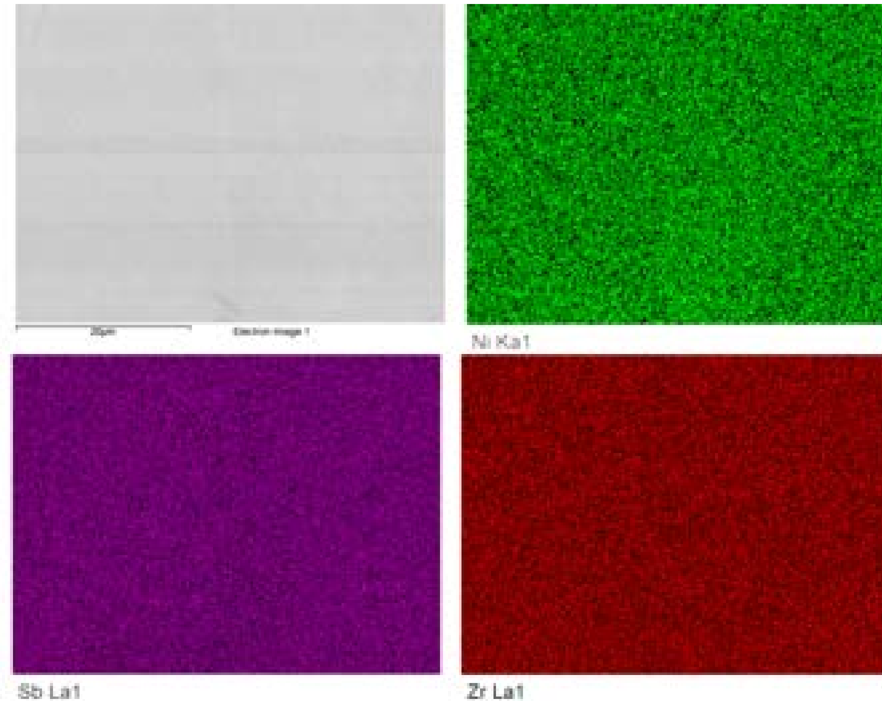

Figure 4.9: Chemical mapping of $Zr_{1.05}NiSb$, false colour map to show homogeneity of the sample

inset. In panel (c), the Inverse Fast Fourier Transform (IFFT) image of regions a1 is shown. The presence of high density of stacking faults due to merging or termination of the lattice planes can be clearly seen. In a similar image in panel (d) of region a2 such defects are not seen.

4.3.2 Electronic structure calculations

In order to understand the electronic properties of these compounds we have performed DFT based calculations with Dr. Prasenjit Ghosh (IISER Pune).The computed lattice parameters are in good agreement with the experimental values (see Table 4.1). In typical hH, in the T–X network, each T is bound tetrahedrally with X and vice-versa. These tetrahedrons are ideal with the four T–X bonds of equal length. However, for the MTX compounds considered in this study, we find that the T–X tetrahedrons are highly distorted (see Fig. 4.11); for each case, of the four T–X bonds, the two shortest bonds are of equal length but the two longer bonds have different bond lengths. The T–X bond lengths for the different compounds are listed in the Table T1 in the 4.2.

A comparison of the bond lengths between ZrNiSi and ZrNiGe where one is moving down the periodic table with respect to X, we observe that all the T–X bond lengths increase. In contrast, when Zr is replaced with Hf in ZrNiSi, we observe that the two shortest T–X bonds have similar lengths (2.36 Å in ZrNiSi vs. 2.35 Å in

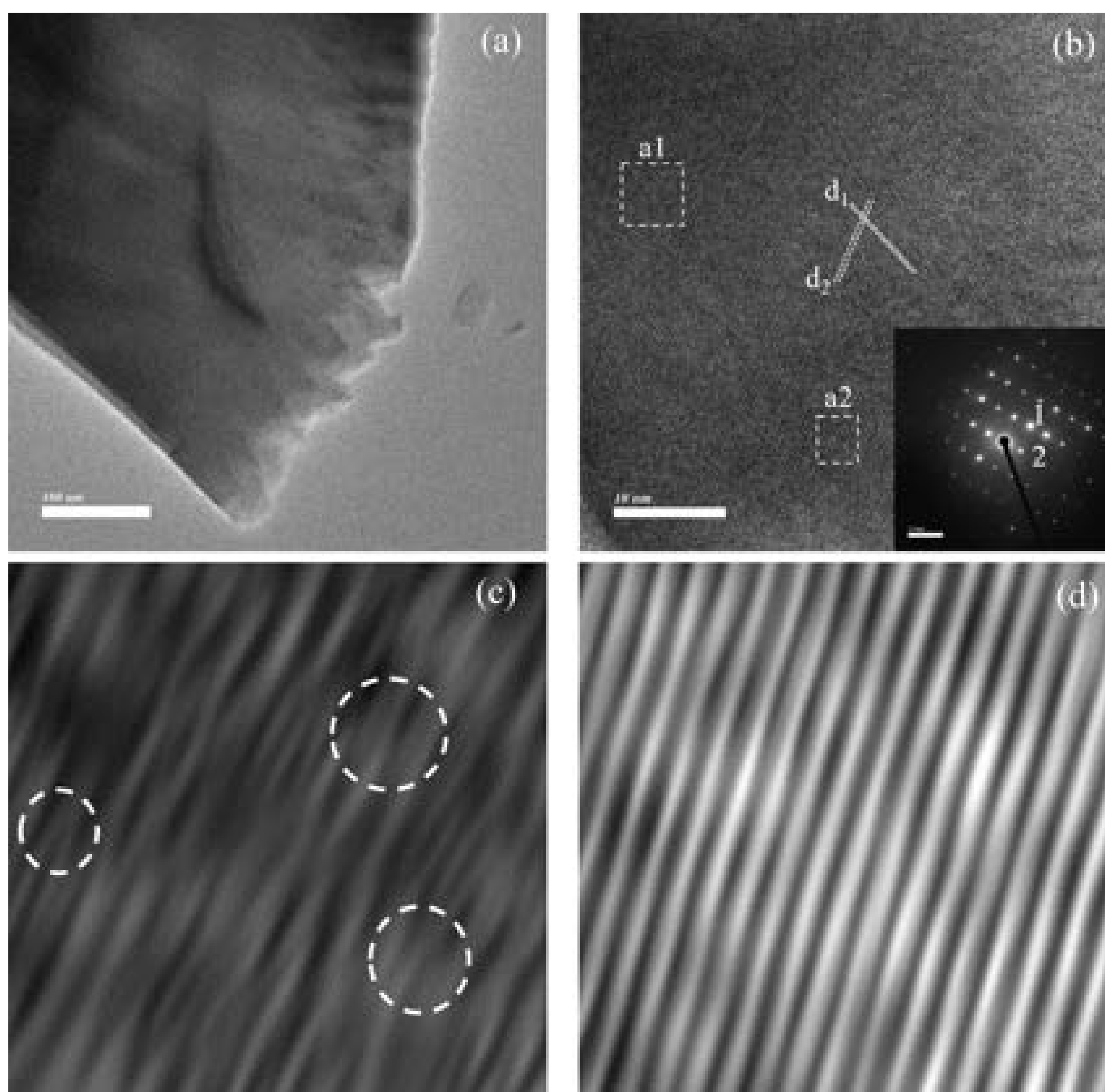

Figure 4.10: The TEM images of a $Zr_{1.05}NiSb$ sample: (a) a low-resolution TEM image of a micrograin; (b) HRTEM image taken by focusing the electron beam on a small region of this micrograin. The lattice planes (013) and (011) are shown with interplanar spacing $d_1 = 0.22$nm(013) and $d_2 = 0.36$nm(011). The SAED image is shown as an inset where the points labeled 1 and 2 correspond to the lattice planes (011) and (013); (c) and (d) zoomed IFFT of the areas shown with white dashed lines marked as a1 and a2 respectively in panel (b), circles have been drawn to show some of the stacking faults in the region a1 which are present in high density as compared to region a2.

HfNiSi) while the length of the other two long bonds has been reduced. In order to understand the nature of the bonding between the different elements, we have plotted the electron density isosurfaces. The isosurfaces for ZrNiSi and NbCoSi as representatives are shown in Fig. 4.12, while those of the other compounds are given in the Fig. 4.13. From these, we find that the charge density is localized primarily on the M, T and X atoms analogous to a charge density distribution usually observed in ionic compounds. However, while on M the charge density is more spherical, on

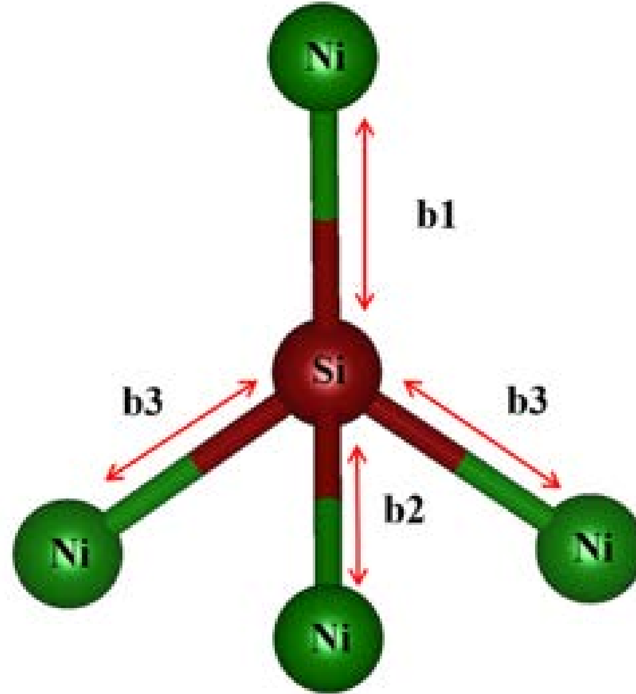

Figure 4.11: TX bonds scheme in ZrNiSi

T and X they are pointed towards each other with slight accumulation in between the T–X bonds. This directional nature of the charge density distribution on T and X, and accumulation of electron density in between the bonds suggests the covalent nature of the bonding between T and X. We note that a similar type of bonding is also observed previously for the hH alloys [130, 41, 103].

The calculated band structure along the high symmetry directions of the irreducible Brillouin zone and the density of states (DOS) along with their contributions from atomic orbitals of M, T and X are shown in Fig. 4.14,4.15 and comparison of

Table 4.2: T-X bond lengths in T-X distorted tetrahedra for different samples (Calculations done in collaboration with Dr. Prasenjit Ghosh).

T-X Bond length	b1(Å)	b2(Å)	b3(Å)
$ZrNiSi$	2.5249	2.4093	2.3607
$HfNiSi$	2.4728	2.4020	2.3542
$ZrNiGe$	2.5317	2.4928	2.4275
$NbCoSi$	2.4023	2.3171	2.2889
$ZrNiSb$	2.6305	2.5555	2.5134

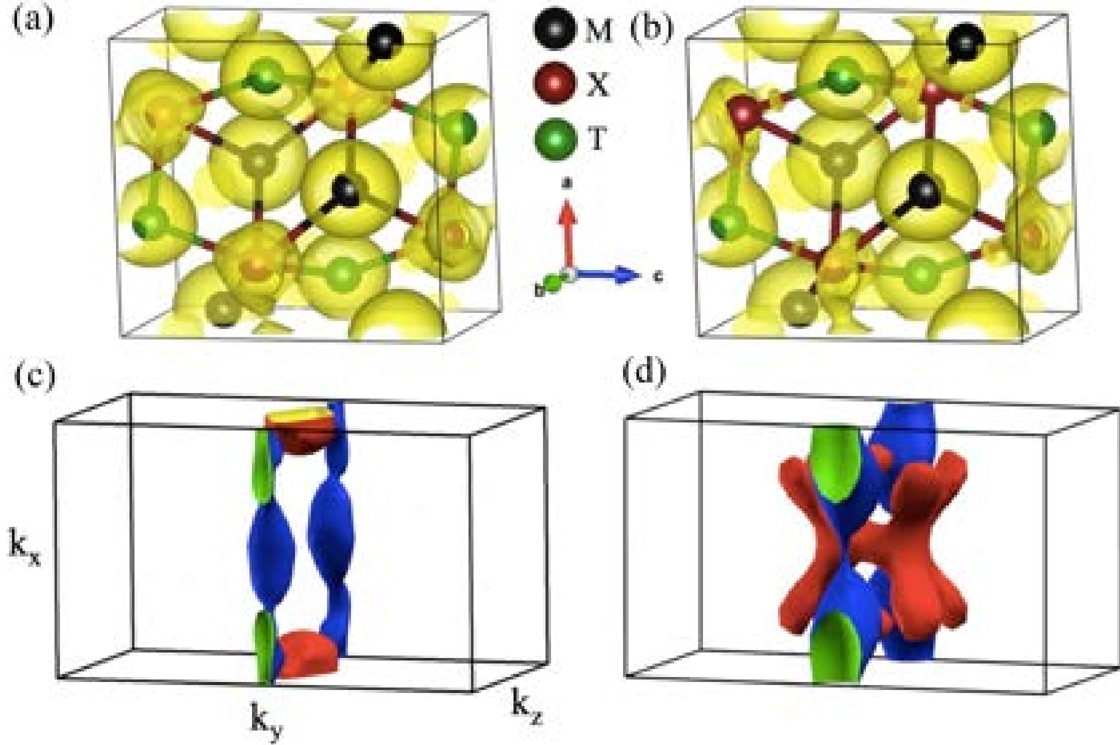

Figure 4.12: Charge density isosurfaces of (a) ZrNiSi and (b) NbCoSi. The isovalues corresponding to these plots are 0.398 and 0.438 e/$\AA^3$ for ZrNiSi and NbCoSi respectively. Fermi surface plots of (c) ZrNiSi and (d) NbCoSi. The electron and hole Fermi surfaces are shown in blue and red, respectively (Calculations done in collaboration with Dr. Prasenjit Ghosh).

the total DOS for all the studied compounds is shown in Fig. 4.16.

Our results are in good agreement with that reported in literature [174]. The electronic structure of NbCoSi, which, to the best of our knowledge, has not been reported previously is shown in Fig.4.15(d). All the compounds are metallic. Moreover all of them except ZrNiSb exhibit a pseudogap-like feature near the Fermi energy (E_F) with a gap size of about 0.1 eV, which is comparable to that previously reported for TiNiSi [86]. The absence of the pseudo-gap in ZrNiSb is due to the extra p–electron added by Sb to the NiSb sublattice, without adding any additional states. As a consequence, E_F is pushed up above the pseudogap resulting in a relatively large density of states at E_F, thereby making this system unstable as is evident from the lack of a stoichiometric sample of this compound. The band structures of ZrNiSi, ZrNiGe and HfNiSi are very similar suggesting that replacing Zr with Hf or Si with Ge, induces only minor structural changes in terms of their lattice parameters and bond lengths. These changes are not large enough to change their electronic properties significantly. Hence, we anticipate them to also exhibit similar transport properties. For these materials, at E_F we find electron and hole pockets located around the X–point and U–point of the BZ, respectively. The Fermi

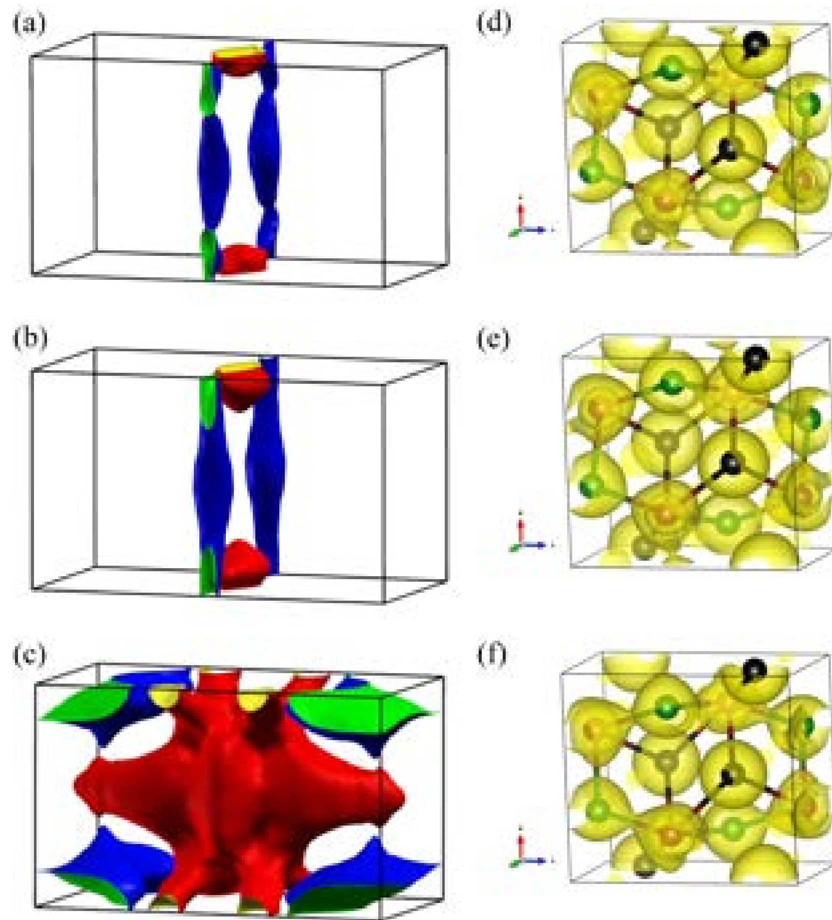

Figure 4.13: Fermi surface plots of (a) HfNiSi (b) ZrNiGe (c) ZrNiSb; Charge density isosurfaces of (d) HfNiSi (e) ZrNiGe (f) ZrNiSb, where the isovalues corresponding to these plots are 0.398, 0.344 and 0.351 $e/\mathring{A}^3$ for HfNiSi, ZrNiGe and ZrNiSb respectively (Calculations done in collaboration with Dr. Prasenjit Ghosh)

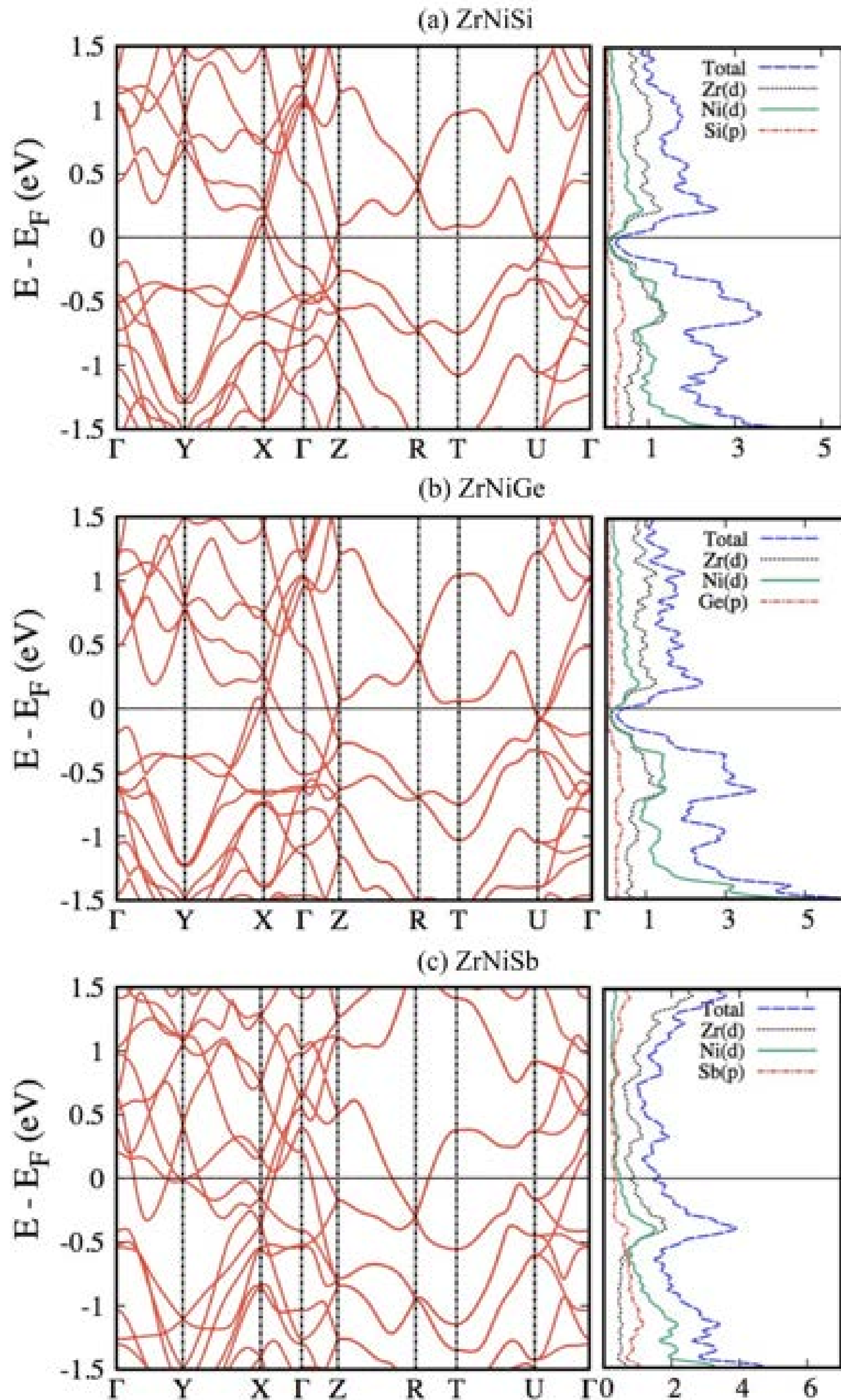

Figure 4.14: Band structure and DOS plots of (a) ZrNiSi, (b) ZrNiGe, (c) ZrNiSb (Calculations done in collaboration with Dr. Prasenjit Ghosh).

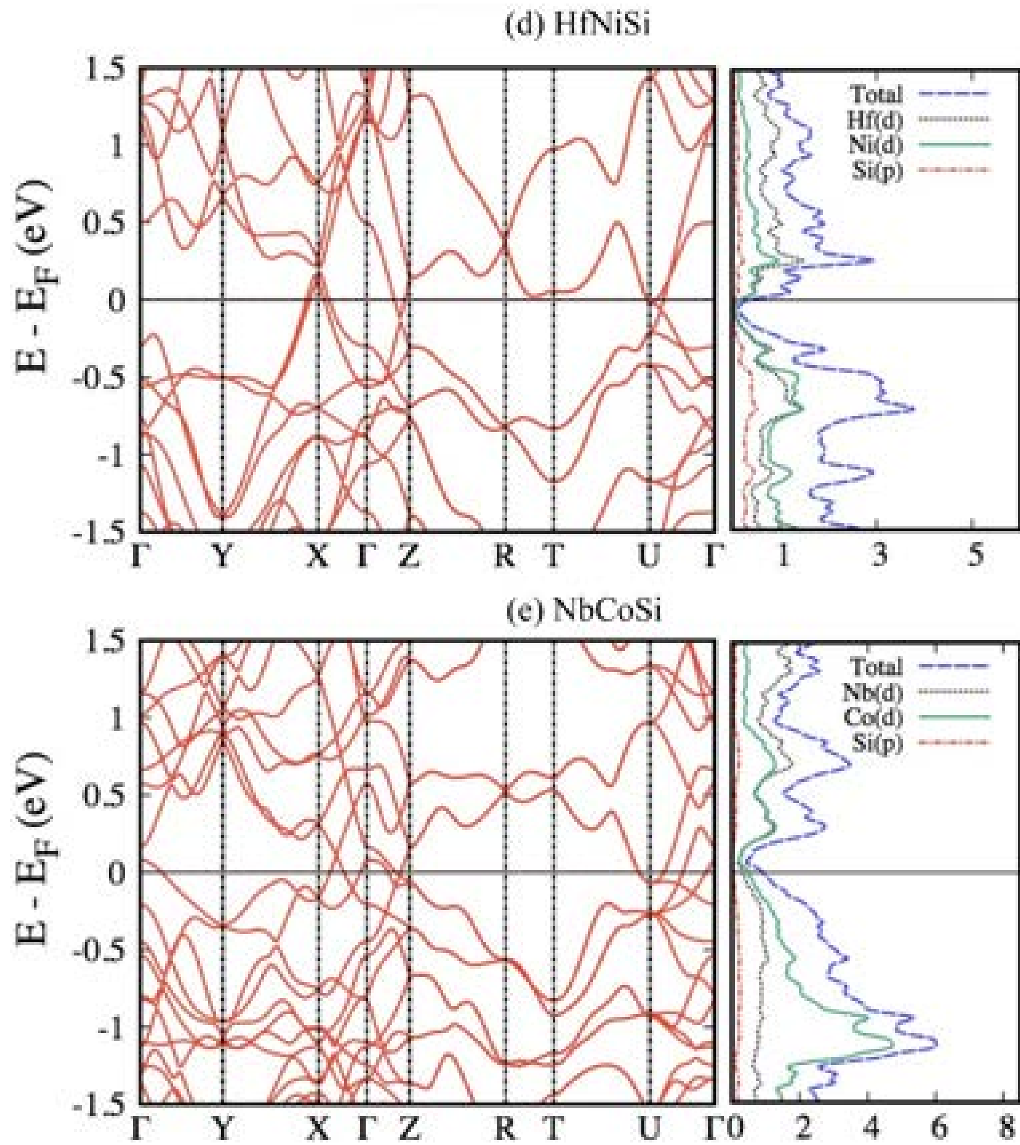

Figure 4.15: Band structure and DOS plots of (a) HfNiSi, (b) NbCoSi. (Calculations done in collaboration with Dr. Prasenjit Ghosh)

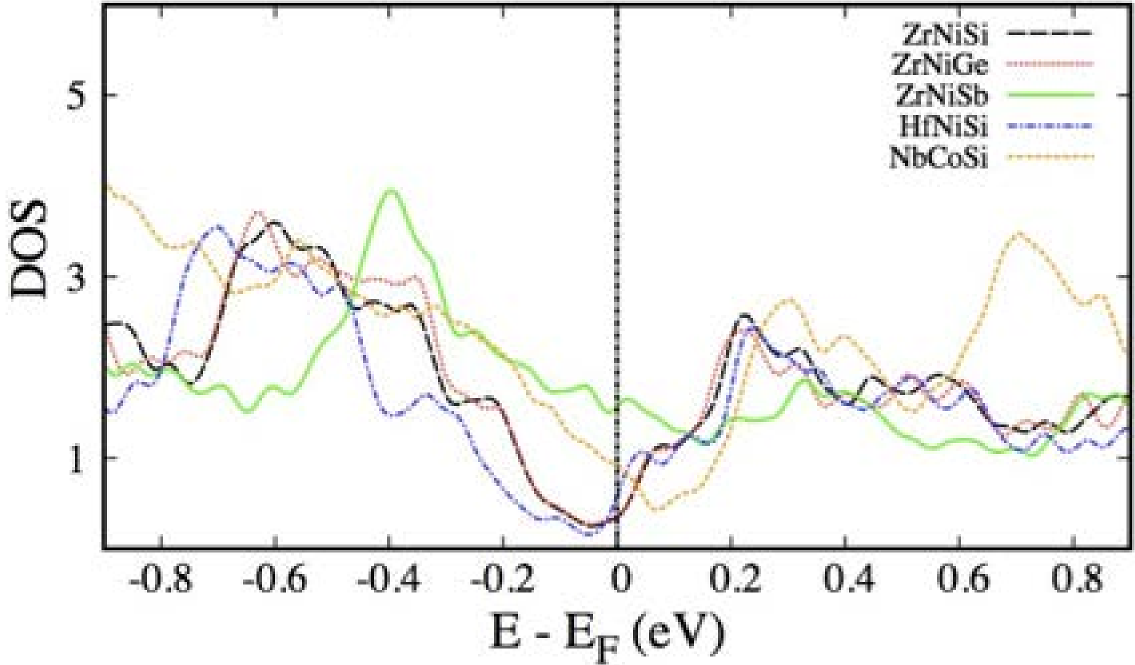

Figure 4.16: Comparison of the total DOS for the five compounds: ZrNiSi, ZrNiGe, ZrNiSb, HfNiSi, NbCoSi. (Calculations done in collaboration with Dr. Prasenjit Ghosh)

surface for ZrNiSi is shown as a representative case in Fig. 4.12(c). Our calculations suggest that in these materials electrons will be the majority carriers. In contrast, in NbCoSi we observe large hole-pockets at Γ point along the lines $\Gamma - Z$ and $\Gamma - X$, and electrons pockets near U–point of the BZ. The Fermi surface is shown in Fig. 4.12(d). In this case the hole pockets (red) are significantly larger than the electron pockets (blue). The Fermi energy is below the pseudogap and the holes will be dominant carriers in this case.

In order to understand the difference between the positions of E_F in ZrNiX (X = Si, Ge) and NbCoSi, though both are isoelectronic, it will be instructive to look into the hybridization of the atomic orbitals. Fig. 4.17 (a) and (b) shows the DOS projected onto the d orbitals of Zr/Nb, d orbitals of Ni/Co and the p orbitals of Si. Depending on the interactions between the atoms, the DOS can be divided into five regions for simplicity (see Fig. 4.17). The nature of hybridization between the atomic orbitals in each region can be understood from the integrated local DOS (ILDOS) isosurfaces, which are shown for each region in Fig. 4.17. As shown, in region I and II the electronic states result primarily from the hybridization of the Ni/Co d states with the p states of Si, resulting in bonding orbitals. In region III, IV and V, the dominant contributions come from the d states of Zr/Nb and Ni/Co. While in region III, the wavefunctions have larger weight on Ni (Co) atoms than on Zr (Nb) atoms in ZrNiSi (NbCoSi); the reverse is true for region V. In contrast, in region IV, Zr (Nb) and Ni (Co) have similar contributions. In this energy window

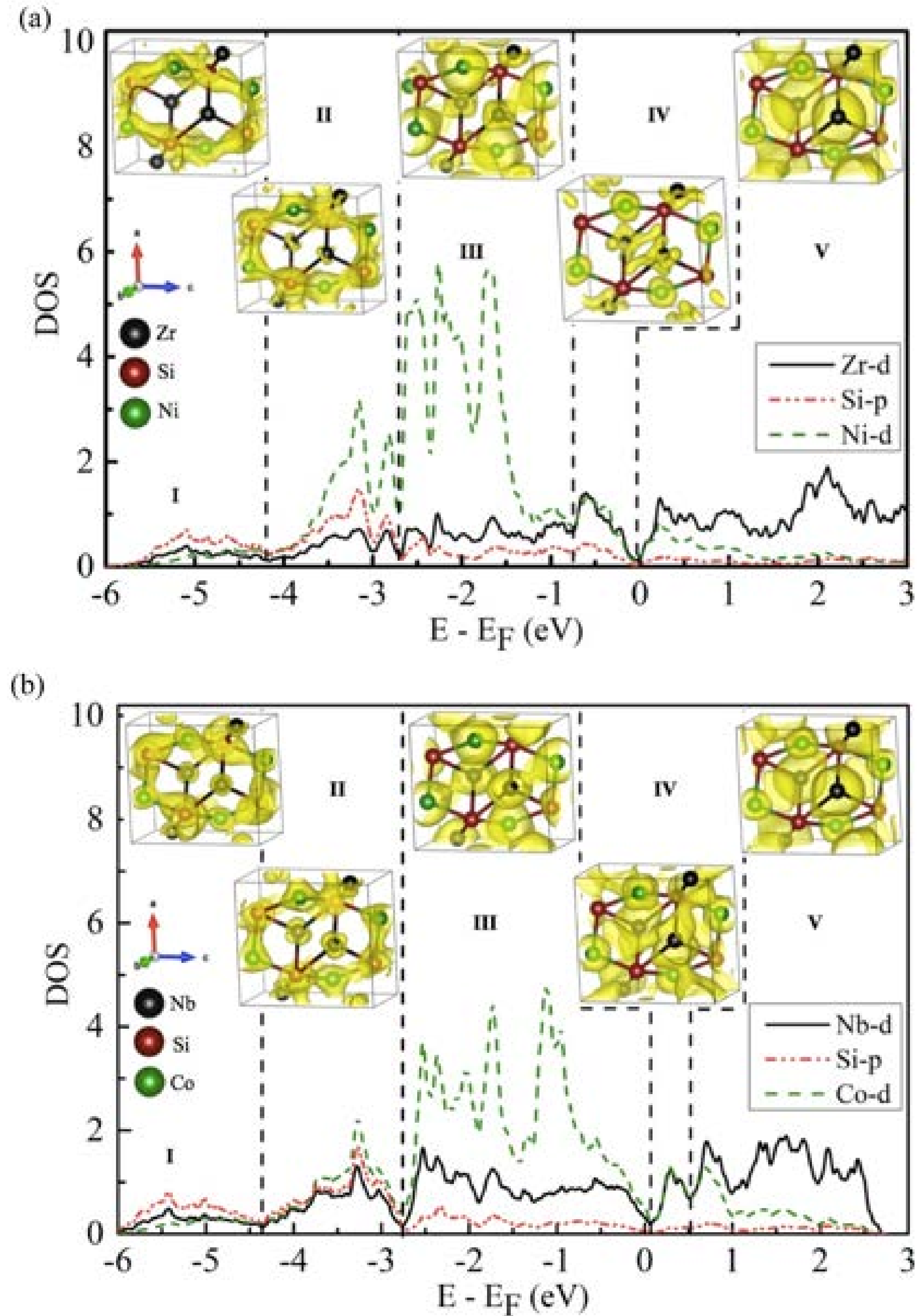

Figure 4.17: DOS projected onto the Zr/Nb and Ni/Co d–states and Si p–states in (a) ZrNiSi and (b) NbCoSi. In each panel, the projected DOS has been divided into five regions. The ILDOS isosurfaces showing the hybridization of the atomic orbitals in each region for the two compounds are shown in the inset. The isovalues corresponding to these plots vary between 0.0121 to 0.162 e/$\mathring{A}^3$. (Calculations done in collaboration with Dr. Prasenjit Ghosh)

some hybridization between Nb/Zr d states and Si p orbitals remain as is evident from the ILDOS. We note that similar hybridization has been previously reported for the hH alloys ZrNiSn [221].

Although there are broad similarities between ZrNiSi and NbCoSi, there are also some notable differences. These are: (i) the regions I-IV are broader in NbCoSi than in ZrNiSi, (ii) in region III, the contribution from Nb d states in NbCoSi is more than Zr d states in ZrNiSi, and (iii) position of E_F is in region III top in NbCoSi, while it is in region V bottom in ZrNiSi, i.e., the states in region IV are occupied in ZrNiSi, while they are empty in NbCoSi.

The broadening of the bands in NbCoSi can be attributed to the larger overlap of the atomic orbitals. This is in accordance with significantly shorter bonds in NbCoSi compared to ZrNiSi. The difference in the Zr/Nb d states contributions in region III can be understood in terms of the Electronegativity Difference (END) between Nb–Co pair in NbCoSi (≈ 0.28), and Zr–Ni pair in ZrNiSi (≈ 0.57). Since states in region III arise from mixing of d orbitals of M and T elements, a larger END implies that the lower energy states will have larger contribution from the more electronegative element, which in the case of ZrNiSi is Ni.

Finally, the differences in the position of Fermi energy can be understood from the fact that the states in region IV arise due to the hybridization of Zr–Si and Zr–Ni in ZrNiSi (and Nb–Si and Nb–Co in NbCoSi). The ILDOS corresponding to these states (Fig. 4.17) shows that the hybridization of Zr/Nb–d states with Si-p states results in bonding type orbital. The corresponding antibonding state lies higher in energy and is not shown in the DOS in Fig. 4.17. The difference in the energy between the bonding and antibonding hybridized orbitals depends on the END between the hybridizing atoms. As END for Zr–Si and Zr–Ni pairs is more than that for Nb–Si and Nb–Co, the splitting of bonding and antibonding orbital will be more for ZrNiSi than for NbCoSi. As a result of this, in ZrNiSi (NbCoSi), region IV of DOS that corresponds to these bonding states, is closer to region III (V). Hence, these states are occupied in ZrNiSi while empty in NbCoSi resulting in the Fermi level lying at the top of region IV in ZrNISi but at its bottom in NbCoSi.

4.3.3 Thermoelectric properties

Electrical Transport

Elelctrical conductivity: Figure 4.18(a) shows the temperature variation of electrical conductivity ($\sigma(T)$). In all cases, a weak temperature dependent behavior is observed. In ZrNiSi, ZrNiGe, HfNiSi and NbCoSi (i.e, samples with a pseudogap), σ near room-temperature ranges from 1000Scm^{-1} to 2000Scm^{-1}. Above room-temperature σ decreases gradually, and with further heating it either shows a

mild upturn (as in ZrNiX for X = Si, Ge) in the range 600K − 700K, or a tendency towards saturation (as in HfNiSi and NbCoSi). The magnitude of σ and its temperature dependence in ZrNiX (X = Si, Ge) is in good agreement with that reported previously for TiNiSi [86].

In degenerate semiconductors, such as the hH compounds, the upturn in σ is typically attributed to the onset of minority charge carriers at high temperatures. On the other hand, in semimetals both types of charge carriers contribute to the electrical conduction ($\sigma = \sigma_n + \sigma_p$) at any temperature. However, as shown in section 4.3.2, the semimetals studied here not only have a pseudogap-like feature in their density of states, they also have majority carriers pockets much larger in volume compared to the minority carriers pockets (see. Fig. 4.12 and Fig. 4.13). Thus, the electrical conductivity of these samples is expected to be mainly due to the majority charge carriers assuming that the mobility μ of minority carriers is not drastically high. The decreasing behavior of σ above 300K, and up to considerably higher temperatures, indeed suggests that the minority contribution remains suppressed until sufficiently high temperatures are reached.

In the antimonide 'ZrNiSb', which has no pseudogap and where DOS at E_F is at least twice as large, σ at room-temperature ($\approx$ 4000Scm^{-1}) has been almost fourfold increased compared to ZrNiSi. The temperature dependence of σ is, however, analogous to that of ZrNiSi with minority carriers contribution leading to a shallow minimum at high temperatures.

On qualitative terms the temperature variation of σ in these samples is analogous to the hH compounds as pointed out above; however, the magnitude of σ in undoped hHs is typically of the order of 100Scm^{-1}, which is smaller than that for the compounds studied here. At the same time, σ in these compounds is at least an order of magnitude smaller than for typical intermetallic alloys and compounds [35]. Thus, the electrical conductivity of our samples is somewhere between those of degenerate semiconductors and intermetallics.

Thermopower: The temperature variation of Seebeck coefficient (S) of our samples is shown in Fig. 4.18(b). S displays a weak temperature dependence, and in agreement with the theoretical prediction, near room-temperature, S is negative for ZrNiSi, ZrNiGe and HfNiSi, and positive for NbCoSi and ZrNiSb.

For ZrNiSi, ZrNiGe and HfNiSi, the Seebeck coefficient remains negative over the whole temperature range. The average value of S for these samples ranges from 10 μVK^{-1} to 20 μVK^{-1}. NbCoSi, and 'ZrNiSb' has a small positive Seebeck coefficient at room-temperature which changes sign upon heating above $\approx$ 750 K. The weak modulations of S with temperature (as in ZrNiSi, ZrNiGe and HfNiSi) or change of sign (as in NbCoSi and 'ZrNiSb') can be attributed to the bipolar nature (i.e., the increasing contribution of the minority charge carriers with temperature).

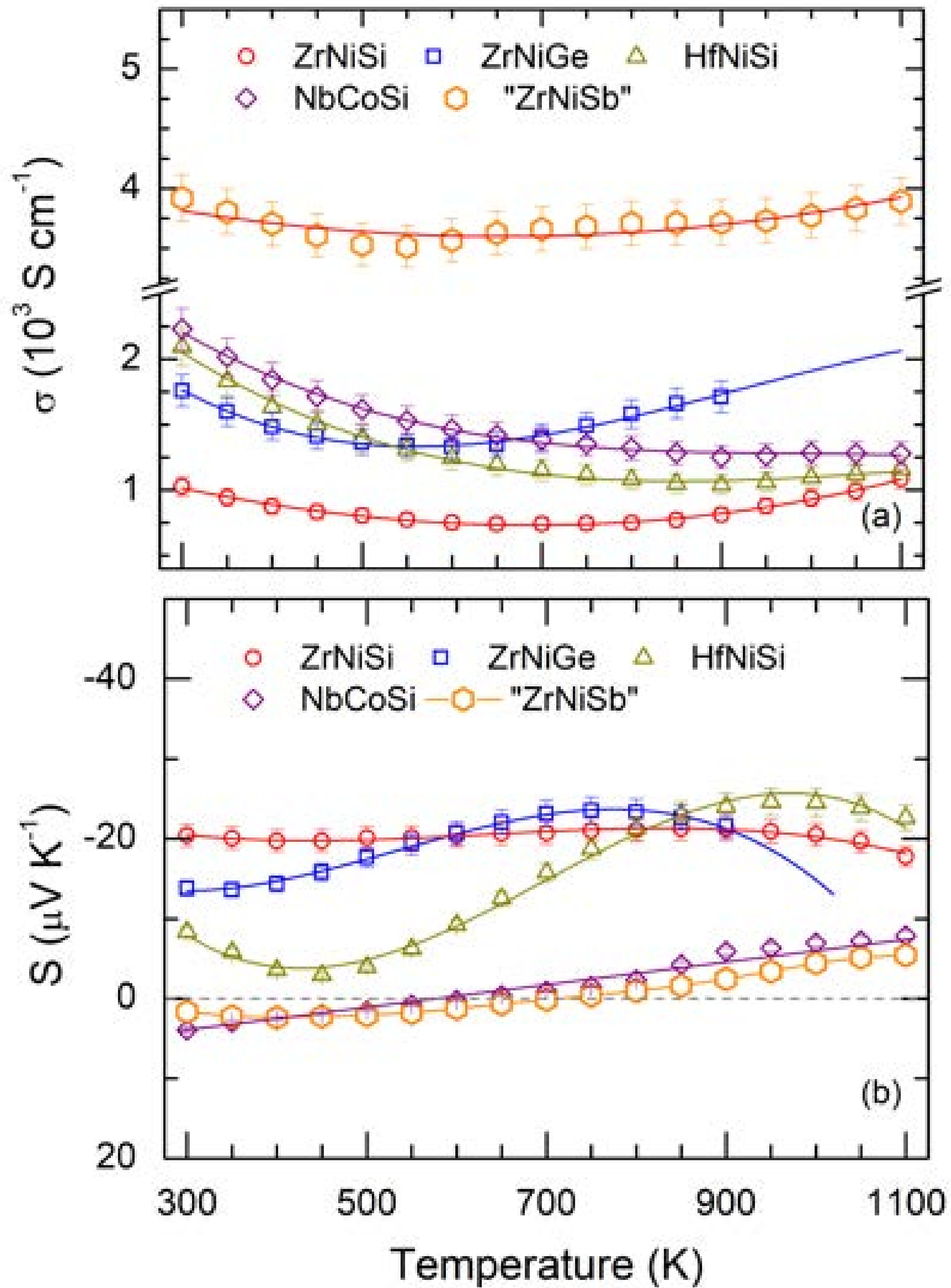

Figure 4.18: Temperature variation of (a) electrical conductivity (σ), and (b) Seebeck coefficient (S) for all the studied samples. Here, 'ZrNiSb' represents the sample with nominal stoichiometry $Zr_{1.05}NiSb$. The lines through the data points are guide to the eye.

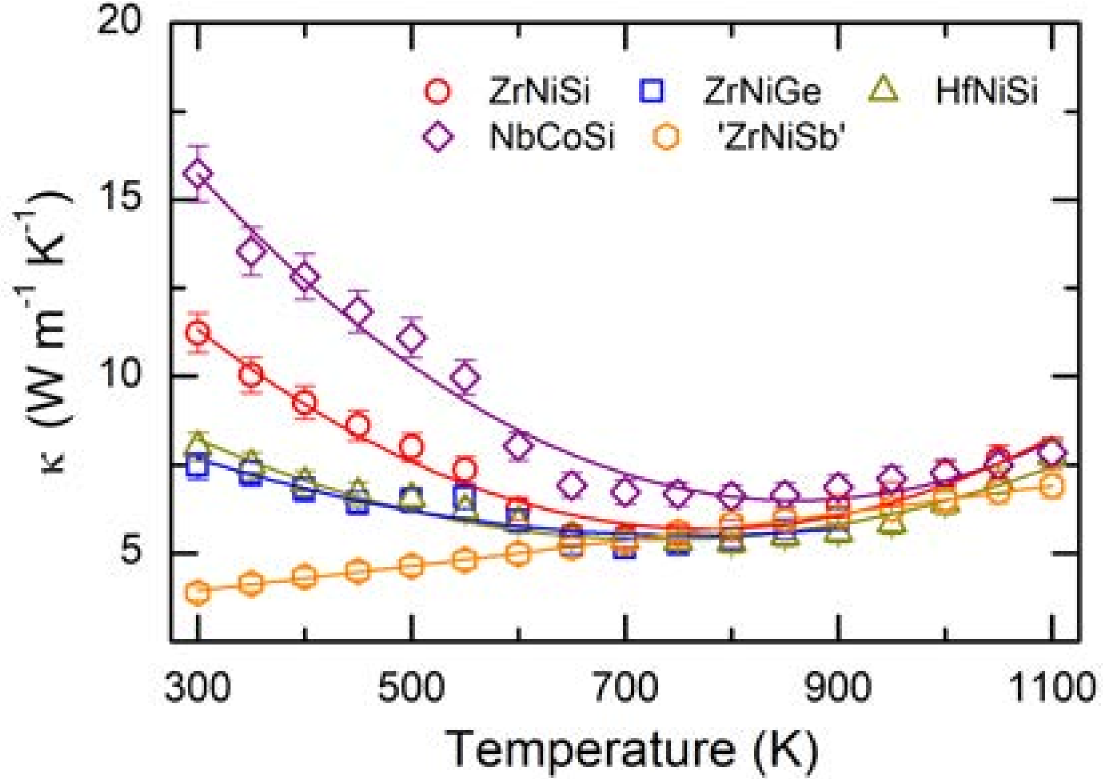

Figure 4.19: The temperature variation of thermal conductivity (κ) of the samples studied here. The legend 'ZrNiSb' corresponds to the sample with nominal composition $Zr_{1.05}NiSb$. Lines through the data points are used as a guide to the eye.

.

However, interpretation of the variation of S with temperature in a multiband system is challenging since S is a complex quantity which is sensitive to several material's parameters, including, the carrier concentration, effective mass, valley degeneracy, and the variation of the electronic density of states at E_F with energy, which itself may have some temperature dependence.

We now compare the Seebeck coefficient of these materials with the well studied hH compounds. In hH MNiSn (M = Ti, Zr and Hf), S is reported to be of the order of 100 μVK^{-1} near 300K, which is almost an order of magnitude higher than what we report here. One reason for this could be the higher electrical conductivity of our samples. However, one should also take into account the fact that hHs have a higher (cubic) crystal symmetry, which leads to a higher valley degeneracy and hence a higher value of the Seebeck coefficient. Finally, the effect of bipolarity in decreasing the average thermopower ($[S_n\sigma_n + S_p\sigma_p]/[\sigma_n + \sigma_p]$) is expected to have more severe consequences for our samples.

Thermal conductivity

The thermal conductivity (κ) of our samples is shown in Fig. 4.19. With the exception of 'ZrNiSb' or $Zr_{1.05}NiSb$, κ in all other samples decreases upon heating followed

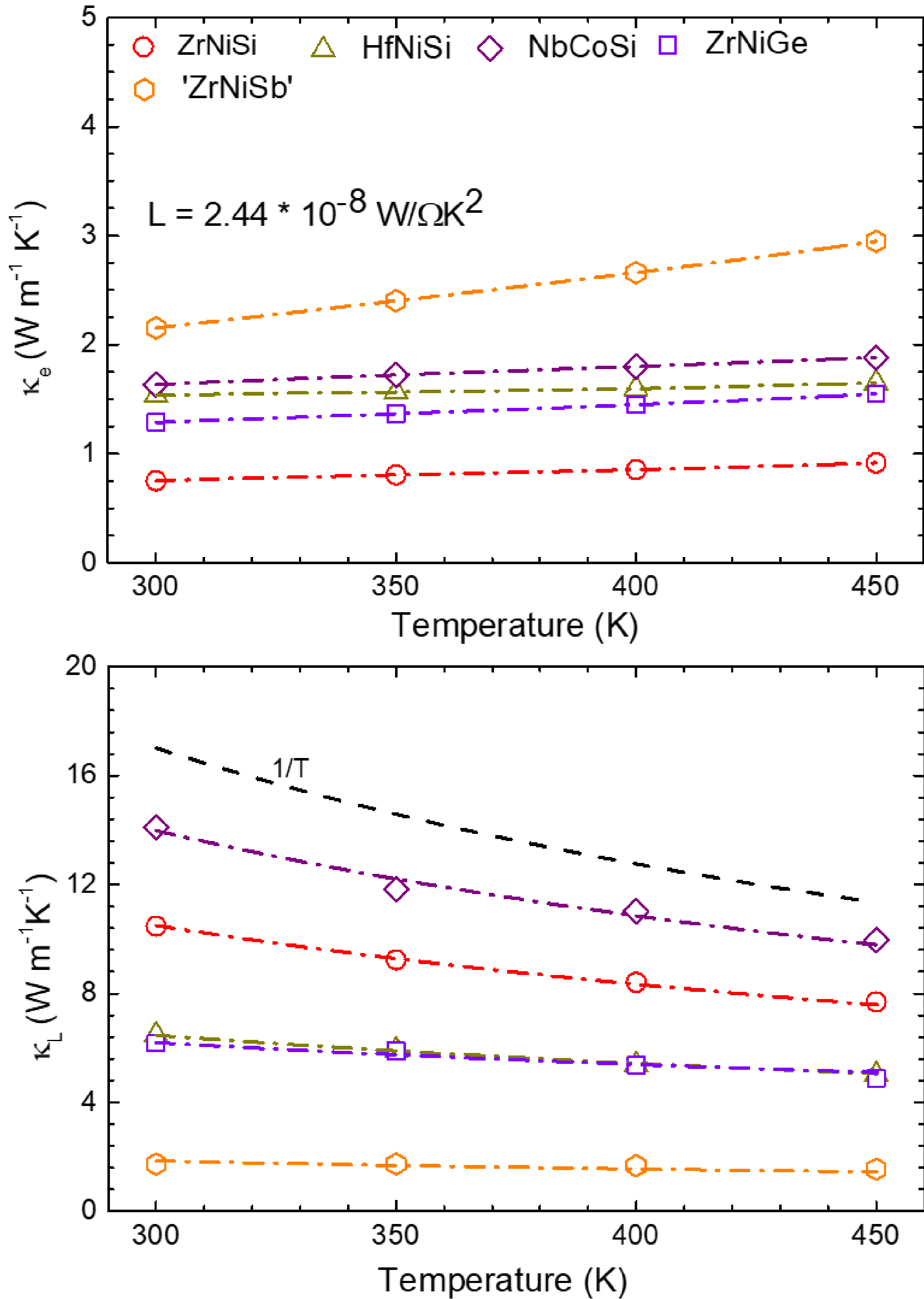

Figure 4.20: The (a) electronic (κ_l) and (b) lattice (κ_l) thermal conductivity. The lines are used as a guide to the eye. In panel (b), the black dashed line at the top shows the $1/T$ dependence.

by a slight increase at high temperatures (T $\sim$ 700K). Near room-temperature, κ is $\approx$ 15Wm^{-1} K^{-1} for NbCoSi, $\approx$ 11Wm^{-1} K^{-1} for ZrNiSi, and $\approx$ 7Wm^{-1} K^{-1} for both ZrNiGe and HfNiSi samples. We note that these values are either comparable to or lower than that previously reported for the hH alloys, including MNiSn (M = Ti, Zr and Hf) and their doped variants [160, 20, 164, 169, 211, 203]. The decreasing behavior of κ above room-temperature can be attributed to the phonon-phonon scattering processes; the upturn at high temperatures, on the other hand, is likely a consequence of bipolarity. Similar upturn due to the onset of minority carriers has also been reported for the hHs alloys [160, 20, 164, 169, 211, 203]. Interestingly, despite being most electrically conducting, the thermal conductivity of 'ZrNiSb' is the lowest, close to 4 Wm^{-1} K^{-1} near room temperature, and it also increases almost linearly upon heating, reaching 7Wm^{-1} K^{-1} at 1100 K suggesting that the lattice component of κ is heavily suppressed for this sample.

Using the Weidemann-Franz law one can get a tentative estimation of the electronic (κ_e) and lattice (κ_l) contributions. The experimental κ can be expressed as an algebraic sum of κ_e and κ_l, i.e., $\kappa = \kappa_e + \kappa_l$. Here, κ_e = L σT where L is the Lorentz number. Strictly speaking, we should have also considered the bipolar contribution [196, 86]; however, due to some specific features of the electronic structure in these compounds (Section 4.3.2) , including the presence of a pseudogap and relatively larger size of the majority charge carriers pockets (electron in ZrNiSi, ZrNiGe, and HfNiSi and holes in NbCoSi) than the minority carrier pockets (see Fig. 4.12), the bipolar contribution is expected to be small unless the sample is heated to high temperatures (i.e., T > 700K or so). For the purpose of a rough estimate, we take the Lorentz number to be 2.44×10^{-8} W ΩK^{-2} as in the metals. This also complies with the fact that in the degenerate semiconductors, such as VEC 18 hH alloys, the Lorentz number obtained by a rigorous calculation is typically only slightly smaller than this value.

The temperature variation of κ_e and κ_l thus obtained is shown in Fig. 4.20. The magnitude of κ_e near 300K is approximately 0.75Wm^{-1} K^{-1} for ZrNiSi ($\approx$ 6% of κ), 1.25Wm^{-1} K^{-1} for ZrNiGe ($\approx$ 17% of κ), 1.5Wm^{-1} K^{-1} for HfNiSi ($\approx$ 20% of κ), 1.7Wm^{-1} K^{-1} for NbCoSi ($\approx$ 10% of κ), and 2.9Wm^{-1} K^{-1} for 'ZrNiSb' ($\approx$ 72% of κ). Since σ has a weak temperature dependence, in the 300K to 500K range, κ_e = LσT shows an increasing behavior roughly proportional to T.

κ_l is plotted in Fig. 4.20b. In ZrNiSi and NbCoSi, κ_l follows a $1/T$ behavior suggesting the dominance of Umklpp scattering. In ZrNiGe and HfNiSi, the presence additional scattering modes is also indicated by a slower than 1/T decrease. Going by their stoichiomtery as determined using EDX, which is relatively off from the ideal value for these samples, we attribute this to the point defect scattering.

Interestingly, even though 'ZrNiSb' has the highest electrical conductivity, its

thermal conductivity is smallest among all the investigated samples, with $\kappa_l < 1\text{Wm}^{-1}\text{ K}^{-1}$. To give a perspective on how small this value is, consider the case of hH alloys where such small values are reported only for very carefully prepared nanostructured samples with high grain-boundary scattering and substantial point-mass fluctuations induced by doping of two or three elements [240, 25, 221]. The thermal diffusivity (D) is the measured quantity from which κ is derived, a comparison of D would help in substantiating this point further. At room-temperature D for our 'ZrNiSb' sample is $\approx 1.9\text{mm}^2\text{s}^{-1}$, which is comparable to a value of $1.5\text{mm}^2\text{s}^{-1}$ reported for the nanostructured $Zr_{0.5}Hf_{0.5}CoSb_{0.8}Sn_{0.2}$ [213], which is one of the smallest D value reported for any hH alloy to the best of our knowledge. Such a low value of κ_l in 'ZrNiSb' is likely due to the presence of high-density of structural disorder as shown in Fig. 4.10. The other factors such as point defect scattering which is expected to be more pronounced here due to off-stoichiometry may further contribute to decreasing κ. Finally, the heavier average atomic mass of 'ZrNiSb' compared to other samples is also expected to play a role.

In general, a relatively low-thermal conductivity of these compounds compared to their hH counterparts, despite almost an order of magnitude higher electrical conductivity is rather interesting, and the role of chair-shaped ... Si–Ni–Si–Ni ... framework (Fig. 4.1b) in the crystal structure of these compounds, which is known to be one of the factors responsible for its ultralow thermal conductivity of SnSe [232], should also be scrutinized in future.

Figure of merit

The figure of merit of the samples are shown in the Fig. 4.21. The variation with temperature for all the samples are nearly. We observe increasing zT of the samples with increasing temperature and a maxima is reached (except NbCoSi) at higher temperature after which it decreases. The highest figure of merit is obtained by ZrNiGe of 0.013 at ∼840 K. HfNiSi has zT_{max} 0.011 at ∼ 1000 K, "ZrNiSb" 0.008 at ∼1060 K, ZrNiSi 0.005 at ∼950 K. No maxima has been achieved for NbCoSi sample till highest temperature i.e. 1100 K, the max zT achieved is 0.001. Though the overall figure of merit is very low but these systems have been to understand their structural, electronic and thermal properties. These samples are semimetallic in nature and have different structure with respect to Heusler compounds. Individually these structure might not be effective as a thermoelectric but doping these systems can enhance their properties. Further these systems can be used to create heterostructures with half-Heuslers to enhance their prpoperties. TiNiSi-structure was recently studied by different groups [100, 12, 86, 156]. [86] has shown in recent work where they obtained 0.005 zT for TiNiSi and doped Ti site with 20 % Vanadium resulting in final zT of 0.032. This motivates us to dope these system further

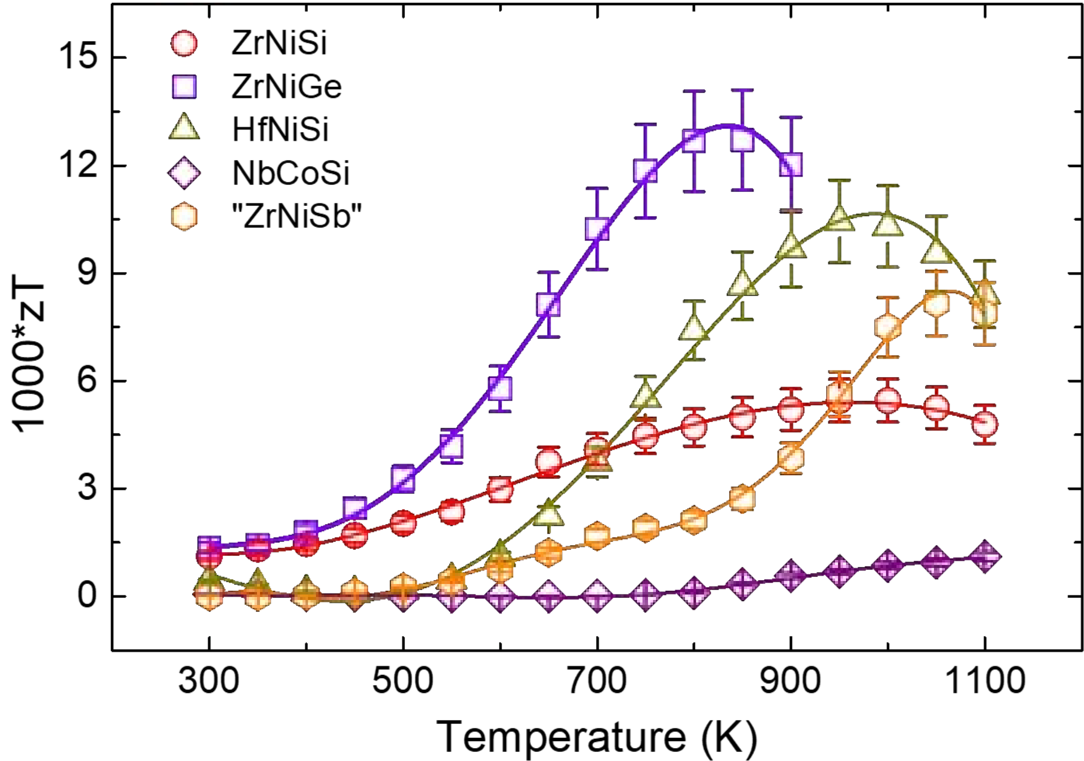

Figure 4.21: Figure of merit (zT) plot Vs temperature for different arc melted samples, namely ZrNiSi, ZrNiGe, HfNiSi, NbCoSi and ZrNiSb.

to obtain better performance.

4.4 Summary and Conclusions

In first part, we investigated the phase stability, formation and thermoelectric properties of ZrNiSi, ZrNiGe, HfNiSi, NbCoSi, and ZrNiSb. All the compounds are shown to crystallize with the orthorhombic TiNiSi structure-type. In ZrNiSb, about 5% excess Zr is required to obtain the pure orthorhombic phase.

Our first-principles electronic band structure calculations reveal that these compounds are semimetals with their Fermi surfaces comprised of small electron and hole pockets.The electronic density of states (DOS) present a pseudogap-like feature with E_F located either slightly below (ZrNiSi, ZrNiGe, and HfNiSi) or slightly above (NbCoSi) the pseudogap. The position of E_F with respect to the pseudogap is explained on the basis of electronegativity difference between the M and the X elements in MTX. In ZrNiSb no pseudogap could be found; however the DOS at E_F are only modestly enhanced with respect to the other studied compounds.

The experimental data supports the theoretical findings with electrical conductivity near room-temperature ranging from $\approx 10^3$Scm^{-1} to $\approx 4 \times 10^3$Scm^{-1}, which decreases upon heating in compliance with their semimetallic nature. The electrical

conductivity of these compounds near 300K is intermediate between that of the degenerate semiconductors and metallic alloys, as one would expect for a semimetal. The thermopower is negative for ZrNiX (X = Si, Ge) and HfNiSe, and positive for NbCoSi and ZrNiSb in agreement with the theoretical results. The average value of Seebeck coefficient is only about 10 μVK^{-1}, which is almost an order of magnitude smaller than is typically reported for the hHs alloys.

The thermal conductivity is found to be generally low for these compounds. In $Zr_{1.05}NiSb$, which has the highest electrical conductivity ($\approx$ 4000Scm^{-1}) at 300K of all the studied compounds, the thermal conductivity is as low as $\approx$ 4Wm^{-1} K^{-1} at room-temperature, which increase slowly upon heating attaining a value of $\approx$ 7Wm^{-1} K^{-1} at 1100K. The lattice contribution for this cmpound is estimated to be $<$ 1Wm^{-1} K^{-1} which is very low. The thermal diffusivity (D) of $Zr_{1.05}NiSb$ at 300K is almost as small as reported for the state-of-the-art nanostructure half-Heusler alloys. The low thermal conductivity, despite a reasonably high electrical conductivity, of the studied compounds is an interesting feature which should invite further investigations. It may be intrinsic, related to the presence of chair-shaped ... Si–Ni–Si–Ni ... framework in the structure whose role should be further scrutinized. Additionally, in $Zr_{1.05}NiSb$, the high-density of structural defects that result due to excess Zr may be important in reducing the lattice thermal conductivity to $<$ 1Wm^{-1} K^{-1}.

To summarize, the orthorhombic MTX compounds studied here show an interesting pseudogap-like feature in their electronic density of states, and their electronic structure is characterized by the presence of electron and hole pockets. They are found to be structurally stable and show a reasonably high electrical conductivity along with very low thermal conductivity. Their utility as thermoelectrics is however limited by their low thermopower. The highest thermoelectric figure-of-merit (zT) is therefore very small ($\approx$ 0.015 at 900K in ZrNiGe). In next chapter, we have tried studying studying doping effect in ZrNiSi sample. We doped Sb at Si site and tried to obtain solubility of Sb in ZrNiSi. ZrNiSi and ZrNiSb both exist in orthorhombic TiNiSi-type structure so doping Sb at Si site will lead to doping electron in samples.

Chapter 5

Doping Si Site in ZrNiSi with Sb

5.1 Introduction

In this part, we investigated some equiatomic MTX compounds, where M and T are respectively early and late transition metal elements and X is an element from the p-block of the periodic table [162]. They exhibit an orthorhombic TiNiSi structure-type which is closely related to the hH phase. The previous first-principles calculations on these materials by Guo et al. show that unless the vibrational entropy term is explicitly considered in the Gibbs free energy, the hH structure is thermodynamically favored who even coined the term "distorted hH" to describe these compounds (see Ref. [57, 60]). Their orthorhombic structure consists of distorted TX_4 tetrahedra with the Si-Ni-Si bond angle close to 110 ° forming a chair-shaped $\cdots \mathrm{Si}-\mathrm{Ni}-\mathrm{Si}-\mathrm{Ni}\cdots$ framework running parallel to the b-axis, which is analogous to a similar framework in the well-known ultralow thermal conductivity compound SnSe [232].

The first-principles density functional theory-based calculations show that these are semimetals with small electron and hole pockets at the Fermi level, and with a sizeable pseudogap in their electronic density of states around the Fermi energy [162]. Their electrical conductivity near room temperature is of the order of $10^3\mathrm{Scm}^{-1}$. However, despite high σ their thermal conductivity was found to be generally low, close to $10\mathrm{Wm}^{-1}\mathrm{K}^{-1}$ in the pristine form for ZrNiSi and $4\mathrm{Wm}^{-1}\mathrm{K}^{-1}$ for ZrNiSb which forms only with a slight Zr excess. But due to their low-thermopower ($< -20\mu\mathrm{VK}^{-1}$ near 300 K), the overall thermoelectric performance remains very low with zT < 0.01. In this chapter, we synthesized alloys $\mathrm{ZrNiSi_{1-x}Sb_x}$, and $\mathrm{Zr_{0.5}Hf_{0.5}NiSi_{0.8}Sb_{0.2}}$ to enhance the Seebeck coefficient and lower the thermal conductivity further. Here, we show that by doping zT can be enhanced by over an order of magnitude. Though the observed zT is still far too low for any practical application, our study establishes provides proof of the concept that the orthorhombic

MTX compounds with suitable dopants can be promising for mid-to-high temperature range TE applications.

5.2 Experimental details

Samples were synthesized using the arc-melting technique under high-purity argon gas. Stoichiometric amounts of Zr (Sigma Aldrich, $\geq$ 99%), Ni (Sigma Aldrich, $\geq$ 99.9%), Si (Sigma Aldrich, 99.5%), Hf pieces (Sigma Aldrich,99.7% trace metal basis) and Sb shots(Alfa Aesar, $\geq$ 99.999%) were used. The starting precursors were weighed according to the required stoichiometry and loaded on the water-cooled copper hearth of the arc furnace. The chamber was evacuated and purged with high-purity argon gas repeatedly several times before striking the arc. A zirconium getter was used to absorb any remnant oxygen in the chamber. The ingot was flipped over and re-melted five to six times to ensure a good homogeneity. 10 % Sb doped and 20 % Sb doped ZrNiSi samples were annealed in evacuated (under dynamic vacuum) sealed quartz tubes. The inner wall of the quartz tube was coated with a thin layer of carbon soot to avoid the reaction of Zr and Ti with the quartz tube. The physical properties were measured only on the as-melted sample. For this purpose, the arc-melted ingots were cut using a low-speed diamond saw (South Bay, USA) into a disc-shaped specimen for the measurement of thermal conductivity, and a rectangular bar-shaped specimen for resistivity and thermopower.

To check the phase formation and presence of secondary phase(s), if any, powder X-ray diffraction was done at various stages of the sample synthesis (Bruker, D8 Advance). The lattice parameters were obtained by least-square refinement using the UNIT CELL program. Polished specimens cut from the as-melted ingots were also examined using a Field Effect Scanning Electron microscope (FESEM) (Ultra Zeiss plus), equipped with an Energy Dispersive X-ray (EDX) analysis attachment (Oxford Instruments). The resistivity and thermopower were measured simultaneously using the Linseis LSR-3 set-up. The average uncertainties in these measurements are less than 5%. The thermal diffusivity (D) was measured using the Linseis LFA-1000 instrument on polished discs that were homogeneously coated with a very thin layer of graphite. The average uncertainty in thermal diffusivity using this set-up is near 5 %. Thermal conductivity (κ) was obtained from the thermal diffusivity by the formula $\kappa = D\rho C_{\rm p}$ where ρ is the mass density, and $C_{\rm p}$ is the specific heat for which we used the value corresponding to the Dulong-Petit limit (3nR = 74.8 $Jmol^{-1}\ K^{-1}$). While this may be a little overestimation, especially near room temperature, we used this to get an upper bound on κ. For mass density, we used the sample dimensions and sample mass both of which were reasonably accurately accessible. The arc-melted ingots were free of micropores as revealed in the polished

specimens' electron and optical microscope images. The mass density is estimated to be close to 95% for all the samples. HRTEM (JEOL JEM 2200FS 200 keV) was used to collect high-resolution images and for obtaining SAED patterns with the GSM-3 software package to assess the crystallinity of our samples. For examining the sample under the HRTEM, a piece of the ingot was hand-ground into a fine powder, which was transferred onto a TEM Cu grid in an ethanol-based solution that was oven-dried at 50°C for close to an hour. The Cu grid was subsequently loaded on the TEM sample stage and plasma cleaned at 250 eV for about 15 minutes.

5.3 Result and discussion

5.3.1 Structural analysis

Powder X-ray diffraction

The powder X-ray diffraction (PXRD) data of our arc-melted $ZrNiSi_{1-x}Sb_x$ (x = $0, 0.05, 0.1, 0.15$ and 0.2) and $Zr_{0.5}Hf_{0.5}NiSi_{0.8}Sb_{0.2}$ are shown in Fig. 5.1. In the parent sample ZrNiSi, all the observed diffraction peaks could be satisfactorily indexed using the orthorhombic symmetry (TiNiSi structure-type, space group *Pnma*). The absence of any extra peak indicates that within the limit of detection of powder XRD the sample is phase pure. The evolution of the XRD pattern with increasing x shows interesting changes. The first thing to notice is that with increasing x the successive PXRD patterns shift progressively towards lower 2θ values indicating an expansion of the unit cell due to bigger Sb atoms replacing Si in the structure. However, with increasing x, the diffraction peaks also became broader, broadening more pronounced for higher values of x. For example, in x = 0.15 the 211 peak is asymmetrically broadened with extra intensity appearing towards its low angle side. However, despite this broadening, up to x = 0.15, there is no difficulty in indexing the main peaks or in tracing their evolution individually. Contrary to this, the PXRD pattern of x = 0.20 sample could not be reliably indexed based on the ZrNiSi pattern, although some similarities between the two patterns can still be seen. For example, the quintet of the closely positioned 210, 112, 202, 211 and 103 peaks can still possibly be identified, but the difficulty lies in the fact that the relative intensity of 210 peak seems to increase up to x = 0.15 and then decreases suddenly for x = 0.2. Clearly, for higher values of x the evolution of PXRD patterns is more intriguing than what one expects from a simple solid solution. Likely, the solid-solutions ZrNi(Si, Sb) away from the Si end leads to a *spinodal* decomposition, which manifests itself in the form of two coexisting orthorhombic TiNiSi type phases with different Si/Sb ratios.

In $HfNiSi_{0.8}Sb_{0.2}$, the diffraction peaks have broadened even further, and there is

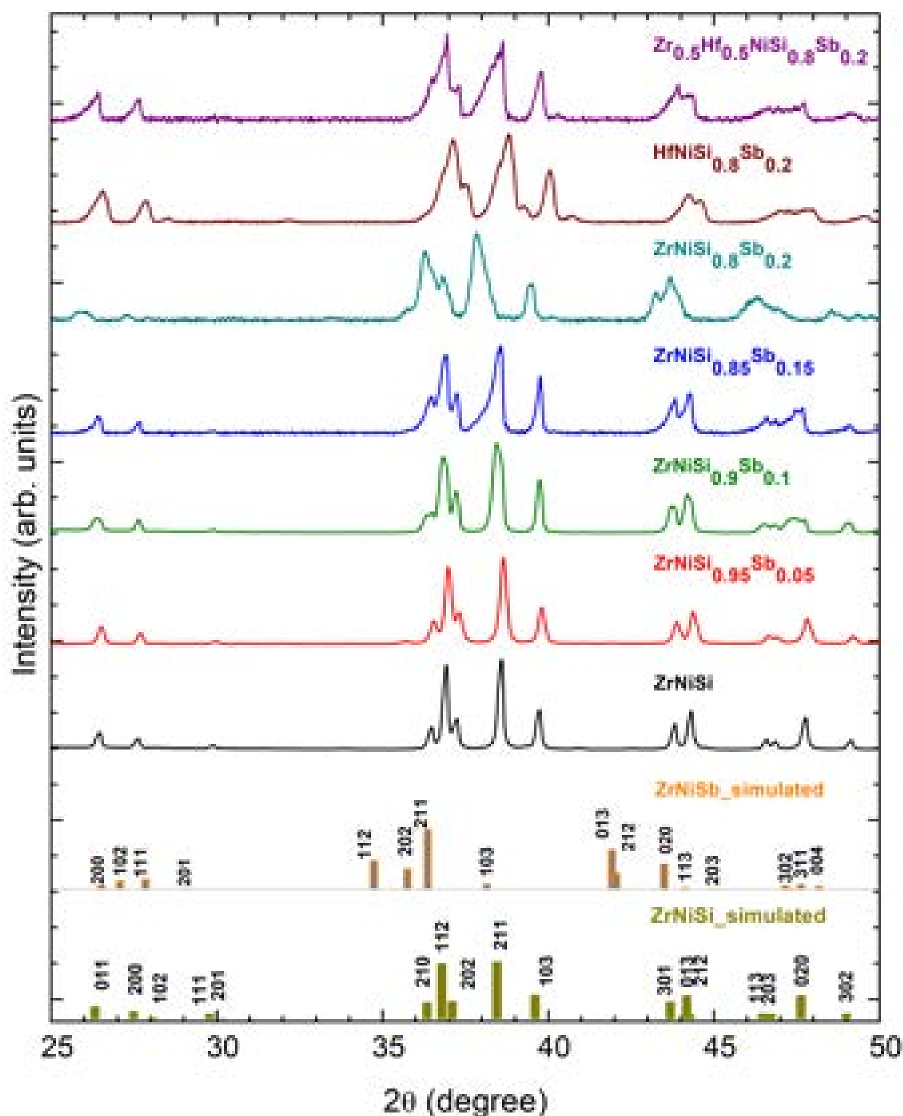

Figure 5.1: Powder x-ray diffraction of all arc-melted samples with nominal composition $ZrNiSi_{1-x}Sb_x$, $HfNiSi_{0.8}Sb_{0.2}$ and $Zr_{0.5}Hf_{0.5}NiSi_{0.8}Sb_{0.2}$. The simulated stick patterns based on the orthorhombic TiNiSi structre type are also shown for ZrNiSi and ZrNiSb

an overall shift of the PXRD pattern to the higher 2θ values compared to $ZrNiSi_{0.8}Sb_{0.2}$, which is consistent with the smaller size of Hf compared to Zr. The small peaks on the low 2θ side of both 211 and 103 peaks could be extra, i.e., due to the presence of secondary phase(s). In $Zr_{0.5}Hf_{0.5}Si_{0.8}Sb_{0.2}$, though the peak broadening is still present, the pattern can be identified with ZrNiSi.

Scanning Electron Microscopy

A few representative backscattered FESEM images and their elemental chemical maps are shown for x = 0.05 and x = 0.15 samples in Fig. 5.2. Similar images for x = 0.10 and x = 0.20 samples are shown in the Fig. 5.3 and Fig. 5.5 respectively.

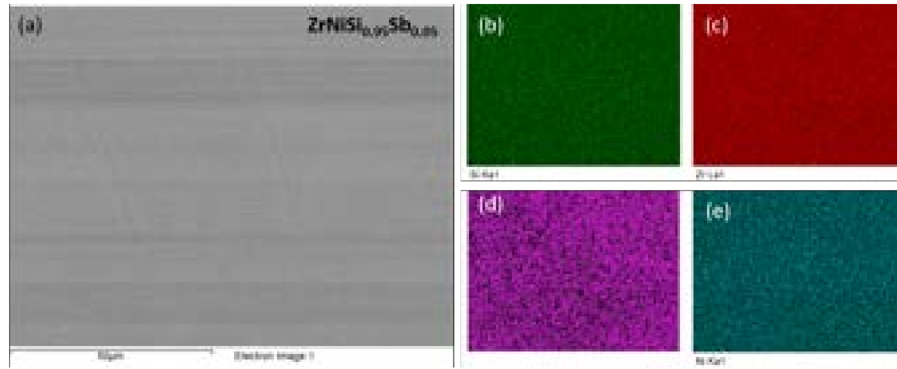

Figure 5.2: (a) Representative backscattered FESEM images of $ZrNiSi_{0.95}Sb_{0.05}$ showing homogeneous chemcial distribution of elements in $ZrNiSi_{0.95}Sb_{0.05}$ (b) Si, (c) Zr, (d) Sb, and (e) Ni.

In x = 0.05 sample, a homogeneous distribution of Zr, Ni, Si and Sb can be seen in agreement with the PXRD pattern in Fig. 5.1. However, in the x = 0.15 sample, clear phase contrast is observed with dark grey and light grey regions seen over the whole imaged area. The elemental color maps further show that while Zr and Ni distribution is uniform all through, the two phases differ with respect to their Sb/Si ratios. In the x = 0.15 sample, the Sb solubility in the dark-grey regions is $\sim$ 4 % (i.e., Sb/Si $\equiv$ 1/24), while the lighter regions have a higher solubility of about 24 % (i.e, Sb/Si $\equiv$ 1/4) as shown in Fig. 5.4.

In the x = 0.1 and x = 0.2 samples also a similar phase segregation has been observed as shown in Fig. 5.3 and Fig. 5.5. We found that with increasing Sb doping the volume fraction of the light-grey region increases. In x = 0.2, the dark to light contrast has reduced considerably which indicates that the composition difference between the two regions diminishes with increasing x. Similarly, in $HfNiSi_{0.8}Sb_{0.2}$ segregation of two phases $Hf_{1.12}Ni_{1.05}Si_{0.46}Sb_{0.36}$ and $Hf_{0.92}Ni_{0.88}Si_{1.17}Sb_{0.03}$ has been seen (Fig. 5.6) . In $Zr_{0.5}Hf_{0.5}NiSi_{0.8}Sb_{0.2}$, the distribution of elements again appears to be homogeneous, as shown in Fig. 5.7.

Effect of annealing

The effect of annealing is shown in Fig. 5.8. After annealing the diffraction peaks in the XRD pattern of x = 0.1 sample became sharper and hence better resolved, matching nicely with the diffraction peaks in the undoped ZrNiSi sample. However, small extra intensity can also be seen on the low-angle side of the 211 peak. The XRD of annealed x = 0.2 sample indicates that this extra intensity is due to a secondary phase as in this case it takes the appearance of a full-fledged peak. Besides this peak several other small secondary peaks are also observed, these are marked with an asterisk.

A better understanding of this emerged from the SEM images and associated

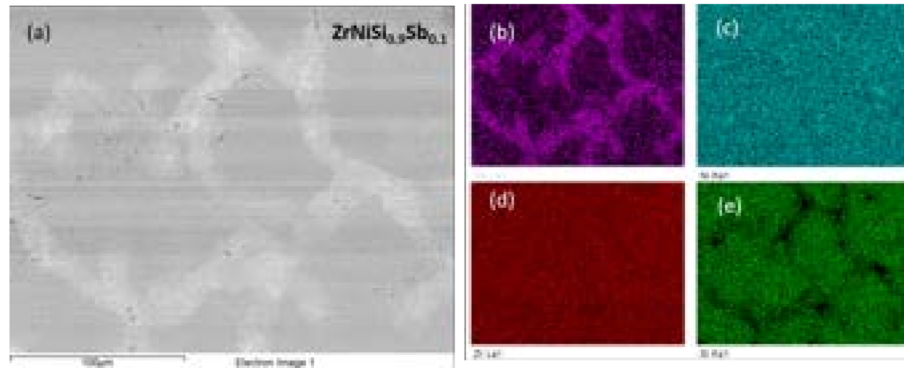

Figure 5.3: (a) Representative backscattered FESEM images of $ZrNiSi_{0.9}Sb_{0.1}$ showing a spinodal-type phase segregation in $ZrNiSi_{0.9}Sb_{0.1}$. The chemical elemental composition in two cases is also shown using the false color representation; (b) Sb, (c) Ni, (d) Zr, and (e) Si.

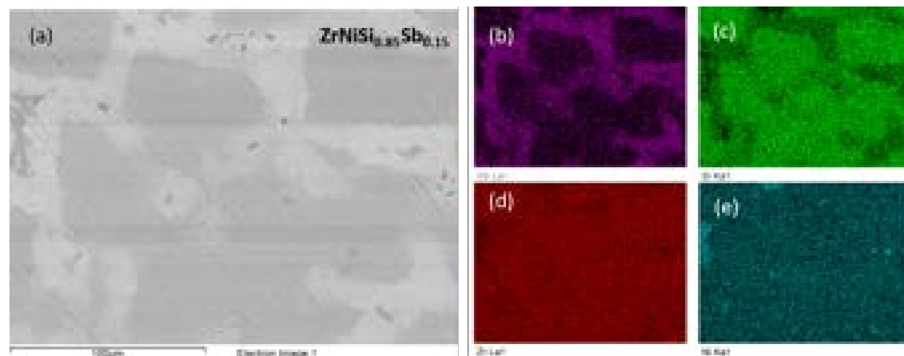

Figure 5.4: (a) Representative backscattered FESEM images of $ZrNiSi_{0.85}Sb_{0.15}$ showing a spinodal-type phase segregation in $ZrNiSi_{0.85}Sb_{0.15}$. The chemical elemental composition in two cases is also shown using the false color representation; (b) Sb, (c) Ni, (d) Zr, and (e) Si.

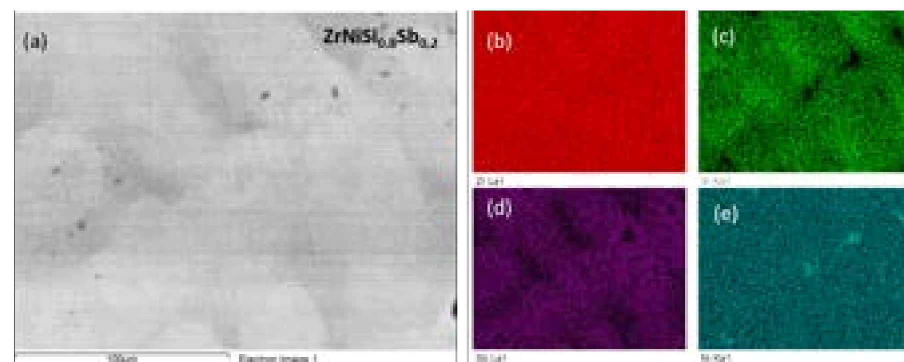

Figure 5.5: (a) Representative backscattered FESEM images of $ZrNiSi_{0.8}Sb_{0.2}$ showing a spinodal-type phase segregation in $ZrNiSi_{0.8}Sb_{0.2}$. The chemical elemental composition in two cases is also shown using the false color representation; (b) Zr, (c) Si, (d) Sb, and (e) Ni.

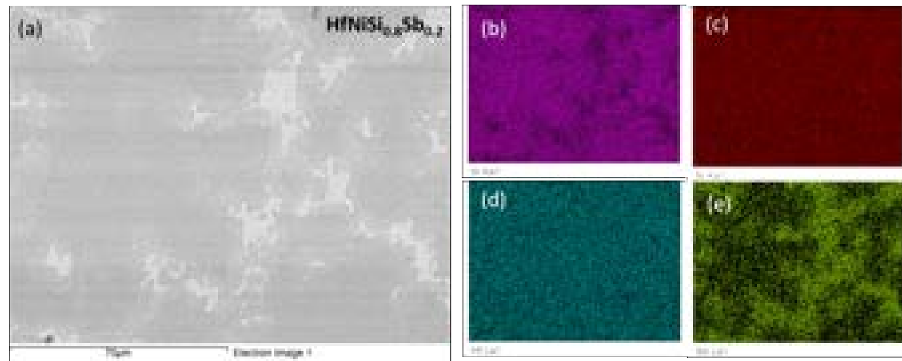

Figure 5.6: (a) Representative backscattered FESEM images of $HfNiSi_{0.8}Sb_{0.2}$ showing a spinodal-type phase segregation in $HfNiSi_{0.8}Sb_{0.2}$. The chemical elemental composition in two cases is also shown using the false color representation; (b) Si, (c) Ni, (d) Hf, and (e) Sb.

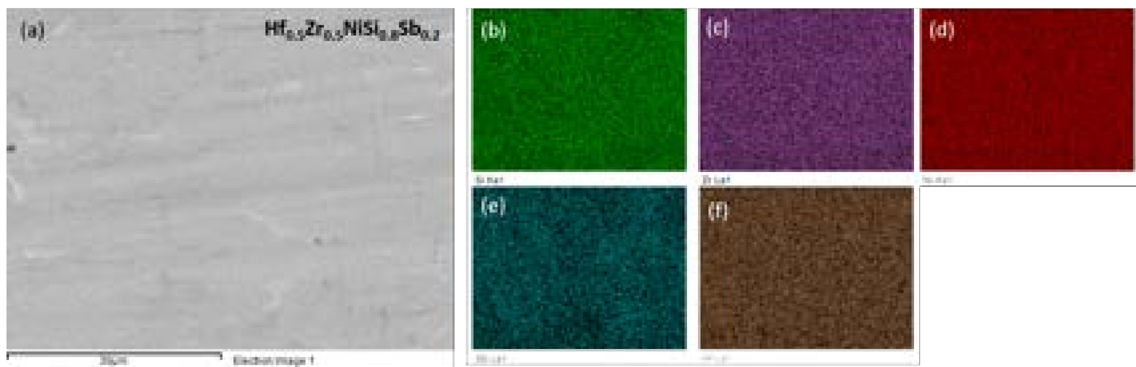

Figure 5.7: (a) Representative backscattered FESEM images of $ZrNiSi_{0.8}Sb_{0.2}$ showing a homogeneous distribution in $Zr_{0.5}Hf_{0.5}NiSi_{0.8}Sb_{0.2}$. The chemical elemental composition in two cases is also shown using the false color representation; (b) Si, (c) Zr, (d) Ni, (e) Sb and (f) Hf .

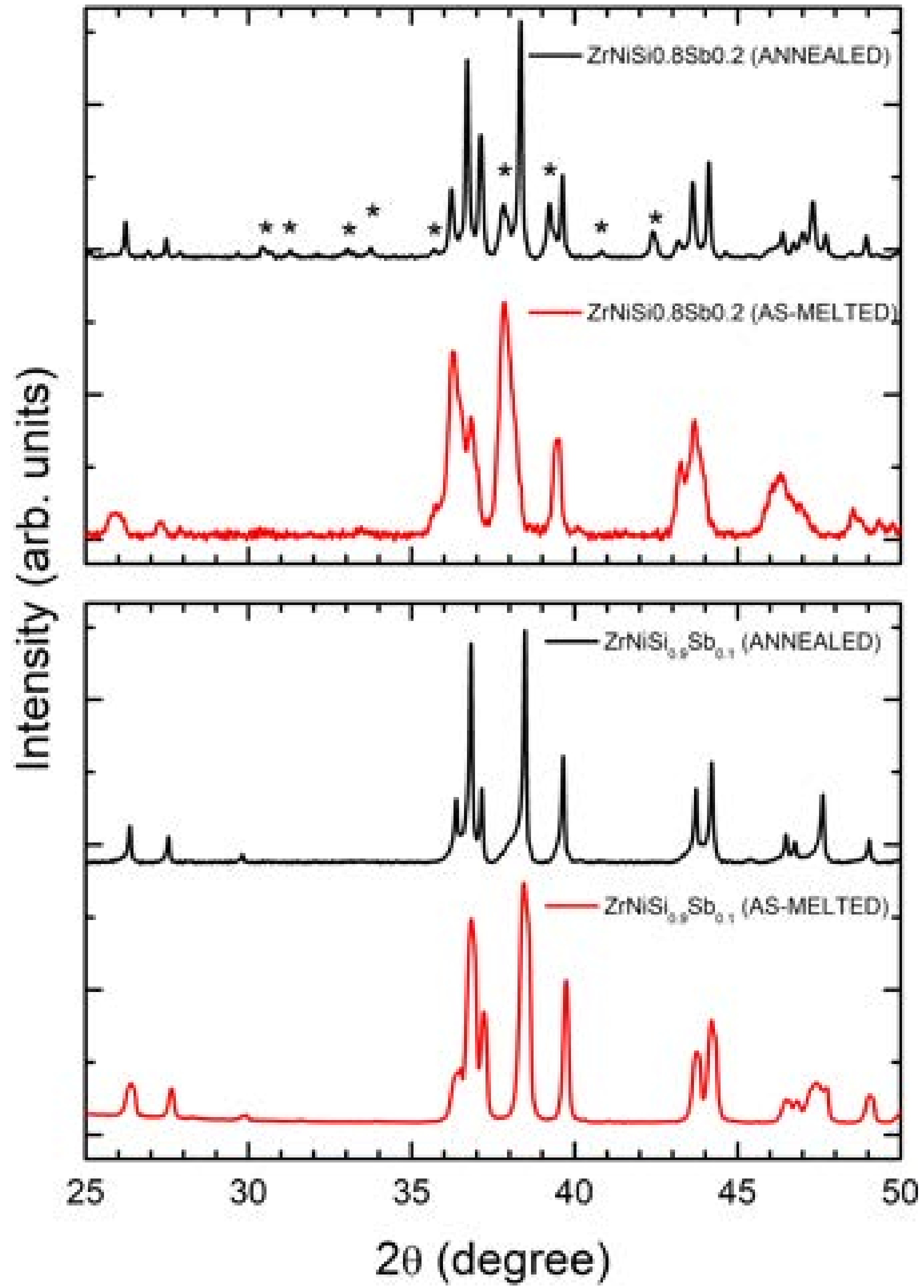

Figure 5.8: A comparison of PXRD pattern of $ZrNiSi_{0.9}Sb_{0.1}$ and $ZrNiSi_{0.8}Sb_{0.2}$ before and after the annealing process. The extra peaks are marked with an asterisk

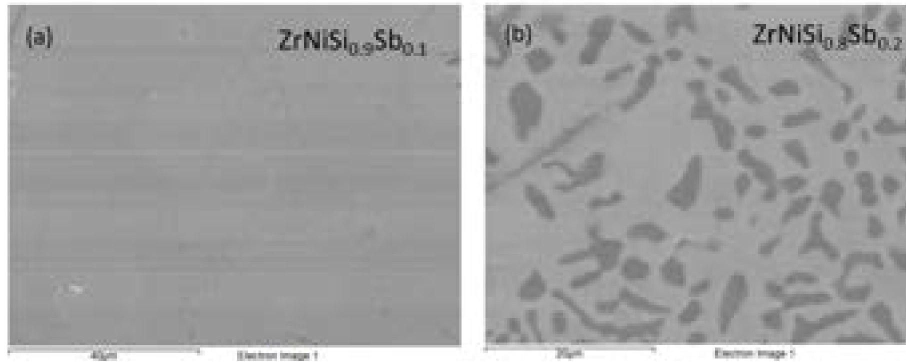

Figure 5.9: Representative backscattered FESEM images of $ZrNiSi_{0.9}Sb_{0.1}$ and $ZrNiSi_{0.8}Sb_{0.2}$ post annealing

EDX analysis of the annealed samples (Fig. 5.9). For x = 0.1, no signs of any extra phase can be seen suggesting a single-phase nature of the sample. The average sample composition is found to $Zr_{1.09}Ni_{0.96}Si_{0.88}Sb_{0.07}$. In the x = 0.2 sample, on the other hand, the SEM image shows a clear phase contrast with two phases present: the light-grey phase with dark-grey islands embedded in it. Their compositions are found to be $Zr_{1.11}Ni_{0.89}Si_{0.47}Sb_{0.53}$ and $ZrNiSi_{0.96}Sb_{0.14}$, respectively. Thus, upon annealing, the composition and volume fraction difference between the two phases becomes much more pronounced compared to the as-melted (or non-annealed) sample.

Transmission Electron Microscopy

In Figs. 5.10, representative HRTEM images are shown for the as-grown ZrNiSi, and $ZrNiSi_{0.8}Sb_{0.2}$ samples. In ZrNiSi, nicely lined-up crystal planes can be seen in the HRTEM image (Fig. 5.10a) indicating a high-crystallinity which is also evident from the sharpness of the diffraction spots in the SAED image shown in Fig. 5.10b or the FFT image shown as an inset in panel (a); a few of the diffraction spots are labeled, and the corresponding lattice planes are marked in the IFFT image shown in panel Fig. 5.10c. The IFFT image also corroborates the high-crystallinity of ZrNiSi.

On the other hand, in $ZrNiSi_{0.8}Sb_{0.2}$, the SAED pattern (Fig. 5.10e) is far more complex with superimposed diffraction spots due to two different phase segregated regions as seen in the FESEM images. A few diffraction spots for one of the phases could be identified and labeled. The IFFT image (Fig. 5.10f) showing the lattice planes corresponding to the spot 211 indicates the presence of stacking faults. The lattice imperfections in the form of stacking faults are also evident in the direct HRTEM image in Fig. 5.10d.

Surprisingly, doping Hf at the Zr site in$ZrNiSi_{0.8}Sb_{0.2}$ (i.e., $Hf_0.5Zr_0.5NiSi_{0.8}Sb0.2$) improved the phase formation and chemical homogeneity considerably which we also

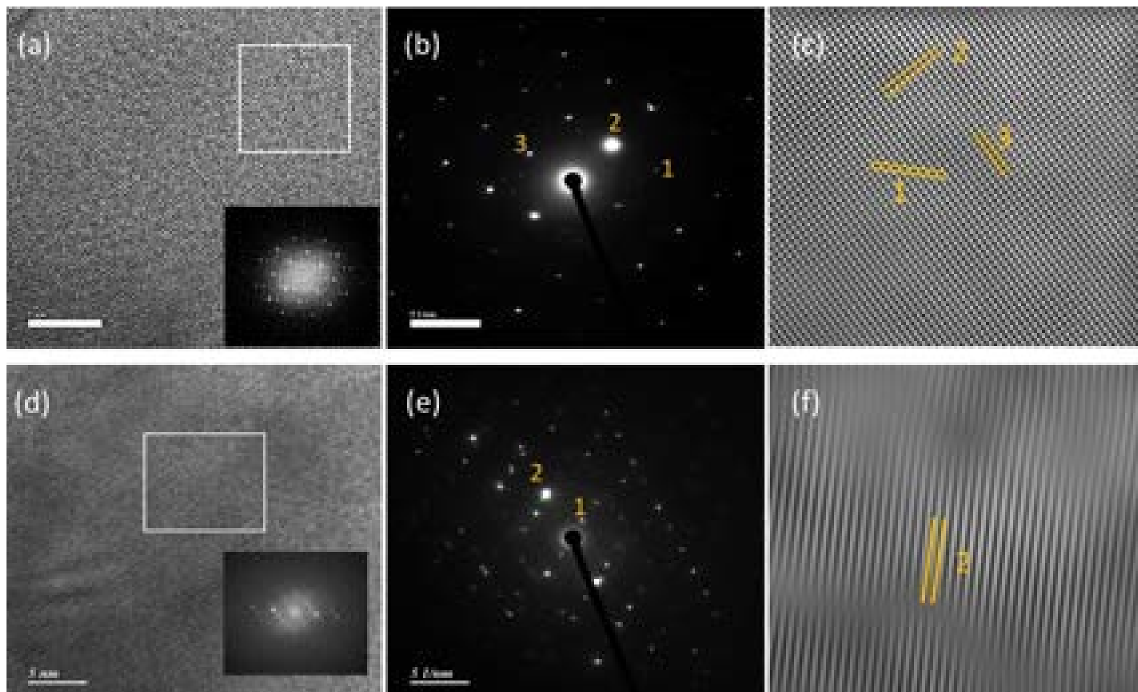

Figure 5.10: Top panel: (a) HRTEM micrograph of ZrNiSi, inset at right bottom shows the FFT image of the micrograph; (b) SAED pattern taken on the micrograph where *hkl* indices of points marked with 1, 2, and 3 corresponding to d[11-2] = 0.156 nm, d[211] = 0.234 nm, and d[103] = 0.227 nm, respectively are shown; (c) IFFT of the white square shown in (a) showing d spacing of planes 1, 2 and 3. Bottom panel: HRTEM micrograph of $ZrNiSi_{0.8}Sb_{0.2}$, the panels (d), (e) and (f) are analogous to (a), (b) and (c). In (e) *hkl* indices of points marked with 1 and 2 are [111] and [211], respectively. In (e) the planes [211] with d[211] = 0.227 nm are shown

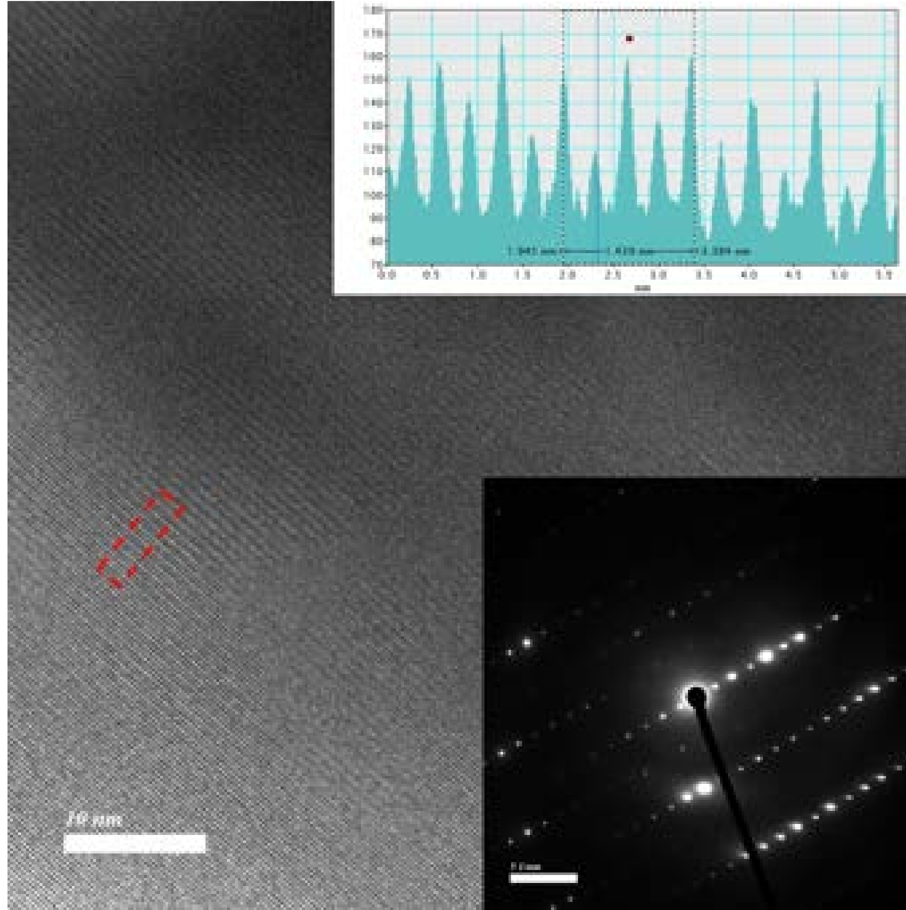

Figure 5.11: A representative HRTM image of a grain of $Zr_{0.5}Hf_{0.5}NiSi_{0.8}Sb_{0.2}$. The lower inset shows the SAED pattern. The upper inset shows the intensity profile along the direction marked within the red square.

observed using the PXRD and SEM imaging, e.g., the absence of phase segregated region in the SEM images. The HRTEM imaging confirmed this observation further. In the majority of the captured images, we observed nicely lined-up lattice planes and sharp SAED spots. A representative HRTEM image is shown in Fig. 5.11. The intensity profile along the marked direction also shows the Hf-Zr ordering.

5.3.2 Transport properties

Charge carrier transport

The Seebeck coefficient (S) of our samples is shown in Fig. 5.12a. The sign of S is negative for all the samples and its value ranges from $-20\mu\text{WK}^{-1}$ to $-40\ \mu\text{WK}^{-1}$ across all samples. In the undoped (x = 0) sample, S remains nearly constant up to 850K after which it decreases slightly. Upon doping 5 % Sb (x = 0.05), the behavior changes significantly as S now exhibits a clear peak near 650K with the peak value of $\approx -30\mu\text{VK}^{-1}$, which decreases to $\approx -20\mu\text{VK}^{-1}$ on either side of the peak. With further increase in x, the peak value increases from up to $-35\mu\text{WK}^{-1}$

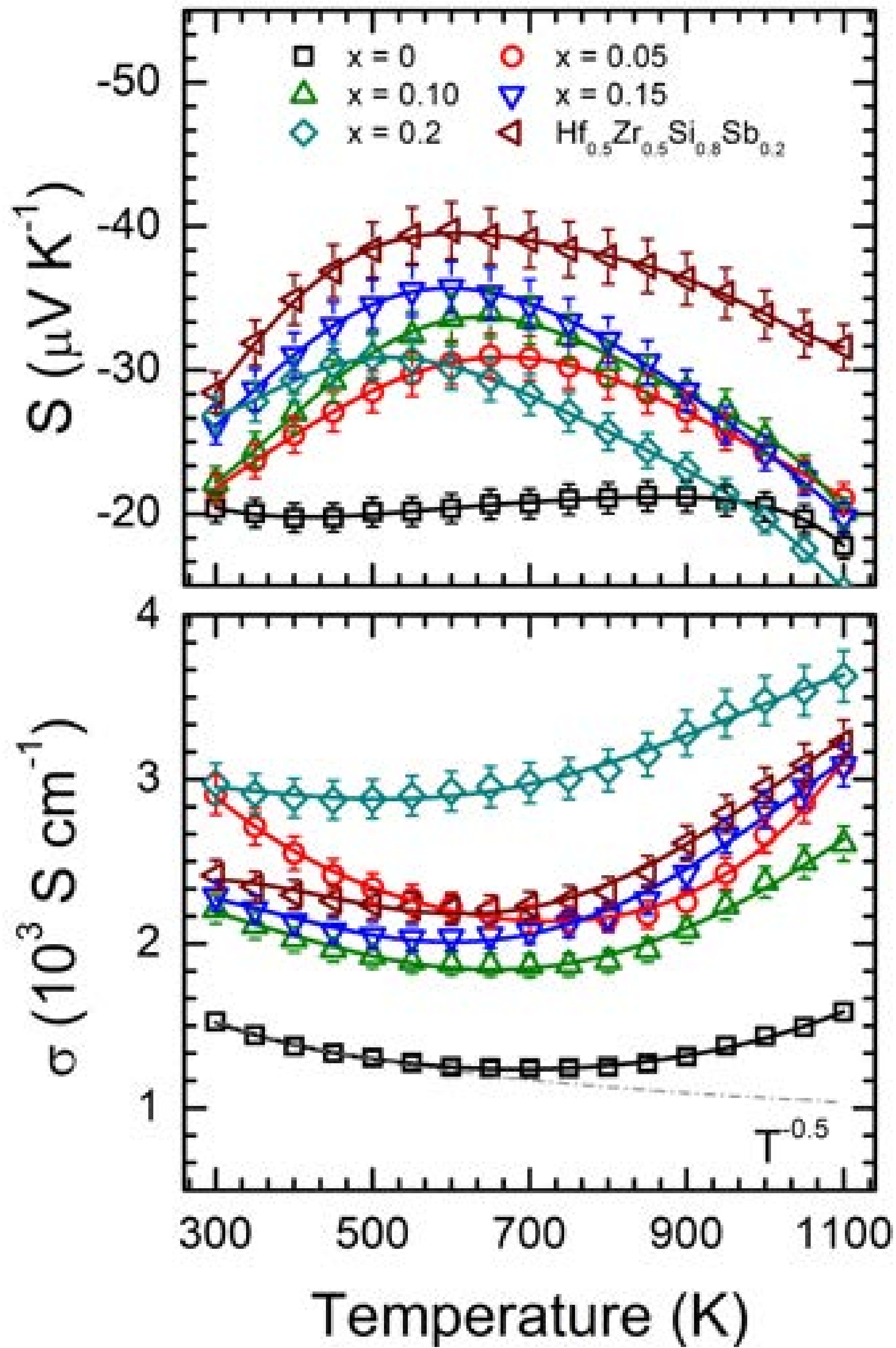

Figure 5.12: Temperature dependence of: (a) Seebeck coefficient (S) and (b) electrical conductivity of $ZrNiSi_{1-x}Sb_x$ and $Zr_{0.5}Hf_{0.5}NiSi_{0.8}Sb_{0.2}$

before decreasing back to $-30\mu WK^{-1}$ in x = 0.2. The temperature at which the maximum S occurs however decreases monotonically with increasing x for 650K for x = 0.05 to 450K for x = 0.2.

The best results are however found for the sample $Hf_{0.5}Zr_{0.5}NiSi_{0.8}Sb_{0.2}$ where S reached a peak value of $-50\mu WK^{-1}$ near 600K. On the low-temperature side of the peak, S decreases quickly to $-28\mu WK^{-1}$ near 300K, but on the high-temperature side the decrease is relatively gentler taking a value close to $-32\ \mu WK^{-1}$ at 1100K. The maximum in S can be attributed to the activation of minority charge carriers at higher temperatures.

The electrical conductivity (σ) of our samples is shown in Fig. 5.12b. In ZrNiSi, σ is around $1000Scm^{-1}$ near 300K which is comparable to the room-temperature electrical conductivity typically reported for the hH compounds [160, 20, 169, 230, 65]. With increasing temperature, σ decreases slowly, showing a shallow minimum near 700K before increasing again roughly at the same rate, reaching a value close to $1000Scm^{-1}$ near 1100K. With 5 % Sb doping, σ increases dramatically to $2500Scm^{-1}$ at 300K, and shows a qualitatively similar temperature dependence to that of the undoped sample. In x = 0.10 and 0.15, σ decreases slightly, and in x = 0.2 it increases again to $2500Scm^{-1}$ at 300K with an increasing behavior with T, reaching a value of $\approx 3000Scm^{-1}$ at 1100K. In $Hf_{0.5}Zr_{0.5}NiSi_{0.8}Sb_{0.2}$, σ is still rather high ($\approx 2000Scm^{-1}$) and shows a temperature dependence qualitatively similar to that of ZrNiSi. Though the electrical conductivity has increased in the doped sample with an increase in Sb doping, as discussed the increase is not according to doping percentage. This abrupt behavior can be understood by relating it to microstructures due to phase segregation shown in FESEM images for all the doped samples. The 5 % doped sample is homogeneous with no phase segregation at all hence conductivity has increased due to extra carriers doped, scattering mechanism not getting affected much. For 10 % and 15 % Sb doped samples we observed more grains due to phase segregation thus though carriers were added scattering increased and we observed decreased electrical conductivity. for 20% Sb doped sample and co-doped sample, we see bigger grain formation which has led to reduced scattering and hence increased electrical conductivity.

One of the major challenges in TE research is to decouple σ and S, as these quantities are generally inversely correlated, not allowing the power factor to enhance. Making a material more electrically conducting without causing S to decrease appreciably is generally considered as a good first step towards improving the zT value [206]. Hence, the simultaneous increase in both S and σ with initial Sb doping or with co-doping of Hf and Sb is very interesting. We will return to this point later in the theory section and try to understand it by investigating the changes in the electronic band structure upon Sb doping.

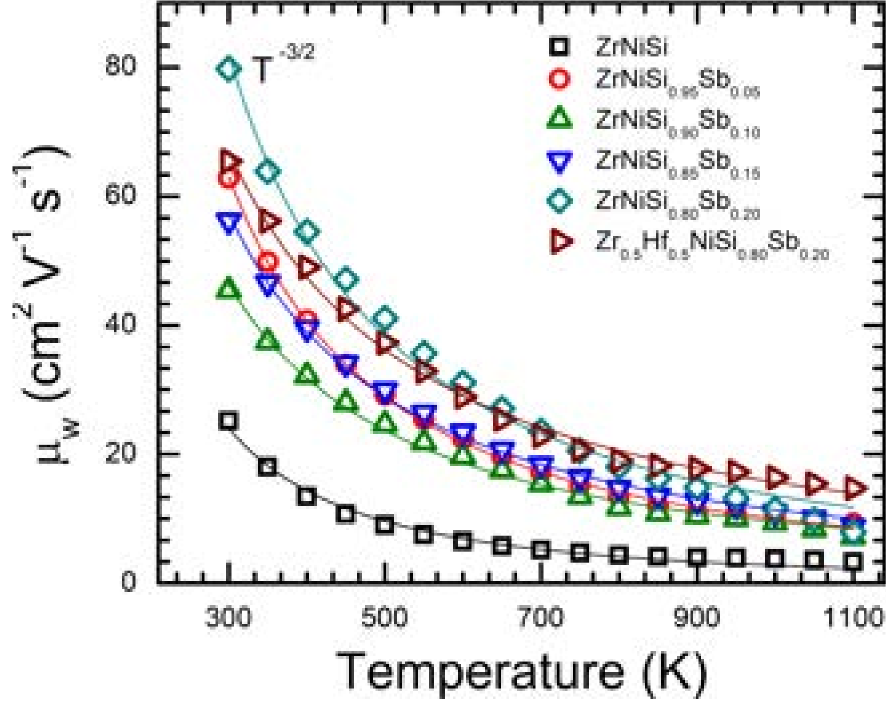

Figure 5.13: Temperature dependence of weighted mobility (μ_w) in $\mathrm{ZrNiSi_{1-x}Sb_x}$ and $\mathrm{Zr_{0.5}Hf_{0.5}NiSi_{0.8}Sb_{0.2}}$
samples

To understand the scattering mechanisms in our samples we discuss the temperature and doping dependence of the carrier mobility. In the absence of temperature-dependent Hall measurements, an understanding of charge carrier mobility can be obtained by estimating the weighted carrier mobility (μ_w), i.e., the electron mobility weighted by the density of electronic states. μ_w can be obtained readily from the Seebeck coefficient and electrical resistivity at any temperature T using the formula given in Ref. [177]. The weighted mobility can throw light on the scattering mechanisms independent from Fermi level or carrier concentration. The μ_w versus temperature variation for various values of Sb doping (x) is shown in Fig. 5.13a.

With increasing Sb doping μ_w increases significantly from $\approx 25\mathrm{cm^2V^{-1}s^{-1}}$ for $\mathrm{x} = 0$ to $\approx 80\mathrm{cm^2V^{-1}s^{-1}}$ for $\mathrm{x} = 0.2$. This should be compared with the value of μ_w for state-of-the art of thermoelectrics p-type PbTe ($\mu_\mathrm{w} \approx 130\mathrm{cm^2V^{-1}s^{-1}}$) [143] and the hH alloys of FeNbSb family ($\mu_\mathrm{w} \approx 330\mathrm{cm^2V^{-1}s^{-1}}$) [44].

For all our samples, the temperature variation of μ_w follows an approximately $T^{-\alpha}$ dependence with α ranging between 1.8 (x = 0) and 1.2 (x = 0.2) suggesting that the electron-phonon scattering mechanism ($\mu \propto \mathrm{T}^{-\frac{3}{2}}$) is the dominant mode of scattering at high temperatures. However, the slight increase in the value of exponent α with x suggests that the alloy scattering, for which the mobility scales as $T^{-\frac{1}{2}}$, plays an increasing role as the Sb doping level increases. The ionized impurity scattering, which causes the mobility to scales as $\mathrm{T}^{\frac{3}{2}}$, only becomes significant at very

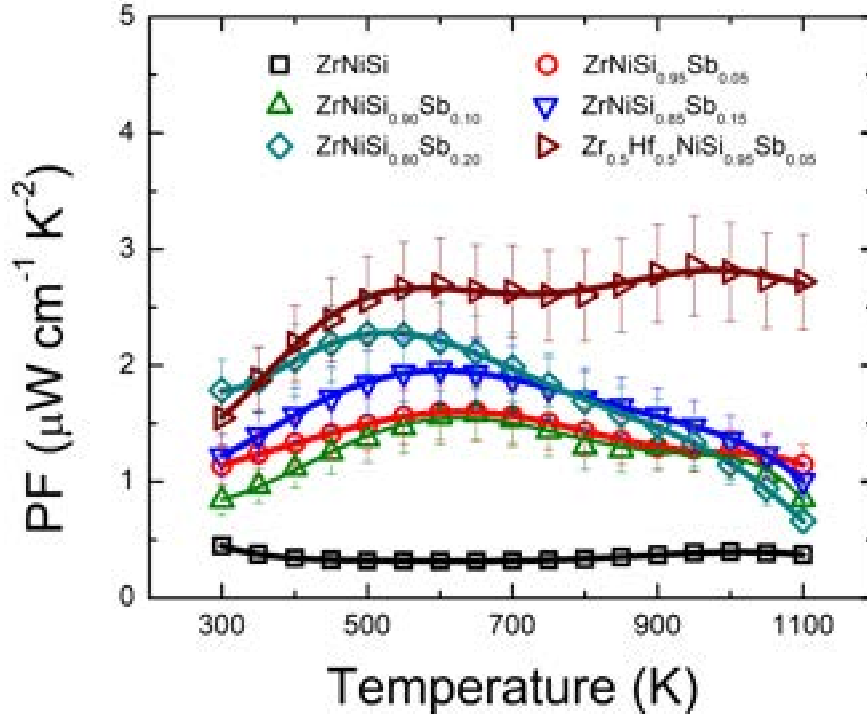

Figure 5.14: Temperature dependence of Power factor (PF) in $ZrNiSi_{1-x}Sb_x$(x = 0, 0.05, 0.1, 0.15, & 0.2) and $Zr_{0.5}Hf_{0.5}NiSi_{0.8}Sb_{0.2}$

low temperatures and hence need not be considered here. A factor of 4 increase in the mobility due to Sb doping can be attributed to the increase in the charge carrier density as each doped Sb atom contributes 1 electron to the system.

The power factor (PF) of our samples is shown in Fig. 5.14. Upon Sb doping, the PF increase by a factor of 4 to 5 over the undoped ZrNiSi whose PF is around 0.4 $\mu Wcm^{-1}K^{-2}$ over the whole temperature range. The best results are obtained for $Hf_{0.5}Zr_{0.5}NiSi_{0.8}Sb_{0.2}$, where the PF around 300 K is almost 4 times that of ZrNiSi, and with an increase in temperature, it increases further, reaching values as high as 7-8 times that of ZrNiSi.

Computational results

To understand the transport behavior of ZrNiSi upon Sb doping, we calculated the electronic band structure for x = 0 and x = 0.125 in collaboration with Dr. Prasenjit Ghosh (see also [162] for more details). The calculated band structures for the two samples are shown in Fig. 5.15(a). We observe that Sb doping does not introduce significant changes in the band structure at low concentrations (x = 15 %). Rather, the primary effect of Sb doping is that it introduces extra electrons into the sample resulting in an upward shift of the Fermi energy into the conduction band. Based on this observation, we will assume that the band structure remains unchanged with Sb doping. The latter only introduces electrons that shift the electron chemical

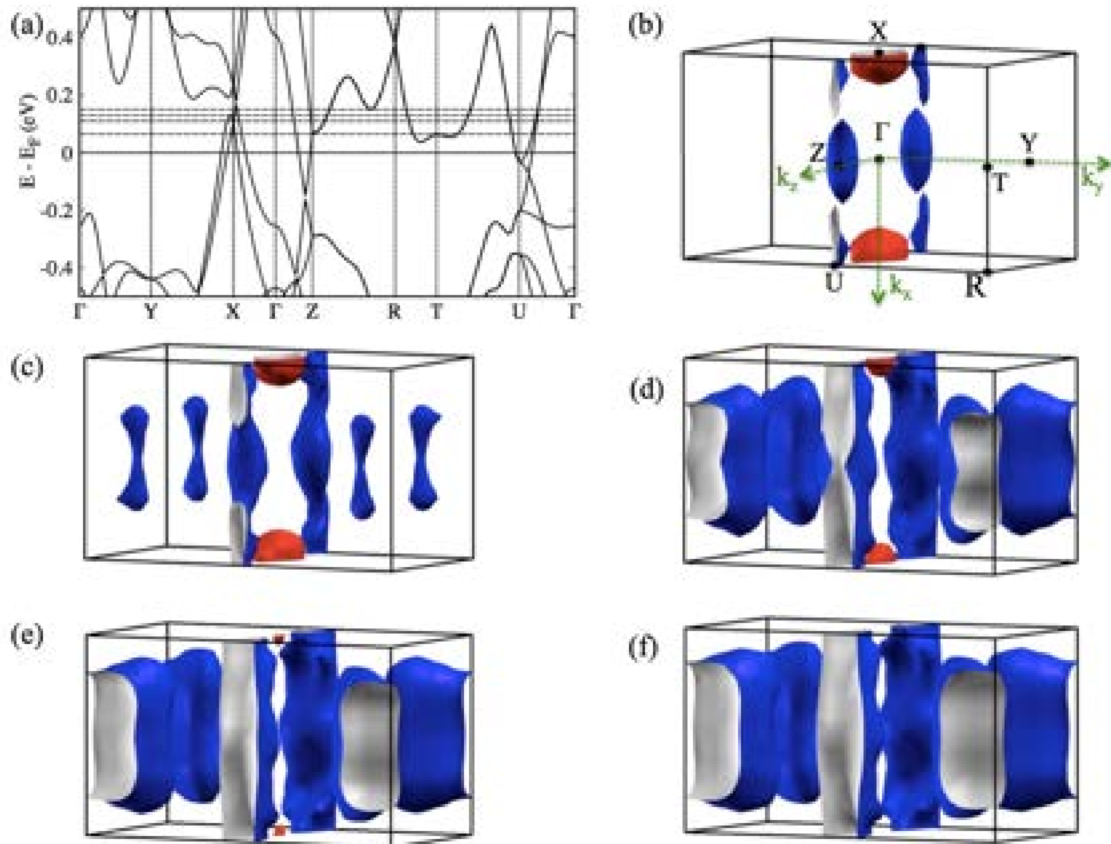

Figure 5.15: (a) Band structure of ZrNiSi (black) and 12.5 % doped (unfolded); the dashed horizontal lines above Fermi energy indicate chemical potential corresponding to 5 %, 10 %, 12.5 % and 15 % electron doping. (b-f) Constant energy surfaces at different electron chemical potentials that corresponds to 0 %, 5 %, 10 %, 12.5 %, 15 % electron doping showing the evolution of the electron (blue) and hole (red) pockects with increased doping. The scale bar in (a) is the magnitude (increasing, white-blue-green) of spectral weight, which characterizes the probability of the primitive cell eigenstates contributing to a particular supercell eigenstate of the same energy (calculated in collaboration with Dr. Prasenjith Ghosh).

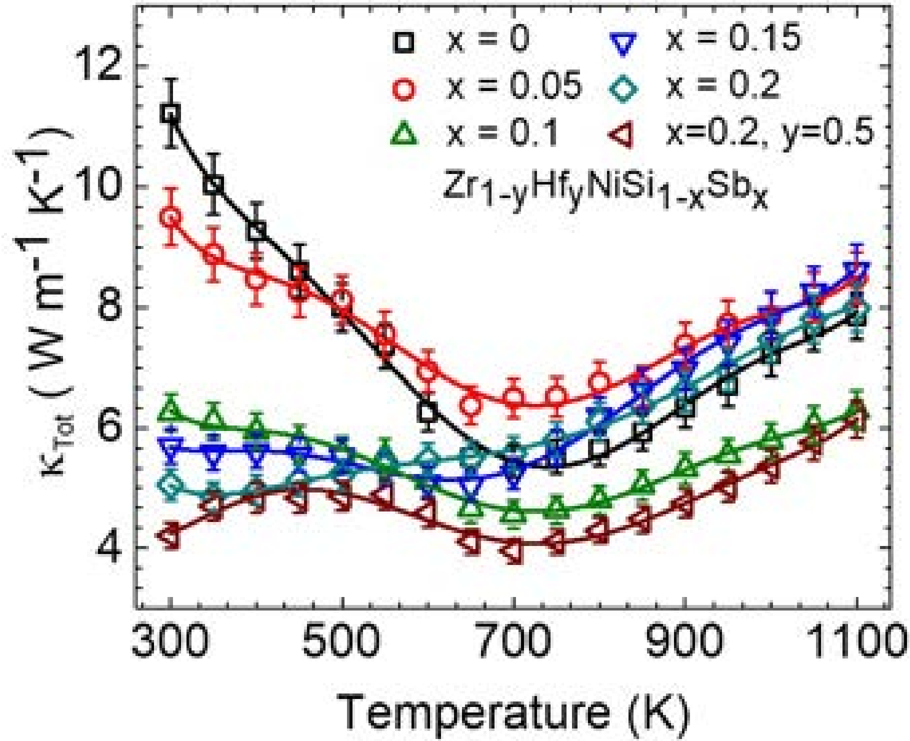

Figure 5.16: The temperature variation of thermal conductivity κ in samples $ZrNiSi_{1-x}Sb_x$($x = 0, 0.05, 0.1, 0.15, \& \ 0.2$) and $Zr_{0.5}Hf_{0.5}NiSi_{0.8}Sb_{0.2}$

potential. This is known as the rigid band approximation.

In our previous work [162], we have shown that for undoped ZrNiSi both electrons and holes contribute to the transport properties as is evident from the presence of electron and hole pockets in the Fermi surface (Fig 5.15(b)). This results in contributions to the Seebeck coefficient from both electrons and holes (bipolar effect). Since S for electrons and holes are opposite in sign, it results in an overall decrease in the Seebeck coefficient. However, as more electrons are introduced in the system due to Sb doping, the chemical potential moves up. As a consequence, the size of the hole pockets (red isosurfaces in Fig 5.15 (b)-(f)) gradually decreases while that of the electron pocket increases (blue isosurfaces in Fig 5.15 (b)-(f)), with the hole pockets reducing to a point at 12.5 % Sb-doping (Fig 5.15 (e)) and completely vanishing at 15% doping. This results in the reduction of the bipolar effect thereby causing the Seebeck coefficient to increase, contrary to the expected trend that the thermopower decreases with an increase in carrier concentration. Beyond this point, the transport properties are determined solely by electrons and we observe the expected decrease in thermopower as the doping concentration is further increased.

Thermal conductivity

The total thermal conductivity (κ_{Tot}) of our samples is shown in Fig. 5.16a. In the undoped sample, κ_{Tot} near 300K is about 12Wm^{-1}K^{-1} and with increase in

temperature it decreases approximately as 1/T due to phonon-phonon scattering. This decreasing trend continues up to T = 700 K above which κ_{Tot} increases reaching a value of about 8Wm^{-1}K^{-1} near 1100 K. Upon doping with Sb κ decreases. In x = 0.05, the value of κ_{Tot} near 300 K is 9Wm^{-1}K^{-1} and in x = 0.1 it decreases further to a value 6Wm^{-1}K^{-1}. With further decrease in Sb doping the decreasing trend continues, but at a relatively slower rate. This strong suppression of κ_{Tot} upon Sb doping can be attributed to the ionized impurity scattering due to doping of group 15 element Sb for the group 14 element Si. The mass difference between Si and Sb will also cause κ_{Tot} to lower further. Consequently, κ_{Tot} in the doped sample with x > 0.1 exhibits a weak temperature dependence. In all samples, heating above 700K led to an increase in κ_{Tot}. Further, the rate of increase (dκ/dT) is found to very nearly the same in all cases, analogous to the behavior of σ. This suggests that the dominant contribution to κ_{Tot} at high temperatures is of electronic origin. The lowest κ_{Tot} ($\approx$ 4Wm^{-1}K^{-1} near 300K) is observed for the $Zr_{0.5}Hf_{0.5}NiSi_{0.8}Sb_{0.2}$, where additional point scattering has been introduced by substituting Hf for Zr.

The experimentally measured κ_{Tot} can be written as an algebraic sum of lattice (κ_{Latt}) and electronic (κ_{ele}) contributions. The κ_e term is further related to σ through the Wiedemann-Franz law: $\kappa_{\text{ele}} = \sigma$LT where L is the Lorenz number, which can be taken as 2.44×10^{-8} W ΩK^{-2}, a value typically used for metals and degenerate semiconductors. Here, we have ignored the bipolar (κ_{bip}) contribution which has considerable contribution at high temperatures. Therefore, our analysis is valid only at temperatures below $\approx$ 500K. Above this temperature, the bipolarity becomes more and more pronounced as the sample temperature further increases which are evident from the temperature variation of S and σ. The plots of κ_{Latt} and κ_{ele} are shown in Fig. 5.17b and 5.17c, respectively. κ_{Latt} is obtained by subtracting κ_{ele} from κ_{Tot}. In pristine ZrNiSi, κ_l is $\approx$ 11Wm^{-1}K^{-1} near 300K and shows as approximately 1/T behavior upon heating suggesting the dominance of Umklapp scattering. With doping the magnitude of κ_l at 300K decreases substantially, and the temperature dependence of κ_l is also weaker than 1/T suggesting the presence of additional scattering mechanisms due to point mass fluctuation, disorder, and the interfaces between the phase segregated regions that appear due to a likely spinodal decomposition. In fact, in samples with 10, 15, and 20 % doping, κ_{Latt} becomes almost temperature independent. In the sample with the highest Sb doping, κ_{Latt} is $\approx$ 2Wm^{-1}K^{-1} over the whole temperature range. At 300K, κ_{Latt} is 93 % of the measured κ_{Tot} for pristine ZrNiSi, 85 % for x = 0.05, 79 % for x = 0.1, 77 % for x = 0.15, 63 % for x = 0.20, and 66% in the co-doped $Zr_{0.5}Hf_{0.5}NiSi_{0.8}Sb_{0.2}$ sample. The estimated κ_{Latt} for co-doped sample slightly exceeds that of $ZrNiSi_{0.8}Sb_{0.2}$ (i.e, without Hf), which appears counter-intuitive. However, this may be related to the fact that doping with Hf for Zr in $ZrNiSi_{0.8}Sb_{0.2}$ improves the phase stability and

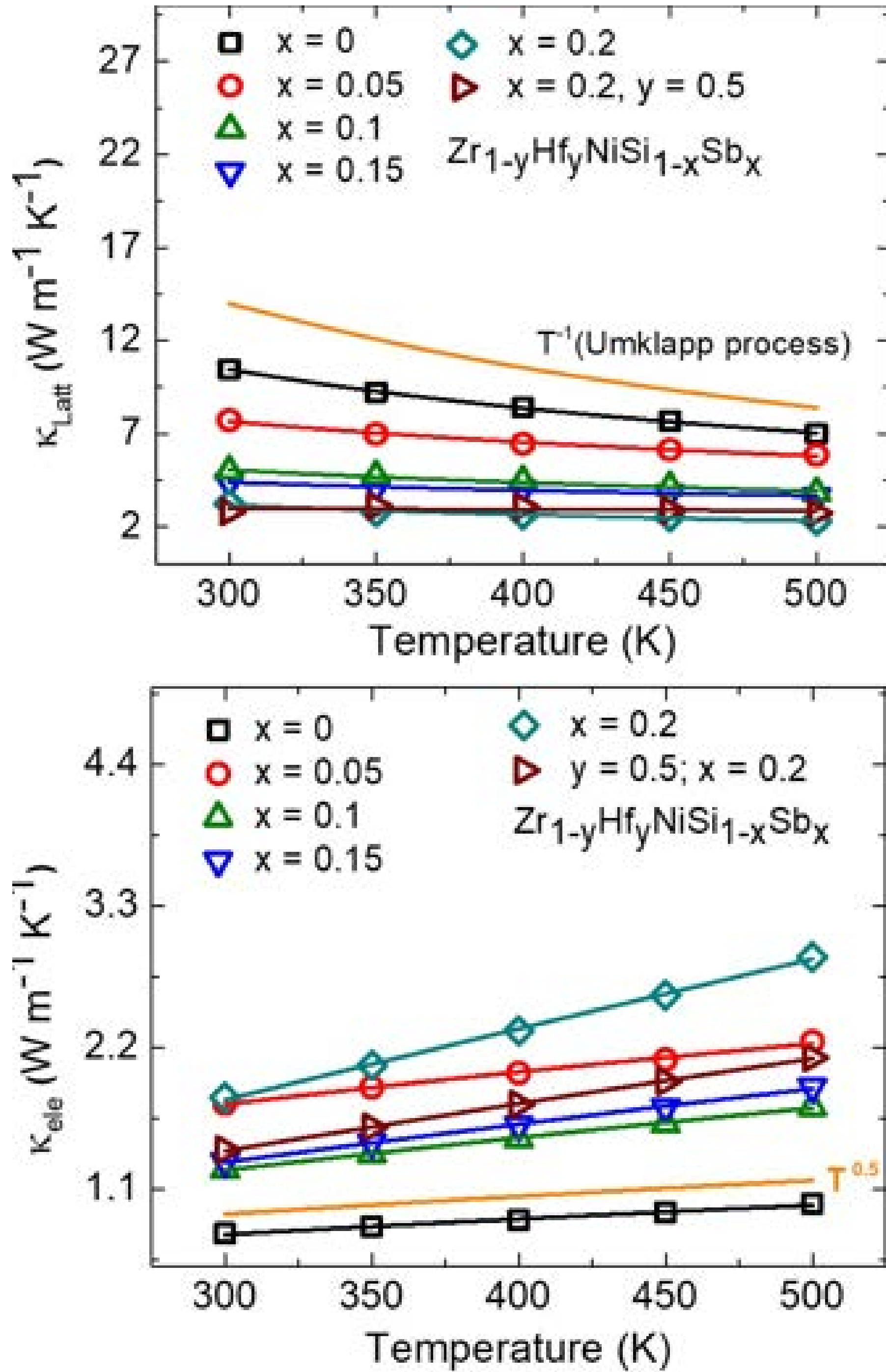

Figure 5.17: The temperature variation of lattice (κ_{Latt}) and electronic (κ_{ele}) components of κ_{Tot} are shown in (a) and (b), respectively for samples $ZrNiSi_{1-x}Sb_x$($x = 0, 0.05, 0.1, 0.15, \& \ 0.2$) and $Zr_{0.5}Hf_{0.5}NiSi_{0.8}Sb_{0.2}$

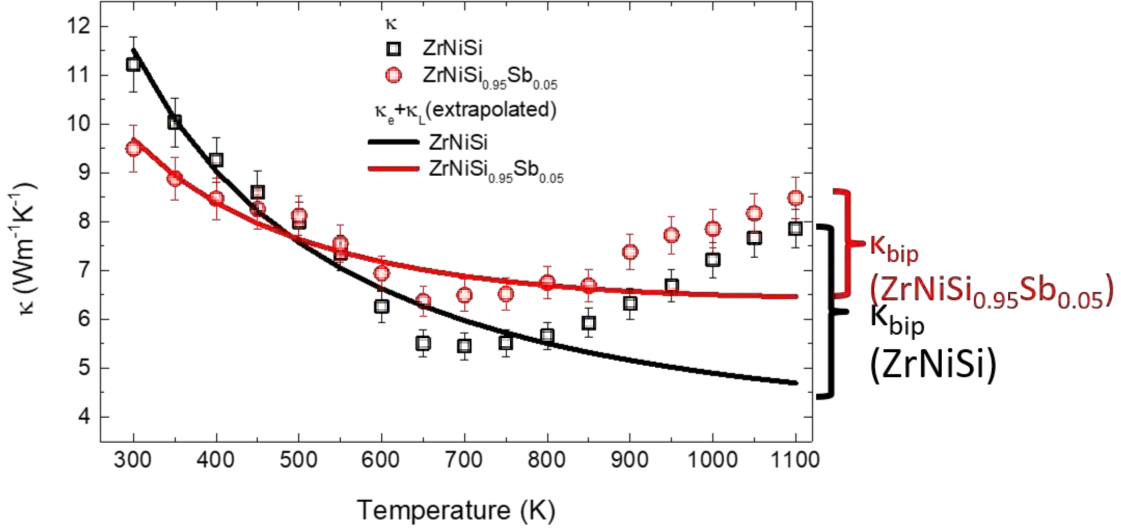

Figure 5.18: Temperature variation of the thermoelectric figure of merit zT of $ZrNiSi_{1-x}Sb_x$ ($x = 0$ and 0.05

chemical homogeneity, as discussed previously in Sec. 5.3.1 and Sec. 5.3.1. The component κ_e shows an increasing behavior with an approximately $T^{0.5}$ dependence which comes from an approximate $T^{-0.5}$ dependence of σ in this temperature range as shown in Fig. 5.12. To understand contribution of bipolarity on thermal conductivity we have tried to estimate κ_{bip} for homogeneous samples $x = 0$ and $x = 0.05$ in Fig. 5.18. To qualitatively estimate κ_{bip} we have extrapolated low temperature κ_{ele} and κ_{Latt} to high temperature and subtracted the sum of the two $(\kappa_{ele} + \kappa_{Latt})$ from κ_{Tot}. Thus, this explains the upturn in the thermal conductivity around 700 K which corroborates with bipolarity observed in electrical conductivity and thermopower measurements.

Thermoelectric figure-of merit

The thermoelectric figure-of-merit zT of our samples is shown in Fig. 5.19. In the pristine ZrNiSi, the zT near 1100K is about 0.005. With x = 0.05 it increases by a factor of 3, and with higher doping levels zT shows a peak near 700K. This temperature coincides with the peak in the Seebeck coefficient or minimum in the temperature variation of σ. In samples doped with x = 0.15 and x = 0.2, a peak zT of ≈ 0.023 is obtained. The observed increase in zT can be attributed to the decoupling of σ and S upon Sb doping, which is manifested as a simultaneous increase in both these quantities with electron doping. This decoupling is specific to ZrNiSi due to its peculiar electronic structure consisting of multiple electron and hole pockets at the Fermi level with conduction and valence bands separated by a pseudogap of about 0.1 eV. Similar enhancement in performance is also observed in the B factor shown in Fig. 5.20. Further enhancement in ZrNiSi is obtained by replacing 50 %

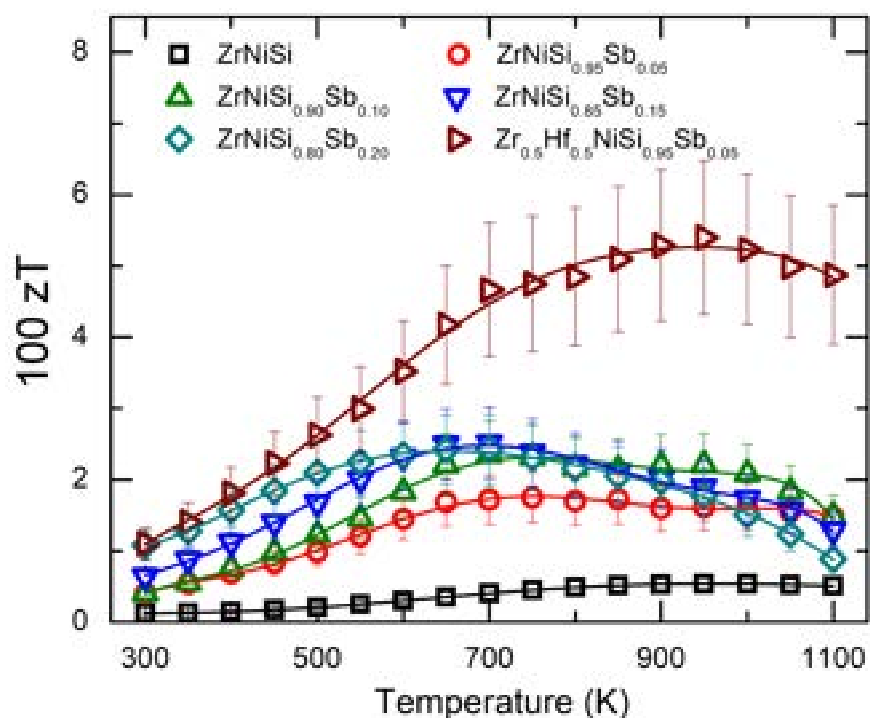

Figure 5.19: Temperature variation of the thermoelectric figure of merit zT of $ZrNiSi_{1-x}Sb_x(x = 0, 0.05, 0.1, 0.15, \& \ 0.2)$ and $Zr_{0.5}Hf_{0.5}NiSi_{0.8}Sb_{0.2}$

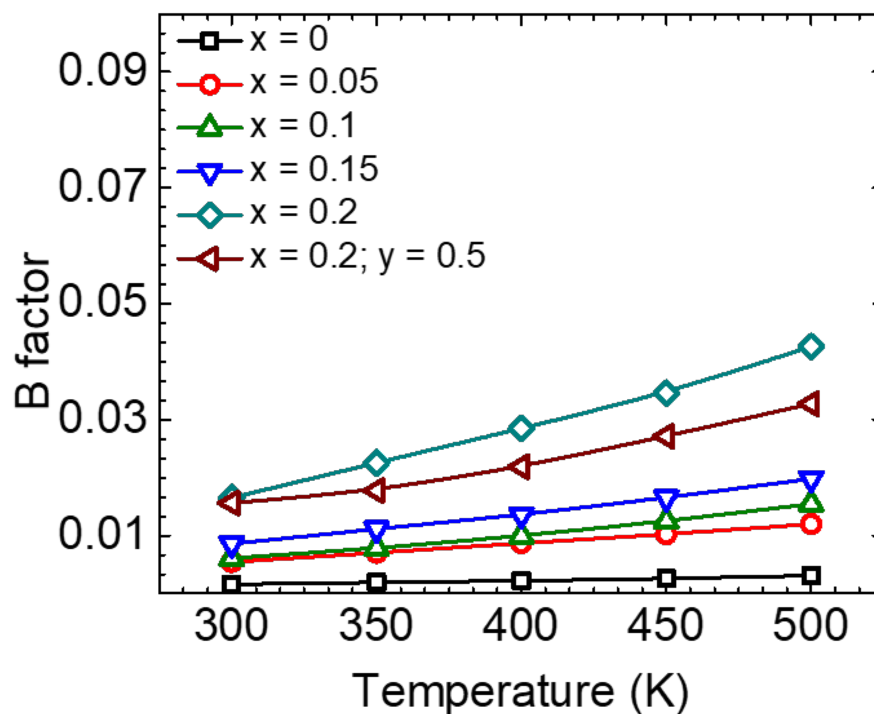

Figure 5.20: Temperature variation of the thermoelectric B factor zT of $ZrNiSi_{1-x}Sb_x(x = 0, 0.05, 0.1, 0.15, \& \ 0.2)$ and $Zr_{0.5}Hf_{0.5}NiSi_{0.8}Sb_{0.2}$ from 300 K to 500 K.

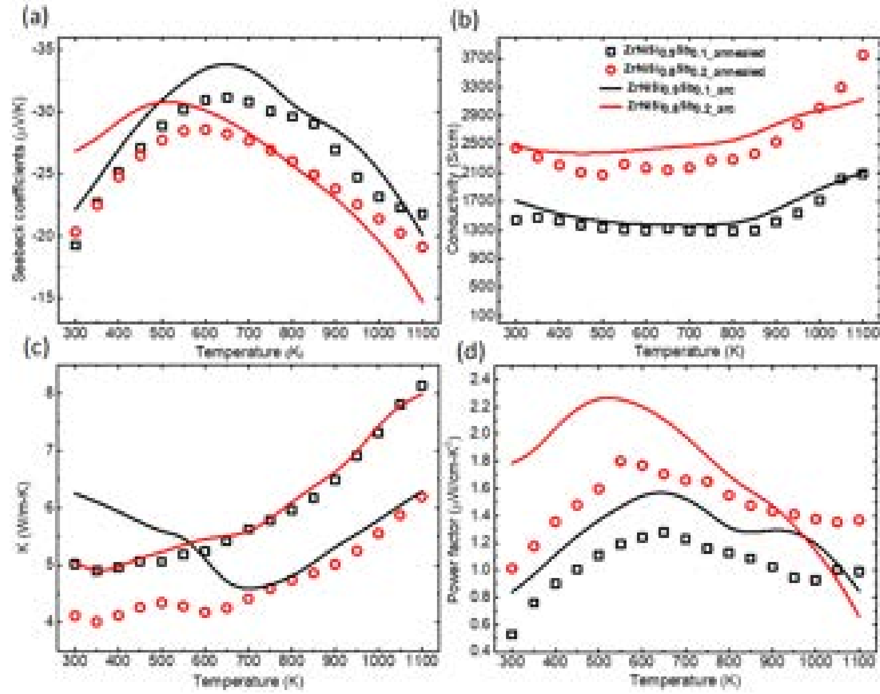

Figure 5.21: of arc melted (solid lines) and annealed (open data) sample of $ZrNiSi_{0.9}Sb_{0.1}$ and $ZrNiSi_{0.8}Sb_{0.2}$ post annealing

of Zr atoms in $ZrNiSi_{0.8}Sb_{0.2}$ by Hf. This not only improved the phase stability and chemical homogeneity, resulting in the highest electrical conductivity of all the samples investigated here but also decreases the total thermal conductivity further. As a result, the peak value of zT for this sample is 0.055, which is more than an order of magnitude enhanced concerning the pristine ZrNiSi. Previously, the highest zT reported for TiNiSi structure-type was 0.032 at 600 K in vanadium doped TiNiSi [86].

Effect of annealing

The thermoelectric properties for annealed samples to understand the effect of heat treatment are shown in Fig. 5.21. The Seebeck coefficient and conductivity have some changes in value concerning arc-melted samples. The thermal conductivity has changed drastically due to changes in the sample morphology before and after the annealing experiments. To understand the change in thermal conductivity we have obtained electronic as well as lattice thermal conductivity parts using Wiedemann-Franz Law as done for arc-melted samples. The plots for κ_e and κ_L are shown in Fig. 5.22, we observe a decrease in Ke value for both the samples concerning their arc melted counterpart. The slope of conductivity increases for x = 0.1 and decreases slightly for x = 0.2 sample after annealing. Lattice thermal conductivity, κ_L of both the samples has decreased and they have nearly similar temperature dependence. Annealing samples result in single-phase formation and spinodal type decomposition

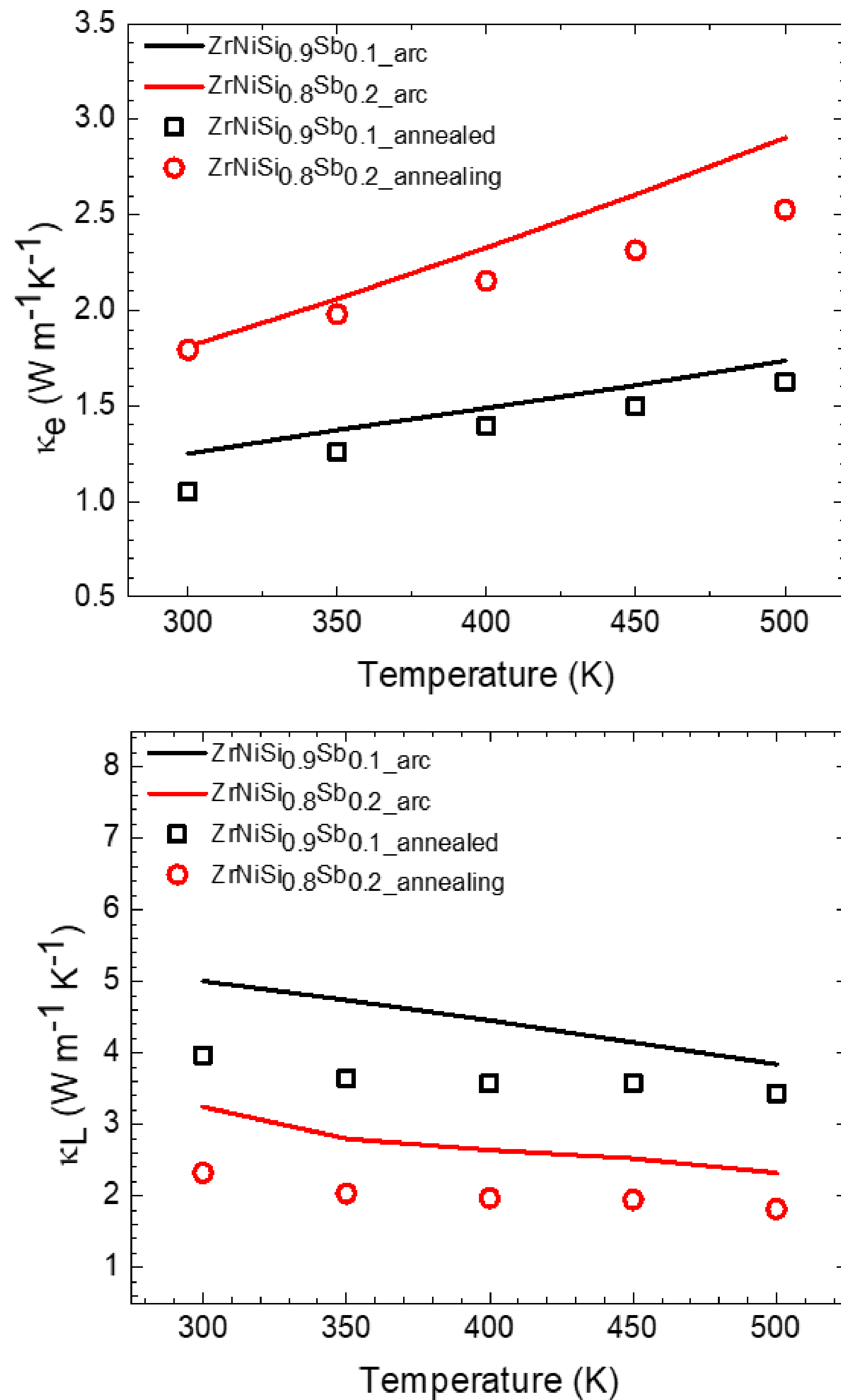

Figure 5.22: κ_e and κ_L of arc melted (solid lines) and annealed (open data) sample of $ZrNiSi_{0.9}Sb_{0.1}$ and $ZrNiSi_{0.8}Sb_{0.2}$ post annealing

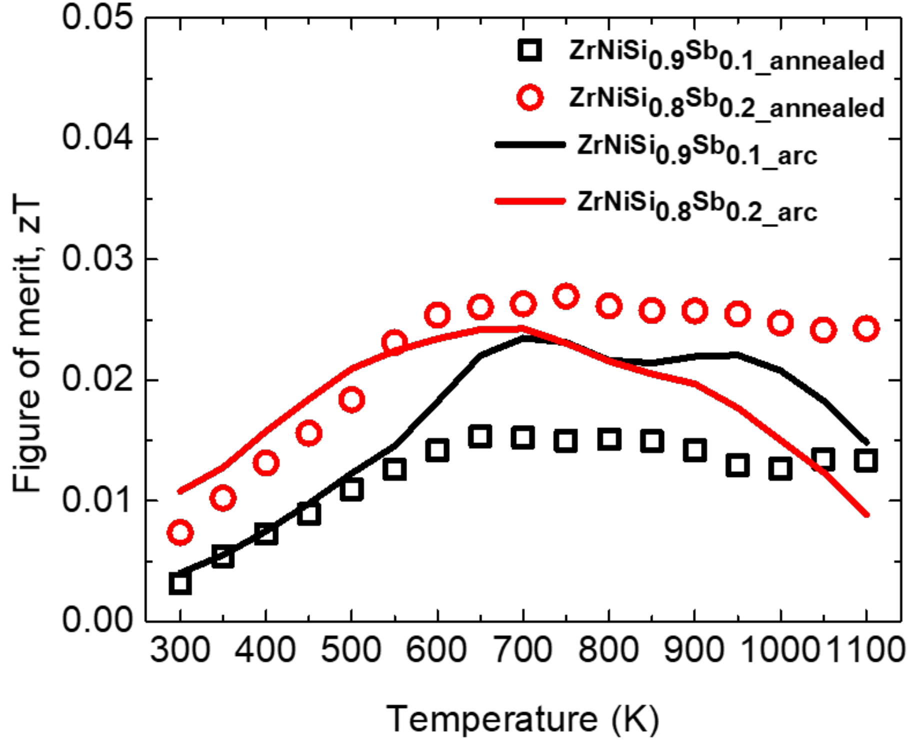

Figure 5.23: Figure of merit of arc melted (solid lines) and annealed (open data) sample of $ZrNiSi_{0.9}Sb_{0.1}$ and $ZrNiSi_{0.8}Sb_{0.2}$ post annealing

in x = 0.2 samples. For x = 0.2 samples the decomposition leads to micron size islands of less Sb content phase where high Sb content phase forms the matrix. As micron-size grains do not affect lattice thermal conductivity much hence thermal conductivity of x = 0.2 is just a little smaller than the x = 0.1 sample. Also the change in the temperature dependence of thermal conductivity of x = 0.1 sample at low temperature (≤ 500 K) is mostly due to increased slope of κ_e and decreased slope of κ_L. Overall thermal conductivity has decreased for x = 0.2 after annealing, as the matrix has higher Sb doping and islands have less Sb content. highly doped Sb matrix thus scatter more phonon.

The figure of merit, zT of annealed samples are shown in comparison to just arc melted samples in Fig. 5.23. The figure of merit, zT of annealed x = 0.1 sample is less than just arc melted sample. For x = 0.2 figure of merit, zT is higher than the arc melted sample due to a decrease in thermal conductivity.

5.4 Summary and Conclusions

In this chapter, we show that by doping with Sb for Si (i.e, an electron doping) in ZrNiSi, S and σ that are known to show an inverse correlation in general, can both be simultaneously increased. In the doped sample, σ at 300K increases from 1000Scm^{-1} to as high as 2500Scm^{-1}; at the same time, the peak value of S could

be enhanced by as much as a factor of two. Our first-principles Density Functional Theory based band structure calculations show that the enhanced σ is doped samples is due to an increase in the carrier concentration upon Sb doping; simultaneously, the hole Fermi surface shrinks and consequently the thermopower, which has both electron and hole contributions in the undoped compound, also increases as the hole contribution to S decreases and electron contribution increases due to flat bands near the T-point of the Brillouin zone. Our calculations also suggest that the hole-pocket should completely disappear around 17 % of Sb doping. Hence for higher doping levels than 17 %, the thermopower should decrease by inverse dependence of S on the carrier concentration ($S \propto n_e^{-\frac{2}{3}}$) in the single parabolic model. Indeed, we find that the thermopower of our 20 % Sb doped decreased concerning the sample with 15 % Sb doping.

As far as the synthesis of Sb-doped ZrNiSi is concerned, we found that up to 5 % doping a single-phase sample can be obtained by simply arc-melting. Nominally 10 % Sb doped sample became phase pure and chemically homogeneous only after annealing for 7 days at 900 °C. The as-melted or unannealed sample showed phase segregation due to a spinodal-type decomposition with two coexisting phases with different Sb/Si ratios. This behavior persisted for higher Sb doping also, and effectively helped lower the thermal conductivity of ZrNiSi by a factor of 6, i.e., from $12 \mathrm{Wm^{-1}K^{-1}}$ to $\approx 2 \mathrm{Wm^{-1}K^{-1}}$ at 300K.

As a result, the peak thermoelectric figure-of-merit (zT) of ZrNiSi increased from 0.005 to 0.023 for 20 % Sb doping. Further enhancement in zT is obtained by Hf doping at the Zr-site which not only improved the phase stability and chemical homogeneity, enhancing σ further but also lowered the total thermal conductivity, resulting in a peak zT value of 0.055 which is more than an order of magnitude higher than for the pristine ZrNiSi.

While the overall zT of 0.055 is too low for any practical application, our work provides proof of the concept that in the semimetals of the orthorhombic TiNiSi family, due to some specific peculiar features of their electronic band structure (presence of a pseudogap, several small electron and hole-pockets, and a flat or dispersionless band around the T-point [162], the electrical conductivity and thermopower can be effectively decoupled over a wide range of electron doping. This principle can be employed on other members of the TiNiSi to improve the zT in this family of compounds further.

Chapter 6

Double Heuslers

6.1 Introduction

We have seen thermoelectric properties of half Heuslers and related structures in previous chapters. Half Heuslers generally show a high thermal conductivity and at the same time a reasonably high power factor. In previous chapters, we show that doping enhances the power factor further and at the same time reduces thermal conductivity due to doping enhanced disorder in structure. In the previous chapter, we examined how 20 % vacancies at the X site in XYZ can stabilize the HH structure with VEC 18 (in stoichiometric XYZ, the VEC is 19) [205, 206, 222]. Stabilizing a new VEC 18 HH is important as the VEC 18 HHs are generally good thermoelectrics due to their filled bonding orbitals separated from the empty antibonding orbitals by a finite bandgap.

In this work, we have tried to stabilize HH alloys with VEC 18 by alloying X_1Y_1Z with VEC 17 and X_2Y_2Z with VEC 19. Here, our choice of VEC 17 X_1Y_1Z is TiFeSb, and that VEC 19 X_2Y_2Z is ZrNiSb. ZrNiSb exists in the orthorhombic phase and does not form in the pure phase in 1:1:1 composition [162]. Similarly, TiFeSb does not form as a pure phase but forms as a combination of the HH phase along with a few secondary phases. Several studies have shown that TiFeSb can exist as a pure HH phase with some off-stoichiometry [178, 4, 182, 223]. It is, therefore, interesting that their solid solutions of the form $(\mathrm{ZrNiSb})_{1-x}(\mathrm{TiFeSb})_x$ form single-phase HH alloys over a wide range of values of x indicating that these alloys are stabilized by their high-configurational entropy. Henceforth, we will refer to these alloys as double Heusler (DH). The DHs are the high-entropy analogs of the HHs where one or more Wyckoff sites in XYZ are shared by two or more elements [6, 59, 117]. The double Heusler alloys realized here exhibit both n-type and p-type behavior depending on the vlue of x: n-type for $x \leq 0.5$ and p-type for $x > 0.5$.

6.2 Experimental Details

Samples were synthesized using the arc-melting technique under high-purity argon gas. Stoichiometric amounts of Zr (Sigma Aldrich, $\geq$ 99%), Ni (Sigma Aldrich, $\geq$ 99.9%), Fe pieces(Alfa Aesar, 99.98 %) ,Ti pieces (Nanoshel, 99.9 %) and Sb shots(Alfa Aesar, $\geq$ 99.999%) were used. The starting precursors were weighed according to the required stoichiometry and loaded on the water-cooled copper hearth of the arc-furnace as described in the experimental chapter. The chamber was evacuated and purged with high-purity argon gas repeatedly several times before striking the arc. A zirconium getter was used to absorb any remnant oxygen in the chamber. The ingot was flipped over and re-melted five to six times to ensure a good homogeneity. The physical properties were measured on the as-melted sample. For this purpose, the arc-melted ingots were cut using a low-speed diamond saw (South Bay, USA) into a disc-shaped specimen for the measurement of thermal conductivity, and a rectangular bar-shaped specimen for resistivity and thermopower.

To check the phase formation and presence of secondary phase(s), if any, powder X-ray diffraction was done at various stages of the sample synthesis (Bruker, D8 Advance). The lattice parameters were obtained by Le-Bail fitting of the Rietveld refinement. Polished specimens cut from the as-melted ingots were also examined using a Field Effect Scanning Electron microscope (FESEM) (Ultra Zeiss plus), equipped with an Energy Dispersive X-ray (EDX) analysis attachment (Oxford Instruments). The resistivity and thermopower were measured simultaneously using the Linseis LSR-3 set-up. The average uncertainties in these measurements are less than 5%. The thermal diffusivity (D) was measured using the Linseis LFA-1000 instrument on polished discs that were homogeneously coated with a very thin layer of graphite. The average uncertainty in thermal diffusivity using this set-up is near $2-3$ %. Thermal conductivity (κ) was obtained from the thermal diffusivity by the formula $\kappa = D\ \rho C_{\mathrm{p}}$ where ρ is the mass density, and C_{p} is the specific heat for which we used the value corresponding to the Dulong-Petit limit (3nR = 74.8Jmol^{-1} K^{-1}). While this may be a little overestimation, especially near room temperature, we used this to get an upper bound on κ. For mass density, we used the sample dimensions and sample mass both of which were reasonably accurately accessible. The arc-melted ingots were free of micropores as revealed in the electron microscope images of the polished specimens. The mass density is estimated to be close to 95% for all the samples. HRTEM (JEOL JEM 2200FS 200 keV) was used to collect high-resolution images and for obtaining SAED patterns with the GMS-3 software package to assess the crystallinity of our samples. For examining the sample under the HRTEM, a piece of the ingot was hand-ground into a fine powder, which was transferred onto a TEM Cu grid in an ethanol-based solution that was oven-dried

at 50°C for close to an hour. The Cu grid was subsequently loaded on the TEM sample stage and plasma cleaned at 250 eV for about 15 minutes.

6.3 Results and Discusssion

6.3.1 Computation results

To understand the electronic transport properties we have optimized the structure of the double Heusler $(ZrNiSb)_{0.5}(TiFeSb)_{0.5}$. The DFT calculation was done in collaboration with Dr. Prasenjit Ghosh. The two possible symmetry compatible structures are shown in Fig. 6.1 and Fig. 6.2. These are labeled as composite1 and composite2. Composite1 was found to have lower enthalpy by 11.5 meV. This was therefore considered for further calculation. The Theoretical lattice parameter of is 6.03 Å for this structure is in good agreement with the experimental value of 6.003 Å. Fig. 6.3 shows the band structure and density of states for this structure. It has an indirect bandgap of 0.33 eV, with valence band maxima at R-point and conduction band minima at Γ-point. It can be seen that Ti d-states have a dominant contribution in the conduction band and Fe d-state has a dominant contribution in the valence band. Further, we have also calculated the phonon dispersion for $\mathbf{(ZrNiSb)_{0.5}(TiFeSb)_{0.5}}$ **(Composite1)** to understand the low thermal conductivity in these samples. Fig. 6.4 shows the phonon dispersion calculated for Composite1. Phonon dispersion is calculated using DFT perturbation theory in collaboration Dr. Prasenjit Ghosh's group. We find that throughout the BZ the phonon frequencies are real except for some long wavelength modes along the $\Gamma \rightarrow R$ direction where there are phonon modes with small imaginary values. However, these are within the error bar of the calculations. Our results suggest that the structure is dynamically stable. The phonon spectrum can be divided into three regions. The density of states, shown in Fig. 6.4(b) shows that for the modes with frequencies less than 150 cm^{-1}, the dominant contributions are coming from the vibrations of Sb atoms while for the modes with frequencies lying between 150 and 250 cm^{-1} all the atoms of the crystal contribute. Further, the modes with frequencies larger than 250 cm^{-1} originate primarily due to the vibrations of Fe atoms. In the Fig. 6.4 we also observe interaction of lower frequency optical phonons with acoustic phonons which generally leads to higher scattering and lower thermal conductivity. To estimate the minimum lattice thermal conductivity ($\kappa_{l,min}$), we used the Cahill's model [**?**] whose formula is given as:

$$\kappa_{l,min} = (\frac{\pi}{6})^{(1/3)} k_B n^{(2/3)} \sum_i v_i (\frac{T}{\theta_i})^2 \int_0^{(\frac{\theta_i}{T})} \frac{x^2 e^x}{(e^x - 1)^2} dx \qquad (6.1)$$

where k_B is the Boltzmann constant, n is the number density of atoms, v_i is the average sound velocity of each of the acoustic modes and θ_i is the corresponding cutoff frequency. In the integral x is a dimensionless quantity given by $x = \frac{\hbar\omega}{k_B T}$; ω and T being the phonon frequencies and temperature, respectively. The values v and θ_i used in minimum lattice thermal conductivity is given in Table 6.1. For this material $n = 5.47 \times 10^{28}$ m^{-3}. The minimum lattice thermal conductivity $\kappa_{Latt,min}$ for this structure is estimated to be around 1.65 $Wm^{-1}K^{-1}$. This is used further to compare with the experimental lattice thermal conductivity.

Table 6.1: Average sound velocities (v) and cut off frequencies θ_i for $(ZrNiSb)_{0.5}(TiFeSb)_{0.5}$. These are used to compute $\kappa_{l,min}$ using Eqn. 6.1.

parameters	v(m/s)	θ_i(K)
TA1 mode	6210.62	109.19
TA2 mode	5822.55	102.28
LA mode	8526.99	130.85

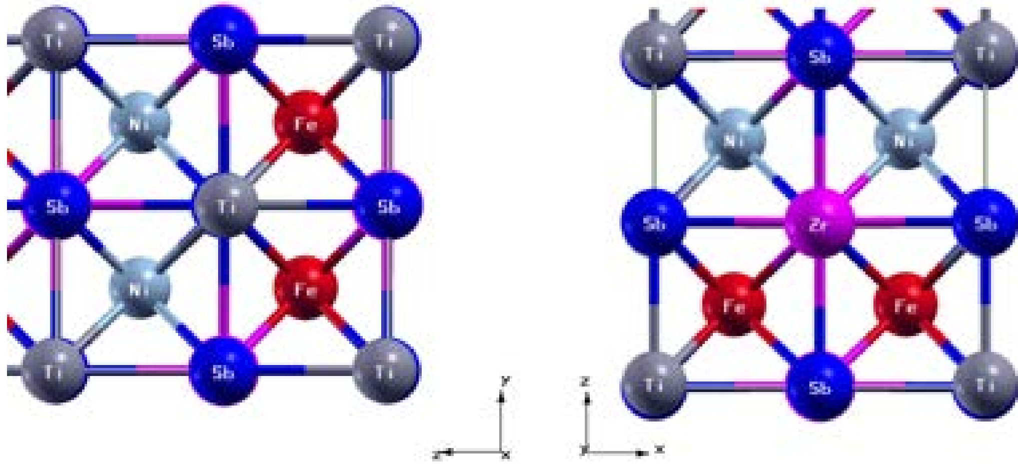

Figure 6.1: Structure of $(ZrNiSb)_{0.5}(TiFeSb)_{0.5}$ composition1.

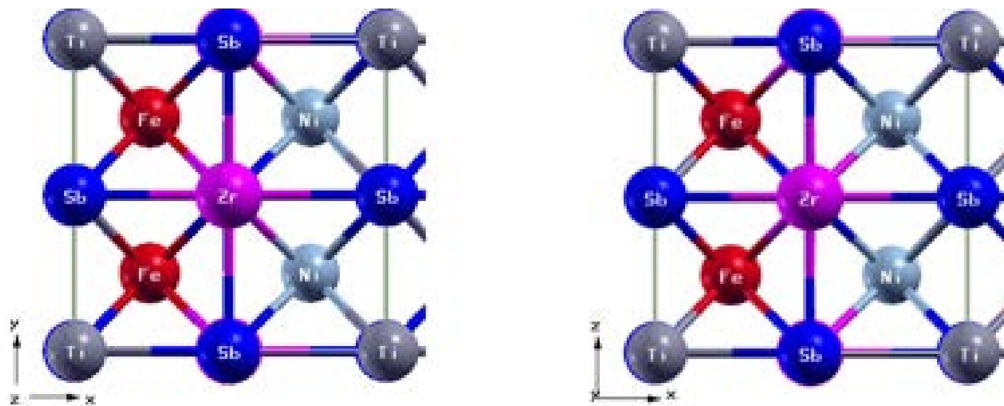

Figure 6.2: Structure of $(ZrNiSb)_{0.5}(TiFeSb)_{0.5}$ composition2.

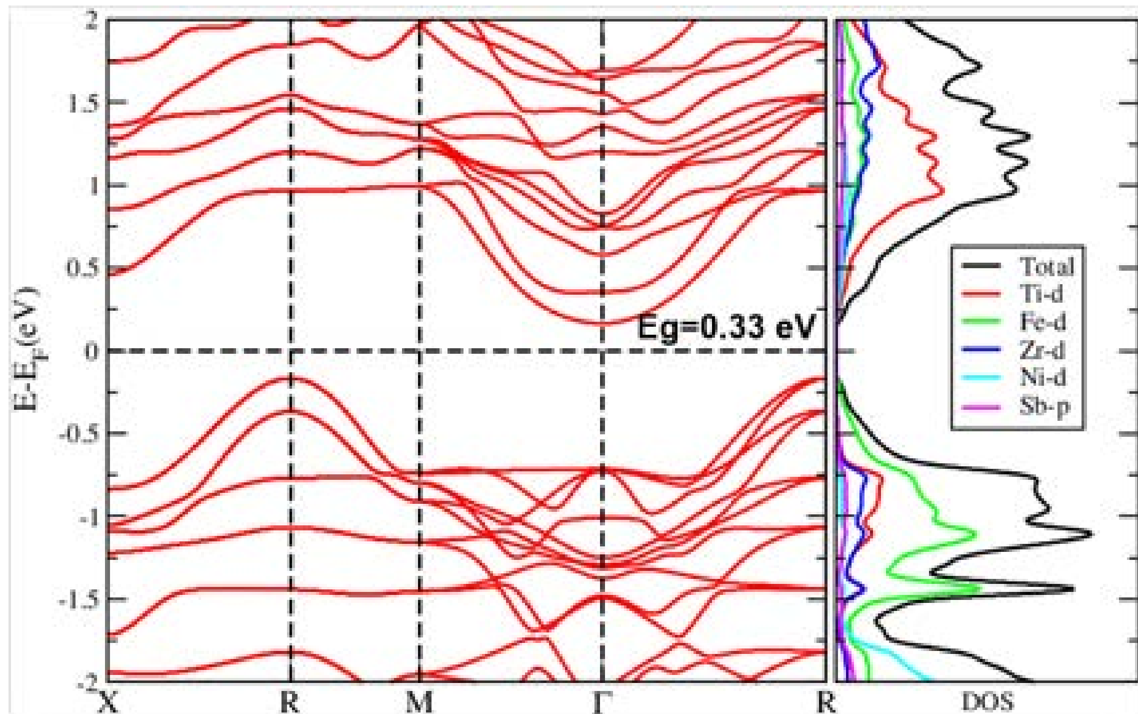

Figure 6.3: Density of states and band structure of $(ZrNiSb)_{0.5}(TiFeSb)_{0.5}$ composition1.

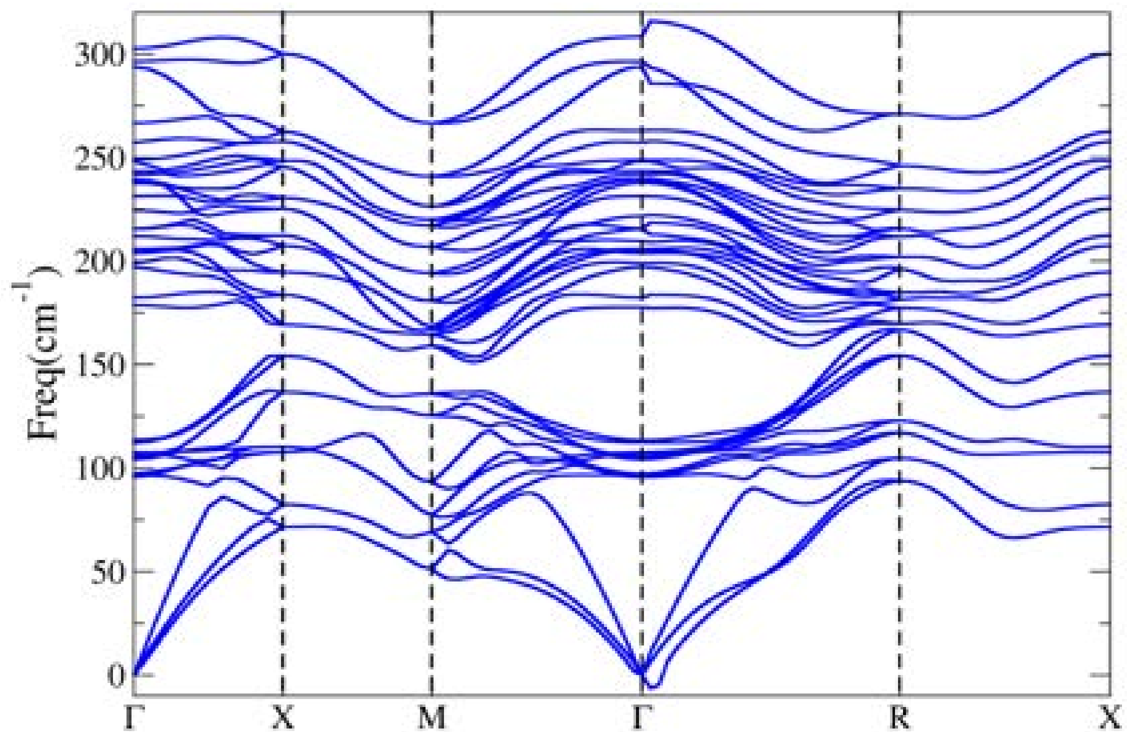

Figure 6.4: Phonon density of states of $(ZrNiSb)_{0.5}(TiFeSb)_{0.5}$ composition1.

6.3.2 Structructural characterization

X-ray diffraction

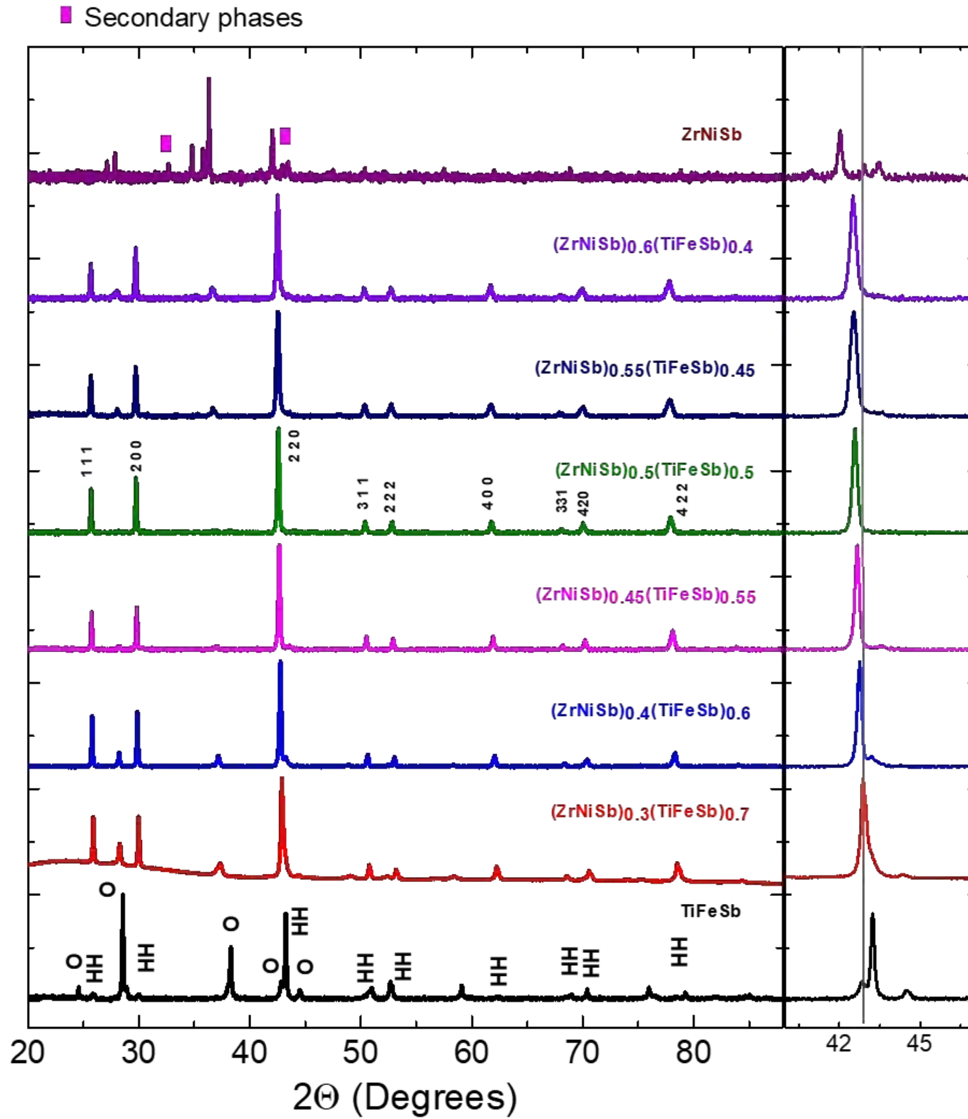

Figure 6.5: Powder Xray diffraction of composites of TiFeSb and ZrNiSb

We synthesized eight compositions of $(ZrNiSb)_{1-x}(TiFeSb)_x$ where (x = 0, 0.4, 0.45, 0.5, 0.55, 0.6, 0.7, 1). The end members ZrNiSb (x = 0) and TiFeSb (x = 1) exist in the orthorhombic phase (space group Pnma) and cubic phase respectively, but they do not form in the pure phase. ZrNiSb is a VEC = 19 compound and TiFeSb is a VEC = 17 compound. Thus composite samples with formula $(ZrNiSb)_{1-x}(TiFeSb)_x$ should have VEC in the range 17 to 19 where $0 < x < 1$. Sample with $x = 0.5$ should have VEC = 18. X-ray diffraction patterns for all the samples are shown in Fig. 1. Sample with $x = 0.5$, show only the peaks related to the half Heusler structure, a few weak extra peaks indicating a very small amounts of a secondary phase is also observed. The secondary phase was mostly identified

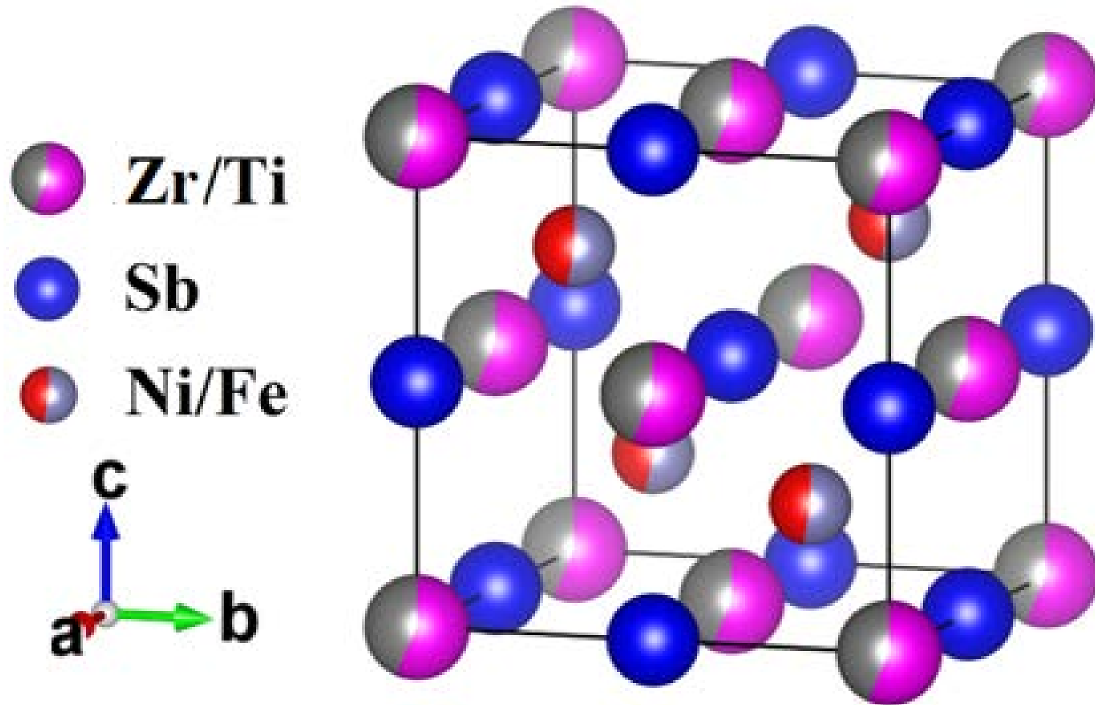

Figure 6.6: The double Heusler alloy $(Zr_{0.5}Ti_{0.5})(Ni_{0.5}Fe_{0.5})Sb$. The unit cell is cubic (space group *F-43m* as that of HH XYZ but with X site shared by Zr and Ti and Y site shared equally by Ni and Fe.)

as an orthorhombic phase similar to the ZrNiSb. The existence of a dominant half Heusler phase rather than a mixture of the two end-members shows the formation of a double Heusler-like phase in these samples. The double Heusler unit cell for the $x = 0.5$ composition is shown in Fig. 6.6.

As shown in the previous chapter, while ZrNiSb can be synthesized in a pure form by taking 5 % excess Zr, TiFeSb in stoichiometric composition form as a mixture of an orthorhombic phase which corresponds to $TiFe_{1-z}Sb$ (TiNiSi-type, Pnma spacegroup) [178, 182, 120] and a possible HH phase. The x-ray powder diffraction data of other samples (x = 0.4, 0.45, 0.55, 0.6, and 0.7) show that for them also the half-Heusler phase is the majority phase and the secondary phase has been identified as orthorhombic phase similar to ZrNiSb . The two-phase Rietveld refinement done on these samples is shown in the Appendix C.

We can clearly see the shift in 220 peaks in Fig. 6.5, which signifies expansion of the lattice parameter with increase in the value of x from x = 0.4 to x = 0.7. The lattice parameter of the HH phase for all the six composites has been plotted in Fig. 6.7. The unit cell volume for the HH (majority) and orthorhombic phase, obtained using the Rietveld refinement, is shown as a function of 'x' in Fig. 6.8. The Lattice volume expansion with an increase in x is observed for both HH and orthorhombic phases. This is due to the incorporation of Zr in the structure which is bigger in size with respect to Ti. Lattice parameter of the sample with $x = 0.5$ is 6.003 Å which

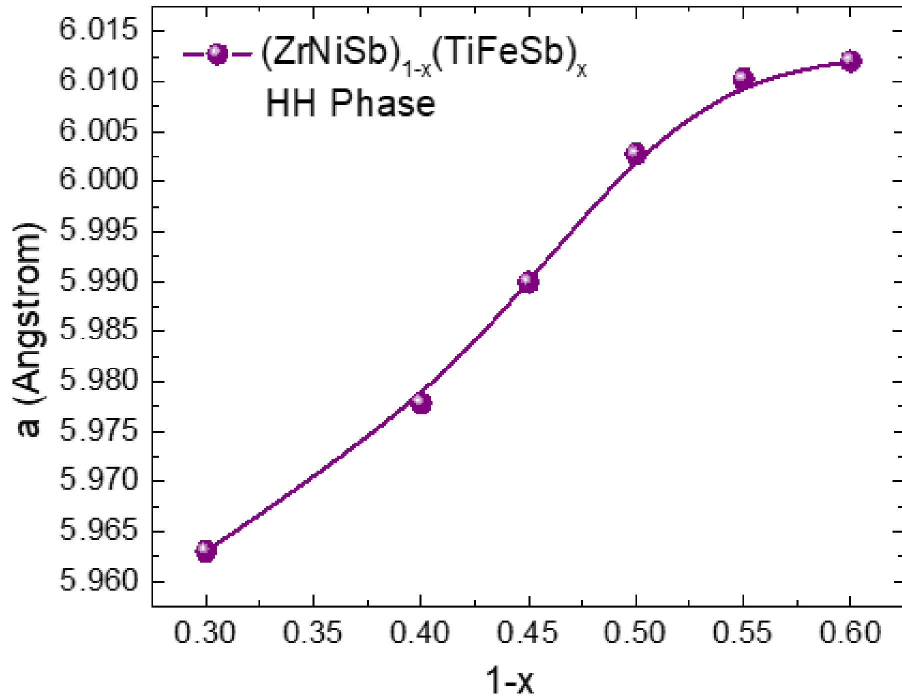

Figure 6.7: Lattice parameter and cell volume of $(ZrNiSb)_{1-x}(TiFeSb)_x$ in half Heusler structure with spacegroup *F-43m* obtained from refinement

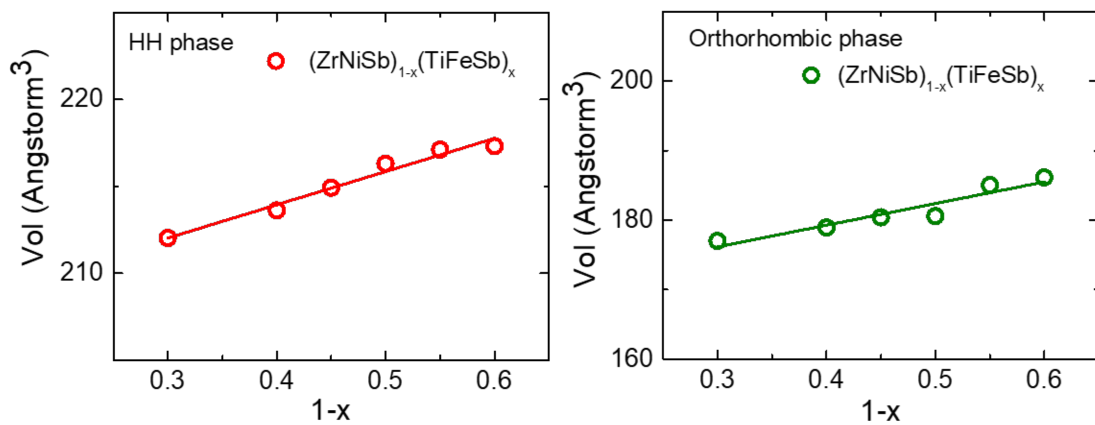

Figure 6.8: (a) ,Unit cell volume of $(ZrNiSb)_{1-x}(TiFeSb)_x$ in half Heusler structure with spacegroup *F-43m* and (b) unit cell volume of secondary phase (orthorhombic TiNiSi structure type, space group Pmna).

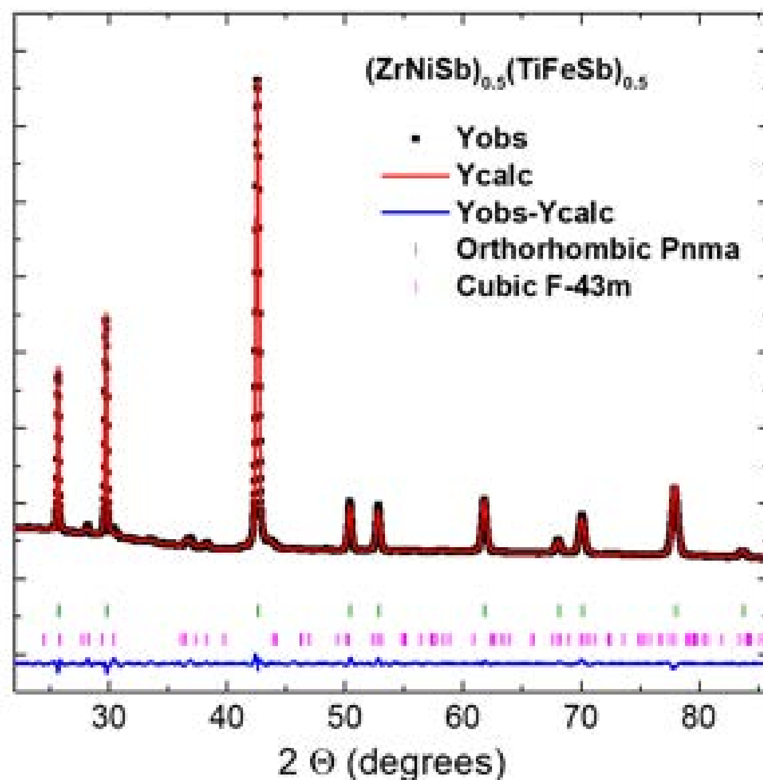

Figure 6.9: Refinement of powder Xray diffraction of $(ZrNiSb)_{0.5}(TiFeSb)_{0.5}$

is similar to 5.987 Å as reported for $TiFe_{1.25}Sb$ in [182]. The phase fraction of the HH phase is more than 93 % but decreases strongly on either side of $x = 0.5$.

Microstructure: FESEM and HRTEM

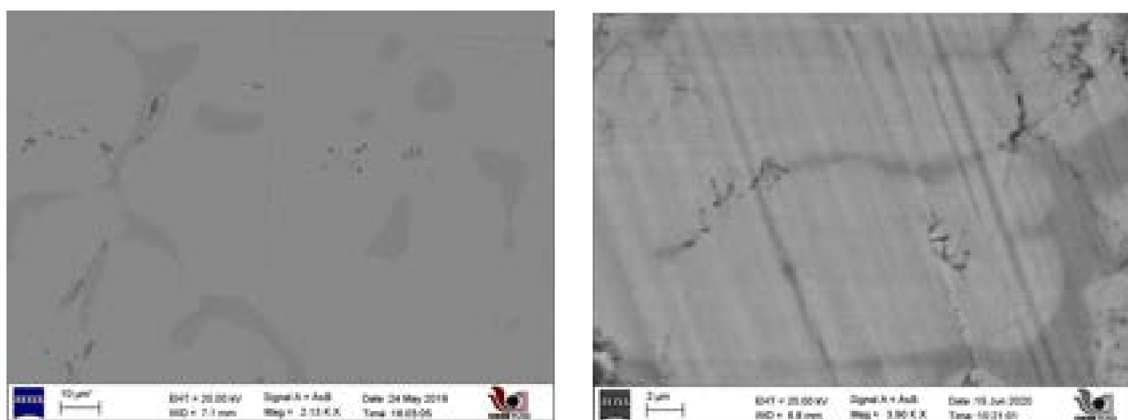

Figure 6.10: FESEM of ZrNiSb and TiFeSb showing existence of two phases

Backscattered FESEM images of TiFeSb and ZrNiSb samples synthesized in the stoichiometric ratio are shown in Fig. 6.10. The presence of impurity phases is evident in these images. TiFeSb has been obtained as a combination of two phases

with two different compositions $Ti_{36}Fe_{24}Sb_{40}$ and $Ti_{20}Fe_{60}Sb_{20}$; similar composition has been reported in a previous work [182] in arc-melted samples. Similarly we have shown the existence of two phases in ZrNiSb as $Zr_{46}Ni_{28}Sb_{25}$ and $Zr_{28}Ni_{38}Sb_{34}$.

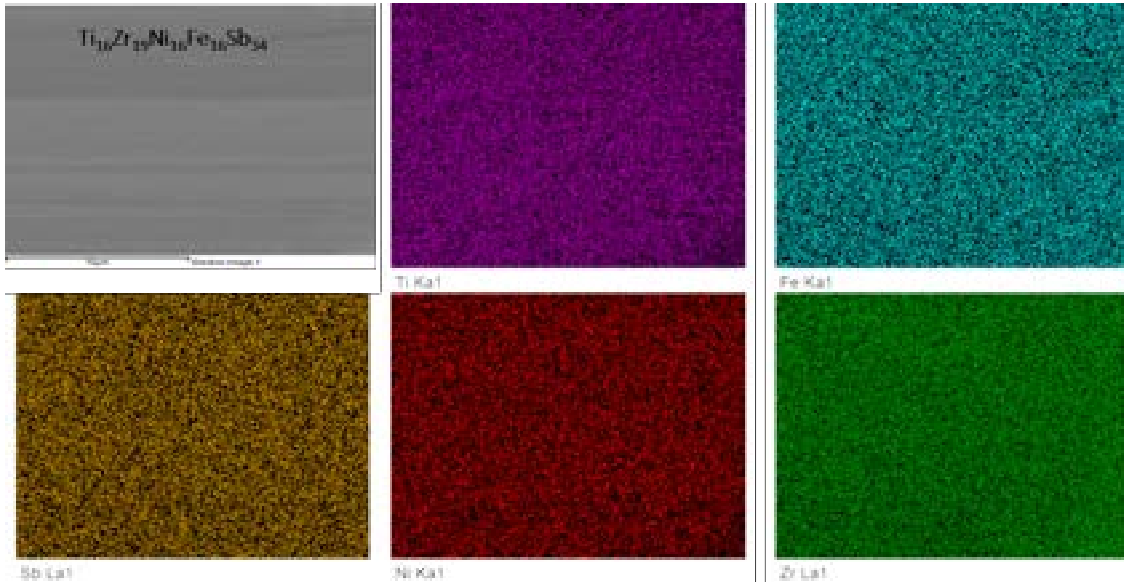

Figure 6.11: Chemical mapping of the double Heusler phase of $(ZrNiSb)_{0.5}(TiFeSb)_{0.5}$ sample using FESEM

In x = 0.5 samples, we see a homogeneous distribution of all the elements as shown in Fig. 6.11 obtained on polished ingot pellets through FESEM. On a large piece of the sample, a careful study using FESEM showed precipitation of $ZrSb_2$-rich and FeSb-rich phases as shown in Fig. 6.13 which is consistent with the powder x-ray diffraction. Elemental mapping shown in Fig. 6.12 also show the FeSb-rich secondary phase. Elemental mapping done using the HRTEM in Fig. 6.20 show a micrometer sized sample piece (agglomerated grains of smaller size), where one can see a homogeneous distribution of the elements according to their nominal composition. The composition obtained experimentally using HRTEM is $Ti_{19}Zr_{14}Ni_{16}Fe_{16}Sb_{33}$ which is close to the nominal composition. Further, we have taken HRTEM micrographs and SAED patterns on this sample. Fig. 6.19 shows a HRTEM micrograph with SAED pattern shown in inset and a FFT image shown in Fig.6.19(b). Diffraction spots due to 220 planes have been marked on FFT and SAED images. A zoomed-in view of the micrograph in Fig. 6.19(c) shows regions enclosed within the broken-line boundaries where the lattice planes show defects or a lack of perfect translational symmetry, which is seen outside these regions.

In sample $x > 0.5$, Fig. 6.14 and Fig. 6.15, we observe a composite microstructure comprising HH phase (main phase) and an orthorhombic secondary phase. In both these phases, we observe a higher concentration of Zr and Ni. Similarly, in samples with $x < 0.5$, Fig. 6.16, Fig. 6.17 and Fig. 6.18, we observe higher concen-

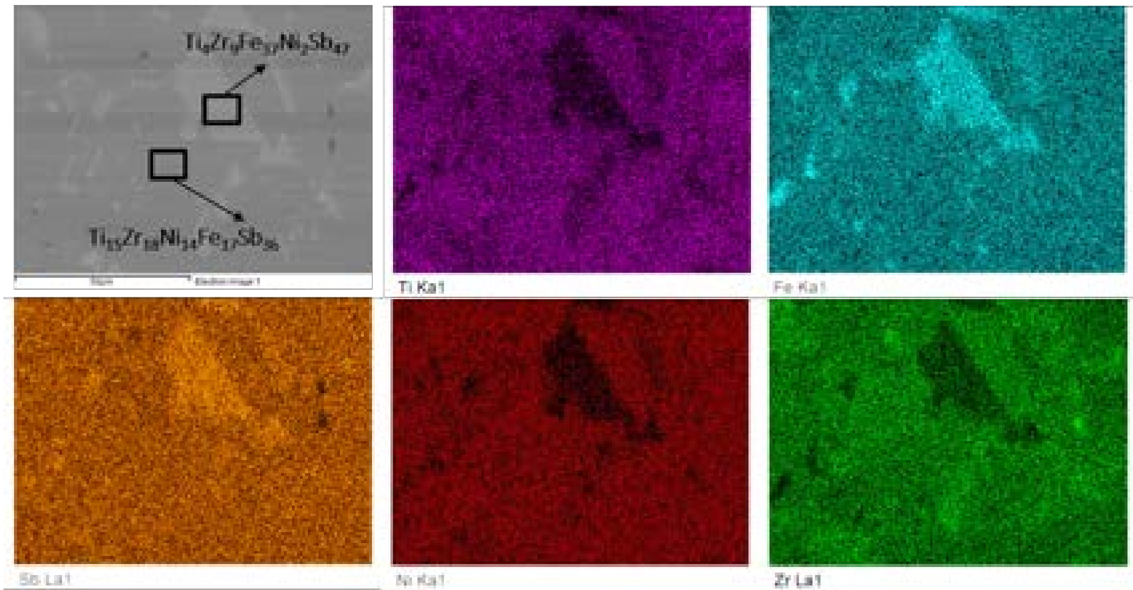

Figure 6.12: Chemical mapping of large area of $(ZrNiSb)_{0.5}(TiFeSb)_{0.5}$ sample using FESEM

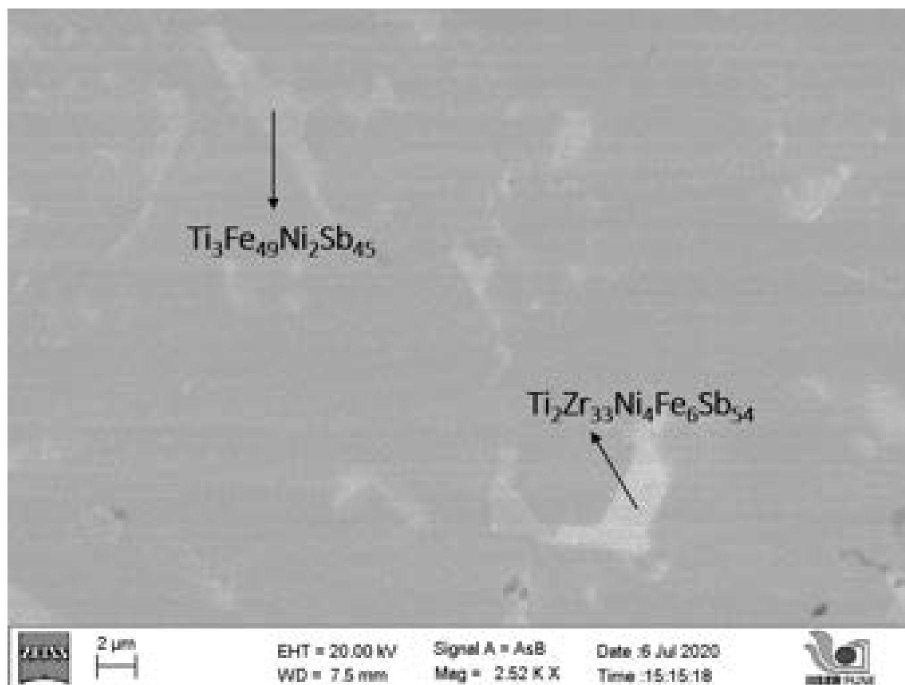

Figure 6.13: Representative backscattered image of the Double Heusler phase using FESEM of $(ZrNiSb)_{0.5}(TiFeSb)_{0.5}$

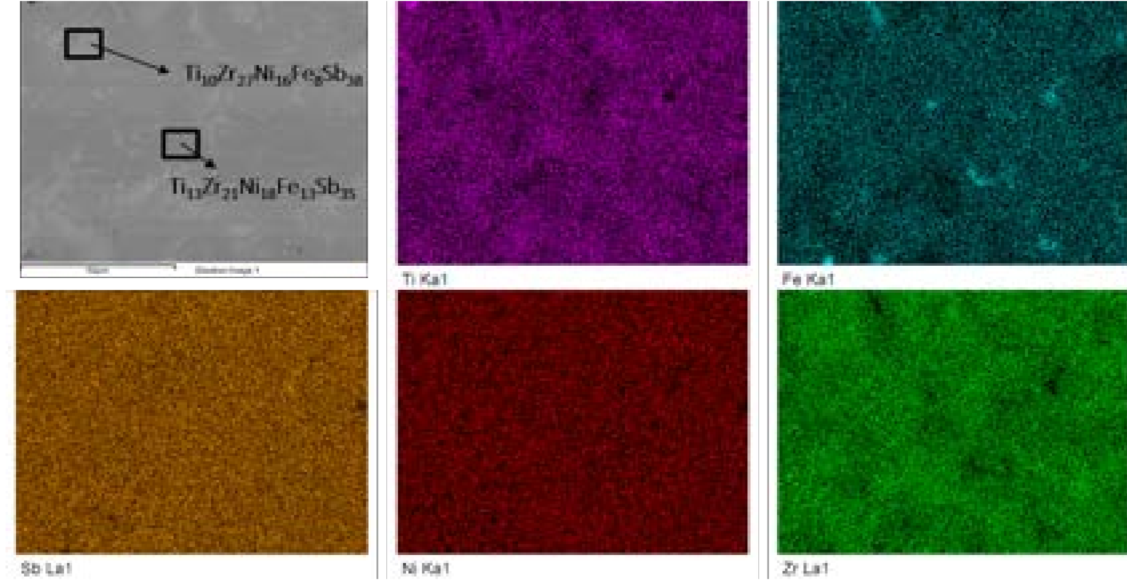

Figure 6.14: Chemical mapping of the Double Heusler phase using FESEM of $(ZrNiSb)_{0.6}(TiFeSb)_{0.4}$

tration of Ti and Fe in both the HH and orthorhombic phase. We also observe the formation of bigger grains of orthorhombic phase in samples as we move away on either side of $x = 0.5$ composition which is consistent with the increase in secondary phase fraction obtained from x-ray diffraction.

6.3.3 Thermoelectric properties

Transport properties of arc melted samples have been shown as two parts: (i) for $x > 0.5$ where a p-type behavior has been observed; and $x \leq 0.5$ when an n-type behavior is observed. We first show and discuss the thermopower and electrical conductivity. Finally, we will discuss the overall figure of merit zT along with the weighted mobility and B factor variation for various compositions.

Thermopower and electrical conductivity

We show the thermopower of our samples in two separate plots, $x > 0.5$ (p-type Fig. 6.21(a)) and $x \leq 0.5$ (n-type Fig. 6.21(b)) with ZrNiSb ($x = 0$) and TiFeSb ($x = 1$) samples shown in both as references. ZrNiSb has a very small thermopower that shows a weak temperature dependence. It undergoes a p-type to n-type transition around $600K$. TiFeSb sample, on the other hand, has p-type behavior with positive thermopower that increases with the temperature slowly but remains less than ~ 40 $\mu V/K$. TiFeSb thermopower of our sample does not match with that reported in [181]. This may be related to the fact that our measurements are done on as-melted samples whereas the measurements in Ref.[181] were done on ball-milled samples. The sample with $x = 0.5$, is n-type and has thermopower ~ -50 $\mu V/K$

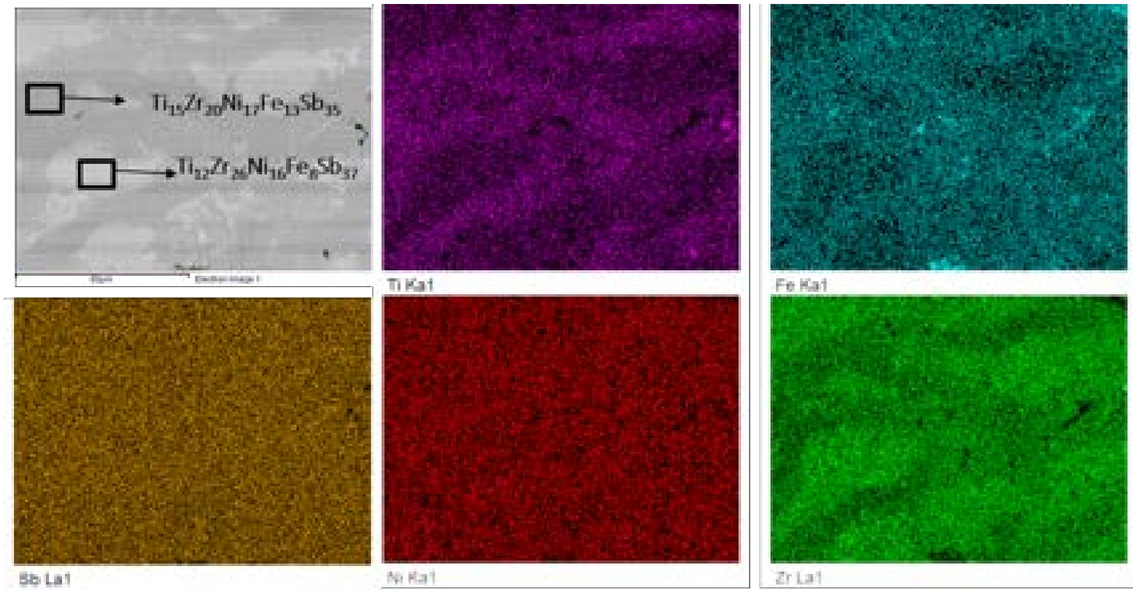

Figure 6.15: Chemical mapping of the Double Heusler phase using FESEM of $(ZrNiSb)_{0.55}(TiFeSb)_{0.45}$

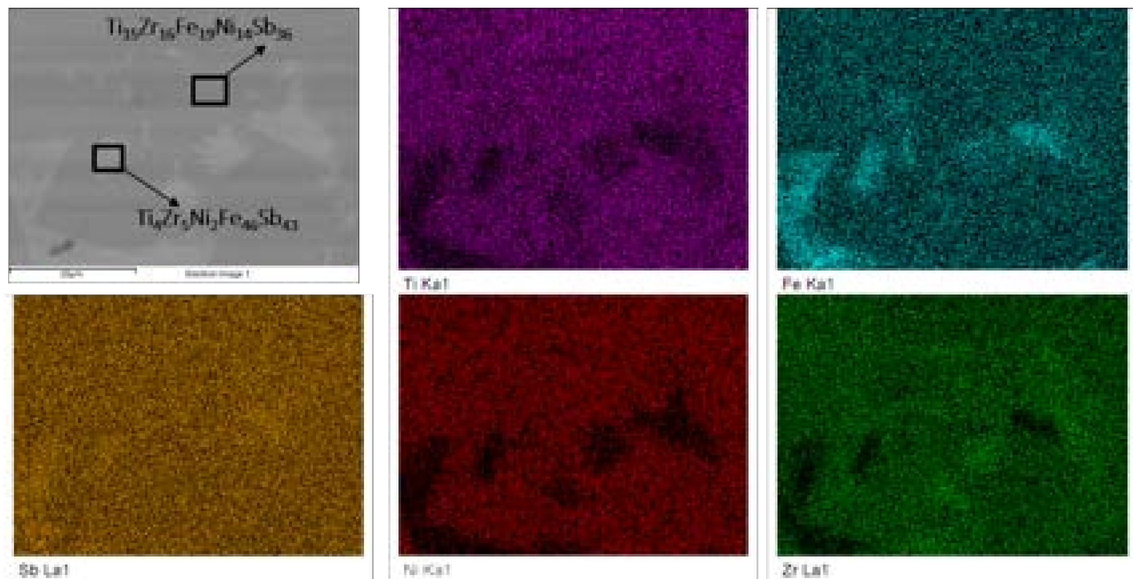

Figure 6.16: Chemical mapping of the Double Heusler phase using FESEM of $(ZrNiSb)_{0.45}(TiFeSb)_{0.55}$

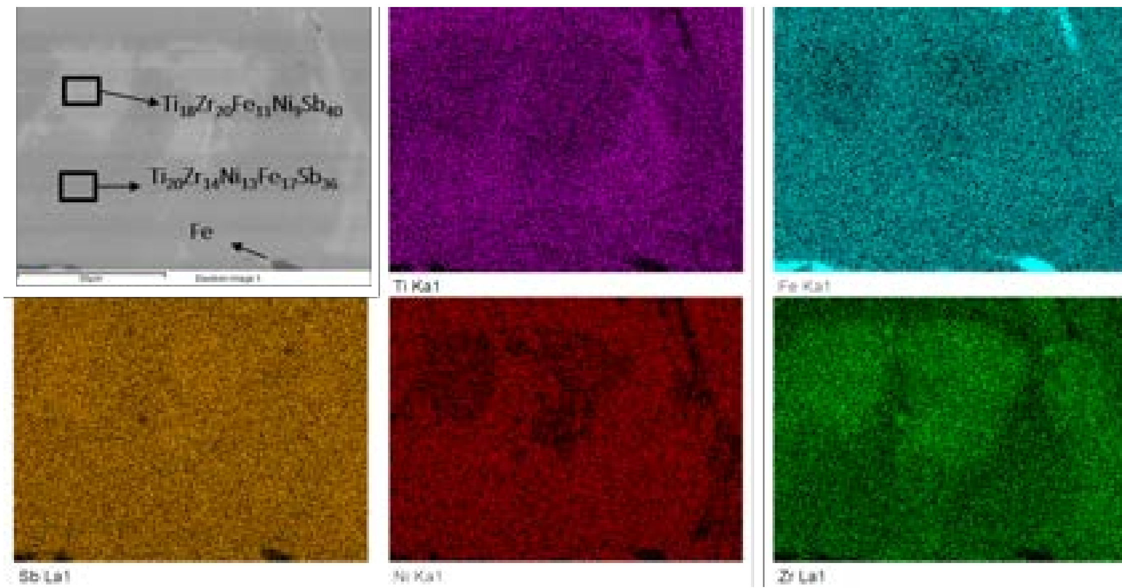

Figure 6.17: Chemical mapping of the Double Heusler phase using FESEM of $(ZrNiSb)_{0.4}(TiFeSb)_{0.6}$

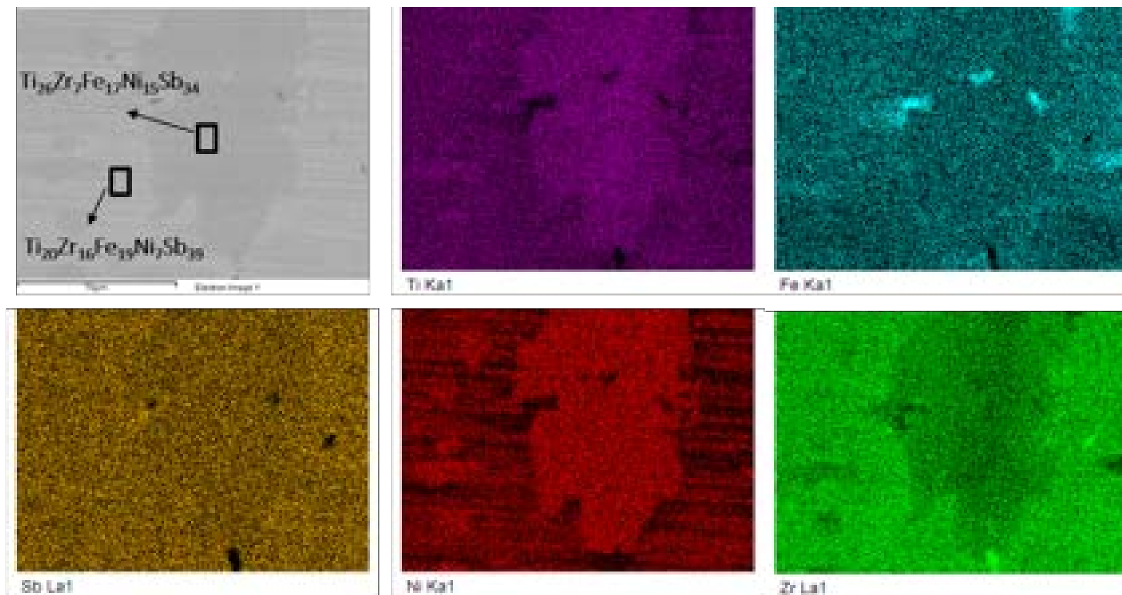

Figure 6.18: Chemical mapping of the Double Heusler phase using FESEM of $(ZrNiSb)_{0.3}(TiFeSb)_{0.7}$

Table 6.2: Phase composition of HH-phase and orthorhombic phase obtained from FESEM chemical mapping of $(\text{ZrNiSb})_{1-x}(\text{TiFeSb})_x$ where $x = 0.4,\ 0.45,\ 0.5,\ 0.55,\ 0.6, and\ 0.7$

x	HH phase	Orthorhombic phase
0.4	$Zr_{21}Ti_{13}Ni_{18}Fe_{13}Sb_{35}$	$Zr_{27}Ti_{10}Ni_{16}Fe_{8}Sb_{38}$
0.45	$Zr_{26}Ti_{12}Ni_{16}Fe_{8}Sb_{37}$	$Zr_{20}Ti_{15}Ni_{17}Fe_{13}Sb_{35}$
0.5	$Zr_{18}Ti_{15}Ni_{14}Fe_{17}Sb_{36}$	$Zr_{9}Ti_{4}Ni_{2}Fe_{37}Sb_{47}$
0.55	$Zr_{16}Ti_{15}Ni_{14}Fe_{19}Sb_{36}$	$Zr_{5}Ti_{4}Ni_{2}Fe_{46}Sb_{43}$
0.6	$Zr_{14}Ti_{20}Ni_{13}Fe_{17}Sb_{36}$	$Zr_{20}Ti_{18}Ni_{9}Fe_{11}Sb_{40}$
0.7	$Zr_{7}Ti_{26}Ni_{15}Fe_{17}Sb_{34}$	$Zr_{16}Ti_{20}Ni_{7}Fe_{19}Sb_{39}$

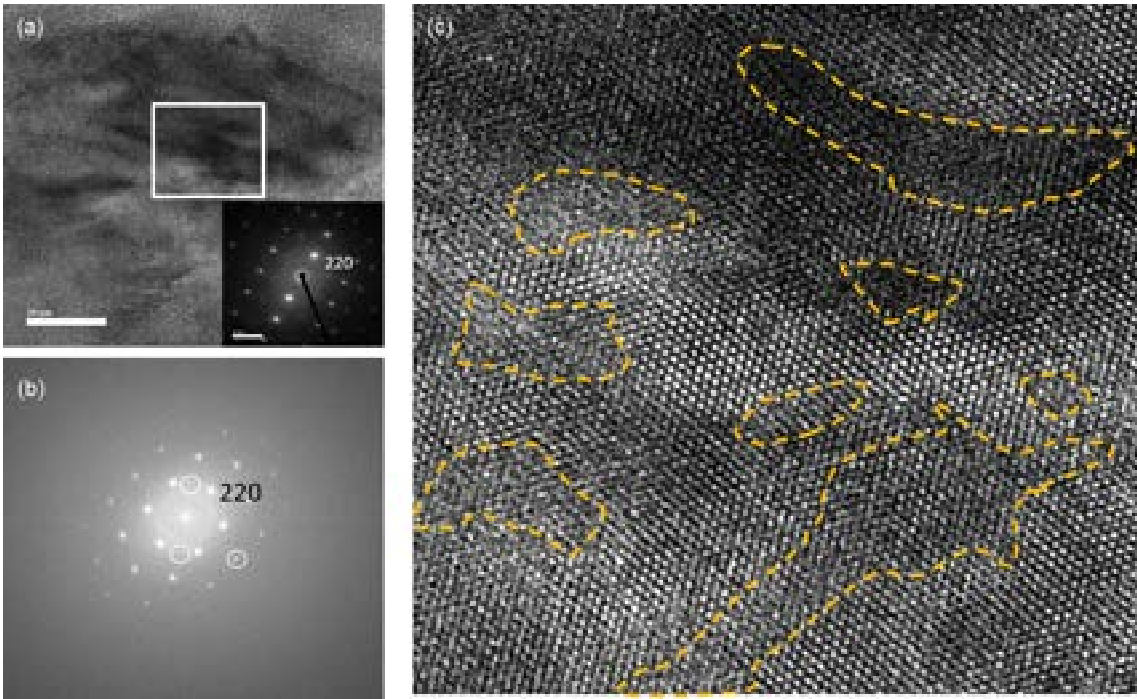

Figure 6.19: (a)HRTEM microstructure of $(\text{ZrNiSb})_{0.5}(\text{TiFeSb})_{0.5}$ SAED image is shown in inset (b) FFT of the microstructure shown in (c) zoomed image of microstructure shown in (a) where we observe disorder in structure.

at room temperature. For this sample the maximum in the thermopower at 750 K gives band gap estimate of $E_g = 0.13\ eV$ using the Goldsmid-sharp formula, i.e., $Eg = 2e|S_{max}|T_{max}$. The maximum value of the thermopower for x = 0.5 is $-90\ \mu V/K$. Samples with $x > 0.5$ are however p-type. The thermopower for $x = 0.7$ sample at room temperature is $\sim 50\mu V/K$ and attain a maximum of $\sim 95\mu V/K$ at 900 K. Using the Goldsmid-Sharp formula the estimated bandgap for this sample will be about 0.16 eV. Sample with $x \leq 0.5$, have n-type behaviour.

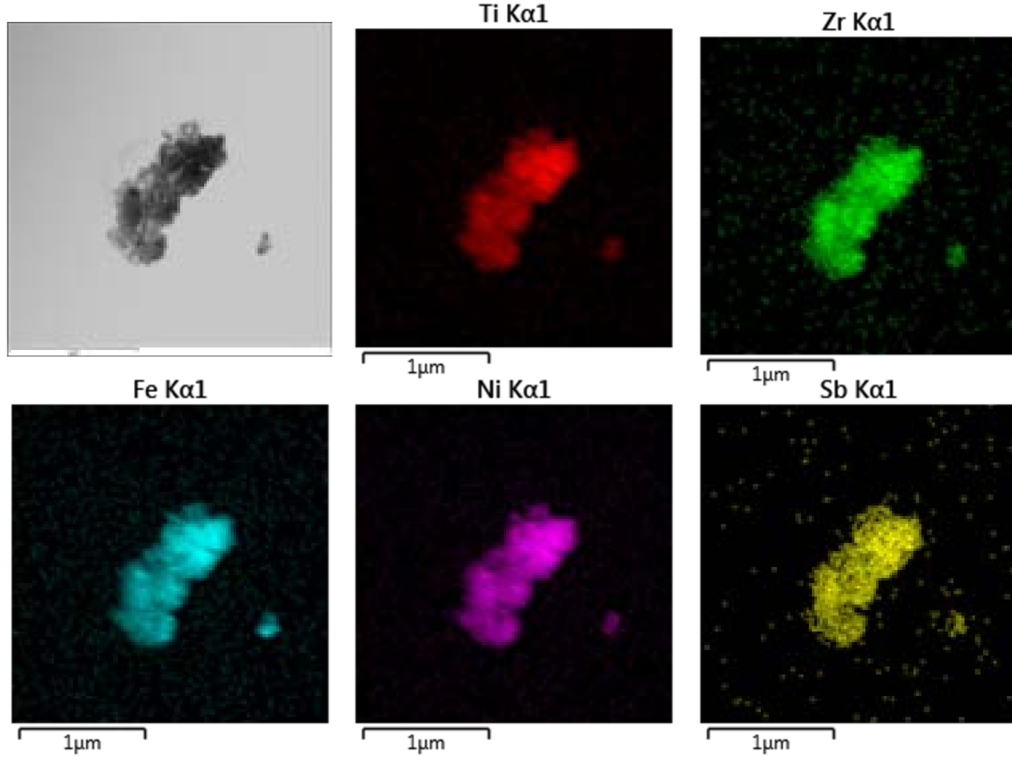

Figure 6.20: Chemical mapping of $(ZrNiSb)_{0.5}(TiFeSb)_{0.5}$ grains using HRTEM imaging

The highest thermopower, in this case, is obtained for $x = 0.4$ with $S = -40\ \mu V/K$ at room temperature, which increases with temperature showing a maximum of $\sim -120\ \mu V/K$ at 950 K. The effective band gap for this sample is estimated to be 0.23 eV. The interesting observation here is that we could obtain both n-type and p-type samples with a common set of elements, which is considered as one of the important requirements for device fabrication. It should however be mentioned that the thermopower in any of our samples is still less as compared to other potential half-Heusler thermoelectric materials like NbCoSb [205, 206, 222], ZrNiSn [160] and TiCoSb [166].

The electrical conductivity has been plotted in Fig. 6.22 in two panels $x > 0.5$ (left) and $x \leq 0.5$ (right). ZrNiSb has a semi-metallic behavior with high conductivity. At room temperature, the electrical conductivity is around $\sim 3800\ S/cm$ which decreases to $\sim 2900\ S/cm$ at 1000 K. TiFeSb on the other hand has low electrical conductivity. It first decreases slightly and then increases to give minima around 500 K. At room temperature, σ is 750 S/cm and its maximum value is 1500 S/cm around 950 K. The electrical conductivity has contributions from the two phases. At high temperatures, it shows a semiconductor-like increasing trend with temperature. The electrical conductivity of intermediate samples is comparatively much lower than either of ZrNiSb or TiFeSb. The lowest electrical conductivity is shown

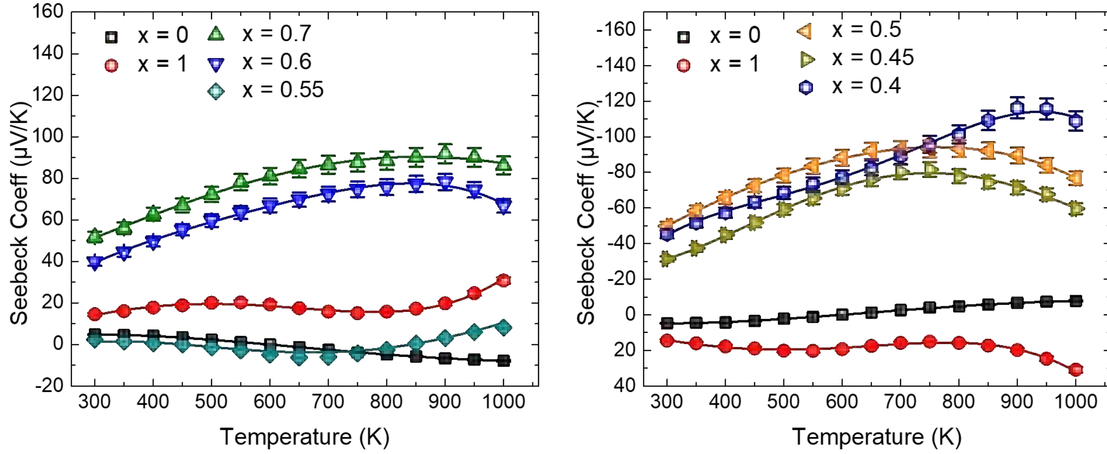

Figure 6.21: Thermopower of different samples of $(ZrNiSb)_{1-x}(TiFeSb)_x$ with x = 0, 0.3, 0.4, 0.45, 0.5, 0.6 and 1

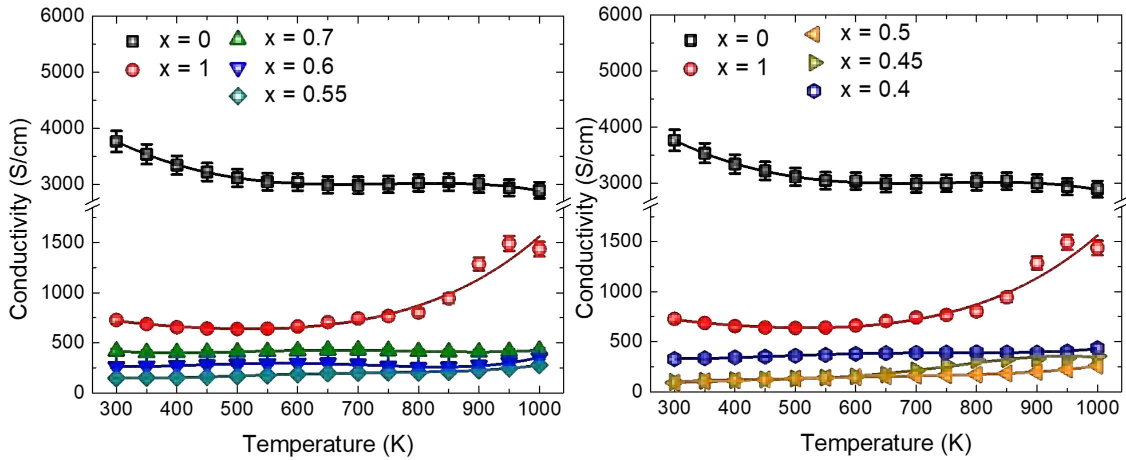

Figure 6.22: Electrical conductivity of different samples of $(ZrNiSb)_{1-x}(TiFeSb)_x$ with x = 0, 0.3, 0.4, 0.45, 0.5, 0.6 and 1

by the $x = 0.5$ sample. On either side of $x = 0.5$, the samples become more conducting. The most conducting sample in $x > 0.5$ range is $x = 0.7$, and that in the $x < 0.5$ range is $x = 0.4$. In all cases, however, the electrical conductivity is only weakly temperature-dependent and $\sigma < 500 S/cm$ over the whole range.

Thermal conductivity

The thermal conductivity of intermetallics is generally pretty high as compared to other materials. Even well-known half-Heuslers like ZrNiSn and NbFeSb show high thermal conductivity. Among the samples studied here, ZrNiSb has the highest thermal conductivity as can be seen from the plot, but these values for thermal conductivity are considerably low as compared to similar known intermetallics, which has been attributed to the presence of high density of defects and disorder [162]. TiFeSb has a low thermal conductivity and this may be due to the existence of

two different phases of TiFeSb as observed using FESEM which shows a composite microstructure with Fe-deficient (orthorhombic) and Fe-excess (cubic) phases.

The total thermal conductivity (κ_{Tot}) of the intermediate samples lie in the range 2.5 - 7 $Wm^{-1}K^{-1}$, which is very small as compared to known ternary half Heuslers. One reason for this is that the DH structure of these samples has 5 elements rather than 3 in normal HH compounds. This increases the randomness in the lattice potential and thus helps in lowering the thermal conductivity due to alloying scattering. The total thermal conductivity in all samples shows weak temperature dependence over the whole temperature range. As we move away from $x = 0.5$ composition, a reduction in thermal conductivity is observed. We have also shown the electronic and lattice thermal conductivity in Fig 6.25 and Fig. 6.24. The electronic thermal conductivity (κ_{ele}) is obtained using the Weidemann-Franz law. The Lorenz number was obtained from the Seebeck coefficient using equation 1.20. Lattice thermal conductivity (κ_{Latt}) is obtained by subtracting κ_{ele} from κ_{Tot}. Due to their low electrical conductivities, the electronic thermal conductivity of the DHs is small and lies between 0 to 1 $Wm^{-1}K^{-1}$. κ_{Latt} in the range 2 - 5 $Wm^{-1}K^{-1}$, which is quite low due to various reasons including a highly disordered structure due to Zr and Ti, and, Ni and Fe, sharing the same Wyckoff positions. We obtained phonon dispersion for our Composite1 structure and using it calculated the minimum lattice thermal conductivity which is shown with a dark line in the lattice thermal conductivity plot Fig. 6.24.The value of ($\kappa_{Latt,min}$) is around 1.65 $Wm^{-1}K^{-1}$ and has weak temperature dependence. Samples $x = 0.7$ and $x = 0.4$ have shown minimum lattice thermal conductivity ($\kappa_{Latt,min}$) at high temperature.

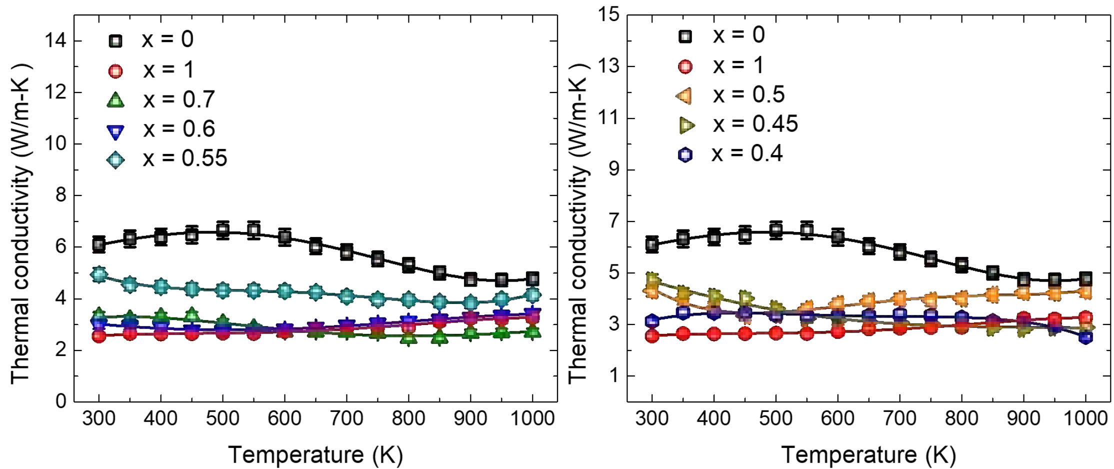

Figure 6.23: Total thermal conductivity of different samples of $(ZrNiSb)_{1-x}(TiFeSb)_x$ with x = 0, 0.3, 0.4, 0.45, 0.5, 0.6 and 1

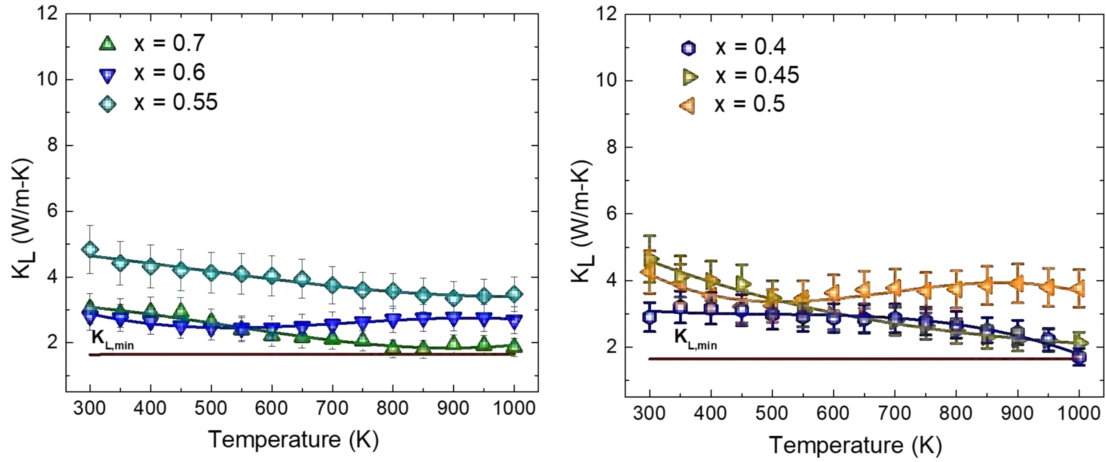

Figure 6.24: Lattice thermal conductivity of different samples of $(\mathrm{ZrNiSb})_{1-x}(\mathrm{TiFeSb})_x$ with x = 0.3, 0.4, 0.45, 0.5 and 0.6.

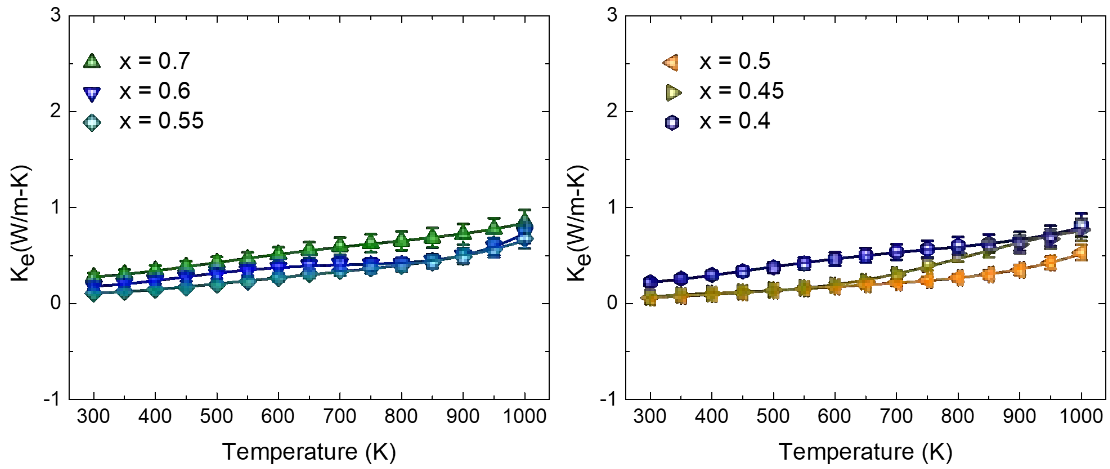

Figure 6.25: Electrical thermal conductivity of different samples of $(\mathrm{ZrNiSb})_{1-x}(\mathrm{TiFeSb})_x$ with x = 0.3, 0.4, 0.45, 0.5 and 0.6.

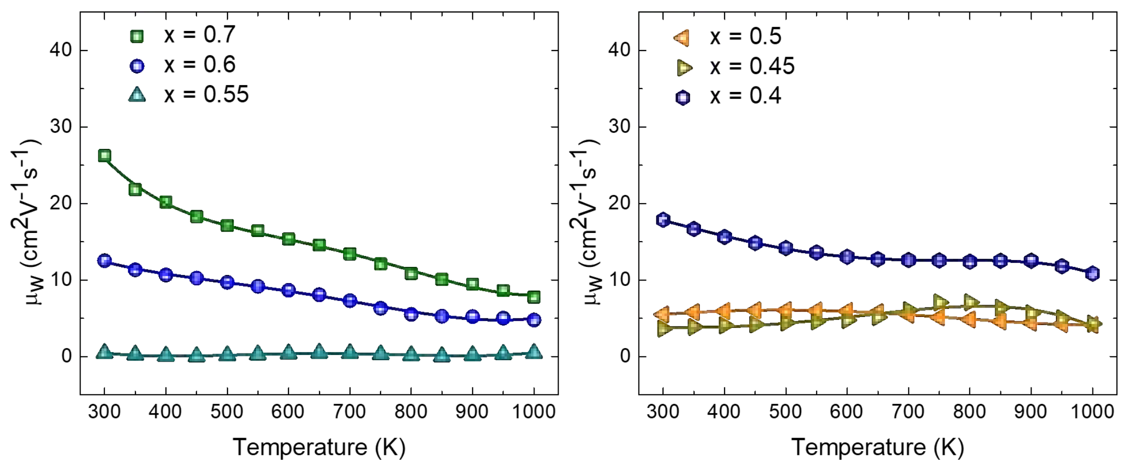

Figure 6.26: Weighted mobility of different samples of $(\mathrm{ZrNiSb})_{1-x}(\mathrm{TiFeSb})_x$ with x = 0.3, 0.4, 0.45, 0.5 and 0.6.

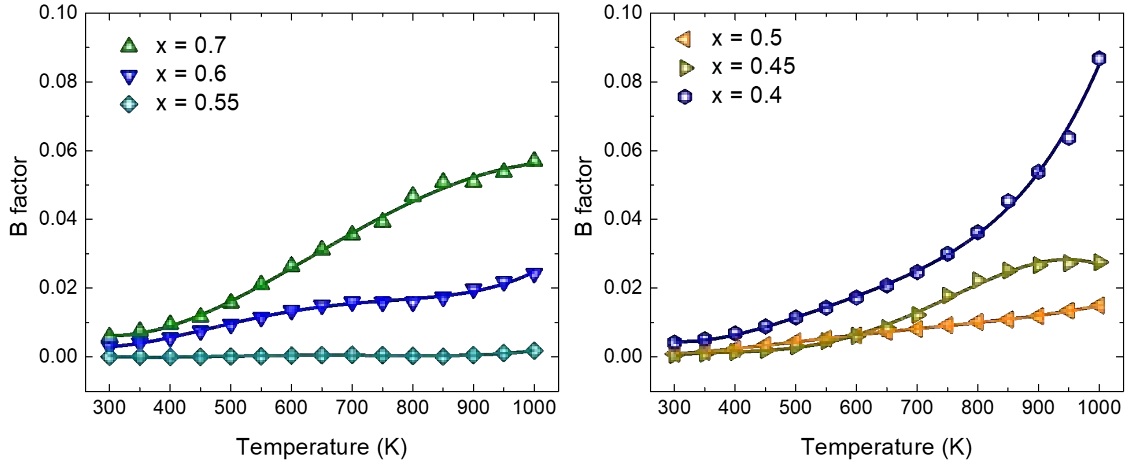

Figure 6.27: Bfactor of different samples of $(ZrNiSb)_{1-x}(TiFeSb)_x$ with x = 0.3, 0.4, 0.45, 0.5 and 0.6.

Weighted mobility, B factor, power factor and figure of merit

The weighted carrier mobility, shown in Fig 6.26 is obtained using the Seebeck coefficient and conductivity of the samples at different temperatures, as shown in equation 1.32. The weighted mobility provides an understanding of the scattering mechanisms in our samples. μ_w is small for all the composites, less than 30 $cm^2V^{-1}s^{-1}$. In n-type samples, we have highest μ_w for $x = 0.4$ and in p-type it is highest for $x = 0.7$. An important factor to note here is that the weighted mobility has a weak temperature dependence for $0.45 \leq x \leq 0.55$, this is due to the highly disordered structure of the DH phase. The β-factor has been shown for our samples in Fig. 6.27. The β-factor is obtained using the equation 1.33.

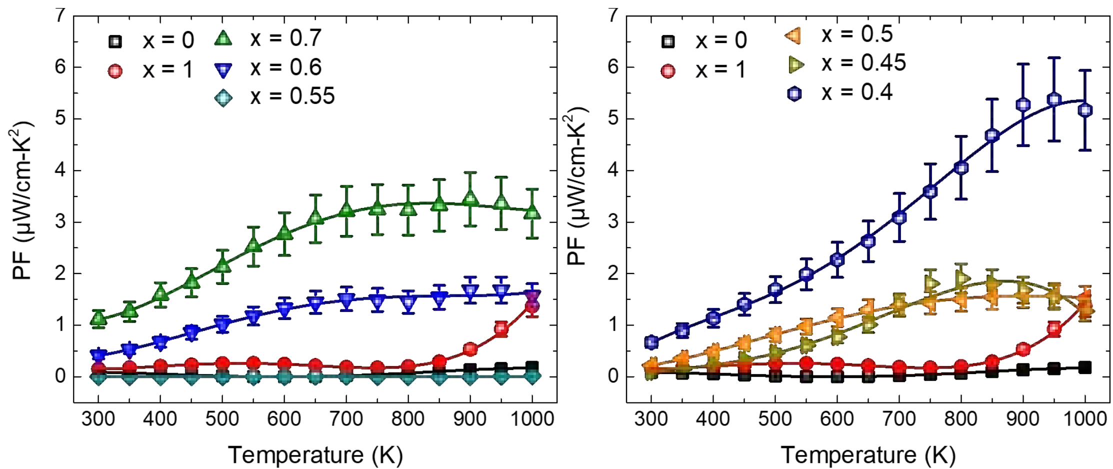

Figure 6.28: Power factor of different samples of $(ZrNiSb)_{1-x}(TiFeSb)_x$ with x = 0, 0.3, 0.4, 0.45, 0.5, 0.6 and 1.

For $x = 0.4$ sample, with temperature we see that the β-factor increases and achieve a value 0.09 at 1000 K. For $x = 0.7$, β-factor approaches 0.06 at 1000 K.

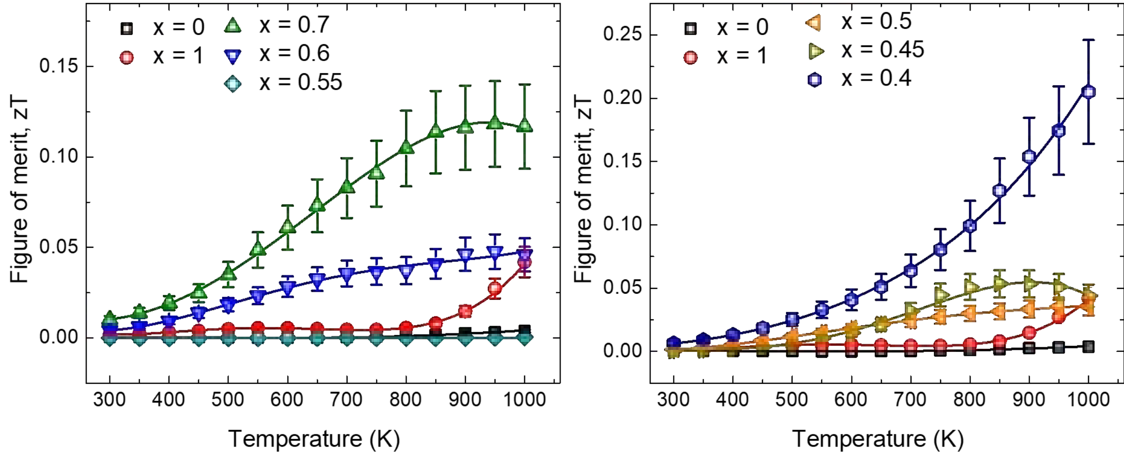

Figure 6.29: Figure of merit, zT of different samples of $(ZrNiSb)_{1-x}(TiFeSb)_x$ with x = 0, 0.3, 0.4, 0.45, 0.5, 0.6 and 1.

The Power factor (PF) of our samples is shown in Fig. 6.28. PF is very small for ZrNiSb and TiFeSb, but shows a significant improvement for $x = 0.5$; and increases further upon moving away from $x = 0.5$ on either side of it. The sample with $x = 0.4$ for n-type show high power factor of 5.5 $\mu W cm^{-1} K^{-2}$ and $x = 0.7$ for p-type show high power factor of 3.5 $\mu W cm^{-1} K^{-2}$, which is consistent with the x dependence of μ_w and β factor plots. The PF of our samples is much less as compared to other known half-Heuslers such as ZrNiSn where PF of 50 $\mu W cm^{-1} K^{-2}$ has been reported [179]. Hence, enhancing the power factor can lead to better performance in these materials owing to their low κ. The figure of merit zT of all the samples is shown in Fig. 6.29. While zT for the end members is very small and almost temperature independent for the end members, a marked improvement is seen for $x = 0.7$ and $x = 0.4$ samples. The zT is 0.2 for x = 0.4 (n-type) and 0.125 for x = 0.7 (p-type) is obtained. These values are significant despite a low power factor and suggest that it would be possible to enhance zT further by enhancing the power factor.

6.4 Conclusion and future perspectives

In this work, we have stabilized a double Heusler phase by mixing ZrNiSb and TiFeSb in eual molar ratio. This is a remarkable result given that neither of the two end members can be realized in pure Heusler phase experimentally. The mixture of these two, however, yields a stable double Heusler phase upon arc melting. The double Heusler phase show both n-type and p-type behavior in $(ZrNiSb)_{1-x}(TiFeSb)_x$, by varying x. The samples with compositions x = 0.55, 0.6 and 0.7 forms as p-type samples and samples with x = 0.4, 0.45 and 0.5 forms as n-type samples. These samples exhibit semiconducting behavior which is clear from the thermopower and the electrical conductivity. The thermal conductivity of these samples is low due

to higher disorder in the DH structure. The highest figure of merit for the p-type sample is 0.125 and for the n-type is 0.2. The enhancement in the figure of merit and power factor is shown with relation to increase in β-factor.

The samples studied here have shown interesting thermoelectric properties. We believe that by nanostructuring and further doping, the zT of these samples can be further enhanced. There is a great opportunity in terms of finding better thermoelectrics among a huge number of possible double-Heuslers or composite structures prepared by following this strategy. Also, it would be of interest to further study if the double-Heusler phase stabilization for the mixed samples is entropy-driven or not. Which will possibly include them in the category of high-entropy alloys that are of significant interest in the current research.

Chapter 7

Summary and Conclusion

In this thesis, we studied the thermoelectric properties of several half-Heusler (HH) compounds and compounds with orthorhombic TiNiSi structure type, which shares some common structural elements with the cubic HH structure. We focused either on new compounds whose thermoelectric properties were either unknown or known only partially, but were theoretically predicted to be promising thermelectrics or on designing some new compounds following the simple chemical principles applicable to the HH compounds, including the valence balanced rule and the valence electron count (VEC). For example, we studied $Nb_{0.8}CoSb$ which has a VEC of 19 in its stoichiometric form but experimentally forms as a pure HH phase only with 20 % Nb vacancies (or the stoichiometry $Nb_{0.8}CoSb$) with VEC 18. The relative stability of VEC 18 comes from their completely filled bonding orbital that are separated from the antibonding orbitals by a small band gap, which makes them useful for thermoelectric applications. Using the same ideas, we prepared a new compound by alloying the compositions TiFeSb (nominal VEC 17) and ZrNiSb (nominal VEC 19). Interestingly, neither TiFeSb nor ZrNiSb forms in the 1 : 1 : 1 stoichiometry. Below we provide a chapter wise summary of our findings which is followed by the outlook section discussing new possibilities for enhancing zT in the compounds studied here.

In chapter 3, the 'defective' HH alloy $Nb_{0.8}CoSb$ was studied by doping Sn at the Sb site. $Nb_{0.8}CoSb$ and the alloys derived from it are called 'defective' due to the presence of a large concentration of vacancies at the Nb-site without which the structure cannot be stabilized. The nominal composition of the samples studied here can be written as $Nb_{0.83}CoSb_{1-x}Sn_x$ ($x = 0, 0.01, 0.05, 0.1, 0.2, 0.3$). The samples $x = 0.2, 0.3$ were found to contain unreacted Sn or a Sn rich phase, hence their thermoelectric properties were not studied in detail. The chemical homogeneity δ of Nb in $Nb_{0.80+\delta}CoSb$ was previously reported to be $0 \leq \delta \leq 0.02$. The excess Nb acts as an electron donor. We show that doping Sn allows Nb composition to be increased progressively far beyond the previously reported homogeneity limit with δ reaching up to 0.05 for $x = 0.1$. The excess Nb in the structure prevents the thermopower

from collapsing despite an increase in the carrier concentration. To understand this we carried out electronic structure calculations that revealed the presence of a low-lying flat band in the conduction band close to the band edge arising due to the excess Nb (δ) in the structure. Further, due to Sn doping the carrier concentration also changes in a controlled manner since while Nb acts as an electron donor, Sn acts oppositely thus slowing down the rate of increases in the carrier concentration with increasing Nb doping. For our 5 % Sn doped sample, we found zT to exceed slightly above 1 at 1100 K. The previously highest reported zT for these alloys was 0.9 at 1100 K. The zT enhancement has been attributed to the band engineering which allows both σ and S to be high simultaneously. We also carried out comprehensive HRTEM investigations to study the nature of vacancies. The presence of diffused bands in the HRTEM indicates short-range vacancy ordering. Interestingly, the short range vacancy ordering persists up to highest Sn doped samples. In order to confirm this, we carried out Raman measurements at room temperature on x = 0, 0.01, and 0.3 samples. The Raman spectra of HHs is expected to show two triple degenerate Raman modes; however, in our samples we found three very broad bands, which could be fitted satisfactorily using eight peaks - indicating the presence of eight Raman active modes.

In chapter 4, we presented experimental and theoretical results on some TiNiSi structure-type orthorhombic compounds ZrNiSi, ZrNiGe, HfNiSi, NbCoSi, and ZrNiSb, some of which were recently reported in literature as promising half-Heuslers for thermoelectric applications using the first-principles density functional theory based calculations. We showed that these compounds indeed crystallize with the orthorhombic TiNiSi structure-type, but in ZrNiSb, 5 % excess Zr should be melted in order to obtain the pure orthorhombic phase. The crystal structure of these compounds exhibits a distinctive chair-shaped ... Si–Ni–Si–Ni ... framework running parallel to the a–axis with Si–Ni–Si bond angle close to 110°. A similar structural architect in SnSe has been argued as one of the factors responsible for its ultralow thermal conductivity. Further, though their structure is orthorhombic, the tetrahedral coordination present in their structure is highly reminiscent of the half-Heusler. For this reason they are also sometimes referred to as distorted hial-Heuslers. The first-principles electronic band structure calculations were done to show their semimetallic nature. In NbCoSi and ZrNiSb, the majority carriers are inferred to be holes whereas in ZrNiSi, ZrNiGe, and HfNiSi electrons are the majority charge carriers. An interesting pseudogap-like feature is observed in their density of states (DOS) except ZrNiSb. The electrical conductivity of these compounds near room-temperature is of the order of 10^3 S cm^{-1}x, somewhere between degenerate semiconductors and metallic alloys. Near room-temperature the thermopower is negative for ZrNiX (X = Si, Ge) and HfNiSi, and positive for NbCoSi and ZrNiSb.

The average Seebeck coefficient of 10 μV K^{-1} is small. However, despite their reasonably high electrical conductivity, the thermal conductivity (κ) was found to be generally low (< 15 W m^{-1} K^{-1} near 300 K). In $Zr_{1.05}NiSb$, which has the highest electrical conductivity ($\approx$ 4000 S cm^{-1}), κ is as low as $\approx$ 4 W m^{-1} K^{-1} at 300 K, of which almost 70 % is estimated to be due to the electronic contribution resulting in a lattice contribution which is < 1 W m^{-1} K^{-1}. This uncommon combination of high electrical conductivity and low thermal conductivity in these compounds is interesting and should be investigated further.

Motivated by the results reported in the previous chapter, in chapter 5 we investigated the effect of electron doping in ZrNiSi. We found that doping with Sb for Si in ZrNiSi, the thermopower and electrical conductivity can both be increased simultaneously, defying the generally seen opposite trend in most materials. In the doped samples, σ at 300 K increases from 1000 S cm^{-1} to as high as 2500 S cm^{-1}; at the same time, the peak value of S, which is -20 μV K^{-1} in ZrNiSi, increases by more than a factor of two. The ascast (ie., unannealed) $ZrNiSi_{1-x}Sb_x$ samples show phase segregation due to a spinodal-type decomposition with two coexisting TiNiSi structure-type phases with different Sb/Si ratios. This contributed to lowering of the thermal conductivity. Consequently, the thermal conductivity in the doped samples drops significantly from 12 $Wm^{-1}K^{-1}$ (x = 0) to nearly 2 $Wm^{-1}K^{-1}$ (x = 0.2) at 300 K. As a result, the peak thermoelectric figure-of-merit (zT) increases from 0.005 (x = 0) to 0.023 x = 0.2. Further enhancement in zT is obtained by codoping of Hf (Zr-site) and Sb (Si-site), which improves the phase stability and chemical homogeneity while keeping the thermal conductivity still very low due to Zr-Hf point mass fluctuation, resulting in a peak zT value of 0.055, i.e., almost an order of magnitude higher value than for the pristine ZrNiSi. While this zT value is still too low for any practical application, our work has laid a proof of the concept that the thermoelectric properties of TiNiSi structure-type semimetals can be enhanced by aliovalent doping. This principle can be employed on other members of the TiNiSi to improve the zT in this family of compounds further. The simultaneous enhancement of σ and S has been explained using the first-principles Density Functional Theory based band structure calculations.

In chapter 6, we investigated the double Heusler alloys. These are compounds with HH XYZ cubic structure but with X site populated by two distinct atoms X and X' in equal proportion, and similarly Y site populated by atoms Y and Y'. This yields a highly disordered structure with chemical formula $X_{0.5}X'_{0.5}Y_{0.5}Y'_{0.5}Z$. We synthesized a new double Heusler alloy by mixing TiFeSb (VEC 17) and ZrNiSb (VEC 19). Both these compounds by themselves do not exist in the pure phase; however, when alloyed in equal proportion a single phase compound with a nominal VEC 18 is realized. The success of this synthesis can be attributed to two factors:

the stability of VEC 18 over VEC 17 or 19 and a high-configurational entropy. Starting from $Ti_{0.5}Zr_{0.5}Fe_{0.5}Ni_{0.5}Sb$, we prepared solid-solutions with composition $(ZrNiSb)_{1-x}(TiFeSb)_x$ where x = 0.4, 0.45, 0.5, 0.55, 0.6, and 0.7. While the x = 0.5 sample is nearly pure, the samples away from this developed secondary phases reminiscent of the end members. The volume fraction of the secondary phases however remains low ($< 20 - 30$ %) even for the extreme values of x. The samples with $x < 0.5$ show a p-type behavior, whereas an n-type behavior is seen for $x > 0.5$. The fact that both n-type and p-type behavior can be obtained within the same family of compounds is interesting. The overall zT value is however small for both types of samples. Further doping experiments should be carried out to improve the power factor.

The defective, distorted and double half Hesulers studied here extend the scope of half Heuslers family for thermoelectric research. This study has thus shown new pathways for exploring thermoelectricity especially for designing thermoelectric modules at high-temperature where the traditional thermoelectrics breakdown either due to melting or phase decomposition. In future, further optimization of defective half Heuslers and their synthesis using spark-plasma sintering can be very useful. In particular, besides their low thermal conductivity, they also exhibit power carrier mobility which limits their performance. Using the method of Sn doping that we demonstrated in this thesis the vacancy concentration can be controlled to strike a tradeoff. As for the distorted HHs, it is believed that they can be stabilized in HH structure by doping or by altering the synthesis protocol. This should be further tried in future research as the cubic HH structure has the advantage of high-symmetry which preserves the band degeneracy leading to a higher thermopower. Recently, White et al. [199] stabilized LiZnSb in HH structure using a low-temperature synthesis method. Similar to DH demonstrated in this thesis, one can also try preparing composites of HHs with chalcogenide compounds. Recently, such composites showing promising properties have been reported in the literature.

Appendix A

Thermoelctric Properties of $Nb_{0.83}CoSb_{1\text{-}x}Sn_x$; x = 0.2 and 0.3

A.1

In chapter 4, we studied thermoelectric properties of $Nb_{0.83}CoSb_{1-x}Sn_x$, here we show the thermoelectric properties of samples with $x = 0.2$ & 0.3. These samples

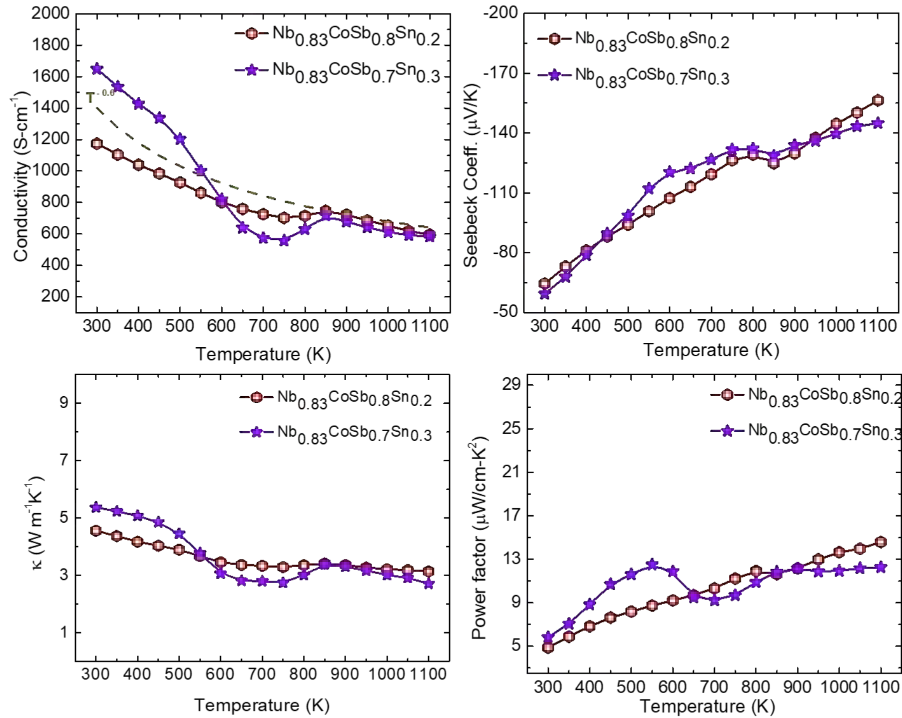

Figure A.1: (a) Electrical Conductivity, (b) Seebeck coeff., (c) thermal conductivity, and (d) power factor of $Nb_{0.83}CoSb_{1-x}Sn_x$ where $x = 0.2$ & 0.3 are shown.

showed some Sn precipitation. Melting of Sn around 500 K resulted in a broad feature in conductivity, thermopower, and thermal conductivity measurements. The Sn

precipitation was confirmed using TGA/DSC analysis and FESEM imaging shown in chapter 4.

The thermoelectric properties of these samples are shown in Fig. A.1. The composition obtained from the Powder x-ray data shown in Fig. 3.9 and Fig. 3.10 is $Nb_{0.87}CoSb_{0.8}Sn_{0.2}$ and $Nb_{0.9}CoSb_{0.7}Sn_{0.3}$ for $x = 0.2$ & 0.3 respectively. Due to the increase in Nb composition the carrier concentration of these two compositions was also high. We can see higher electrical conductivities and lower Seebeck coefficients for these samples in comparison to other samples studied in Fig. 3.24 and Fig. 3.25. Thermal conductivities of these two samples have also increased due to a decrease in vacancy as seen in Fig. 3.30. Power factors of these samples have reduced considerably in comparison to samples shown in Fig. 3.28.

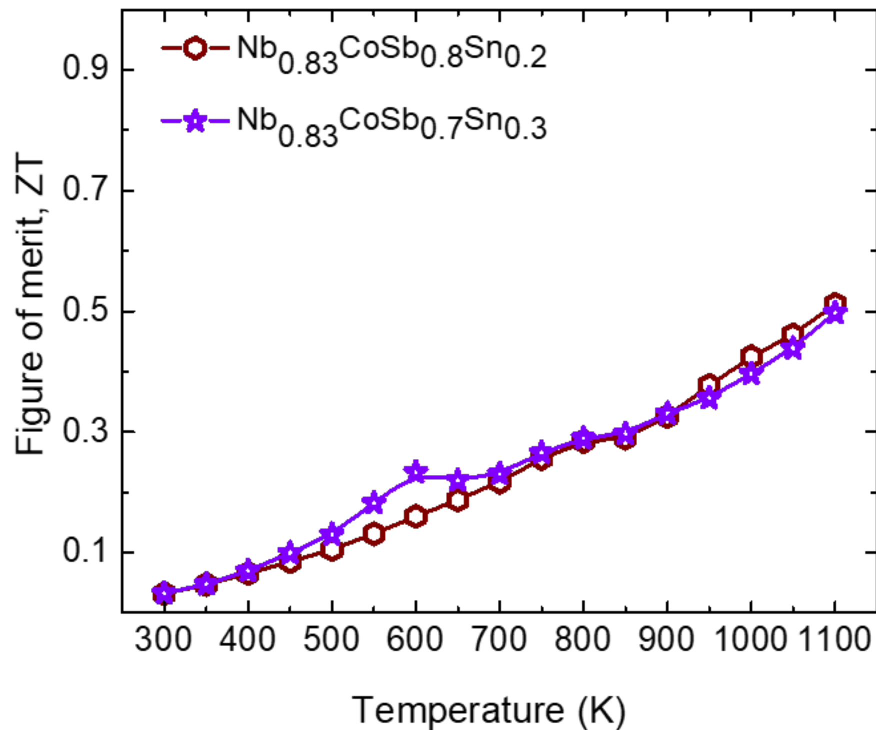

Figure A.2

The figure of merit zT of these two samples are shown in Fig. A.2, zT of these two samples are much lower in comparison to samples shown in Fig. 3.35.

Appendix B

Hall Data of $Nb_{0.83}CoSb_{1\text{-}x}Sn_x$

B.1

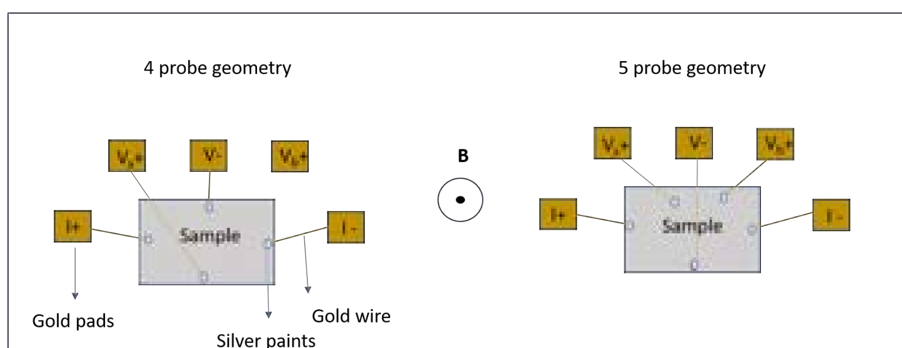

Figure B.1: Schematic of connection used for Hall measurements on Hall puck in PPMS(a) four-probe geometry (b) five-probe geometry

Schematic of four-probe and five-probe Hall measurements are shown in Fig. B.1. In five-probe geometry, we obtain a null point using potentiometer bridge between V_{a+} and V_{b+} against V_-. Thus, the voltage obtained V_H directly gives the Hall voltage ($V_{xy} = V_H$ in Equ. 2.7). In four-probe connection, either of V_{a+} or V_{b+} is used and potentiometer is manually set to 0 for V_{a+} and 1 for V_{b+}, the connection on sample is made manually opposite to V_-. In four-probe transverse voltge is obtained for positive (V_{H+}) and negative cycle (V_{H-}) of magnetic field. V_{xy} is obtained as $(V_{H+} + V_{H-})/2$ to remove any contribution of V_{xx} (voltage difference in the direction of current due to V_+ and V_- not being exactly opposite to each other on the line perpendicular to flow of current). This is discussed in section 2.3.1. The Hall carrier concentration is obtained using Equ. 2.7 and are shown in Fig. 3.12 . The difference in the sign of slope is due to the difference in the connection geometry as mentioned in Fig. B.1. Plots of V_H (V_xy) is shown for all the samples in Fig. B.2 - Fig. B.7. Calculation of carrier concentration is also shown in for all the sample using the slope (V/B), thickness of sample (t) and current (I) using the formula :

$n = 1/(V/B) * 1/e * I/t$, where e is electronic charge.

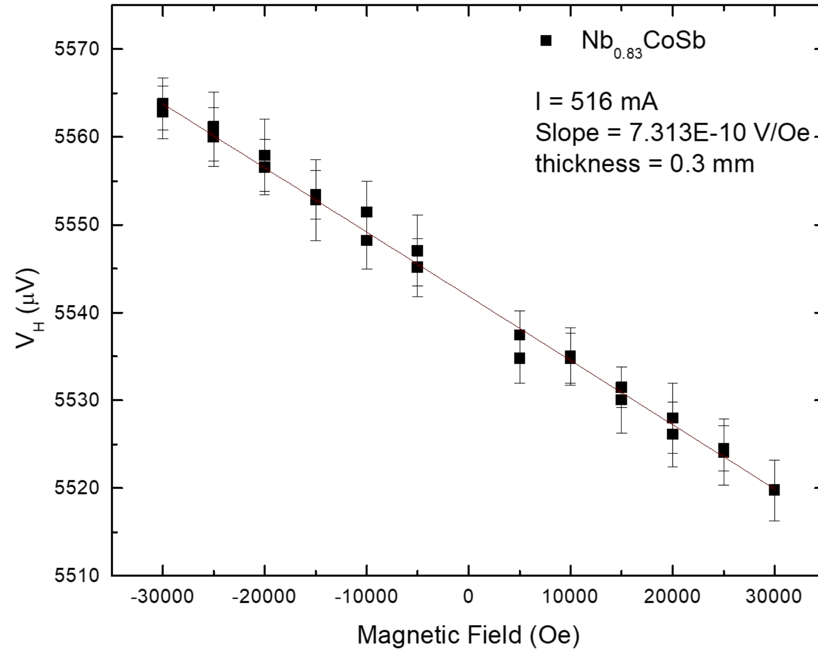

Figure B.2: Hall voltage plotted against magnetic field for $Nb_{0.83}CoSb$ taken in five probe geometry at 70 K.

Carrier concentration calculations for $Nb_{0.83}CoSb$

$Current\ (I) = 516\ mA$

$Slope\ (V/B) = 7.313 \times 10^{-6}\ V/T$

$sample\ thickness(t) = 0.3mm = 0.3 \times 10^{-3}m$

$e = 1.6 \times 10^{-19}\ Coulombs$

$n = 1/(V/B) * 1/e * I/t$

$n = 1.47 \times 10^{21}\ cm^{-3}$

Carrier concentration calculations for $Nb_{0.83}CoSb_{0.99}Sn_{0.01}$

$Current\ (I) = 200\ mA$

$Slope\ (V/B) = 1.87 \times 10^{-6}\ V/T$

$sample\ thickness(t) = 0.27mm = 0.27 \times 10^{-3}m$

$e = 1.6 \times 10^{-19}\ Coulombs$

$n = 1/(V/B) * 1/e * I/t$

$n = 2.47 \times 10^{21}\ cm^{-3}$

Carrier concentration calculations for $Nb_{0.83}CoSb_{0.95}Sn_{0.05}$

$Current\ (I) = 200\ mA$

$Slope\ (V/B) = 2.62 \times 10^{-6}\ V/T$

$sample\ thickness(t) = 0.18mm = 0.18 \times 10^{-3}m$

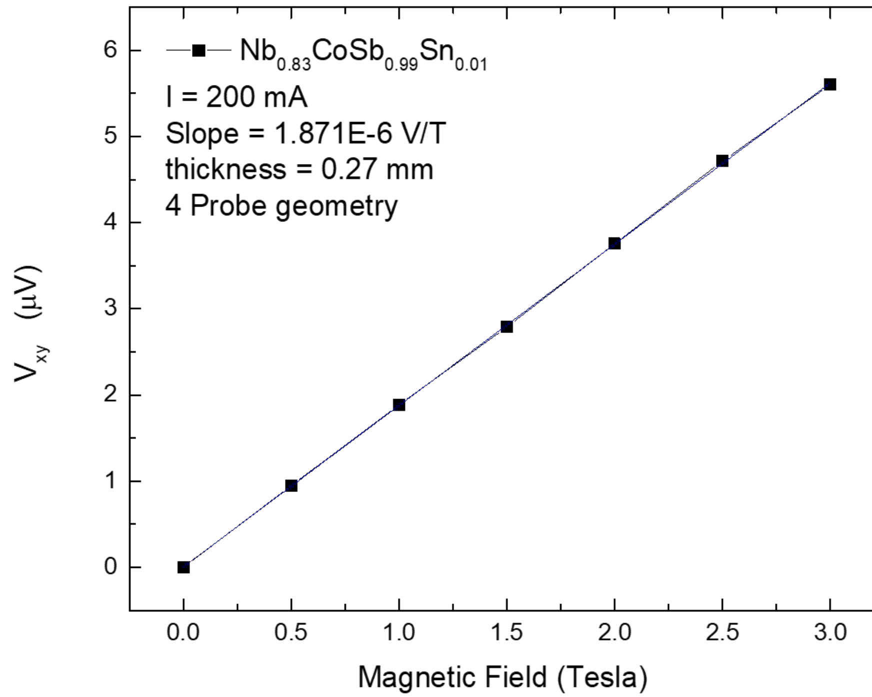

Figure B.3: Hall voltage plotted against magnetic field for $Nb_{0.83}CoSb_{0.99}Sn_{0.01}$ taken in four-probe geometry at 70 K.

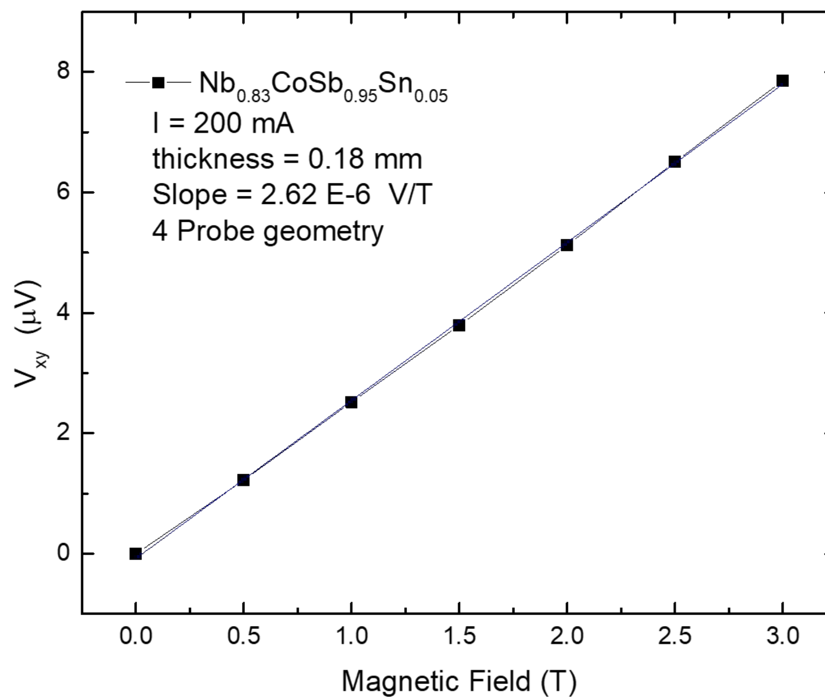

Figure B.4: Hall voltage plotted against magnetic field for $Nb_{0.83}CoSb_{0.95}Sn_{0.05}$ taken in four-probe geometry at 70 K.

$e = 1.6 \times 10^{-19}$ $Coulombs$
$n =\ 1/(V/B) * 1/e * I/t$
$n = 2.64 \times 10^{21}$ cm^{-3}

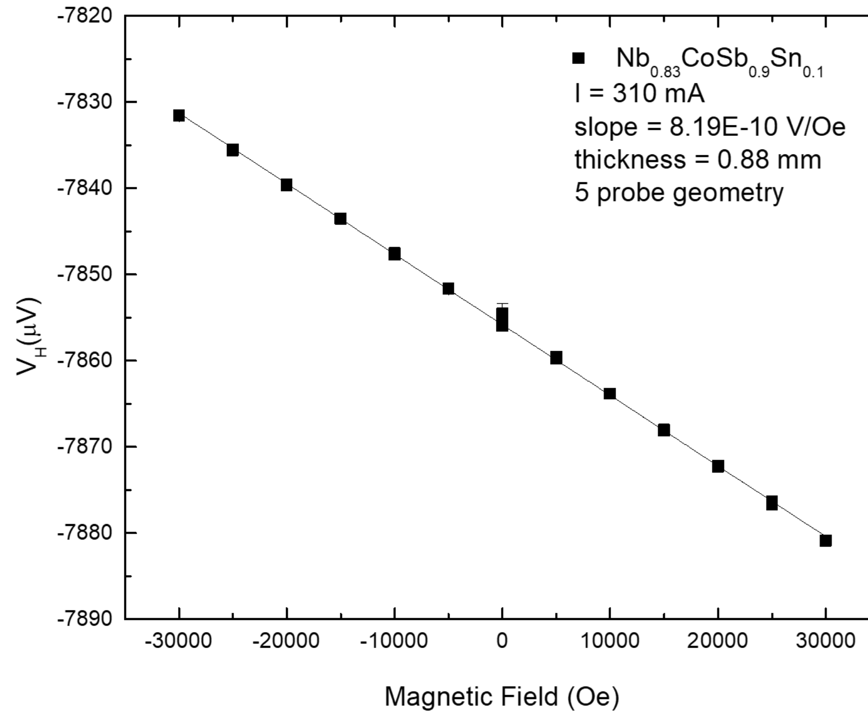

Figure B.5: Hall voltage plotted against magnetic field for $Nb_{0.83}CoSb_{0.9}Sn_{0.1}$ taken in five probe geometry at 70 K.

Carrier concentration calculations for $\mathbf{Nb_{0.83}CoSb_{0.9}Sn_{0.1}}$

$Current\ (I) = 310\ mA$
$Slope\ (V/B) = 8.18 \times 10^{-6}\ V/T$
$sample\ thickness(t) = 0.88mm = 0.88 \times 10^{-3}m$
$e = 1.6 \times 10^{-19}$ $Coulombs$
$n =\ 1/(V/B) * 1/e * I/t$
$n = 2.69 \times 10^{21}$ cm^{-3}

Carrier concentration calculations for $\mathbf{Nb_{0.83}CoSb_{0.8}Sn_{0.2}}$

$Current\ (I) = 413\ mA$
$Slope\ (V/B) = 2.99 \times 10^{-6}\ V/T$
$sample\ thickness(t) = 0.27mm = 0.27 \times 10^{-3}m$
$e = 1.6 \times 10^{-19}$ $Coulombs$
$n =\ 1/(V/B) * 1/e * I/t$
$n = 3.2 \times 10^{21}$ cm^{-3}

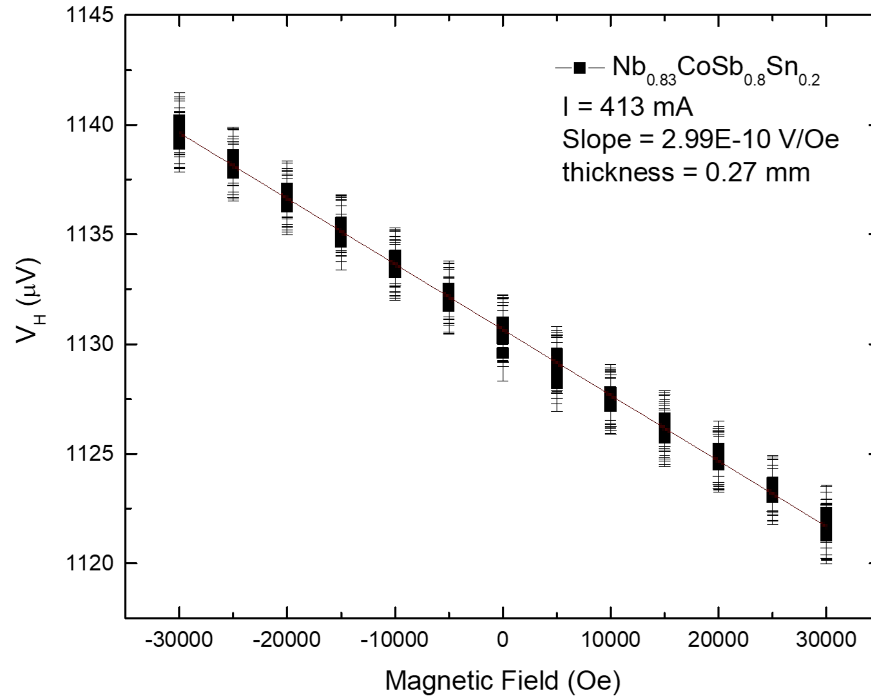

Figure B.6: Hall voltage plotted against magnetic field for $Nb_{0.83}CoSb_{0.8}Sn_{0.2}$ taken in five probe geometry at 70 K.

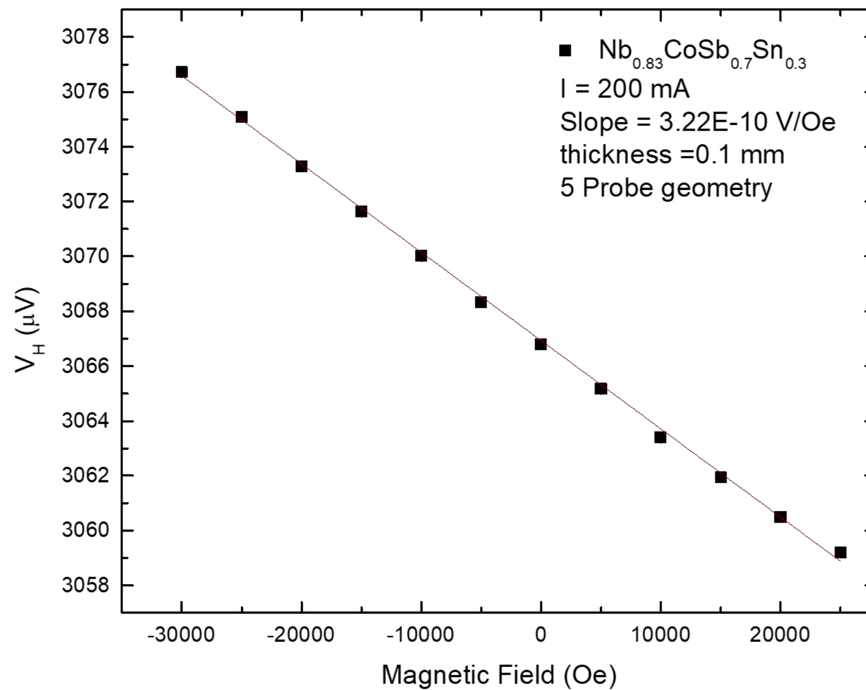

Figure B.7: Hall voltage plotted against magnetic field for $Nb_{0.83}CoSb_{0.7}Sn_{0.3}$ taken in five probe geometry at 70 K.

Carrier concentration calculations for $\mathbf{Nb_{0.83}CoSb_{0.7}Sn_{0.3}}$

$Current\ (I) = 200\ mA$

$Slope\ (V/B) = 3.2 \times 10^{-6}\ V/T$

$sample\ thickness(t) = 0.1mm = 0.1 \times 10^{-3} m$

$e = 1.6 \times 10^{-19}\ Coulombs$

$n = 1/(V/B) * 1/e * I/t$

$n = 3.9 \times 10^{21}\ cm^{-3}$

Appendix C

Two Phase Refinement of $(ZrNiSb)_{1\text{-}x}(TiFeSb)_x$

C.1

In chapter 6, We have studied the samples with compositions $(ZrNiSb)_{1-x}(TiFeSb)_x$ where $x = 0.4,\ 0.45,\ 0.5,\ 0.55,\ 0.6, and\ 0.7$. A two phase Reitveld refinement is done on all the samples to understand the phase composition. The refinement could not converge to a very low χ^2 value due to presence of other impurity phases of Fe, FeSb and $ZrSb_2$, but gives a rough estimate of increase in secondary orthorhombic phase as evident from the x-ray diffraction peaks of orthorhombic phase. The refined data has been shown for $0.4 \leq x \leq 0.7$, in Fig. C.1- Fig. C.6. The Table. C.1 show the values for χ^2, R_p, R_{wp}, R_{exp} and composition in HH phase obtained from the refinement.

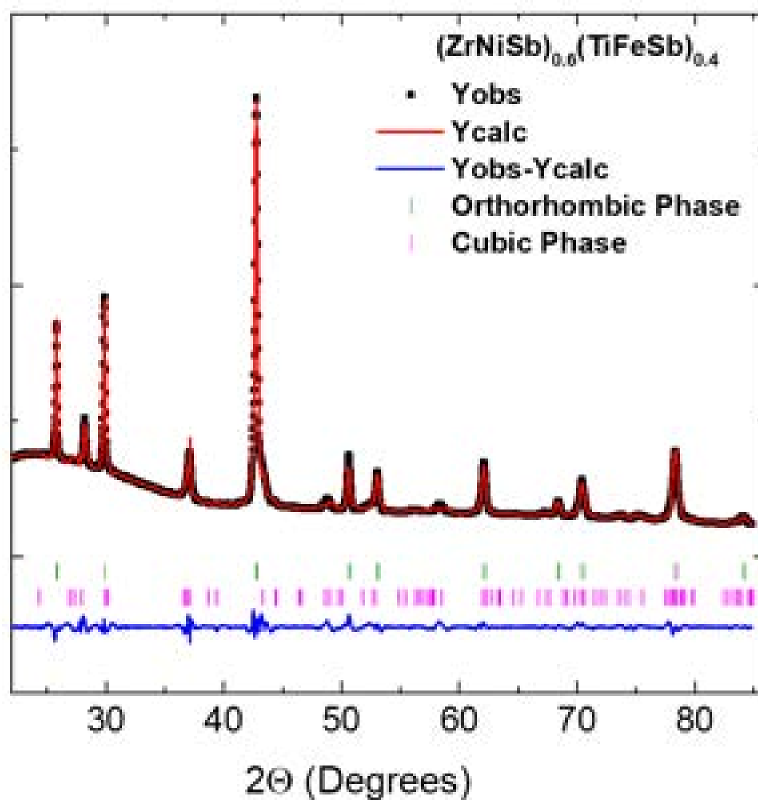

Figure C.1: Refinement of powder Xray diffraction of $(ZrNiSb)_{0.6}(TiFeSb)_{0.4}$

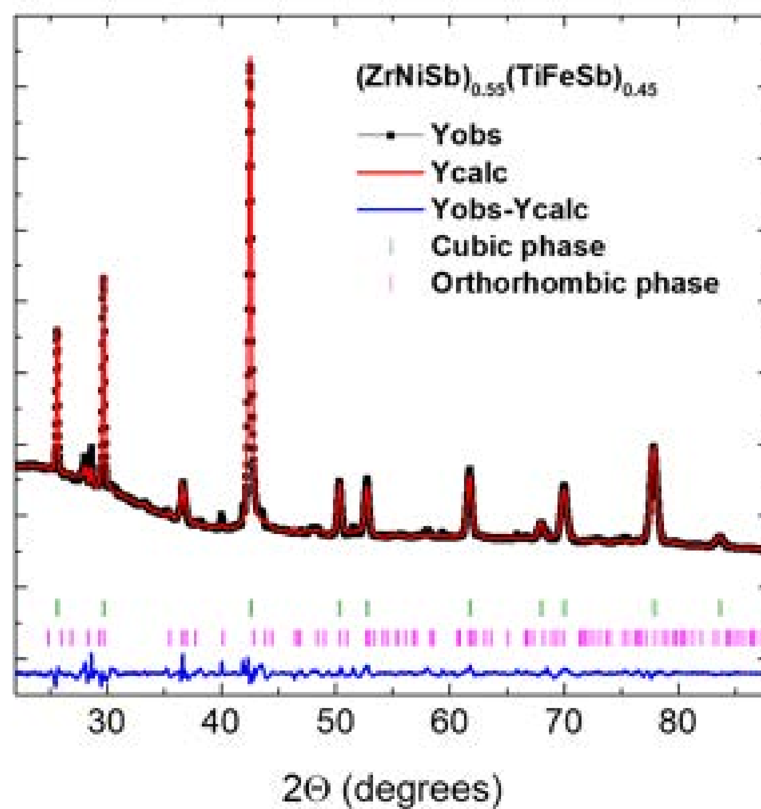

Figure C.2: Refinement of powder Xray diffraction of $(ZrNiSb)_{0.55}(TiFeSb)_{0.45}$

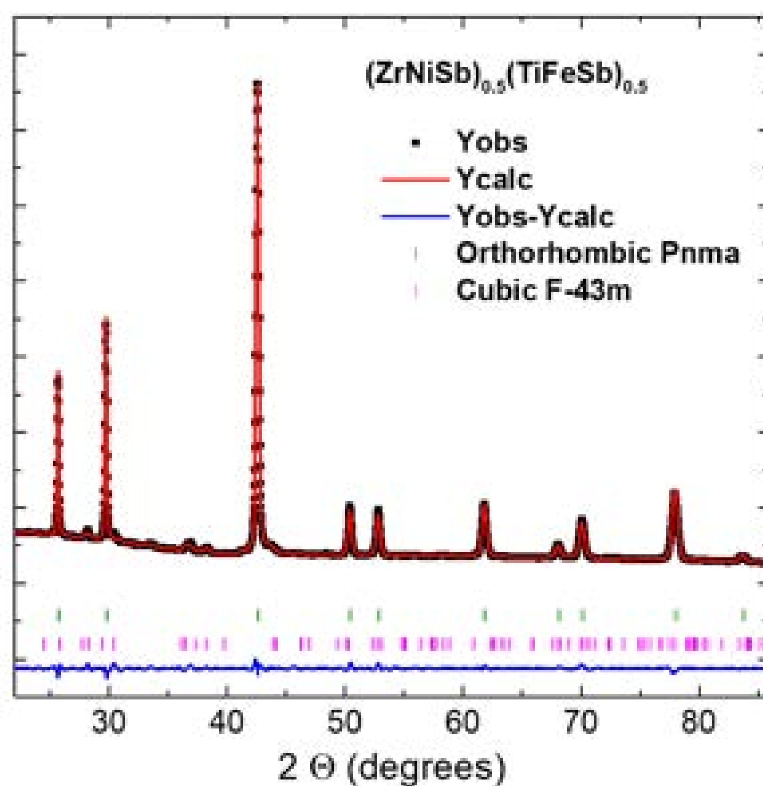

Figure C.3: Refinement of powder Xray diffraction of $(ZrNiSb)_{0.5}(TiFeSb)_{0.5}$

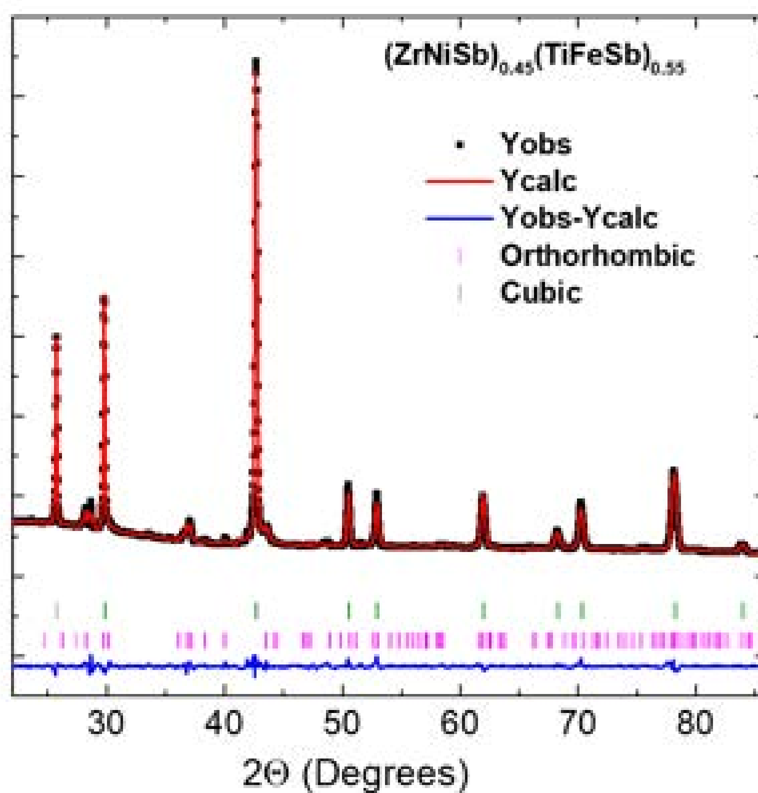

Figure C.4: Refinement of powder Xray diffraction of $(ZrNiSb)_{0.45}(TiFeSb)_{0.55}$

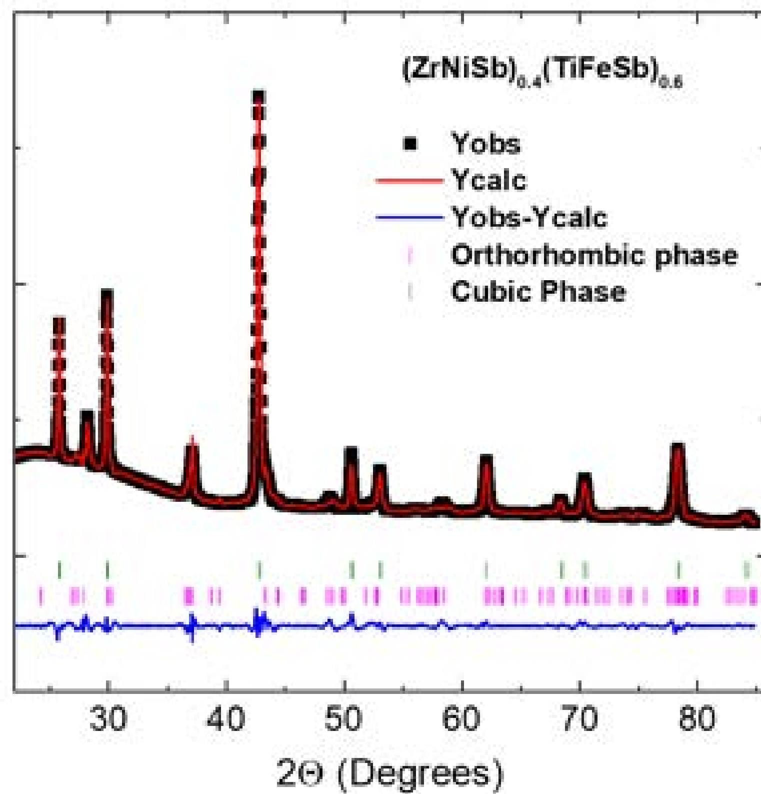

Figure C.5: Refinement of powder Xray diffraction of $(ZrNiSb)_{0.4}(TiFeSb)_{0.6}$

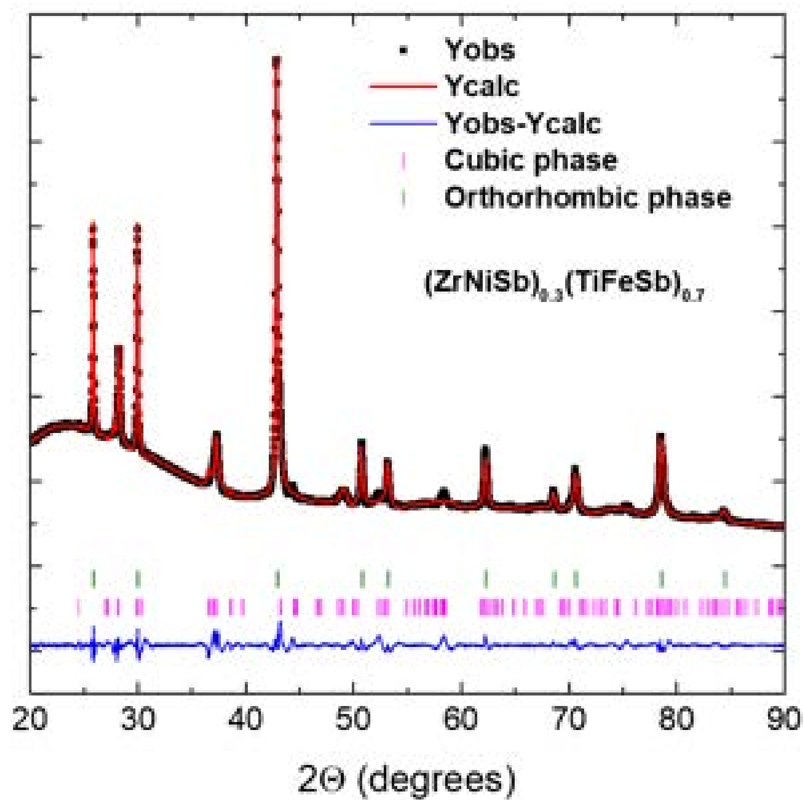

Figure C.6: Refinement of powder Xray diffraction of $(ZrNiSb)_{0.3}(TiFeSb)_{0.7}$

Table C.1: Parameters obtained from Reitveld refinement of the $(\text{ZrNiSb})_{1-x}(\text{TiFeSb})_x$ where $x = 0.4,\ 0.45,\ 0.5,\ 0.55,\ 0.6, and\ 0.7$ showing χ^2, R_p, R_{wp}, R_{exp} and composition in HH phase

x	χ^2	R_p	R_{wp}	R_{exp}	Composition
0.4	20.3	12.8	11.0	2.44	$Zr_{0.58}Ti_{0.40}Ni_{0.66}Fe_{0.40}Sb$
0.45	16.4	17.1	12.3	3.04	$Zr_{0.56}Ti_{0.38}Ni_{0.51}Fe_{0.49}Sb$
0.5	15.3	9.49	7.22	1.85	$Zr_{0.58}Ti_{0.50}Ni_{0.58}Fe_{0.56}Sb$
0.55	21.7	11.6	9.66	2.08	$Zr_{0.43}Ti_{0.54}Ni_{0.45}Fe_{0.55}Sb$
0.6	21.4	15.7	12.8	2.77	$Zr_{0.44}Ti_{0.60}Ni_{0.50}Fe_{0.60}Sb$
0.7	18.0	20.1	15.3	3.61	$Zr_{0.27}Ti_{0.73}Ni_{0.32}Fe_{0.7}Sb$

Appendix D

Crystal Growth of "defective" half-Heusler $Nb_{0.83}CoSb$

D.1 Introduction

The Heusler alloys and compounds constitute a vast family that can be broadly grouped under four categories: (a) Full Heusler (FH), XY_2Z, (b) Half Heusler (HF), XYZ, inverse Heusler X_2YZ (iH), and quaternary Heusler $XX'YZ$ or $XYY'Z$ (QH). Here, X and Y are typically transition metals and Z is an element of the main group. They exhibit a broad range of very interesting properties, spanning diverse applied and basic research areas in materials science, physics and chemistry, including spintronics, topological phases in condensed matter, and thermoelectricity among others [19, 202]. The HH compound (XYZ) having a valence electron count (VEC) 18 are of special interest in the area of thermoelectric due to their close filled electronic structure (somewhat akin to closed-shell structure of the group IV or III-V semiconductors) with filled bonding electronic state and unfilled antibonding states separated by a small bandgap [221]. Some important examples of VEC 18 HHs include, XNiSn (X = Ti, Zr, and Hf) and XFeSb (X = Nb and Ta) [221, 149].

Interestingly, a few VEC 19 HHs, namely, XCoSb (X = V, Nb, and Ta) have recently attracted significant attention for reasons that are explained further [81, 225, 222, 205, 5]. Xia et al. showed that NbCoSb forms as a single-phase HH only in the composition $Nb_{0.8+\delta}CoSb$ with a small homogeneity range $-0.01 \leq \delta \leq 0.05$ [205]. This was rationalized later by Anand et al. who argued on the basis of valence balanced rule to derive the thermodynamic stability of such alloys. $Nb_{0.8}CoSb$ has an 'effective" VEC of 18 and it also obeys the valence balanced rule, which stabilizes the HH phase without any impurities at this specific composition [5]. Their electronic structure follows from the 18-electron rule, where δ in $Nb_{0.8+\delta}CoSb$ results in electron doping. Since Nb is highly electropositive, even a slight excess above 0.8 acts as a

heavy donor leading to a degenerate behavior.

Currently, there is a significant interest in 'defective' hH alloys as they not only show high thermoelectric figure-of-metric (zT $\sim$ 0.9 at 1100 K $Nb_{0.83}CoSb$) owing to the presence of defects which suppress the lattice thermal conductivity significantly, but they also exhibit a short-range vacancy ordering [206, 157, 180, 124] To investigate the nature of the vacancy ordering in more detail it will be desirable to have single crystals of defective HH available for more advanced experiments. Since this is an emerging class of new defect stabilized HHs, a careful analysis of their crystal structure will be helpful in understanding their transport and thermal properties. With this as the initial motivation, we set out to grow crystals of $Nb_{0.8}CoSb$. Here, we show that very high-quality crystals of this 'defective' HH can be obtained using the chemical vapor transport (CVT) technique. The grown crystals were examined using several complementary structural characterization techniques. The high resolution transmission electron microscope images show the presence of prominent diffused bands characteristic of the vacancy ordering in these alloys. The electrical resistivity, measured between room-temperature and 77 K, shows a linear behavior characteristic of heavily doped semiconductors. The differential scanning calorimetry reveals an hitherto unknown phase-transition in these crystals above a temperature of 1000°, We believe that this is the vacancy order-disorder transition predicted in a previous work [5].

D.2 Experimental Methods

In the first step, a polycrystalline ingot of $Nb_{0.83}CoSb$ was obtained by arc-melting high-purity Nb (Sigma Aldrich 99.9%), Co (Sigma Aldrich 99.5%), and Sb (Alfa Aesar 99.999%) taken in molar ratio 0.83 : 1 : 1.1. The 0.1 mol excess Sb was added to compensate for the weight-loss during melting. The 0.03 excess Nb is within the homogeneity range. This specific value is chosen as the thermoelectric figure-of-merit reported previously is maximum for this composition. The excess Nb acts as an electron donor and results in heavy electron doping. The ingot was flipped over and re-melted several times to ensure its chemical homogeneity. The powder obtained by grounding the arc-melted ingot was used for crystal growth using the chemical vapor transport (CVT) technique. About 1 g of this powder was sealed in an evacuated quartz ampoule with approximately 220 mg of iodine. The ampoule was loaded in an Ar-filled glove-box (MBraun). The vacuum sealing was done outside under a static vacuum of about 10^{-4} mbar. The sealed ampoule was kept in a horizontal position inside a tube furnace. The furnace temperature was slowly increased to 950° in 10 h. After waiting at this temperature for 10 minutes, the temperature was increased to 1050° in 1 h. The crystal growth took place at

1050° over a period of 4 days at the end of which the furnace was allowed to cool down to room-temperature in 12 h. The estimated gradient across the length of the ampoule was around 80 K. The sample powder was placed at the hot end (source) and the crystal grew at the colder end of the ampoule.

The phase purity of the grown crystals was confirmed by powder x-ray diffraction (PXRD). For this purpose small crystal pieces were crushed into fine powders and PXRD was recorded in the Bragg-Brentano geometry using a Bruker, D8 Advance diffractometer. In a second experiment, a flat single-crystal specimen was mounted on the sample holder of the powder diffractometer. Appropriate precaution was taken to keep the crystal surface in the diffraction plane of the diffractometer. The powder data was analyzed using the Rietveld refinement to obtain the structural parameters. Single crystals were examined using a scanning electron microscope equipped with an energy dispersive absorption X-ray spectroscopy (EDAXS) attachment (Zeiss Ultra plus). The x-ray Laue diffraction was done in the back reflection geometry (Photonic Science, UK). The thermogravimetric analysis (TGA) and differential scanning calorimetry (DSC) was performed under high-purity Ar-gas between room-temperature and 1350° (Jupiter F1 StA 449 Netzsch). The electrical resistance was measured by the four-probe method between room-temperature and 77 K using a homebuilt setup. High-resolution transmission electron microscopy (HRTEM) was used for high-resolution imaging and for obtaining SAED patterns (JEOL JEM 2200FS 200 Kev). For this purpose, the fine powder obtained by crushing a crystal piece was mixed with ethanol. The solution was drop cast and dried over a copper grit with an amorphous carbon layer over it.

D.3 Results and Discussion

Fig. D.1 (a) shows a few representative crystal specimens of $Nb_{0.83}CoSb$ grown here. The average size of these crystals along their longest dimension varied from 1 mm to 2 mm. A zoomed-in view of a specimen that is about 2 mm in length is shown in Fig. D.1 (b) as a representative. The mirror-like shiny surface is shown with an arrow where the image of the graph paper on which the crystal is placed can be seen. As we shall see later, the large mirror-like crystal facets correspond to the (111) family of planes. The grown crystals exhibit a metallic luster and are resistant to air/moisture. Some of the crystal pieces were crushed into fine powders for PXRD. A typical powder x-ray diffraction pattern in the Bragg Brentano geometry is shown in Fig. D.2 (a). No identifiable secondary phase was observed. The data are refined using the cubic $F\bar{4}3m$ symmetry. The calculated and the difference profiles for the best-fit are shown in Fig. D.2 (a). The wyckoff positions, coordinates and occupancies Nb, Co, and Sb obtained from the Rietveld refinement are shown in

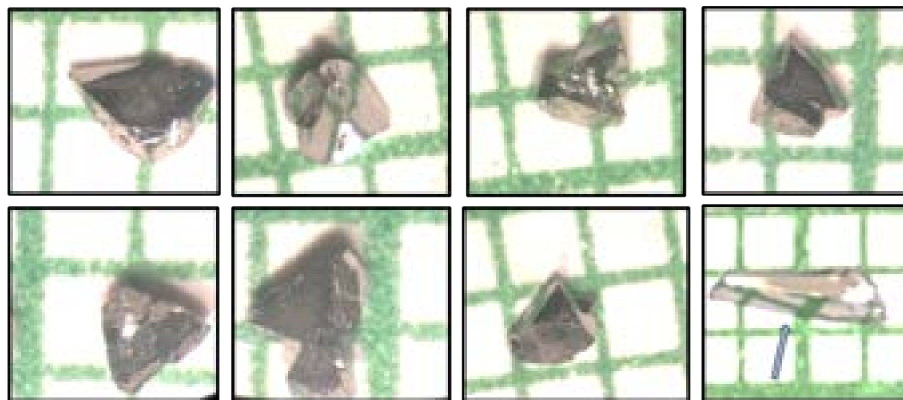

Figure D.1: (a-h) Some single crystals of $Nb_{0.83}CoSb$ are shown, these were obtained from CVT growth. (h) A single crystal of length > 2 mm of $Nb_{0.83}CoSb$ has been shown.

Table D.1. The Nb occupancy of 0.82 is close to its nominal value. No noticeable antisite disorder could be observed. The x-ray diffraction pattern on a single crystal specimen in the Bragg-Brentano geometry as shown in Fig. D.2 (b). In this case, the observed pattern shows only two sharp peaks that were indexed as 111 and 222 . The absence of any other peak indicates the single-crystalline nature of the specimen. The sharpness of the peaks is an indicator of the high-quality of the grown crystals. From the hkl indices of the observed peaks it can be inferred that the crystal surface reflecting the x-ray beam corresponds to the (111) family of planes. The crystal structure drawn using the Rietveld data is shown in Fig. D.3.

A typical back- reflection Laue pattern of $Nb_{0.83}CoSb$ single crystal has been shown in Fig. D.4. This image was captured on a crystal facet such as the one shown in Fig. 1 h (bottom right). The crystallographic orientation of such a facet is along the high symmetry [111] direction. The sharpness of Laue spots indicate the high quality of our crystals. The presence of diffuse scattering around the Laue spots indexed as 213 (or 312) (see inset for a zoomed in view of the spot 213) is likely due to the short-range vacancy ordering that we shall return to in the HRTEM section. A few representative FESEM images taken on some of the crystal specimens are shown in Fig. D.5. These images show triangular shaped cleaved facets reminiscent of the tetrahedral coordination of the elements in the hH structure. A typical chemical map from this surface is shown Fig. D.6 using the false-color representation. This shows a very homogeneous distribution of the elements across the entire imaged area of about 20×20 μm^2.

In Fig. D.7, HRTEM micrographs are shown in panels (a) , and the corresponding SAED pattern has been shown in panels (b). The fast fourier transform (FFT) of the micrograph has been shown in the inset of panel (a). In SAED and FFT of the micrographs, in addition to the fundamental diffraction spots corresponding to the lattice planes, weak diffuse bands making wave-like patterns around these

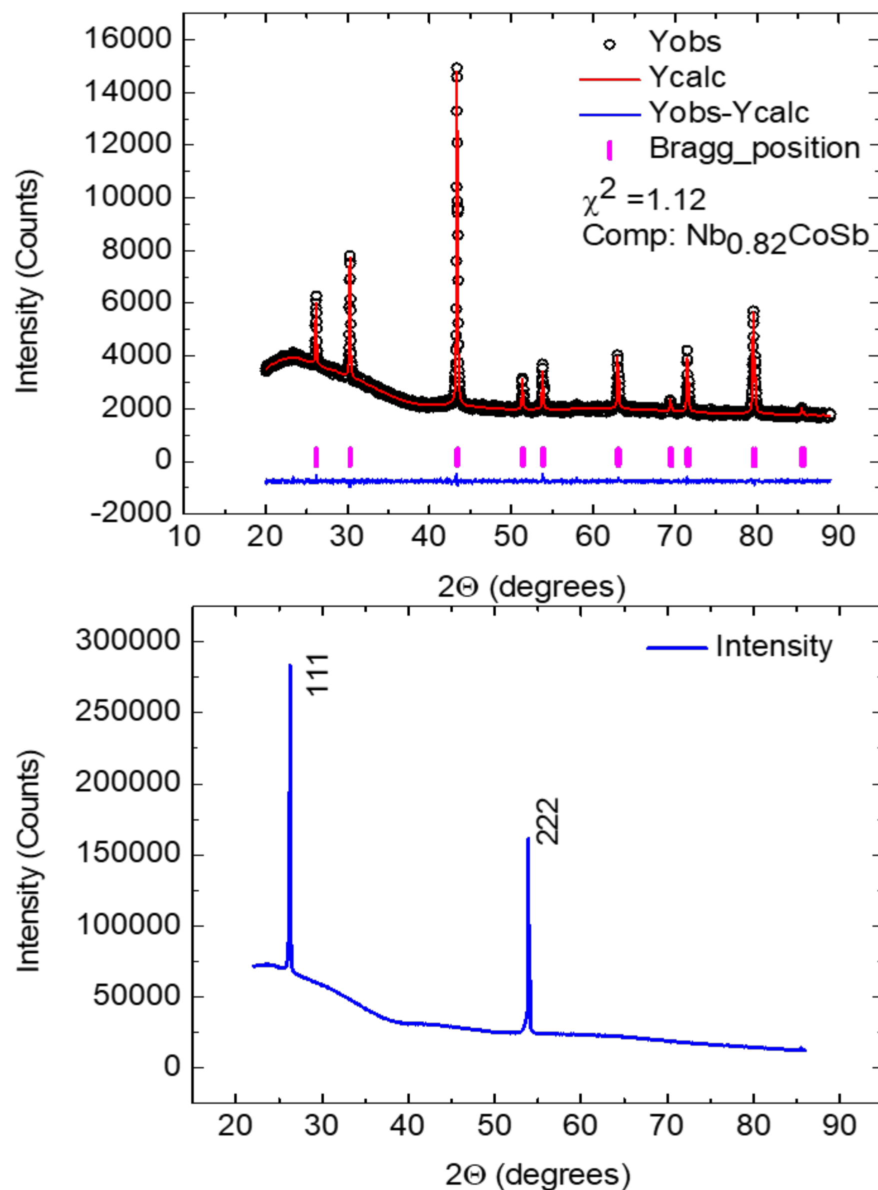

Figure D.2: (a) X-ray diffraction pattern obtained on a single crystalline piece of $Nb_{0.83}CoSb$. The single-crystal X-ray diffraction shows peaks of [111] family of planes. (b)Powder X-ray diffraction pattern on a finely ground single crystal of $Nb_{0.83}CoSb$. The X-ray diffraction pattern can be recognized by the cubic $F-43m$ phase. The diffraction pattern was refined using FullProf Suite and the composition obtained is $Nb_{0.82}CoSb$.

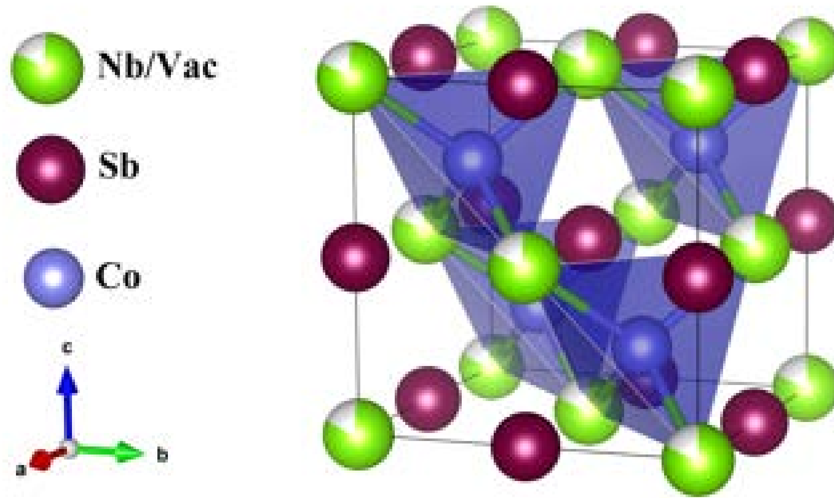

Figure D.3: Crystal structure of the sample obtained through Reitveld refinement. Inset show zoomed image of area marked with white dashed line around spot marked as 213 hkl plane.

Table D.1: Crystallographic data obtained for $Nb_{0.83}CoSb$ single crystal using Reitveld refinement.

Nominal composition:	$Nb_{0.83}CoSb$		
Structure:	Cubic		
Spacegroup no. and Hermann-Mauguin Symbol	216, $F\bar{4}3m$		
Unit cell dimension	5.8984 $\mathring{A}$		
	$\alpha = \beta = \gamma = 90°$		
Volume	205.2172 cm^3		
Density	8.314 g/cm^3		
Z	4		
R_{wp}	15.1		
R_{exp}	14.15		
$\chi^2 = (R_{wp}/R_{exp})^2$	1.14		
Obtained composition (refinement):	$Nb_{0.82}CoSb$		
Wyckoff positions:			
	x	y	z
Nb	0	0	0
Co	0.5	0.5	0.5
Sb	0.25	0.25	0.25

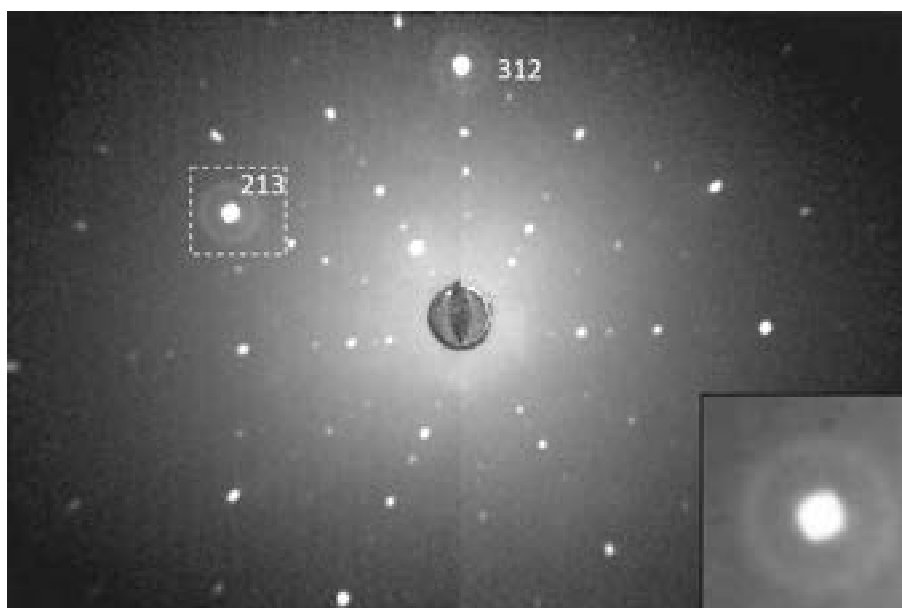

Figure D.4: A representative Laue back reflection diffraction pattern obtained on Fig. D.1(h).

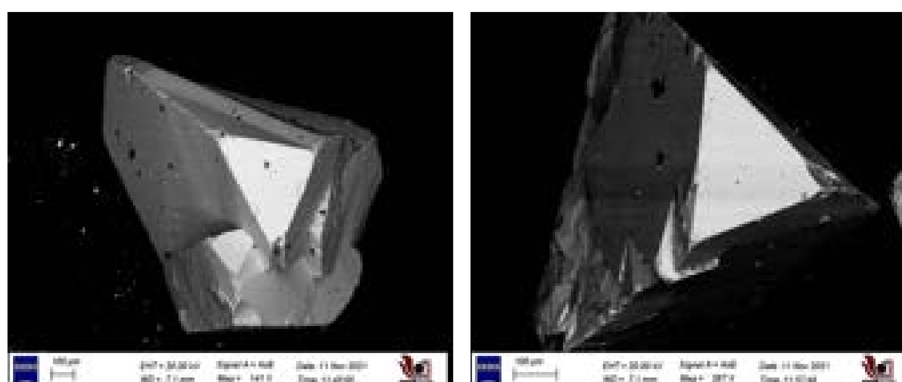

Figure D.5: Few representative FESEM images of $Nb_{0.83}CoSb$ single crystals taken in backscattering mode.

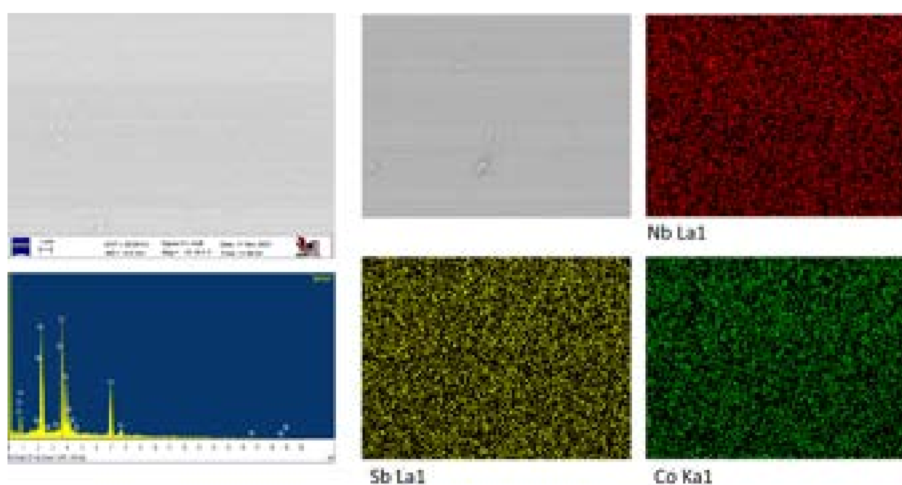

Figure D.6: A representative FESEM image showing chemical mapping done on a single crystal of $Nb_{0.83}CoSb$ backscattering mode.

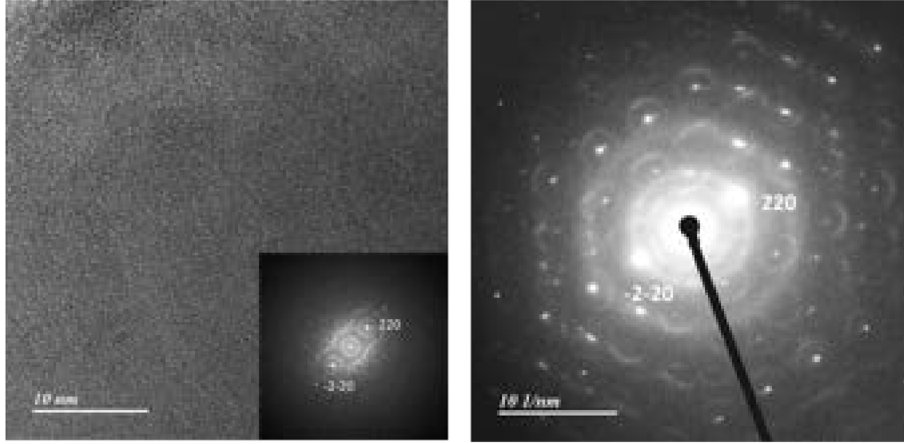

Figure D.7: The high-resolution TEM images taken on pulverized $Nb_{0.83}CoSb$ single crystal showing micrograph in (a), and the SAED pattern in (b). The presence of diffused bands forming wave-like patterns, coexisting with the sharp diffraction spots can be seen in the SAED pattern. The weak spots and the hexagonal patterns at the bottom left and top right corners indicate the presence of superstructure. The 220 planes are labeled in the SAED pattern. The inset in panel (a) shows the FFT of the micrograph

points can also be seen. These diffuse bands are due to the short-range vacancy ordering at the Nb-site [206]. The presence of weak spots arranged in hexagonal pattern in the bottom left and top right corner in panel (b) shows the presence of superstructure. Thus, the Nb sublattice can be described as a hybrid structure with coexisting ordered, short-range order and long-range ordered regions. Roth et al. [157] showed that both the short-range and long-range ordering can be explained by assuming that the Nb vacancies in the Nb sublattice tend to avoid each other to the maximum extent possible.

The TGA/DSC data taken on a single crystal piece of $Nb_{0.83}CoSb$ is shown in FIg. D.8. The measurements were carried out in a high-purity flowing Argon gas between room temperature and 1300 °C. The sample shows no significant change in its mass till the highest temperature. However, the DSC data show a sharp endothermic peak at 1193 °C while heating. Upon cooling, the peak appears at 1061.5°C indicating that the transition is reversible. In a previous study, an order-disorder transition (i.e., from a short-ranged vacancy ordered state to a completely disordered state) was predicted to occur around 300°C [222]. However, in previous high-temperature HRTEM experiments the diffused band were seen upto temperatures as high as 800°C [206]. The expected order-disorder transition therefore remained undetected. We believe that the peak in our DSC measurements is related to the order-disorder transition of the vacancies. Since the structural symmetry in the room-temperature phase is already rather high (Cubic $F\overline{4}3m$), the likelihood of a transition to even higher symmetry at high temperatures is very low if not nil.

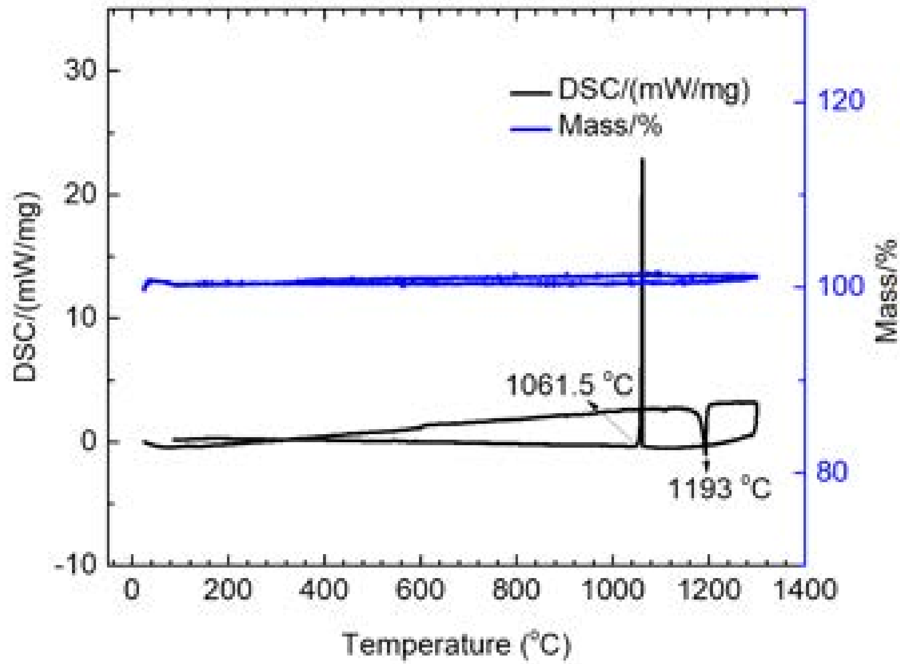

Figure D.8: The TGA/DSC signals for a $Nb_{0.83}CoSb$ crystal specimen measured under an inert atmosphere. The sharp peaks, discussed in the main text, are not due to melting or decomposition of the sample.

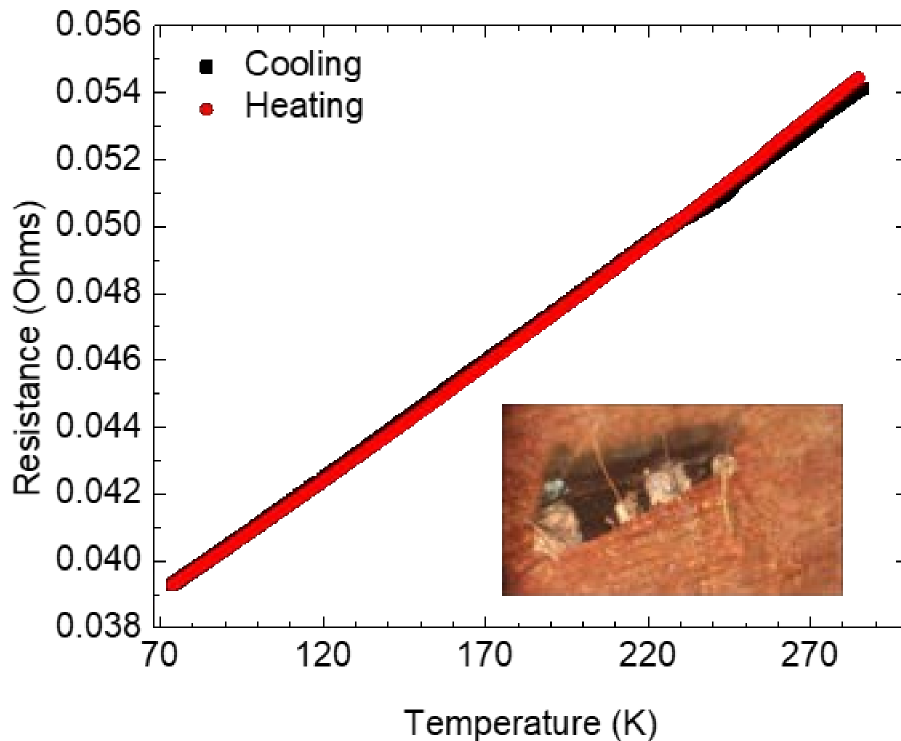

Figure D.9: Temperature variation of resistance of the single crystal of $Nb_{0.83}CoSb$ measured using a lab-based low temperature (Liq. Nitrogen) four-probe setup using Keithley instruments and Lab-View program. In the inset, we have shown a single crystal with gold wire contact using silver paint for resistance measurements.

The temperature variation of the electrical resistance of a single crystal sample of $Nb_{0.83}CoSb$ is shown in Fig. D.9. The data were collected both while cooling and heating. An image of the crystal with the four-probe contacts made using gold wire and silver epoxy is shown in the inset. Upon cooling, the sample resistance decreases almost linearly as for metals and degenerate semiconductors. Since the cross-sectional area is not uniform, the electrical resistivity could not be obtained. However, from the measured data we can conclude that the crystal is fairly conducting and $dR/dT > 0$.

D.4 Summary and Conclusion

To summarize, we have grown mm-size high-quality single crystals of a technologically important 'defective' half-Heusler alloy$Nb_{0.83}CoSb$. The crystals were grown using the chemical vapor transport method using iodine as the transporting agent. The grown crystals were chemically homogeneous and showed large mirror-like shiny surfaces oriented perpendicular to the <111> axis. The orientation was confirmed using the x-ray Laue diffraction technique. The Laue spots were sharp indicating a high-crystal quality. In the Laue diffraction, besides the fundamental Laue spots, diffuse rings were also seen for a few high-symmetric spots indicating that the long-range atomic arrangement in the structure of $Nb_{0.83}CoSb$ coexists with a short-range ordering. This short-range ordering is the ordering of the Nb vacancies at the Nb site. This was confirmed using HRTEM where the fundamental electron diffraction spots were accompanied by diffuse, wave-like, patterns running around the fundamental spots. The DSC measurements revealed a sharp endothermic peak at 1191° while heating and 1131° upon cooling. This is likely due to the order-disorder transition that was predicted to occur in a previous study. The sample shows an almost linear resistivity behavior between room-temperature and liquid nitrogen temperature as expected from a heavily doped degenerate semiconductor. In the future, it would be interesting to investigate the nature of Nb vacancy ordering using other spectroscopic techniques. The order-disorder transition at high temperatures needs further confirmation. The electrical resistivity measurements should be extended down to much lower temperatures as the measure of residual resistivity can also throw light on the degree of vacancy ordering in crystals prepared for various values of Nb stoichiometry which can vary, as per previous reports, from 0.79 to 0.85. The diffuse bands in HRTEM are also previously shown to be highly sensitive to the Nb stoichiometry which adds further motivation for growing $Nb_{0.83+\delta}CoSb$ crystals for various values of δ.

Bibliography

[1] R. Akram, Q. Zhang, D. Yang, Y. Zheng, Y. Yan, X. Su, and X. Tang. Enhanced thermoelectric properties of la-doped zrnisn half-heusler compound. *Journal of electronic materials*, 44(10):3563–3570, 2015.

[2] R. Akram, Y. Yan, D. Yang, X. She, G. Zheng, X. Su, and X. Tang. Microstructure and thermoelectric properties of sb doped hf0. 25zr0. 75nisn half-heusler compounds with improved carrier mobility. *Intermetallics*, 74:1–7, 2016.

[3] R. Akram, Y. Yan, M. Hussain, X. She, and X. Tang. Thermoelectric properties of phase separated ti substituted zr0. 75hf0. 25nisn0. 985sb0. 015 half-heuslers. *Progress in Natural Science: Materials International*, 30(1):74–79, 2020.

[4] S. Al Azar and A. Mousa. Structural, electronic and magnetic properties of ti1+ x fesb and tife 0.75 m 0.25 sb (m= ni, mn) heusler alloys. In *APS March Meeting Abstracts*, volume 2016, pages T1–148, 2016.

[5] S. Anand, K. Xia, T. Zhu, C. Wolverton, and G. J. Snyder. Temperature dependent n-type self doping in nominally 19-electron half-heusler thermoelectric materials. *Advanced Energy Materials*, 8(30):1801409, 2018. doi: https://doi.org/10.1002/aenm.201801409. URL https://onlinelibrary.wiley.com/doi/abs/10.1002/aenm.201801409.

[6] S. Anand, M. Wood, Y. Xia, C. Wolverton, and G. J. Snyder. Double half-heuslers. *Joule*, 3(5):1226–1238, 2019.

[7] J. Androulakis, C.-H. Lin, H.-J. Kong, C. Uher, C.-I. Wu, T. Hogan, B. A. Cook, T. Caillat, K. M. Paraskevopoulos, and M. G. Kanatzidis. Spinodal decomposition and nucleation and growth as a means to bulk nanostructured thermoelectrics: Enhanced performance in pb1-xsnxte-pbs. *Journal of the American Chemical Society*, 129(31):9780–9788, 2007. doi: 10.1021/ja071875h. URL https://doi.org/10.1021/ja071875h. PMID: 17629270.

[8] J. Androulakis, I. Todorov, D.-Y. Chung, S. Ballikaya, G. Wang, C. Uher, and M. Kanatzidis. Thermoelectric enhancement in pbte with k or na codoping from tuning the interaction of the light- and heavy-hole valence bands. *Phys. Rev. B*, 82:115209, Sep 2010. doi: 10.1103/PhysRevB.82.115209. URL https://link.aps.org/doi/10.1103/PhysRevB.82.115209.

[9] J. Androulakis, I. Todorov, J. He, D.-Y. Chung, V. Dravid, and M. Kanatzidis. Thermoelectrics from abundant chemical elements: High-performance nanostructured pbse–pbs. *Journal of the American Chemical Society*, 133(28): 10920–10927, 2011. doi: 10.1021/ja203022c. URL https://doi.org/10.1021/ja203022c. PMID: 21650209.

[10] I. Austin. The optical properties of bismuth telluride. *Proceedings of the Physical Society (1958-1967)*, 72(4):545, 1958.

[11] T. Azumi and A. Maesono. Measuring technique of thermal diffusivity and specific heat capacity by laser flash method.; knowhow for measurement by using the new jis method. laser flash ho ni yoru netsukakusanritsu to hinetsu yoryo no sokutei gijutsu.; shin jis wo tsukatte sokuteisuru kotsu. *Nyu Seramikkusu (New Ceramics);(Japan)*, 5(2), 1992.

[12] C. Barreteau, J.-C. Crivello, J.-M. Joubert, and E. Alleno. Optimization of criteria for an efficient screening of new thermoelectric compounds: The tinisi structure-type as a case-study. *ACS Combinatorial Science*, 22(12):813–820, 2020. doi: 10.1021/acscombsci.0c00133. URL https://doi.org/10.1021/acscombsci.0c00133.

[13] D. Bérardan, E. Guilmeau, A. Maignan, and B. Raveau. In2o3: Ge, a promising n-type thermoelectric oxide composite. *Solid State Communications*, 146 (1-2):97–101, 2008.

[14] J. Billingham, P. S. Bell, and M. H. Lewis. Vacancy short-range order in substoichiometric transition metal carbides and nitrides with the nacl structure. i. electron diffraction studies of short-range ordered compounds. *Acta Crystallographica Section A*, 28:602–606, 1972.

[15] K. Biswas, J. He, Q. Zhang, G. Wang, C. Uher, V. P. Dravid, and M. Kanatzidis. Investigation of the thermoelectric properties of the pbte-srte system. *MRS Proceedings*, 1267:1267–DD06–05, 2010. doi: 10.1557/PROC-1267-DD06-05.

[16] BP. Statistical review of world energy 2020 — 69th edition, 2020. URL https://www.bp.com/content/dam/bp/business-sites/en/

global/corporate/pdfs/energy-economics/statistical-review/bp-stats-review-2020-full-report.pdf. Statistical Review of World Energy 2021 — 70th edition.

[17] J. Cape and G. Lehman. Temperature and finite pulse-time effects in the flash method for measuring thermal diffusivity. *Journal of applied physics*, 34(7): 1909–1913, 1963.

[18] J. Carrete, W. Li, N. Mingo, S. Wang, and S. Curtarolo. Finding unprecedentedly low-thermal-conductivity half-heusler semiconductors via high-throughput materials modeling. *Phys. Rev. X*, 4:011019, Feb 2014. doi: 10.1103/PhysRevX.4.011019. URL https://link.aps.org/doi/10.1103/PhysRevX.4.011019.

[19] F. Casper, T. Graf, S. Chadov, B. Balke, and C. Felser. Half-heusler compounds: novel materials for energy and spintronic applications. *Semiconductor Science and Technology*, 27(6):063001, apr 2012. doi: 10.1088/0268-1242/27/6/063001. URL https://doi.org/10.1088/0268-1242/27/6/063001.

[20] Y. W. Chai, T. Oniki, T. Kenjo, and Y. Kimura. The effect of an iso-electronic ti–zr substitution on heusler nanoprecipitation and the thermo-electric properties of a (ti0.2,zr0.8)ni1.1sn half-heusler alloy. *Journal of Alloys and Compounds*, 662:566 – 577, 2016. ISSN 0925-8388. doi: https://doi.org/10.1016/j.jallcom.2015.12.098. URL http://www.sciencedirect.com/science/article/pii/S0925838815318880.

[21] N. S. Chauhan, S. Bathula, A. Vishwakarma, R. Bhardwaj, B. Gahtori, A. Kumar, and A. Dhar. Vanadium-doping-induced resonant energy levels for the enhancement of thermoelectric performance in hf-free zrnisn half-heusler alloys. *ACS Applied Energy Materials*, 1(2):757–764, 2018.

[22] N. S. Chauhan, S. Bathula, A. Vishwakarma, R. Bhardwaj, K. K. Johari, B. Gahtori, M. Saravanan, and A. Dhar. Compositional tuning of zrnisn half-heusler alloys: Thermoelectric characteristics and performance analysis. *Journal of Physics and Chemistry of Solids*, 123:105–112, 2018.

[23] N. S. Chauhan, S. Bathula, B. Gahtori, Y. V. Kolen'ko, R. Shyam, N. K. Upadhyay, and A. Dhar. Spinodal decomposition in (ti, zr)cosb half-heusler: A nanostructuring route toward high efficiency thermoelectric materials. *Journal of Applied Physics*, 126(12):125110, 2019. doi: 10.1063/1.5109091. URL https://doi.org/10.1063/1.5109091.

[24] N. S. Chauhan, S. Bathula, A. Vishwakarma, R. Bhardwaj, K. K. Johari, B. Gahtori, and A. Dhar. Enhanced thermoelectric performance in p-type zrcosb based half-heusler alloys employing nanostructuring and compositional modulation. *Journal of Materiomics*, 5(1):94–102, 2019.

[25] S. Chen and Z. Ren. Recent progress of half-heusler for moderate temperature thermoelectric applications. *Materials Today*, 16(10):387–395, 2013. ISSN 1369-7021. doi: https://doi.org/10.1016/j.mattod.2013.09.015. URL https://www.sciencedirect.com/science/article/pii/S136970211300312X.

[26] Y. Chen, M. D. Nielsen, Y.-B. Gao, T.-J. Zhu, X. Zhao, and J. P. Heremans. Snte–agsbte2 thermoelectric alloys. *Advanced Energy Materials*, 2(1):58–62, 2012.

[27] H. Cheng, X. Xu, H. Hng, and J. Ma. Characterization of al-doped zno thermoelectric materials prepared by rf plasma powder processing and hot press sintering. *Ceramics International*, 35(8):3067–3072, 2009.

[28] L. M. Clark III and R. E. Taylor. Radiation loss in the flash method for thermal diffusivity. *Journal of Applied Physics*, 46(2):714–719, 1975. doi: 10.1063/1.321635. URL https://doi.org/10.1063/1.321635.

[29] R. D. Cowan. Pulse method of measuring thermal diffusivity at high temperatures. *Journal of Applied Physics*, 34(4):926–927, 1963.

[30] L. M. Cowen, J. Atoyo, M. J. Carnie, D. Baran, and B. C. Schroeder. Organic materials for thermoelectric energy generation. *ECS Journal of Solid State Science and Technology*, 6(3):N3080, 2017.

[31] S. J. Crerar and A. Mar. Ternary silicides m2cr4si5 (m=ti, zr, hf): filled variants of the ta4site4 structure type. *Journal of Solid State Chemistry*, 177(7):2523–2529, 2004. ISSN 0022-4596. doi: https://doi.org/10.1016/j.jssc.2004.03.040. URL https://www.sciencedirect.com/science/article/pii/S002245960400146X.

[32] A. Degiovanni. Diffusivity and flash method. *Revue Générale de Thermique*, 16(185):420–442, 1977.

[33] A. V. Dmitriev, R. N. Pletnev, and Y. G. Zainulin. Effect of oxygen on short-range order of vacancies in vc/sub x/. *Inorg. Mater. (Engl. Transl.); (United States)*. URL https://www.osti.gov/biblio/6182976.

[34] J.-A. Dolyniuk, B. Owens-Baird, J. Wang, J. V. Zaikina, and K. Kovnir. Clathrate thermoelectrics. *Materials Science and Engineering: R: Reports*, 108:1–46, 2016.

[35] R. Dremov, N. Koblyuk, Y. Mudryk, L. Romaka, and V. Sechovský. Electrical resistivity and magnetism in some ternary intermetallics. *Journal of Alloys and Compounds*, 317-318:293–296, 2001. ISSN 0925-8388. doi: https://doi.org/10.1016/S0925-8388(00)01351-7. URL https://www.sciencedirect.com/science/article/pii/S0925838800013517. The 13th International Conference on Solid Compounds of Transition Elements.

[36] B. Du, H. Li, J. Xu, X. Tang, and C. Uher. Enhanced figure-of-merit in se-doped p-type agsbte2 thermoelectric compound. *Chemistry of Materials*, 22 (19):5521–5527, 2010.

[37] L. Dusza. Combined solution of the simultaneous heat loss and finite pulse corrections with the laser flash method. *High Temperatures. High Pressures (Print)*, 27(5):467–473, 1995.

[38] enerdata. Global energy trends - 2021, 2021. URL https://www.enerdata.net/publications/reports-presentations/world-energy-trends.html. Global Energy Trends - 2021 Edition 3 Jun 2021.

[39] T. Eriksson, L. Bergqvist, T. Burkert, S. Felton, R. Tellgren, P. Nordblad, O. Eriksson, and Y. Andersson. Cycloidal magnetic order in the compound irmnsi. *Phys. Rev. B*, 71:174420, May 2005. doi: 10.1103/PhysRevB.71.174420. URL https://link.aps.org/doi/10.1103/PhysRevB.71.174420.

[40] T. Fang, X. Zhao, and T. Zhu. Band structures and transport properties of high-performance half-heusler thermoelectric materials by first principles. *Materials*, 11(5), 2018. ISSN 1996-1944. doi: 10.3390/ma11050847. URL https://www.mdpi.com/1996-1944/11/5/847.

[41] C. Felser, L. Wollmann, S. Chadov, G. H. Fecher, and S. S. P. Parkin. Basics and prospective of magnetic heusler compounds. *APL Materials*, 3(4):041518, 2015. doi: 10.1063/1.4917387. URL https://doi.org/10.1063/1.4917387.

[42] Z. Feng, Y. Fu, A. Putatunda, Y. Zhang, and D. J. Singh. Electronic structure as a guide in screening for potential thermoelectrics: Demonstration for half-heusler compounds. *Phys. Rev. B*, 100:085202, Aug 2019. doi: 10.1103/PhysRevB.100.085202. URL https://link.aps.org/doi/10.1103/PhysRevB.100.085202.

[43] C. Fu, T. Zhu, Y. Pei, H. Xie, H. Wang, G. J. Snyder, Y. Liu, Y. Liu, and X. Zhao. High band degeneracy contributes to high thermoelectric performance in p-type half-heusler compounds. *Advanced Energy Materials*, 4(18): 1400600, 2014.

[44] C. Fu, S. Bai, Y. Liu, Y. Tang, L. Chen, X. Zhao, and T. Zhu. Realizing high figure of merit in heavy-band p-type half-heusler thermoelectric materials. In *Nature communications*, 2015.

[45] C. Fu, H. Wu, Y. Liu, J. He, X. Zhao, and T. Zhu. Enhancing the figure of merit of heavy-band thermoelectric materials through hierarchical phonon scattering. *Advanced Science*, 3(8):1600035, 2016. doi: 10.1002/advs.201600035. URL https://onlinelibrary.wiley.com/doi/abs/10.1002/advs.201600035.

[46] C. Fu, M. Yao, X. Chen, L. Z. Maulana, X. Li, J. Yang, K. Imasato, F. Zhu, G. Li, G. Auffermann, et al. Revealing the intrinsic electronic structure of 3d half-heusler thermoelectric materials by angle-resolved photoemission spectroscopy. *Advanced Science*, 7(1):1902409, 2020.

[47] Y. Gelbstein, J. Davidow, S. N. Girard, D. Y. Chung, and M. Kanatzidis. Controlling metallurgical phase separation reactions of the ge0. 87pb0. 13te alloy for high thermoelectric performance. *Advanced Energy Materials*, 3(6): 815–820, 2013.

[48] S. Ghosh, A. Ghosh, P. Sen, and K. Mandal. Giant room-temperature magnetocaloric effect across the magnetostructural transition in $(MnNiSi)_{1-x}(FeCoGa)_x$ alloys. *Phys. Rev. Applied*, 14:014016, Jul 2020. doi: 10.1103/PhysRevApplied.14.014016. URL https://link.aps.org/doi/10.1103/PhysRevApplied.14.014016.

[49] T. Ghosh, S. Roychowdhury, M. Dutta, and K. Biswas. High-performance thermoelectric energy conversion: A tale of atomic ordering in agsbte2. *ACS Energy Letters*, 6(8):2825–2837, 2021.

[50] S. N. Girard, J. He, X. Zhou, D. Shoemaker, C. M. Jaworski, C. Uher, V. P. Dravid, J. P. Heremans, and M. G. Kanatzidis. High performance na-doped pbte–pbs thermoelectric materials: Electronic density of states modification and shape-controlled nanostructures. *Journal of the American Chemical Society*, 133(41):16588–16597, 2011. doi: 10.1021/ja206380h. URL https://doi.org/10.1021/ja206380h. PMID: 21902270.

[51] K. Gofryk, D. Kaczorowski, T. Plackowski, A. Leithe-Jasper, and Y. Grin. Magnetic and transport properties of rare-earth-based half-heusler phases $r$pdbi: Prospective systems for topological quantum phenomena. *Phys. Rev. B*, 84:035208, Jul 2011. doi: 10.1103/PhysRevB.84.035208. URL https://link.aps.org/doi/10.1103/PhysRevB.84.035208.

[52] H. Goldsmid. *Introduction to Thermoelectricity*. Springer Series in Materials Science. Springer Berlin Heidelberg, 2009. ISBN 9783642007163. URL https://books.google.co.in/books?id=LYN3nDy0FccC.

[53] H. Goldsmid and R. Douglas. The use of semiconductors in thermoelectric refrigeration. *British Journal of Applied Physics*, 5(11):386, 1954.

[54] H. J. Goldsmid. Improving the thermoelectric figure of merit. *Science and Technology of Advanced Materials*, 22(1):280–284, 2021.

[55] C. Goupil, H. Ouerdane, K. Zabrocki, W. Seifert, N. F. Hinsche, and E. Muller. *Thermodynamics and Thermoelectricity*, chapter 1, pages 1–74. John Wiley & Sons, Ltd., 2016. ISBN 9783527338405. doi: https://doi.org/10.1002/9783527338405.ch1. URL https://onlinelibrary.wiley.com/doi/abs/10.1002/9783527338405.ch1.

[56] T. Graf, S. S. P. Parkin, and C. Felser. Heusler compounds—a material class with exceptional properties. *IEEE Transactions on Magnetics*, 47(2):367–373, 2011. doi: 10.1109/TMAG.2010.2096229.

[57] S. Guo, T. Jia, and Y. Zhang. Electrical property dominated promising half-heusler thermoelectrics through high-throughput material computations. *The Journal of Physical Chemistry C*, 123(31):18824–18833, 2019. doi: 10.1021/acs.jpcc.9b04580. URL https://doi.org/10.1021/acs.jpcc.9b04580.

[58] S. Guo, S. Anand, Y. Zhang, and G. J. Snyder. Vibrational entropy stabilizes distorted half-heusler structures. *Chemistry of Materials*, 32(11):4767–4773, 2020. doi: 10.1021/acs.chemmater.0c01404. URL https://doi.org/10.1021/acs.chemmater.0c01404.

[59] S. Guo, Z. Liu, Z. Feng, T. Jia, S. Anand, G. J. Snyder, and Y. Zhang. Prediction of improved thermoelectric performance by ordering in double half-heusler materials. *Journal of Materials Chemistry A*, 8(44):23590–23598, 2020.

[60] S. Guo, Z. Liu, Z. Feng, T. Jia, S. Anand, G. J. Snyder, and Y. Zhang. Prediction of improved thermoelectric performance by ordering in double half-heusler materials. *J. Mater. Chem. A*, 8:23590–23598, 2020. doi: 10.1039/D0TA08364J. URL http://dx.doi.org/10.1039/D0TA08364J.

[61] M. Gürth, G. Rogl, V. Romaka, A. Grytsiv, E. Bauer, and P. Rogl. Thermoelectric high zt half-heusler alloys ti1- x- yzrxhfynisn ($0 \leq x \leq 1; 0 \leq y \leq 1$). *Acta Materialia*, 104:210–222, 2016.

[62] T. Harmening, H. Eckert, C. M. Fehse, C. P. Sebastian, and R. Pöttgen. 45sc solid state nmr studies of the silicides sctsi (t=co, ni, cu, ru, rh, pd, ir, pt). *Journal of Solid State Chemistry*, 184(12):3303–3309, 2011. ISSN 0022-4596. doi: https://doi.org/10.1016/j.jssc.2011.10.025. URL https://www.sciencedirect.com/science/article/pii/S0022459611005676.

[63] J. He and T. M. Tritt. Advances in thermoelectric materials research: Looking back and moving forward. *Science*, 357(6358), 2017. ISSN 0036-8075. doi: 10.1126/science.aak9997. URL https://science.sciencemag.org/content/357/6358/eaak9997.

[64] J. He and T. M. Tritt. Advances in thermoelectric materials research: Looking back and moving forward. *Science*, 357(6358):eaak9997, 2017.

[65] R. He, L. Huang, Y. Wang, G. Samsonidze, B. Kozinsky, Q. Zhang, and Z. Ren. Enhanced thermoelectric properties of n-type nbcosn half-heusler by improving phase purity. *APL Materials*, 4(10):104804, 2016. doi: 10.1063/1.4952994. URL https://doi.org/10.1063/1.4952994.

[66] R. He, L. Huang, Y. Wang, G. Samsonidze, B. Kozinsky, Q. Zhang, and Z. Ren. Enhanced thermoelectric properties of n-type nbcosn half-heusler by improving phase purity. *Apl Materials*, 4(10):104804, 2016.

[67] T. J. Hendricks and W. T. Choate. Engineering scoping study of thermoelectric generator systems for industrial waste heat recovery. 2006.

[68] J. P. Heremans, B. Wiendlocha, and A. M. Chamoire. Resonant levels in bulk thermoelectric semiconductors. *Energy & Environmental Science*, 5(2): 5510–5530, 2012.

[69] M. Hirschberger, S. Kumar, Z. Wang, Q. Gibson, C. Belvin, B. Bernevig, R. Cava, and N. Ong. The chiral anomaly and thermopower of weyl fermions in the half-heusler gdptbi. *Nature Materials*, 15, 02 2016. doi: 10.1038/nmat4684.

[70] J. M. Hodges, S. Hao, J. A. Grovogui, X. Zhang, T. P. Bailey, X. Li, Z. Gan, Y.-Y. Hu, C. Uher, V. P. Dravid, et al. Chemical insights into pbse–x% hgse: high power factor and improved thermoelectric performance by alloying with discordant atoms. *Journal of the American Chemical Society*, 140(51):18115–18123, 2018.

[71] H. Hohl, A. P. Ramirez, C. Goldmann, G. Ernst, B. Wölfing, and E. Bucher. Efficient dopants for zrnisn-based thermoelectric materials. *Journal of Physics: Condensed Matter*, 11(7):1697, 1999.

[72] M. Hong, Z.-G. Chen, L. Yang, Y.-C. Zou, M. S. Dargusch, H. Wang, and J. Zou. Realizing zt of 2.3 in ge1- x- ysbxinyte via reducing the phase-transition temperature and introducing resonant energy doping. *Advanced materials*, 30 (11):1705942, 2018.

[73] M. Hong, J. Zou, and Z.-G. Chen. Thermoelectric gete with diverse degrees of freedom having secured superhigh performance. *Advanced materials*, 31(14): 1807071, 2019.

[74] M. Hong, W. Lyv, M. Li, S. Xu, Q. Sun, J. Zou, and Z.-G. Chen. Rashba effect maximizes thermoelectric performance of gete derivatives. *Joule*, 4(9): 2030–2043, 2020.

[75] https://www.jeol.co.jp/en/science/em.html. Jem 2200fs.

[76] https://www.linseis.com/en/products/thermoelektrik/lsr 3/. Linseis.

[77] https://www.linseis.com/wp-content/uploads/2020/09/Linseis LFA-1000-Thermal-Conductivity-Tester-v4.pdf. Linseis.

[78] https://www.netzsch-thermal-analysis.com/en/products-solutions/simultaneous-thermogravimetry-differential-scanning-calorimetry/sta-449-f1 jupiter/. Tga/dsc jupiter f1 sta 449.

[79] H. Hu, K. Xia, Y. Wang, C. Fu, T. Zhu, and X. Zhao. Fast synthesis and improved electrical stability in n-type ag2te thermoelectric materials. *Journal of Materials Science & Technology*, 91:241–250, 2021.

[80] T. Hu, D. Yang, X. Su, Y. Yan, Y. You, W. Liu, C. Uher, and X. Tang. Interpreting the combustion process for high-performance zrnisn thermoelectric materials. *ACS Applied Materials & Interfaces*, 10(1):864–872, 2018. doi: 10.1021/acsami.7b15273. URL https://doi.org/10.1021/acsami.7b15273. PMID: 29236464.

[81] L. Huang, R. He, S. Chen, H. Zhang, K. Dahal, H. Zhou, H. Wang, Q. Zhang, and Z. Ren. A new n-type half-heusler thermoelectric material nbcosb. *Materials Research Bulletin*, 70:773–778, 2015.

[82] L. Huang, Q. Zhang, Y. Wang, R. He, J. Shuai, J. Zhang, C. Wang, and Z. Ren. The effect of sn doping on thermoelectric performance of n-type half-heusler nbcosb. *Physical Chemistry Chemical Physics*, 19(37):25683–25690, 2017.

[83] L. Huang, J. Wang, X. Chen, R. He, J. Shuai, J. Zhang, Q. Zhang, and Z. Ren. The effects of excess co on the phase composition and thermoelectric properties of half-heusler nbcosb. *Materials*, 11(5), 2018. ISSN 1996-1944. doi: 10.3390/ma11050773. URL https://www.mdpi.com/1996-1944/11/5/773.

[84] L. Huang, J. Wang, X. Mo, X. Lei, S. Ma, C. Wang, and Q. Zhang. Improving the thermoelectric properties of the half-heusler compound vcosb by vanadium vacancy. *Materials*, 12(10), 2019. ISSN 1996-1944. doi: 10.3390/ma12101637. URL https://www.mdpi.com/1996-1944/12/10/1637.

[85] X. Huang, Z. Xu, and L. Chen. The thermoelectric performance of zrnisn/zro2 composites. *Solid State Communications*, 130(3-4):181–185, 2004.

[86] Y. Huang, H. Nagai, K. Hayashi, and Y. Miyazaki. Preparation and thermoelectric properties of pseudogap intermetallic (ti1-xvx)nisi solid solutions. *Journal of Alloys and Compounds*, 771:111–116, Jan. 2019. ISSN 0925-8388. doi: 10.1016/j.jallcom.2018.08.238. Publisher Copyright: © 2018 Elsevier B.V. Copyright: Copyright 2020 Elsevier B.V., All rights reserved.

[87] IEA. Global energy review 2021, 2021. URL https://www.iea.org/reports/global-energy-review-2021. Global Energy Review 2021 Part of Global Energy Review Flagship report — April 2021.

[88] K. K. Johari, R. Bhardwaj, N. S. Chauhan, B. Gahtori, S. Bathula, S. Auluck, and S. Dhakate. Band structure modification and mass fluctuation effects of isoelectronic germanium-doping on thermoelectric properties of zrnisn. *ACS Applied Energy Materials*, 3(2):1349–1357, 2019.

[89] G. Joshi, X. Yan, H. Wang, W. Liu, G. Chen, and Z. Ren. Enhancement in thermoelectric figure-of-merit of an n-type half-heusler compound by the nanocomposite approach. *Advanced Energy Materials*, 1(4):643–647, 2011. doi: 10.1002/aenm.201100126. URL https://onlinelibrary.wiley.com/doi/abs/10.1002/aenm.201100126.

[90] G. Joshi, R. He, M. Engber, G. Samsonidze, T. Pantha, E. Dahal, K. Dahal, J. Yang, Y. Lan, B. Kozinsky, et al. Nbfesb-based p-type half-heuslers for power generation applications. *Energy & Environmental Science*, 7(12):4070–4076, 2014.

[91] M. G. Kanatzidis. Nanostructured thermoelectrics: the new paradigm? *Chemistry of materials*, 22(3):648–659, 2010.

[92] A. Katre, J. Carrete, and N. Mingo. Unraveling the dominant phonon scattering mechanism in the thermoelectric compound zrnisn. *Journal of Materials Chemistry A*, 4(41):15940–15944, 2016.

[93] S. M. Kauzlarich, S. R. Brown, and G. J. Snyder. Zintl phases for thermoelectric devices. *Dalton Transactions*, (21):2099–2107, 2007.

[94] H.-S. Kim, Z. M. Gibbs, Y. Tang, H. Wang, and G. J. Snyder. Characterization of lorenz number with seebeck coefficient measurement. *APL Materials*, 3(4): 041506, 2015. doi: 10.1063/1.4908244. URL https://doi.org/10.1063/1.4908244.

[95] H.-S. Kim, K. H. Lee, and S. il Kim. Understanding bipolar thermal conductivity in terms of concentration ratio of minority to majority carriers. *Journal of Materials Research and Technology*, 14:639–646, 2021. ISSN 2238-7854. doi: https://doi.org/10.1016/j.jmrt.2021.06.087. URL https://www.sciencedirect.com/science/article/pii/S2238785421006426.

[96] J. Kim and J.-H. Lim. Organic-inorganic hybrid thermoelectric material synthesis and properties. *Journal of the Korean Ceramic Society*, 54(4):272–277, 2017.

[97] M. Kostenko, A. Rempel, S. Sharf, and A. Lukoyanov. Short-range order in disordered transition metal oxides, carbides, and nitrides with the b1 structure. *Physics of the Solid State*, 57:637–651, 04 2015. doi: 10.1134/S1063783415040137.

[98] K. Koumoto, Y. Wang, R. Zhang, A. Kosuga, and R. Funahashi. Oxide thermoelectric materials: a nanostructuring approach. *Annual review of materials research*, 40:363–394, 2010.

[99] I. Kudman. Thermoelectric properties of dilute pbte-gete alloys. *Metallurgical Transactions*, 2(1):163–168, 1971.

[100] G. A. Landrum, R. Hoffmann, J. Evers, and H. Boysen. The tinisi family of compounds: Structure and bondin. *Inorganic Chemistry*, 37(22):5754–5763, 1998. doi: 10.1021/ic980223e. URL https://doi.org/10.1021/ic980223e.

[101] K. H. Lee, S.-i. Kim, H.-S. Kim, and S. W. Kim. Band convergence in thermoelectric materials: Theoretical background and consideration on bi–sb–te

alloys. *ACS Applied Energy Materials*, 3(3):2214–2223, 2020. doi: 10.1021/acsaem.9b02131. URL https://doi.org/10.1021/acsaem.9b02131.

[102] W. Lee, S. Lee, H. Kim, and Y. Kim. Organic thermoelectric devices with pedot: Pss/zno hybrid composites. *Chemical Engineering Journal*, 415:128935, 2021.

[103] C. Li, Y. Zhao, B. Chi, Y. Gong, and C. Sun. The effects of chemical bonding on the topological property of half- heusler compounds: First principle calculation. *Computational Condensed Matter*, 1:8–13, 2014. ISSN 2352-2143. doi: https://doi.org/10.1016/j.cocom.2014.08.002. URL https://www.sciencedirect.com/science/article/pii/S2352214314000033.

[104] F. Li, J.-F. Li, L.-D. Zhao, K. Xiang, Y. Liu, B.-P. Zhang, Y.-H. Lin, C.-W. Nan, and H.-M. Zhu. Polycrystalline bicuseo oxide as a potential thermoelectric material. *Energy & Environmental Science*, 5(5):7188–7195, 2012.

[105] J. Li, J. Sui, Y. Pei, C. Barreteau, D. Berardan, N. Dragoe, W. Cai, J. He, and L.-D. Zhao. A high thermoelectric figure of merit zt¿ 1 in ba heavily doped bicuseo oxyselenides. *Energy & Environmental Science*, 5(9):8543–8547, 2012.

[106] J. Li, Z. Chen, X. Zhang, Y. Sun, J. Yang, and Y. Pei. Electronic origin of the high thermoelectric performance of gete among the p-type group iv monotellurides. *NPG Asia Materials*, 9(3):e353–e353, 2017.

[107] J. Li, Z. Chen, X. Zhang, H. Yu, Z. Wu, H. Xie, Y. Chen, and Y. Pei. Simultaneous optimization of carrier concentration and alloy scattering for ultrahigh performance gete thermoelectrics. *Advanced Science*, 4(12):1700341, 2017.

[108] J. Li, X. Zhang, S. Lin, Z. Chen, and Y. Pei. Realizing the high thermoelectric performance of gete by sb-doping and se-alloying. *Chemistry of Materials*, 29(2):605–611, 2017.

[109] Y. Li, J. Han, Q. Xiang, C. Zhang, and J. Li. Enhancing thermoelectric properties of p-type sige by simo addition. *Journal of Materials Science: Materials in Electronics*, 30, 05 2019. doi: 10.1007/s10854-019-01245-9.

[110] Y. Li, J. Qiao, Y. Zhao, Q. Lan, P. Mao, J. Qiu, K. Tai, C. Liu, and H. Cheng. A flexible thermoelectric device based on a bi2te3-carbon nanotube hybrid. *Journal of Materials Science & Technology*, 58:80–85, 2020.

[111] Y. Li, Y. Zhao, J. Qiao, S. Jiang, J. Qiu, J. Tan, L. Zhang, Z. Gai, K. Tai, and C. Liu. A flexible and infrared-transparent bi2te3-carbon nanotube ther-

moelectric hybrid for both active and passive cooling. *ACS Applied Electronic Materials*, 2(9):3008–3016, 2020.

[112] Z. Li, C. Xiao, S. Fan, Y. Deng, W. Zhang, B. Ye, and Y. Xie. Dual vacancies: an effective strategy realizing synergistic optimization of thermoelectric property in bicuseo. *Journal of the American Chemical Society*, 137(20):6587–6593, 2015.

[113] L. Liang, J. Fan, M. Wang, G. Chen, and G. Sun. Ternary thermoelectric composites of polypyrrole/pedot: Pss/carbon nanotube with unique layered structure prepared by one-dimensional polymer nanostructure as template. *Composites Science and Technology*, 187:107948, 2020.

[114] H. Lin, L. Wray, Y. Xia, S.-Y. Xu, S. Jia, R. Cava, A. Bansil, and M. Z. Hasan. Half-heusler ternary compounds as new multifunctional experimental platforms for topological quantum phenomena. *Nature materials*, 9:546–9, 07 2010. doi: 10.1038/nmat2771.

[115] S. Liu, J. Wang, J. Jia, X. Hu, and S. Liu. Synthesis and thermoelectric performance of li-doped nio ceramics. *Ceramics International*, 38(6):5023–5026, 2012.

[116] S.-h. Liu, J.-f. Jia, J. Wang, X. HU, X.-c. WANG, and S.-j. LIU. Synthesis and properties of nio based thermoelectric oxide. *Journal of Materials Science and Engineering*, 4, 2012.

[117] T.-Y. Liu, J. C. Huang, W.-S. Chuang, H.-S. Chou, J.-Y. Wei, C.-Y. Chao, Y.-C. Liao, and J. S. Jang. Spinodal decomposition and mechanical response of a tizrnbta high-entropy alloy. *Materials*, 12(21), 2019. ISSN 1996-1944. doi: 10.3390/ma12213508. URL https://www.mdpi.com/1996-1944/12/21/3508.

[118] Y. Liu, Y. Lin, Z. Shi, C.-W. Nan, and Z. Shen. Preparation of ca3co4o9 and improvement of its thermoelectric properties by spark plasma sintering. *Journal of the American Ceramic Society*, 88(5):1337–1340, 2005.

[119] Y. Liu, P. Sahoo, J. P. A. Makongo, X. Zhou, S.-J. Kim, H. Chi, C. Uher, X. Pan, and P. F. P. Poudeu. Large enhancements of thermopower and carrier mobility in quantum dot engineered bulk semiconductors. *Journal of the American Chemical Society*, 135(20):7486–7495, 2013. doi: 10.1021/ja311059m. URL https://doi.org/10.1021/ja311059m. PMID: 23607819.

[120] Z. Liu, S. Guo, Y. Wu, J. Mao, Q. Zhu, H. Zhu, Y. Pei, J. Sui, Y. Zhang, and Z. Ren. Design of high-performance disordered half-heusler thermoelectric materials using 18-electron rule. *Advanced Functional Materials*, 29(44): 1905044, 2019.

[121] Z.-Y. Liu, J.-L. Zhu, X. Tong, S. Niu, and W.-Y. Zhao. A review of cosb 3-based skutterudite thermoelectric materials. *Journal of Advanced Ceramics*, pages 1–27, 2020.

[122] M. Marshall, J. Sanford, W. Shelton, and W. Xie. The crystal structures and magnetic properties of tifesi coexisting in hexagonal and orthorhombic symmetries. *Journal of Alloys and Compounds*, 864(C), 2021. doi: 10.1016/j.jallcom.2021.158617. URL https://par.nsf.gov/biblio/10215262.

[123] Y. P. Maslakovets. Heat energy conversion in electrical one by semiconductor thermocouples. *DSc Thesis, AF Ioffe Physical-Technical Institute*, 1949.

[124] J. Miranda and T. Gruhn. Interplay between electronic states and structural stability in cation-deficient vcosb, nbcosb, and tacosb half-heuslers. *Journal of Electronic Materials*, 51(5):2043–2053, 2022.

[125] H. Muta, T. Kanemitsu, K. Kurosaki, and S. Yamanaka. High-temperature thermoelectric properties of nb-doped mnisn (m= ti, zr) half-heusler compound. *Journal of Alloys and Compounds*, 469(1-2):50–55, 2009.

[126] A. Nag and V. Shubha. Oxide thermoelectric materials: A structure–property relationship. *Journal of electronic materials*, 43(4):962–977, 2014.

[127] Y. Nakajima, R. Hu, K. Kirshenbaum, A. Hughes, P. Syers, X. Wang, K. Wang, R. Wang, S. R. Saha, D. Pratt, J. W. Lynn, and J. Paglione. Topological ¡i¿r¡/i¿pdbi half-heusler semimetals: A new family of noncentrosymmetric magnetic superconductors. *Science Advances*, 1(5):e1500242, 2015. doi: 10.1126/sciadv.1500242.

[128] B. R. K. Nanda and I. Dasgupta. Electronic structure and magnetism in half-heusler compounds. 15(43):7307–7323, oct 2003. doi: 10.1088/0953-8984/15/43/014. URL https://doi.org/10.1088/0953-8984/15/43/014.

[129] G. Naydenov, P. Hasnip, V. Lazarov, and M. Probert. Huge power factor in p-type half-heusler alloys nbfesb and tafesb. *Journal of Physics: Materials*, 2, 04 2019. doi: 10.1088/2515-7639/ab16fb.

[130] L. Offernes, P. Ravindran, and A. Kjekshus. Electronic structure and chemical bonding in half-heusler phases. *Journal of Alloys and Compounds*, 439

(1):37–54, 2007. ISSN 0925-8388. doi: https://doi.org/10.1016/j.jallcom.2006.08.316. URL https://www.sciencedirect.com/science/article/pii/S0925838806013594.

[131] H. Ohta, K. Sugiura, and K. Koumoto. Recent progress in oxide thermoelectric materials: p-type ca3co4o9 and n-type srtio3-. *Inorganic chemistry*, 47(19): 8429–8436, 2008.

[132] M. Ohtaki. Recent aspects of oxide thermoelectric materials for power generation from mid-to-high temperature heat source. *Journal of the Ceramic Society of Japan*, 119(1395):770–775, 2011.

[133] M. Ohtaki, D. Ogura, K. Eguchi, and H. Arai. High-temperature thermoelectric properties of in2o3-based mixed oxides and their applicability to thermoelectric power generation. *Journal of Materials Chemistry*, 4(5):653–656, 1994.

[134] K. P. Ong, D. J. Singh, and P. Wu. Analysis of the thermoelectric properties of n-type zno. *Physical Review B*, 83(11):115110, 2011.

[135] H. B. Ozisik, E. Deligoz, H. Ozisik, and E. Ateser. Phonon transport properties of nbcosb compound. *Materials Research Express*, 2020.

[136] A. Page, P. Poudeu, and C. Uher. A first-principles approach to half-heusler thermoelectrics: Accelerated prediction and understanding of material properties. *Journal of Materiomics*, 2(2):104–113, 2016.

[137] S. Pal, R. Arora, S. Roychowdhury, L. Harnagea, K. Saurabh, S. Shenoy, D. Muthu, K. Biswas, U. Waghmare, and A. Sood. Pressure-induced phase transitions in the topological crystalline insulator snte and its comparison with semiconducting snse: Raman and first-principles studies. *Physical Review B*, 101(15):155202, 2020.

[138] M. Papapetrou, G. Kosmadakis, A. Cipollina, U. Commare, and G. Micale. Industrial waste heat: Estimation of the technically available resource in the eu per industrial sector, temperature level and country. *Applied Thermal Engineering*, 138, 04 2018. doi: 10.1016/j.applthermaleng.2018.04.043.

[139] J. Park, D. Kwak, S. Yoon, and S. Choi. Thermoelectric properties of bi, nb co-substituted camno3 at high temperature. *Journal of Alloys and Compounds*, 487(1-2):550–555, 2009.

[140] K. Park and J. Lee. Enhanced thermoelectric properties of naco2o4 by adding zno. *Materials Letters*, 62(15):2366–2368, 2008.

[141] K. Park, J. Seong, and S. Nahm. Improvement of thermoelectric properties with the addition of sb to zno. *Journal of Alloys and Compounds*, 455(1-2): 331–335, 2008.

[142] W. Parker, R. Jenkins, C. Butler, and G. Abbott. Flash method of determining thermal diffusivity, heat capacity, and thermal conductivity. *Journal of applied physics*, 32(9):1679–1684, 1961.

[143] Y. Pei, A. D. LaLonde, H. Wang, and G. J. Snyder. Low effective mass leading to high thermoelectric performance. *Energy & Environmental Science*, 5(7):7963–7969, 2012. ISSN 1754-5692. doi: 10.1039/C2EE21536E. URL https://doi.org/10.1039/C2EE21536E.

[144] Y.-L. Pei, J. He, J.-F. Li, F. Li, Q. Liu, W. Pan, C. Barreteau, D. Berardan, N. Dragoe, and L.-D. Zhao. High thermoelectric performance of oxyselenides: intrinsically low thermal conductivity of ca-doped bicuseo. *NPG Asia Materials*, 5(5):e47–e47, 2013.

[145] V. Ponnambalam, B. Zhang, T. M. Tritt, and S. J. Poon. Thermoelectric properties of half-heusler bismuthides zrco 1- x ni x bi (x= 0.0 to 0.1). *Journal of electronic materials*, 36(7):732–735, 2007.

[146] S. J. Poon. Electronic and thermoelectric properties of half-heusler alloys. *Semiconductors and Semimetals: Recent Trends in Thermoelectric Materials Research II Vol*, 70:37–75, 2001.

[147] Y. Qin, L. Yang, J. Wei, S. Yang, M. Zhang, X. Wang, and F. Yang. Doping effect on cu2se thermoelectric performance: A review. *Materials*, 13(24):5704, 2020.

[148] P. Qiu, J. Yang, X. Huang, X. Chen, and L. Chen. Effect of antisite defects on band structure and thermoelectric performance of zrnisn half-heusler alloys. *Applied Physics Letters*, 96(15):152105, 2010.

[149] R. J. Quinn and J.-W. G. Bos. Advances in half-heusler alloys for thermoelectric power generation. *Materials Advances*, 2(19):6246–6266, 2021.

[150] P. R. Raghuvanshi, S. Mondal, and A. Bhattacharya. A high throughput search for efficient thermoelectric half-heusler compounds. *J. Mater. Chem. A*, 8:25187–25197, 2020. doi: 10.1039/D0TA06810A. URL http://dx.doi.org/10.1039/D0TA06810A.

[151] A. A. Rempel. Atomic and vacancy ordering in nonstoichiometric carbides. *Physics-Uspekhi*, 39:31–56, 1996.

[152] G.-K. Ren, J.-L. Lan, K. J. Ventura, X. Tan, Y.-H. Lin, and C.-W. Nan. Contribution of point defects and nano-grains to thermal transport behaviours of oxide-based thermoelectrics. *npj Computational Materials*, 2(1):1–9, 2016.

[153] Q. Ren, W. D. Hutchison, J. Wang, A. J. Studer, and S. J. Campbell. Magnetic and structural transitions tuned through valence electron concentration in magnetocaloric mn(co1–xnix)ge. *Chemistry of Materials*, 30(4):1324–1334, 2018. doi: 10.1021/acs.chemmater.7b04970. URL https://doi.org/10.1021/acs.chemmater.7b04970.

[154] W. Ren, H. Zhu, Q. Zhu, U. Saparamadu, R. He, Z. Liu, J. Mao, C. Wang, K. Nielsch, Z. Wang, et al. Ultrahigh power factor in thermoelectric system nb0. 95m0. 05fesb (m= hf, zr, and ti). *Advanced Science*, 5(7):1800278, 2018.

[155] researchandmarkets. Global thermoelectric generator market 2017-2021, 2021. URL https://www.researchandmarkets.com/reports/4368822/global-thermoelectric-generator-market-2017-2021. Global Thermoelectric Generator Market 2017-2021.

[156] L. Romaka, A. Tkachuk, Y. Stadnyk, and V. Romaka. Phase equilibria in zr–ni–sb ternary system at 870k. *Journal of Alloys and Compounds*, 470 (1):233–236, 2009. ISSN 0925-8388. doi: https://doi.org/10.1016/j.jallcom.2008.03.030. URL https://www.sciencedirect.com/science/article/pii/S0925838808004465.

[157] N. Roth, T. Zhu, and B. B. Iversen. A simple model for vacancy order and disorder in defective half-Heusler systems. *IUCrJ*, 7(4):673–680, Jul 2020. doi: 10.1107/S2052252520005977. URL https://doi.org/10.1107/S2052252520005977.

[158] S. Roychowdhury, T. Ghosh, R. Arora, M. Samanta, L. Xie, N. K. Singh, A. Soni, J. He, U. V. Waghmare, and K. Biswas. Enhanced atomic ordering leads to high thermoelectric performance in agsbte2. *Science*, 371(6530):722–727, 2021.

[159] M. Rull-Bravo, A. Moure, J. Fernández, and M. Martín-González. Skutterudites as thermoelectric materials: revisited. *Rsc Advances*, 5(52):41653–41667, 2015.

[160] S. Sakurada and N. Shutoh. Effect of ti substitution on the thermoelectric properties of (zr,hf)nisn half-heusler compounds. *Applied Physics Letters*, 86 (8):082105, 2005. doi: 10.1063/1.1868063.

[161] I. Samira, S. Ziti, H. Labrim, and L. Bahmad. Half-metallicity and magnetism in the full heusler alloy fe2mnsn with l21 and xa stability ordering phases. *Journal of Low Temperature Physics*, 202, 02 2021. doi: 10.1007/s10909-021-02562-2.

[162] K. Saurabh, A. Kumar, P. Ghosh, and S. Singh. Low thermal conductivity and semimetallic behavior in some tinisi structure-type compounds. *Phys. Rev. Materials*, 5:085406, Aug 2021. doi: 10.1103/PhysRevMaterials.5.085406. URL https://link.aps.org/doi/10.1103/PhysRevMaterials.5.085406.

[163] M. Sauvage and E. Parthé. Vacancy short-range order in substoichiometric transition metal carbides and nitrides with the NaCl structure. II. Numerical calculation of vacancy arrangement. *Acta Crystallographica Section A*, 28(6): 607–616, Nov 1972. doi: 10.1107/S0567739472001536. URL https://doi.org/10.1107/S0567739472001536.

[164] J. Schmitt, Z. Gibbs, J. Snyder, and C. Felser. Resolving the true band gap of zrnisn half-heusler thermoelectric materials. *Mater. Horiz.*, 2, 09 2014. doi: 10.1039/C4MH00142G.

[165] J. Schmitt, Z. M. Gibbs, G. J. Snyder, and C. Felser. Resolving the true band gap of zrnisn half-heusler thermoelectric materials. *Materials Horizons*, 2(1): 68–75, 2015.

[166] T. Sekimoto, K. Kurosaki, H. Muta, and S. Yamanaka. Thermoelectric and thermophysical properties of ticosb-zrcosb-hfcosb pseudo ternary system prepared by spark plasma sintering. *Materials transactions*, 47(6):1445–1448, 2006.

[167] F. Serrano-Sánchez, T. Luo, J. Yu, W. Xie, C. Le, G. Auffermann, A. Weidenkaff, T. Zhu, X. Zhao, J. A. Alonso, et al. Thermoelectric properties of n-type half-heusler nbcosn with heavy-element pt substitution. *Journal of Materials Chemistry A*, 8(29):14822–14828, 2020.

[168] J. Shen, L. Fan, C. Hu, T. Zhu, J. Xin, T. Fu, D. Zhao, and X. Zhao. Enhanced thermoelectric performance in the n-type nbfesb half-heusler compound with heavy element ir doping. *Materials Today Physics*, 8:62–70, 2019.

[169] Q. Shen, L. Chen, T. Goto, T. Hirai, J. Yang, G. P. Meisner, and C. Uher. Effects of partial substitution of ni by pd on the thermoelectric properties of zrnisn-based half-heusler compounds. *Applied Physics Letters*, 79(25):4165–4167, 2001. doi: 10.1063/1.1425459. URL https://doi.org/10.1063/1.1425459.

[170] W. Shin and N. Murayama. High performance p-type thermoelectric oxide based on nio. *Materials Letters*, 45(6):302–306, 2000.

[171] J. Shiomi, K. Esfarjani, and G. Chen. Thermal conductivity of half-heusler compounds from first-principles calculations. *Physical Review B*, 84(10): 104302, 2011.

[172] J. Shuai, H. Geng, Y. Lan, Z. Zhu, C. Wang, Z. Liu, J. Bao, C.-W. Chu, J. Sui, and Z. Ren. Higher thermoelectric performance of zintl phases (eu0. 5yb0. 5) 1- xcaxmg2bi2 by band engineering and strain fluctuation. *Proceedings of the National Academy of Sciences*, 113(29):E4125–E4132, 2016.

[173] J. Shuai, J. Mao, S. Song, Q. Zhu, J. Sun, Y. Wang, R. He, J. Zhou, G. Chen, D. J. Singh, et al. Tuning the carrier scattering mechanism to effectively improve the thermoelectric properties. *Energy & Environmental Science*, 10 (3):799–807, 2017.

[174] B. Singh, X. Zhou, H. Lin, and A. Bansil. Saddle-like topological surface states on the $tT'x$ family of compounds (t, T' = transition metal, x = Si, ge). *Phys. Rev. B*, 97:075125, Feb 2018. doi: 10.1103/PhysRevB.97.075125. URL https://link.aps.org/doi/10.1103/PhysRevB.97.075125.

[175] M. Søndergaard, M. Christensen, S. Johnsen, C. Stiewe, T. Dasgupta, E. Mueller, and B. Iversen. Thermoelectric and microstructural properties of pb0.9-xsn0.1gexte compounds prepared bt spinodal decomposition. *Journal of Solid State Chemistry*, 184(5):1172–1175, 2011. ISSN 0022-4596. doi: https://doi.org/10.1016/j.jssc.2011.02.028. URL https://www.sciencedirect.com/science/article/pii/S002245961100096X.

[176] G. J. Snyder and E. S. Toberer. Complex thermoelectric materials. *Materials for sustainable energy: a collection of peer-reviewed research and review articles from Nature Publishing Group*, pages 101–110, 2011.

[177] G. J. Snyder, A. H. Snyder, M. Wood, R. Gurunathan, B. H. Snyder, and C. Niu. Weighted mobility. *Advanced Materials*, 32(25):2001537, 2020.

[178] K. K. Strand. Synthesis and characterization of thermoelectric half-heusler alloy tifesb. Master's thesis, 2014.

[179] Y. Sun, W. Qiu, L. Zhao, H. He, L. Yang, L. Chen, H. Deng, X. Shi, and J. Tang. Defects engineering driven high power factor of zrnisn-based half-heusler thermoelectric materials. *Chemical Physics Letters*, 755: 137770, 2020. ISSN 0009-2614. doi: https://doi.org/10.1016/j.cplett.2020.

137770. URL https://www.sciencedirect.com/science/article/pii/S0009261420306850.

[180] S. Tan, P. Nan, K. Xia, H. Yang, T. Zhu, B. Ge, and W. Zhang. Sublattice short-range order and modified electronic structure in defective half-heusler nb0.8cosb. *The Journal of Physical Chemistry C*, 125(1):1125–1133, 2021. doi: 10.1021/acs.jpcc.0c10018. URL https://doi.org/10.1021/acs.jpcc.0c10018.

[181] A. Tavassoli, F. Failamani, A. Grytsiv, G. Rogl, P. Heinrich, H. Müller, E. Bauer, M. Zehetbauer, and P. Rogl. On the half-heusler compounds nb1-x {Ti, Zr, Hf} xfesb: Phase relations, thermoelectric properties at low and high temperature, and mechanical properties. *Acta materialia*, 135:263–276, 2017.

[182] A. Tavassoli, A. Grytsiv, G. Rogl, V. Romaka, H. Michor, M. Reissner, E. Bauer, M. Zehetbauer, and P. Rogl. The half heusler system ti 1+ x fe 1.33- x sb–ticosb with sb/sn substitution: phase relations, crystal structures and thermoelectric properties. *Dalton Transactions*, 47(3):879–897, 2018.

[183] M. Thesberg, H. Kosina, and N. Neophytou. On the lorenz number of multiband materials. *Physical Review B*, 95(12):125206, 2017.

[184] T. Tian, L. Cheng, J. Xing, L. Zheng, Z. Man, D. Hu, S. Bernik, J. Zeng, J. Yang, Y. Liu, et al. Effects of sintering on the microstructure and electrical properties of zno-based thermoelectric materials. *Materials & Design*, 132: 479–485, 2017.

[185] E. S. Toberer, A. F. May, and G. J. Snyder. Zintl chemistry for designing high efficiency thermoelectric materials. *Chemistry of Materials*, 22(3):624–634, 2010.

[186] E. S. Toberer, P. Rauwel, S. Gariel, J. Taftø, and G. J. Snyder. Composition and the thermoelectric performance of β-zn4sb3. *Journal of materials chemistry*, 20(44):9877–9885, 2010.

[187] M. Torres, F. Costa, D. Flahaut, K. Touati, S. Rasekh, N. Ferreira, J. Allouche, M. Depriester, M. Madre, A. Kovalevsky, et al. Significant enhancement of the thermoelectric performance in ca3co4o9 thermoelectric materials through combined strontium substitution and hot-pressing process. *Journal of the European Ceramic Society*, 39(4):1186–1192, 2019.

[188] M. Torres, M. Mora, H. Amaveda, M. Madre, and A. Sotelo. Effect of substrate on the microstructure and thermoelectric performances of sr-doped ca3co4o9 thick films. *Ceramics International*, 45(5):5431–5435, 2019.

[189] N. Toshima. Recent progress of organic and hybrid thermoelectric materials. *Synthetic Metals*, 225:3–21, 2017.

[190] T. M. Tritt. Thermoelectric materials: new directions and approaches: symposium held march 31-april 3, 1997, san francisco, california, usa. 478, 1997.

[191] T. Tsubota, M. Ohtaki, K. Eguchi, and H. Arai. Thermoelectric properties of al-doped zno as a promising oxide material for high-temperature thermoelectric conversion. *J. Mater. Chem.*, 7:85–90, 1997. doi: 10.1039/A602506D. URL http://dx.doi.org/10.1039/A602506D.

[192] R. Venkatasubramanian, T. Colpitts, E. Watko, M. Lamvik, and N. El-Masry. Mocvd of bi2te3, sb2te3 and their superlattice structures for thin-film thermoelectric applications. *Journal of crystal growth*, 170(1-4):817–821, 1997.

[193] A. A. Vu, S. F. Robertson, D. Ke, A. Bandyopadhyay, and S. Bose. Mechanical and biological properties of zno, sio2, and ag2o doped plasma sprayed hydroxyapatite coating for orthopaedic and dental applications. *Acta biomaterialia*, 92:325–335, 2019.

[194] H. Wang, J. Wang, X. Cao, and G. J. Snyder. Thermoelectric alloys between pbse and pbs with effective thermal conductivity reduction and high figure of merit. *Journal of Materials Chemistry A*, 2(9):3169–3174, 2014.

[195] J. Wang, X.-C. Liu, S.-Q. Xia, and X.-T. Tao. Ca1–xrexag1–ysb (re = la, ce, pr, nd, sm;$0 \leq x \leq 1; 0 \leq y \leq 1$): Interesting structural transformation and enhanced high-temperature thermoelectric performance. *Journal of the American Chemical Society*, 135(32):11840–11848, 2013. doi: 10.1021/ja403653m. URL https://doi.org/10.1021/ja403653m.

[196] S. Wang, J. Yang, T. Toll, J. Yang, W. Zhang, and X. Tang. Conductivity-limiting bipolar thermal conductivity in semiconductors. *Scientific Reports*, 5 (1), 5 2015. ISSN 2045-2322. doi: 10.1038/srep10136. URL https://doi.org/10.1038/srep10136.

[197] Y. Wang, Y. Sui, H. Fan, X. Wang, Y. Su, W. Su, and X. Liu. High temperature thermoelectric response of electron-doped camno3. *Chemistry of Materials*, 21(19):4653–4660, 2009.

[198] Y. Wang, Y. Sui, X. Wang, and W. Su. Effects of substituting la3+, y3+ and ce4+ for ca2+ on the high temperature transport and thermoelectric properties of camno3. *Journal of Physics D: Applied Physics*, 42(5):055010, 2009.

[199] M. A. White, K. J. Baumler, Y. Chen, A. Venkatesh, A. M. Medina-Gonzalez, A. J. Rossini, J. V. Zaikina, E. M. Chan, and J. Vela. Expanding the i–ii–v phase space: soft synthesis of polytypic ternary and binary zinc antimonides. *Chemistry of Materials*, 30(17):6173–6182, 2018.

[200] I. T. Witting, T. C. Chasapis, F. Ricci, M. Peters, N. A. Heinz, G. Hautier, and G. J. Snyder. The thermoelectric properties of bismuth telluride. *Advanced Electronic Materials*, 5(6):1800904, 2019.

[201] I. T. Witting, F. Ricci, T. C. Chasapis, G. Hautier, and G. J. Snyder. The thermoelectric properties of-type bismuth telluride: Bismuth selenide alloys. *Research*, 2020, 2020.

[202] L. Wollmann, A. K. Nayak, S. S. Parkin, and C. Felser. Heusler 4.0: Tunable materials. *Annual Review of Materials Research*, 47(1):247–270, 2017. doi: 10.1146/annurev-matsci-070616-123928. URL https://doi.org/10.1146/annurev-matsci-070616-123928.

[203] W. Wong-Ng, J. W. Lynn, Q. Huang, C. M. Brown, J. A. Kaduk, and G. Joshi. Observation of drastic change of generalized phonon density-of-states in nanostructured half-heusler using inelastic neutron scattering. *Applied Physics Letters*, 107(21):213901, 2015. doi: 10.1063/1.4936163. URL https://doi.org/10.1063/1.4936163.

[204] L. Wu, X. Li, S. Wang, T. Zhang, J. Yang, W. Zhang, L. Chen, and J. Yang. Resonant level-induced high thermoelectric response in indium-doped gete. *NPG Asia Materials*, 9(1):e343–e343, 2017.

[205] K. Xia, Y. Liu, S. Anand, G. J. Snyder, J. Xin, J. Yu, X. Zhao, and T. Zhu. Enhanced thermoelectric performance in 18-electron nb0. 8cosb half-heusler compound with intrinsic nb vacancies. *Advanced Functional Materials*, 28(9): 1705845, 2018.

[206] K. Xia, P. Nan, S. Tan, Y. Wang, B. Ge, W. Zhang, S. Anand, X. Zhao, G. J. Snyder, and T. Zhu. Short-range order in defective half-heusler thermoelectric crystals. *Energy Environ. Sci.*, 12:1568–1574, 2019. doi: 10.1039/C8EE03654C. URL http://dx.doi.org/10.1039/C8EE03654C.

[207] Y. Xia, S. Bhattacharya, V. Ponnambalam, A. Pope, S. Poon, and T. Tritt. Thermoelectric properties of semimetallic (zr, hf) cosb half-heusler phases. *Journal of applied physics*, 88(4):1952–1955, 2000.

[208] Y. Xiao and L. Zhao. Charge and phonon transport in pbte-based thermoelectric materials. npj quantum mater. 2018, 3, 55.

[209] H. Xie, H. Wang, C. Fu, Y. Liu, G. J. Snyder, X. Zhao, and T. Zhu. The intrinsic disorder related alloy scattering in zrnisn half-heusler thermoelectric materials. In *Scientific reports*, 2014.

[210] H. Xie, H. Wang, C. Fu, Y. Liu, G. J. Snyder, X. Zhao, and T. Zhu. The intrinsic disorder related alloy scattering in zrnisn half-heusler thermoelectric materials. *Scientific reports*, 4(1):1–6, 2014.

[211] W. Xie, A. Weidenkaff, X. Tang, Q. Zhang, J. Poon, and T. M. Tritt. Recent advances in nanostructured thermoelectric half-heusler compounds. *Nanomaterials*, 2(4):379–412, 2012. ISSN 2079-4991. doi: 10.3390/nano2040379. URL https://www.mdpi.com/2079-4991/2/4/379.

[212] J. Yan, F. Liu, G. Ma, B. Gong, J. Zhu, X. Wang, W. Ao, C. Zhang, Y. Li, and J. Li. Suppression of the lattice thermal conductivity in nbfesb-based half-heusler thermoelectric materials through high entropy effects. *Scripta Materialia*, 157:129–134, 2018.

[213] X. Yan, G. Joshi, W. Liu, Y. Lan, H. Wang, S. Lee, J. W. Simonson, S. J. Poon, T. M. Tritt, G. Chen, and Z. F. Ren. Enhanced thermoelectric figure of merit of p-type half-heuslers. *Nano Letters*, 11(2):556–560, 2011. doi: 10.1021/nl104138t. URL https://doi.org/10.1021/nl104138t. PMID: 21186782.

[214] L. Yang, Z.-G. Chen, G. Han, M. Hong, Y. Zou, and J. Zou. High-performance thermoelectric cu2se nanoplates through nanostructure engineering. *Nano Energy*, 16:367–374, 2015.

[215] K. Yazawa and A. Shakouri. 2016 15th ieee intersociety conference on thermal and thermomechanical phenomena in electronic systems (itherm). pages 1489–1493, 2016. doi: 10.1109/ITHERM.2016.7517724.

[216] L. Yin, J. Zhou, L. Gao, C. Zhao, J. Chen, X. Lu, J. Wang, J. Weng, and B. Feng. Characterization and osteogenic activity of srtio3/tio2 nanotube heterostructures on microporous titanium. *Surface and Coatings Technology*, 330:121–130, 2017.

[217] C.-C. Yu, H.-j. Wu, P.-Y. Deng, M. T. Agne, G. J. Snyder, and J. P. Chu. Thin-film metallic glass: an effective diffusion barrier for se-doped agsbte2 thermoelectric modules. *Scientific reports*, 7(1):1–9, 2017.

[218] J. Yu, C. Fu, Y. Liu, K. Xia, U. Aydemir, T. C. Chasapis, G. J. Snyder, X. Zhao, and T. Zhu. Unique role of refractory ta alloying in enhancing the figure of merit of nbfesb thermoelectric materials. *Advanced Energy Materials*, 8(1):1701313, 2018.

[219] J. Yu, K. Xia, X. Zhao, and T. Zhu. High performance p-type half-heusler thermoelectric materials. *Journal of Physics D: Applied Physics*, 51(11):113001, 2018.

[220] B. Yuan, B. Wang, L. Huang, X. Lei, L. Zhao, C. Wang, and Q. Zhang. Effects of sb substitution by sn on the thermoelectric properties of zrcosb. *Journal of Electronic Materials*, 46(5), 2017.

[221] W. Zeier, J. Schmitt, G. Hautier, U. Aydemir, Z. Gibbs, C. Felser, and G. Snyder. Engineering half-heusler thermoelectric materials using zintl chemistry. *Nature Reviews Materials*, 1(6), May 2016. ISSN 2058-8437. doi: 10.1038/natrevmats.2016.32.

[222] W. G. Zeier, S. Anand, L. Huang, R. He, H. Zhang, Z. Ren, C. Wolverton, and G. J. Snyder. Using the 18-electron rule to understand the nominal 19-electron half-heusler nbcosb with nb vacancies. *Chemistry of Materials*, 29(3): 1210–1217, 2017. doi: 10.1021/acs.chemmater.6b04583. URL https://doi.org/10.1021/acs.chemmater.6b04583.

[223] F. Zelenka, P. Brož, J. Vřešt'ál, J. Buršík, A. Zemanová, G. Rogl, and P. Rogl. Study of thermal stability of half-heusler alloys tife1. 33sb and tixnb1-xfesb (x= 0, 0.15) by differential thermal analysis and knudsen effusion method. *Calphad*, 74:102292, 2021.

[224] D.-B. Zhang, H.-Z. Li, B.-P. Zhang, D.-d. Liang, and M. Xia. Hybrid-structured zno thermoelectric materials with high carrier mobility and reduced thermal conductivity. *RSC advances*, 7(18):10855–10864, 2017.

[225] H. Zhang, Y. Wang, L. Huang, S. Chen, H. Dahal, D. Wang, and Z. Ren. Synthesis and thermoelectric properties of n-type half-heusler compound vcosb with valence electron count of 19. *Journal of Alloys and Compounds*, 654: 321–326, 2016. ISSN 0925-8388. doi: https://doi.org/10.1016/j.jallcom.2015.09.082. URL https://www.sciencedirect.com/science/article/pii/S0925838815310598.

[226] Q. Zhang, B. Liao, Y. Lan, K. Lukas, W. Liu, K. Esfarjani, C. Opeil, D. Broido, G. Chen, and Z. Ren. High thermoelectric performance by resonant dopant indium in nanostructured snte. *Proceedings of the National Academy of Sciences*, 110(33):13261–13266, 2013.

[227] X. Zhang, Z. Bu, S. Lin, Z. Chen, W. Li, and Y. Pei. Gete thermoelectrics. *Joule*, 4(5):986–1003, 2020.

[228] Y. Zhang, Y.-J. Heo, M. Park, and S.-J. Park. Recent advances in organic thermoelectric materials: Principle mechanisms and emerging carbon-based green energy materials. *Polymers*, 11(1):167, 2019.

[229] D. Zhao, M. Zuo, Z. Wang, X. Teng, and H. Geng. Synthesis and thermoelectric properties of tantalum-doped zrnisn half-heusler alloys. *Functional Materials Letters*, 07(03):1450032, 2014. doi: 10.1142/S1793604714500325. URL https://doi.org/10.1142/S1793604714500325.

[230] D. Zhao, L. Wang, L. Bo, and D. Wu. Synthesis and thermoelectric properties of ni-doped zrcosb half-heusler compounds. *Metals*, 8(1), 2018. ISSN 2075-4701. doi: 10.3390/met8010061. URL https://www.mdpi.com/2075-4701/8/1/61.

[231] D. Zhao, M. Zuo, L. Bo, and Y. Wang. Synthesis and thermoelectric properties of pd-doped zrcobi half-heusler compounds. *Materials*, 11:728, 05 2018. doi: 10.3390/ma11050728.

[232] L. Zhao, S. Lo, Y. Zhang, H. Sun, G. Tan, C. Uher, C. Wolverton, V. Dravid, and M. Kanatzidis. Ultralow thermal conductivity and high thermoelectric figure of merit in snse crystals. *Nature*, 508(7496):373–377, 2014. ISSN 0028-0836. doi: 10.1038/nature13184.

[233] L.-D. Zhao, J. He, D. Berardan, Y. Lin, J.-F. Li, C.-W. Nan, and N. Dragoe. Bicuseo oxyselenides: new promising thermoelectric materials. *Energy & Environmental Science*, 7(9):2900–2924, 2014.

[234] Y. Zhao, C. Rinzler, and A. Allanore. Molten semiconductors for high temperature thermoelectricity. 6(3):N3010–N3016, dec 2016. doi: 10.1149/2.0031703jss. URL https://doi.org/10.1149/2.0031703jss.

[235] Y. Zheng, X. Y. Tan, X. Wan, X. Cheng, Z. Liu, and Q. Yan. Thermal stability and mechanical response of bi2te3-based materials for thermoelectric applications. *ACS Applied Energy Materials*, 3(3):2078–2089, 2020. doi: 10.1021/acsaem.9b02093. URL https://doi.org/10.1021/acsaem.9b02093.

[236] J. Zhou, H. Zhu, T.-H. Liu, Q. Song, R. He, J. Mao, Z. Liu, W. Ren, B. Liao, D. J. Singh, et al. Large thermoelectric power factor from crystal symmetry-protected non-bonding orbital in half-heuslers. *Nature communications*, 9(1):1–9, 2018.

[237] M. Zhou, Z. M. Gibbs, H. Wang, Y. Han, C. Xin, L. Li, and G. J. Snyder. Optimization of thermoelectric efficiency in snte: the case for the light band. *Physical Chemistry Chemical Physics*, 16(38):20741–20748, 2014.

[238] H. Zhu, R. He, J. Mao, Q. Zhu, C. Li, J. Sun, W. Ren, Y. Wang, Z. Liu, Z. Tang, et al. Discovery of zrcobi based half heuslers with high thermoelectric conversion efficiency. *Nature communications*, 9(1):1–9, 2018.

[239] P. Zhu, Y. Imai, Y. Isoda, Y. Shinohara, X. Jia, and G. Zou. Enhanced thermoelectric properties of pbte alloyed with sb2te3. *Journal of Physics: Condensed Matter*, 17(46):7319, 2005.

[240] T. Zhu, C. Fu, H. Xie, Y. Liu, and X. Zhao. High efficiency half-heusler thermoelectric materials for energy harvesting. *Advanced Energy Materials*, 5(19):1500588, 2015. doi: https://doi.org/10.1002/aenm.201500588. URL https://onlinelibrary.wiley.com/doi/abs/10.1002/aenm.201500588.

[241] T. Zhu, H. Bai, J. Zhang, G. Tan, Y. Yan, W. Liu, X. Su, J. Wu, Q. Zhang, and X. Tang. Realizing high thermoelectric performance in sb-doped ag2te compounds with a low-temperature monoclinic structure. *ACS Applied Materials & Interfaces*, 12(35):39425–39433, 2020.

[242] D. F. Zou, S. H. Xie, Y. Y. Liu, J. G. Lin, and J. Y. Li. Electronic structure and thermoelectric properties of half-heusler zr0.5hf0.5nisn by first-principles calculations. *Journal of Applied Physics*, 113(19):193705, 2013. doi: 10.1063/1.4804939. URL https://doi.org/10.1063/1.4804939.